

REPORT DOCUMENTATION PAGE

1

Form Approved OMB NO. 0704-0188

The public reporting burden for this collection of information is estimated to average 1 hour per response, including the time for reviewing instructions, searching existing data sources, gathering and maintaining the data needed, and completing and reviewing the collection of information. Send comments regarding this burden estimate or any other aspect of this collection of information, including suggestions for reducing this burden, to Washington Headquarters Services, Directorate for Information Operations and Reports, 1215 Jefferson Davis Highway, Suite 1204, Arlington VA, 22202-4302. Respondents should be aware that notwithstanding any other provision of law, no person shall be subject to any penalty for failing to comply with a collection of information if it does not display a currently valid OMB control number.

PLEASE DO NOT RETURN YOUR FORM TO THE ABOVE ADDRESS.

1. REPORT DATE (DD-MM-YYYY) 15-09-2014	2. REPORT TYPE Final Report	3. DATES COVERED (From - To) 15-Jul-2010 - 14-Jul-2013		
4. TITLE AND SUBTITLE Particle Methods for Electromagnetic Wave Propagation Problems		5a. CONTRACT NUMBER W911NF-10-1-0305		
		5b. GRANT NUMBER		
		5c. PROGRAM ELEMENT NUMBER 611102		
6. AUTHORS R. Janaswamy		5d. PROJECT NUMBER		
		5e. TASK NUMBER		
		5f. WORK UNIT NUMBER		
7. PERFORMING ORGANIZATION NAMES AND ADDRESSES University of Massachusetts - Amherst Research Administration Building 70 Butterfield Terrace Amherst, MA 01003 -9242		8. PERFORMING ORGANIZATION REPORT NUMBER		
9. SPONSORING/MONITORING AGENCY NAME(S) AND ADDRESS (ES) U.S. Army Research Office P.O. Box 12211 Research Triangle Park, NC 27709-2211		10. SPONSOR/MONITOR'S ACRONYM(S) ARO		
		11. SPONSOR/MONITOR'S REPORT NUMBER(S) 57313-EL.9		
12. DISTRIBUTION AVAILABILITY STATEMENT Approved for Public Release; Distribution Unlimited				
13. SUPPLEMENTARY NOTES The views, opinions and/or findings contained in this report are those of the author(s) and should not be construed as an official Department of the Army position, policy or decision, unless so designated by other documentation.				
14. ABSTRACT 1. A rigorous proof of the relation between the solutions of wave and telegraph equations in 3D via a random time induced by a Poisson process has been provided using techniques of stochastic calculus. Application of this relation to wave propagation in dispersive media (Lorentz and Drude media) is discussed. 2. Sparse grid collocation methods that are used for uncertainty quantification have been applied to electromagnetic wave propagation problems. Two applications are considered: the first application involves wave propagation in				
15. SUBJECT TERMS Wave Propagation, Stochastic Methods				
16. SECURITY CLASSIFICATION OF: a. REPORT UU		17. LIMITATION OF ABSTRACT UU	15. NUMBER OF PAGES	19a. NAME OF RESPONSIBLE PERSON Ramakrishna Janaswamy
b. ABSTRACT UU		c. THIS PAGE UU		19b. TELEPHONE NUMBER 413-545-0937

Report Title

Particle Methods for Electromagnetic Wave Propagation Problems

ABSTRACT

1. A rigorous proof of the relation between the solutions of wave and telegraph equations in 3D via a random time induced by a Poisson process has been provided using techniques of stochastic calculus. Application of this relation to wave propagation in dispersive media (Lorentz and Drude media) is discussed.
2. Sparse grid collocation methods that are used for uncertainty quantification have been applied to electromagnetic propagation problems. Two applications are considered--the first application involves waves propagating in dielectric media with uncertain permittivities and permeabilities, in which several cases with increasing random space dimensionality are exemplified. The objective in the second application is to compute expected signal strength above flat Earth surface at ranges far from transmitter location, where randomness is present due to uncertain refractive index of the atmosphere. The uncertainty is extracted from published measurements, and constitutes long-term variation. Two different sparse grid algorithms are demonstrated and the deterministic evaluators are accessed as a black box by the sparse grid algorithms. Strengths of the two algorithms are differentiated depending on the characteristics of the randomness.

Enter List of papers submitted or published that acknowledge ARO support from the start of the project to the date of this printing. List the papers, including journal references, in the following categories:

(a) Papers published in peer-reviewed journals (N/A for none)

Received Paper

- 09/15/2014 10.00 Selman Ozbayat, Ramakrishna Janaswamy. Effective Local Absorbing Boundary Conditions for a Finite Difference Implementation of the Parabolic Equation, IEEE Transactions on Antennas and Propagation, (05 2011): 0. doi: 10.1109/TAP.2011.2122300
- 09/15/2014 11.00 R Janaswamy. Transitional probabilities for the 4-state random walk on a lattice, Journal of Physics A: Mathematical and Theoretical, (04 2008): 0. doi: 10.1088/1751-8113/41/15/155306
- 09/15/2014 12.00 R. Janaswamy. Transitional probabilities for the four-state random walk on a lattice in the presence of partially reflecting boundaries, Journal of Mathematical Physics, (2009): 0. doi: 10.1063/1.3122768
- 09/15/2014 13.00 Ramakrishna Janaswamy. On the EM Degrees of Freedom in Scattering Environments, IEEE Transactions on Antennas and Propagation, (10 2011): 0. doi: 10.1109/TAP.2011.2163776
- 10/01/2013 6.00 R. Janaswamy. On random time and on the relation between wave and telegraph equations, IEEE Transactions on Antennas and Propagation, (05 2013): 0. doi: 10.1109/TAP.2013.2237739
- 10/01/2013 7.00 Ramakrishna Janaswamy. Errata to "On random time and on the relation between wave and telegraph equations" [May 13 2735-2744], IEEE Transactions on Antennas and Propagation, (06 2013): 0. doi: 10.1109/TAP.2013.2262155
- 10/01/2013 8.00 Ramakrishna Janaswamy. Direct Solution of Current Density Induced on a Rough Surface by Forward Propagating Waves, IEEE Transactions on Antennas and Propagation, (07 2013): 0. doi: 10.1109/TAP.2013.2254692

TOTAL: **7**

(b) Papers published in non-peer-reviewed journals (N/A for none)

Received

Paper

TOTAL:

Number of Papers published in non peer-reviewed journals:

(c) Presentations

Number of Presentations: 0.00

Non Peer-Reviewed Conference Proceeding publications (other than abstracts):

Received

Paper

TOTAL:

Number of Non Peer-Reviewed Conference Proceeding publications (other than abstracts):

Peer-Reviewed Conference Proceeding publications (other than abstracts):

Received Paper

08/29/2011 1.00 S. Ozbayat, R. Janaswamy. A Stochastic Formulation to Telegrapher's Equationin Higher Dimensions, 2011 IEEE Internation Symposium on Antennas and Propagation. 03-JUL-11, . : ,

08/30/2012 2.00 R. Janaswamy. Evaluation of Certain Integrals Using the Stochastic Formulation of the Lossy Wave Equationi, 2012 IEEE International Symposium on Antennas & Propagation. 09-JUL-12, . : ,

10/01/2013 5.00 Selman Ozbayat, Ramakrishna Janaswamy. Quantification of High DImensional Uncertainty in Propagation Over Random Media, 2013 IEEE International Symposium on Antennas and Propagation & USNC/URSI National Radio Science Meeting. 08-JUL-13, . : ,

TOTAL: **3**

Number of Peer-Reviewed Conference Proceeding publications (other than abstracts):

(d) Manuscripts

Received Paper

08/30/2012 3.00 R. Janaswamy. On Random Time and on the Relation Between Wave and Telegraph Equations, IEEE Antennas and Propagaton Transactions (03 2012)

08/30/2012 4.00 R. Janaswamy. Exact Current Density on a Rough Surface Induced by Forward Propagating Waves, IEEE Antennas and Propagaton Transactions (07 2012)

09/15/2014 14.00 . Assessment of Adaptive Sparse Grid Collocation Methods in Wave Propagation Environments with Uncertainty, ()

TOTAL: **3**

Books

Received Book

TOTAL:

Received Book Chapter

TOTAL:

Patents Submitted**Patents Awarded****Awards**

Inducted into the IEEE Wave Propagation Standards Committee

Graduate Students

<u>NAME</u>	<u>PERCENT SUPPORTED</u>	Discipline
Selman Ozbayat	0.80	
Hua Bai	0.10	
Narayan Balu	0.10	
FTE Equivalent:	1.00	
Total Number:	3	

Names of Post Doctorates

<u>NAME</u>	<u>PERCENT SUPPORTED</u>
FTE Equivalent:	
Total Number:	

Names of Faculty Supported

<u>NAME</u>	<u>PERCENT SUPPORTED</u>	National Academy Member
Ramakrishna Janaswamy	0.09	No
FTE Equivalent:	0.09	
Total Number:	1	

Names of Under Graduate students supported

<u>NAME</u>	<u>PERCENT SUPPORTED</u>	Discipline
Casey Wolseifer	0.25	Electrical Engineering
FTE Equivalent:	0.25	
Total Number:	1	

Student Metrics

This section only applies to graduating undergraduates supported by this agreement in this reporting period

The number of undergraduates funded by this agreement who graduated during this period: 1.00

The number of undergraduates funded by this agreement who graduated during this period with a degree in science, mathematics, engineering, or technology fields:..... 1.00

The number of undergraduates funded by your agreement who graduated during this period and will continue to pursue a graduate or Ph.D. degree in science, mathematics, engineering, or technology fields:..... 1.00

Number of graduating undergraduates who achieved a 3.5 GPA to 4.0 (4.0 max scale):..... 1.00

Number of graduating undergraduates funded by a DoD funded Center of Excellence grant for Education, Research and Engineering:..... 0.00

The number of undergraduates funded by your agreement who graduated during this period and intend to work for the Department of Defense 0.00

The number of undergraduates funded by your agreement who graduated during this period and will receive scholarships or fellowships for further studies in science, mathematics, engineering or technology fields: 0.00

Names of Personnel receiving masters degrees

<u>NAME</u>
Hua Bai
Total Number:

Names of personnel receiving PhDs

<u>NAME</u>
Selman Ozbayat
Total Number:

Names of other research staff

<u>NAME</u>	<u>PERCENT SUPPORTED</u>
FTE Equivalent:	
Total Number:	

Sub Contractors (DD882)

Inventions (DD882)

In this project we were exploring the use of particle-based techniques (viz. those based on random walks or Poisson processes) for solving wave propagation problems. By far, the biggest motivation for considering these particle-based methods is that they are very attractive for implementing on parallel machines without requiring any mutual communication between nodes. The model equations for time-harmonic case included the Helmholtz equation and the parabolic equation. The latter is an approximation of the Helmholtz equation and assumes the wave propagation angles to deviate slightly (less than or equal to 15 degrees in practice) from a nominal direction. In terrestrial radiowave propagation problems, this nominal direction is often taken to be the horizontal direction. The model equations for time-instantaneous case included the higher dimensional wave equation and the telegrapher equation. The telegrapher's equation is relevant because a variation of it is encountered in the treatment of pulse propagation in a dispersive medium.

In 2D, interference phenomena that is hallmark of time-harmonic wave propagation can still be modeled by random walk of particles by assigning parity or spin to particles in addition to translational motion [8]. We first considered TM propagation (field vanishing on the boundaries) in a parallel plate waveguide by the 4-state random walk (FRW) subject to Dirichlet boundary conditions [9]. In order to accommodate semi-infinite boundaries with the parabolic equation, we first worked out an efficient local transparent boundary condition for low grazing angle waves for use with Crank-Nicolson finite-difference implementations in [10]. Previous implementations of the parabolic equation relied on non-local transparent boundary condition, which can computationally very expensive. Our solution should significantly reduce the implementation of the transparent boundary conditions.

Even though the 4-state particle-based technique could reproduce results obtained by traditional approaches, the method was limited to rather small physical dimension along the direction of propagation because the number of possible trajectories increased exponentially with range (there will be two possibilities at the first range step, four possibilities at the second range step, and so on).

A second paradigm we pursued was the treatment of telegraph equation by particle -based methods [1]. Most previous works related to this problem concentrated on building random walk models tied to the Brownian motion. However, it had previously been shown by Kac (demonstrated for 1-D with zero initial velocity conditions and conjectured for higher dimensions) in the early 70s that the solution of a lossy wave equation (which is a modified telegrapher's equation) can be obtained from that of a corresponding lossless wave equation by simply changing the time variable in the latter by a randomized time variable that depends on a Poisson process and then performing an averaging operation with respect to the underlying Poisson process. The statistics of the Poisson process are governed by the loss present in the medium. This resulted in a very interesting stochastic representation for the solution of telegrapher equation, which could be conveniently implemented on a parallel type of computing machine. In [4] we presented 1) a mathematical proof of Kac's conjecture in higher space dimensions using concepts from stochastic calculus; no such formal proof existed in the literature prior to this work, 2) given the important role played by the random time in such stochastic representations, we presented a new expression for the first order statistics of the random time, and 3) demonstrated how the stochastic representation can be utilized to arrive at some useful schemes for computing multidimensional fields in dispersive media. In particular, the Lorentz and Drude media were considered in [4]. Evaluation of some integrals arising in wave propagation by such Poisson process driven random time was presented in [2].

A third major focus of this project was developing techniques for quantifying random uncertainties in wave propagation problems. Sparse grid collocation methods were used in [3], [6] for uncertainty quantification in electromagnetic propagation problems. Two applications were considered. The first application involved waves propagating in dielectric media with uncertain permittivities and

Permeabilities. Several cases with increasing random space dimensionality were exemplified. The objective in the second application was to compute expected signal strength above flat Earth surface at ranges far from transmitter location, where randomness was present due to uncertain refractive index of the atmosphere. The uncertainty was extracted from published measurements and constituted for long-term variations. Two different sparse grid algorithms were demonstrated in [6], and the deterministic evaluators were accessed as a black box by the sparse grid algorithms.

Other relevant problems that were addressed in the current project were (1) Simple formulas were derived for the electromagnetic degrees of freedom in random scattering environments for a network of nodes communicating with each other [7]. Both near fields and far-fields were considered in the formulation. (2) A new Volterra integral equation of the second kind with square integrable kernel was derived for paraxial propagation of radiowaves over a gently varying, perfectly conducting rough surface [5]. The formulation is valid for both deterministic and random rough surfaces. The integral equation was solved exactly in terms of an infinite series and the necessary and sufficient conditions for the solution to exist and converge were established. Super exponential convergence of the Neumann series for arbitrary surface slope was established through asymptotic analysis. Expressions were derived for the determination of the number of terms needed to achieve a given accuracy, the latter depending on the parameters of the rough surface, the frequency of operation and the maximum range. Numerical results with truncated series were compared with that obtained by solving the integral equation numerically for a sinusoidal surface, Gaussian hill, and a random rough surface with Pierson–Moskowitz roughness spectrum. The first term on the series solution by itself yields the well known Ament roughness reduction factor for determining the mean field over a random rough surface. This term will only incorporate the variance and mean of the rough surface. Correlation function of the rough

surface will enter through the second term of the Neumann series and will open the door for the availability of analytical formulas for the mean complex field and the mean power. Availability of such analytical expressions for the mean field will be useful in propagation modeling for radar detection and wireless communications and in the electronic and thermal modeling of nano-devices.

References

- [1] S. Ozbayat and R. Janaswamy, ``A stochastic formulation of telegraph equation in higher dimensions," 2011 IEEE International Symposium on Antennas and Propagation, July 6-10, 2011, Spokane, WA.
- [2] R. Janaswamy, ``Evaluation of certain integrals using stochastic formulation of the lossy wave equation," paper 563-7, 2012 IEEE International Symposium on Antennas and Propagation, July 8-14, 2012, Chicago, IL.
- [3] S. Ozbayat and R. Janaswamy, ``Quantification of high dimensional uncertainty in propagation over random terrain," paper 518.5, 2013 IEEE International Symposium on Antennas and Propagation, July 7-13, Orlando, FL.
- [4] R. Janaswamy, ``On random time and on the relation between wave and telegraph equations," IEEE Transactions Antennas Propagat., vol. 61(5), pp. 2735-2744, May 2013.
- [5] R. Janaswamy, ``Direct solution of current density induced on a rough surface by forward propagating waves," IEEE Trans. Antennas Propagat., vol. 61(7), pp. 3728-3738, July 2013.
- [6] S. Ozbayat and R. Janaswamy, ``Efficiency of adaptive sparse grid collocation methods in wave propagation environments with uncertainty," submitted IEEE Trans. Antennas Propagat., September 2013.
- [7] R. Janaswamy, ``On the EM degrees of freedom in scattering environments," IEEE Trans Antennas Propagat., vol. 59(10), 3872-3881, October 2011.
- [8] R. Janaswamy, ``Transitional probabilities for the 4-state random walk on a lattice," J. Phys. A: Math. Theor., vol. 41, 155306 (11pp), 2008.
- [9] R. Janaswamy, ``Transitional probabilities for the four-state random walk on a lattice in the presence of partially reflecting boundaries," J. Math. Phys., vol. 50, 053301 (11pp), 2009.
- [10] S. Ozbayat and R. Janaswamy, ``Effective Local absorbing boundary conditions for a finite difference implementation of the parabolic equation," IEEE Trans. Antennas Propagat., vol. 59 (5), pp. 1616-1625, May 2011.

Technology Transfer

UMassAmherst



A Stochastic Formulation to Telegrapher's Equation in Higher Dimensions

Selman Özbayat and Ramakrishna Janaswamy

Electrical and Computer Engineering
University of Massachusetts Amherst

Spokane, WA
July 6th, 2011



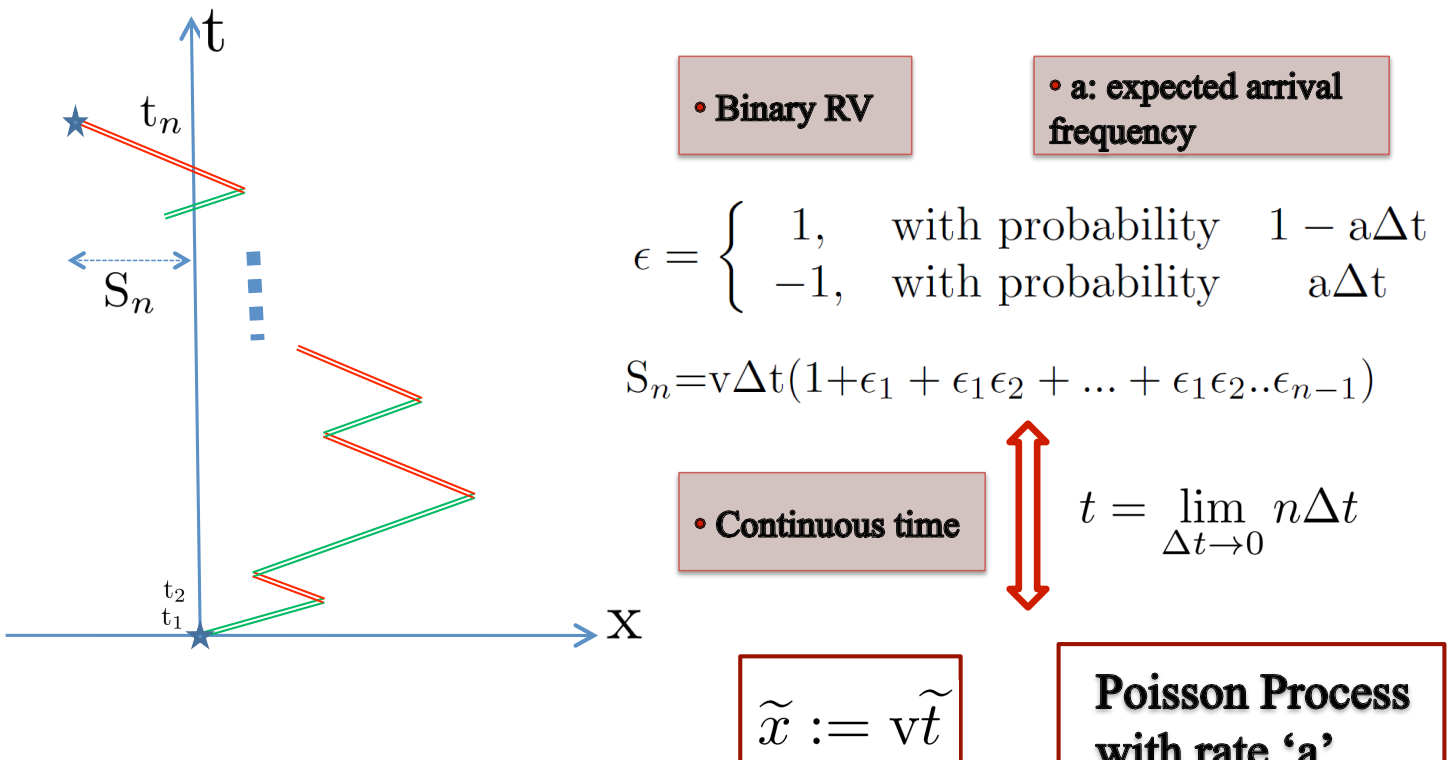


Motivation

- Particle based Random Walks (RW)
- Parallel Realizations
- No mesh generation
- Promise: Complex and intricate geometries
- Telegrapher's Equation (TE)
 - Lossy Wave Equation in Time Domain
 - Loss \longleftrightarrow Poisson Process

UMassAmherst

Goldstein (1951)-Kac (1974) Approach: Collisions in 1-D



UMassAmherst

Rare events in continuous-time: Poisson RP

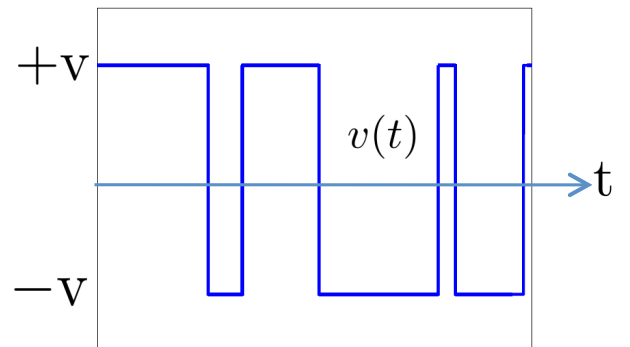
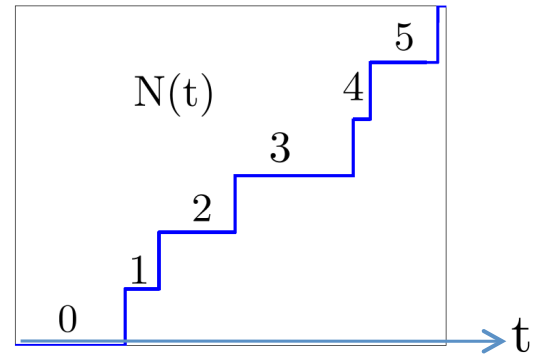
$$\text{Prob } \{N(t) = k\} = e^{-at} \frac{(at)^k}{k!}$$

- Continuous analogue of S_n

$$\begin{aligned}\tilde{x}(t) &= \int v(\tau) d\tau = \int_0^t v(-1)^{N(\tau)} d\tau \\ &= vt\end{aligned}$$

- Random time

$$\tilde{t} := \int_0^t (-1)^{N(\tau)} d\tau \quad |\tilde{t}| < t$$



UMassAmherst

Relation to Wave Equation

•1-D WE

$$\frac{\partial^2 F}{\partial x^2} = \frac{1}{v^2} \frac{\partial^2 F}{\partial t^2}$$

• Initial
Conditions

$$\begin{aligned}\phi(x) &:= F(x, t=0) \\ g(x) &:= \left. \frac{\partial F(x,t)}{\partial t} \right|_{t=0}\end{aligned}$$

• Solution:
d'Alembert's
Formula

$$F_{WE}(x, t) = \frac{1}{2} [\phi(x - vt) + \phi(x + vt)] + \frac{1}{2v} \int_{x-vt}^{x+vt} g(\zeta) d\zeta$$

•1-D TE

$$\frac{\partial^2 F}{\partial x^2} = \frac{1}{v^2} \frac{\partial^2 F}{\partial t^2} + \frac{2a}{v^2} \frac{\partial F}{\partial t}$$

$$F_{TE}(x, t) = \left\langle F_{WE}(x, \tilde{t}) \right\rangle_{N_r}$$

Randomize the
time variable

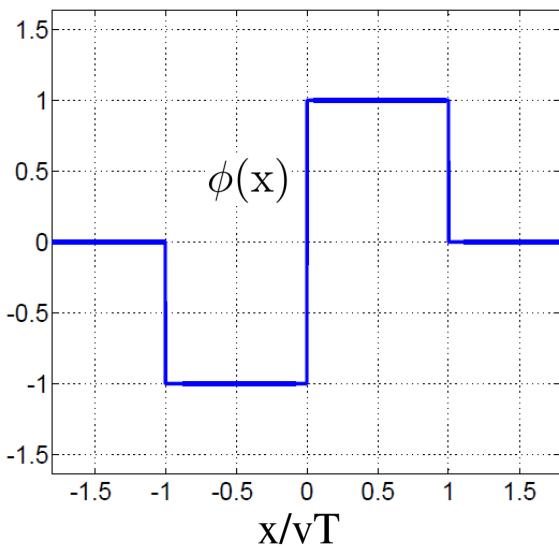
$$t \leftrightarrow \tilde{t} = \int_0^t (-1)^{N(\tau)} d\tau$$

Arithmetic average of
randomized functions

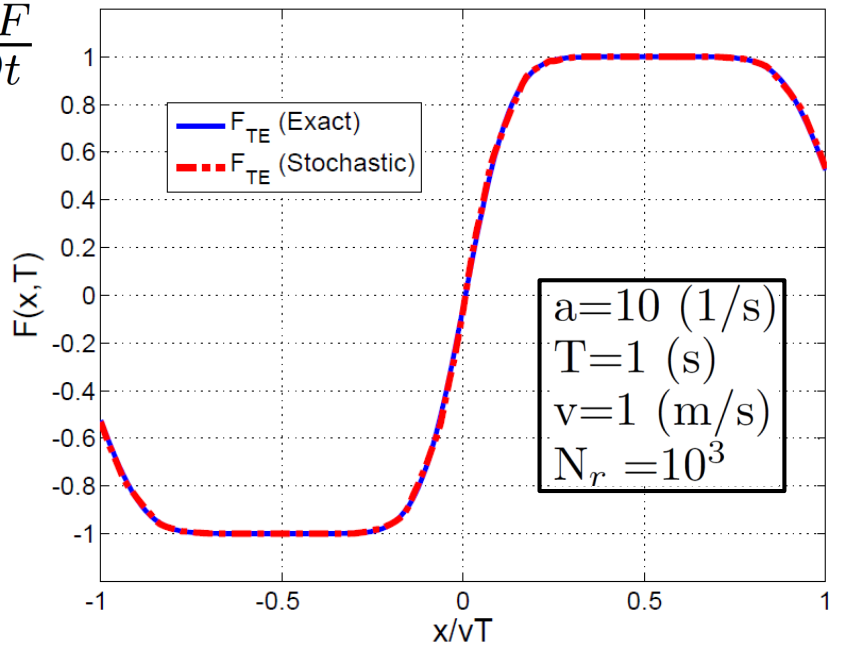
UMassAmherst

Results in 1-D: $\phi(x) \neq 0$ $g(x)=0$

$$\frac{\partial^2 F}{\partial x^2} = \frac{1}{v^2} \frac{\partial^2 F}{\partial t^2} + \frac{2a}{v^2} \frac{\partial F}{\partial t}$$



$$F_{TE}(x, t) = \frac{1}{2} \left\langle \phi(x - vt) + \phi(x + vt) \right\rangle$$

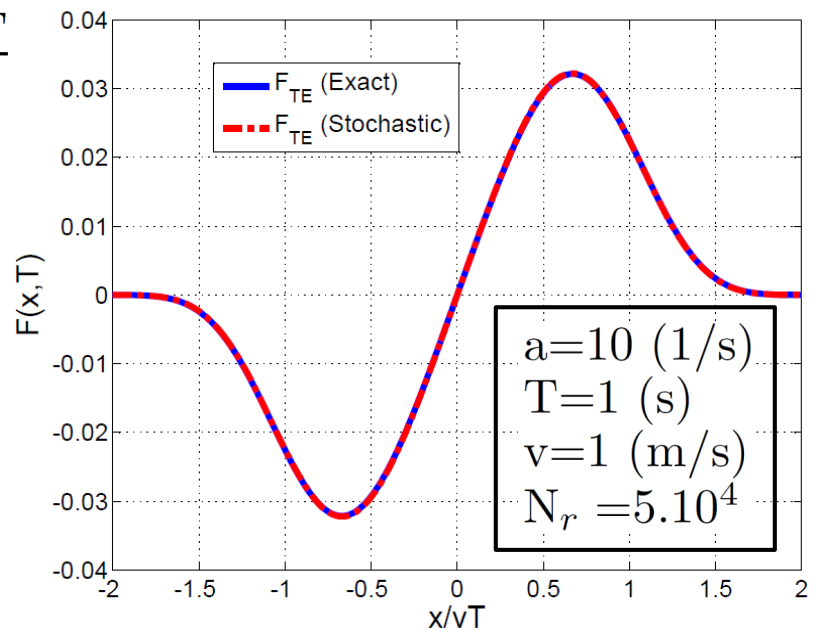
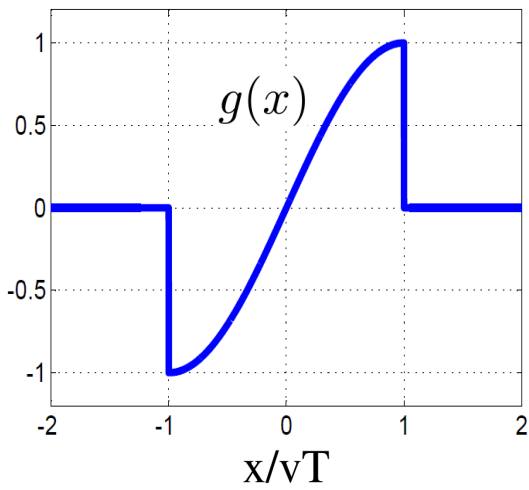


- TE solution : spread out in space

UMassAmherst

Non-zero initial rate: $\phi(x) = 0 \quad g(x) \neq 0$

$$\frac{\partial^2 F}{\partial x^2} = \frac{1}{v^2} \frac{\partial^2 F}{\partial t^2} + \frac{2a}{v^2} \frac{\partial F}{\partial t}$$



$$F_{TE}(x, t) = \frac{1}{2v} \left\langle \int_{x-v\tilde{t}}^{x+v\tilde{t}} g(\zeta) d\zeta \right\rangle$$

- Several attempts for higher dimensional problems

UMassAmherst

A 2-D Model: Orsingher, 1986

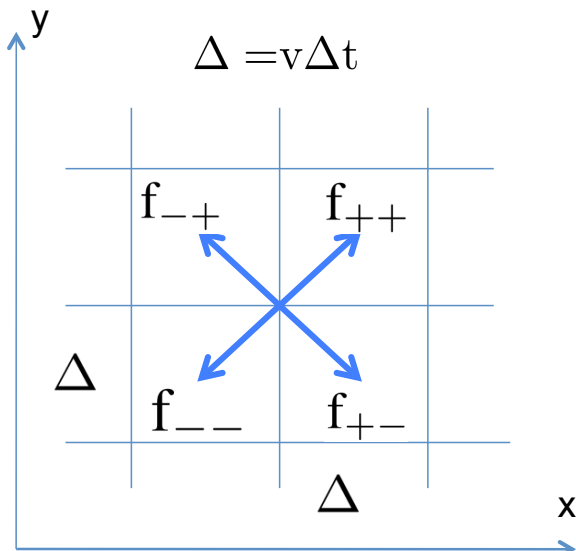
$$\frac{\partial^2 F}{\partial t^2} + 2a \frac{\partial F}{\partial t} = \frac{v^2}{2} \nabla^2 F \quad \boxed{2D-TE}$$

4-state walk

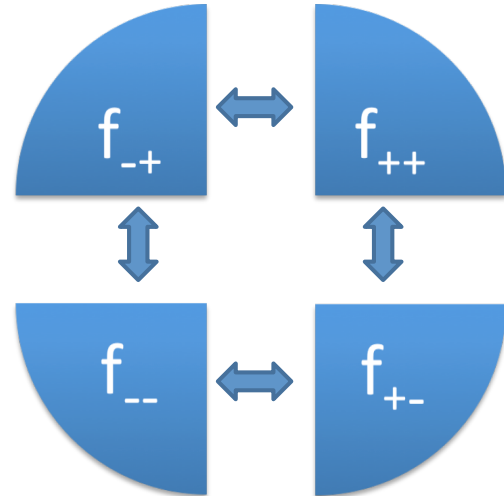
Scattering events:
Poisson (a)

Vertical or
horizontal move
during each Δt

No back-
scattering

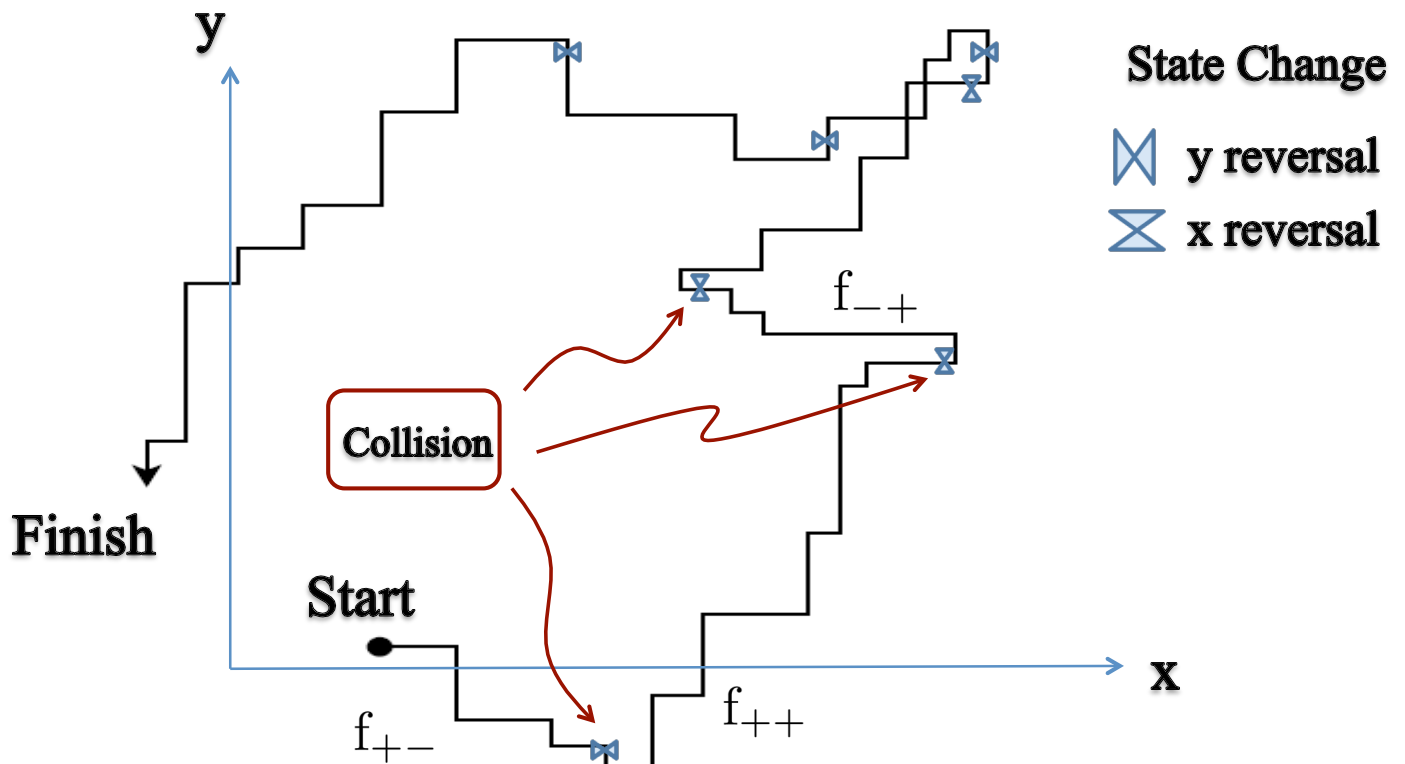


$$F = F_{++} + F_{+-} + F_{-+} + F_{--}$$



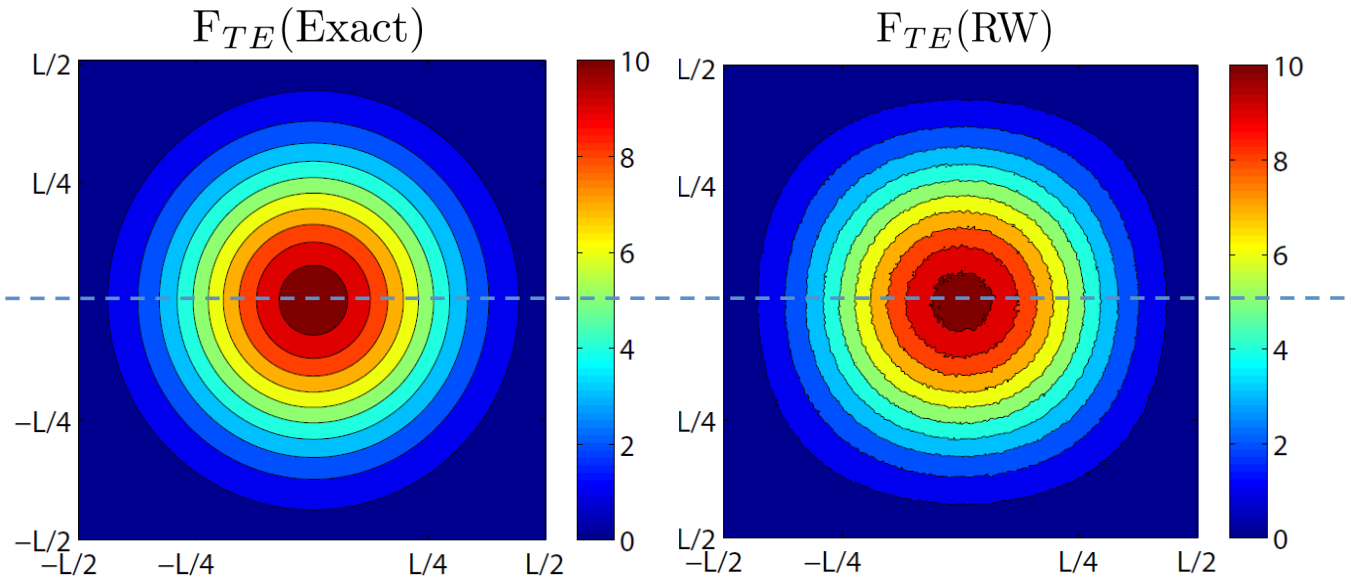
UMassAmherst

Sample Trajectory



UMassAmherst

IVP in 2D: $\phi(\rho) = \frac{\delta(\rho)}{2\pi\rho}$ $g(\rho) = 0$



$$\frac{\partial^2 F}{\partial t^2} + 2a \frac{\partial F}{\partial t} = \frac{v^2}{2} \nabla^2 F$$

$$a=20 \text{ (1/s)} \quad v=1 \text{ (m/s)}$$

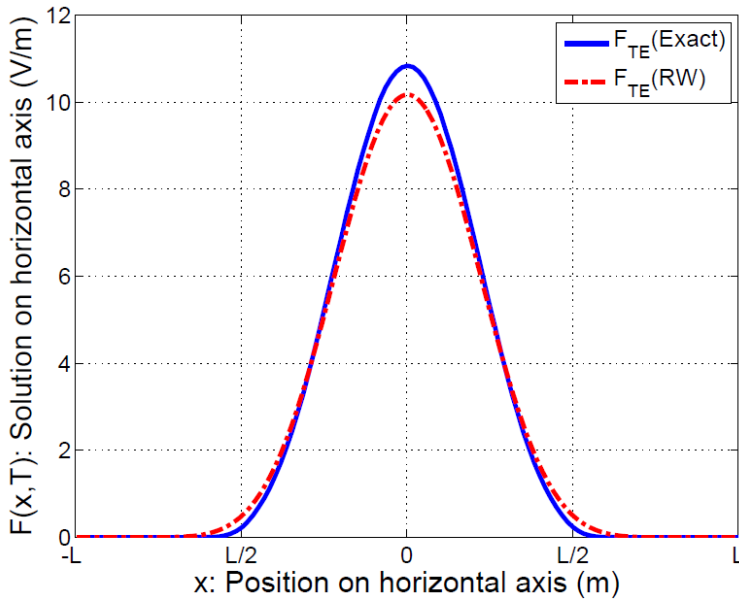
$$L=vT=0.6 \text{ (m)} \quad N_r=2.10^8$$

$$\Delta t = 5.10^{-3} \text{ (s)}$$

10

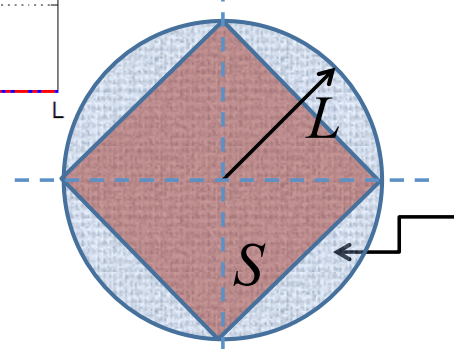
UMassAmherst

IVP in 2D: $\phi(\rho) = \frac{\delta(\rho)}{2\pi\rho}$ $g(\rho) = 0$



$$L=vT$$

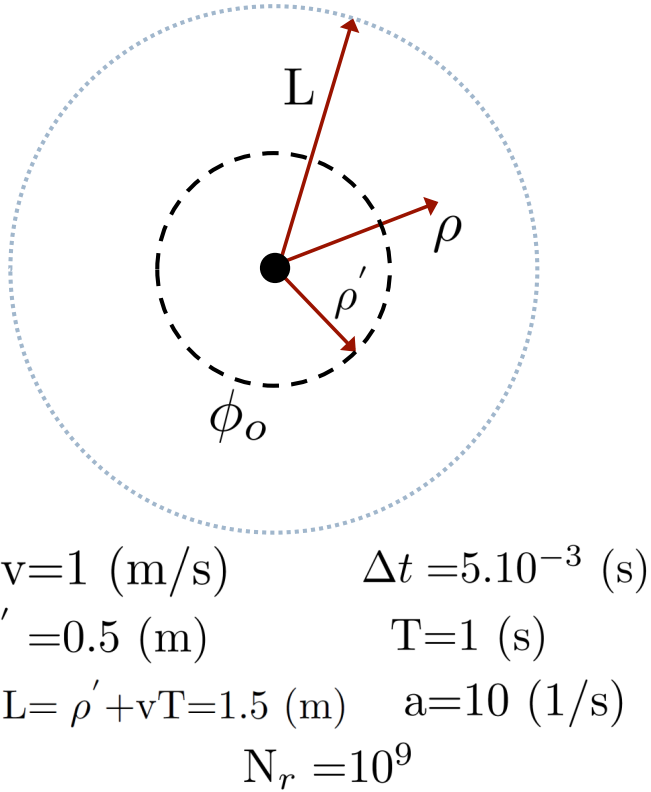
- Non-trivial normalization problem
- Not all IC's equally inaccurate
- Smaller "a": worse convergence



Not populated outside S :
non-isotropic RW

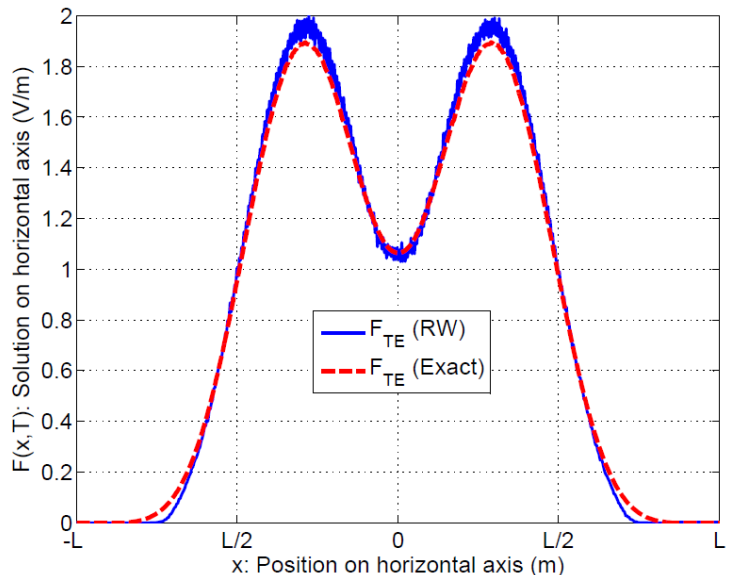
UMassAmherst

Problem 2: Distributed initial source



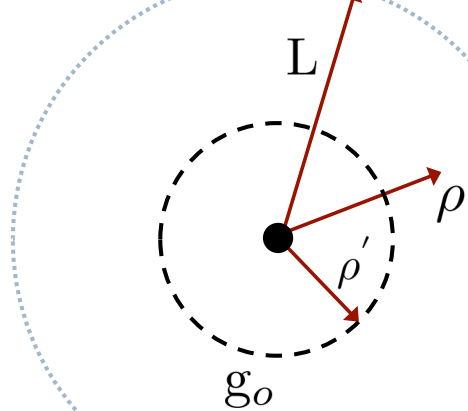
$$\phi(\rho) := F(\rho, t=0) = \begin{cases} \phi_o, & \rho = \rho' \\ 0, & \text{elsewhere} \end{cases}$$

$$g(\rho) := \frac{\partial F(\rho, t)}{\partial t} \Big|_{t=0} = 0$$



UMassAmherst

Problem 3: Distributed initial rate



$$v = 1 \text{ (m/s)}$$

$$\Delta t = 5 \cdot 10^{-3} \text{ (s)}$$

$$\rho' = 0.5 \text{ (m)}$$

$$T = 1 \text{ (s)}$$

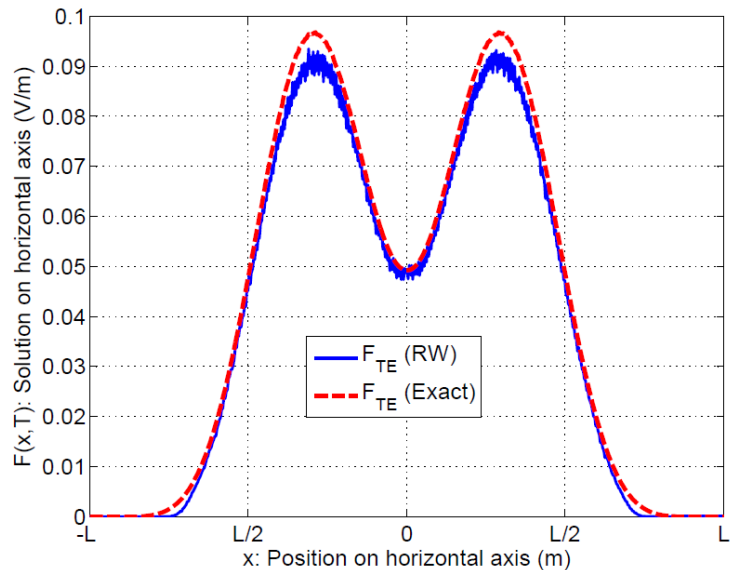
$$L = \rho' + vT = 1.5 \text{ (m)}$$

$$a = 10 \text{ (1/s)}$$

$$N_r = 10^9$$

$$\phi(\rho) := F(\rho, t=0) = 0$$

$$g(\rho) := \left. \frac{\partial F(\rho, t)}{\partial t} \right|_{t=0} = \begin{cases} g_o, & \rho = \rho' \\ 0, & \text{elsewhere} \end{cases}$$





Conclusions

- Demonstrated
 - 1D walks with initial distribution and rate
 - Implemented a 2D RW (non-isotropic)
- Need to develop isotropic RW models.
- Extension to real problems.

Evaluation of Certain Integrals Using Stochastic Formulation of the Lossy Wave Equation

Ramakrishna Janaswamy

Department of Electrical & Computer Engineering
University of Massachusetts, Amherst, MA 01003
Email: janaswamy@ecs.umass.edu

Abstract—The relationship between the solution of a lossy wave equation and that of a lossless wave equation established via the Poisson process is exploited to derive some new integral identities.

I. INTRODUCTION

It has previously been shown by Kac [1] that the solution of a lossy wave equation in multiple space dimensions can be obtained from that of a corresponding lossless wave equation by simply changing the time variable t in the latter by a randomized time variable \tilde{t} that depends on a Poisson process. In 1D a particle travels in space with a constant velocity v whose direction will be altered by collisions present in the medium and occurring at random times through a Poisson process. The statistics of the Poisson process are, in turn, governed by the loss present in the medium. In this paper, we use this relationship to demonstrate how to derive new expressions for the various moments of the randomized time as well as establish some new integral identities.

II. THEORY

For a wave propagating in a linear, homogeneous conducting medium characterized by the usual electrical parameters (ϵ, μ, σ) , the Cartesian components of the fields satisfy the lossy wave equation [2]

$$v^2 \nabla^2 \psi = \frac{\partial^2 \psi}{\partial t^2} + \frac{1}{\tau} \frac{\partial \psi}{\partial t}, \quad (1)$$

where t is the time-variable, $v = 1/\sqrt{\mu\epsilon}$ is the speed of light in a lossless medium with parameters (ϵ, μ) , and $\tau = \epsilon/\sigma$ is the relaxation time of charges in the conducting medium. In a lossless medium $\tau \rightarrow \infty$ and (1) reduces to the dispersionless wave equation. Equation (1) is supplemented by the initial conditions

$$\psi(\mathbf{r}; t=0) = f(\mathbf{r}), \quad \frac{\partial \psi}{\partial t}(\mathbf{r}; t=0) = g(\mathbf{r}), \quad (2)$$

where $\mathbf{r} = (x, y, z)$ and possibly by boundary conditions resulting from physical boundaries. Kac [1] constructed a stochastic model for (1) by associating the relaxation time with a Poisson random process $N(t)$ that takes on only integer values $k = 0, 1, \dots$ and governed by the law

$$\text{Prob}\{N(t) = k\} = e^{-\frac{t}{2\tau}} \frac{(\frac{t}{2\tau})^k}{k!}. \quad (3)$$

The quantity $N(t)$ may be thought of as the number of random collisions experienced in a time interval t by a particle

traveling in the conducting medium. The average number of collisions $\bar{N}(t)$ in an interval t is equal to $\bar{N}(t) = \sum_{k=0}^{\infty} k \text{Prob}\{N(t) = k\} = t/2\tau$. A random time \tilde{t} related to the Poisson process is first defined as

$$\tilde{t} = \int_0^t \nu(\alpha) d\alpha. \quad (4)$$

The integrand $\nu(t) = (-1)^{N(t)}$ in (4) takes on values ± 1 depending on whether $N(t)$ is even or odd and is known as the *telegraph signal* in the literature [3]. In the special case of a lossless medium, $N(t) \equiv 0$ and $\tilde{t} = t$. However, in general, $-t \leq \tilde{t} \leq t$. Using this random time, one may express the solution $\psi(\mathbf{r}; t)$ to the lossy wave equation (1) in terms of the solution $\varphi(\mathbf{r}; t)$ to the lossless wave equation as [1]

$$\psi(\mathbf{r}; t) = \langle \varphi(\mathbf{r}; \tilde{t}) \rangle, \quad (5)$$

where $\langle \cdot \rangle$ denotes the expectation operator with respect to the randomness of the Poisson process $N(\alpha)$. In 1D with $\mathbf{r} = xx$, the solution of the lossy wave equation in an unbounded medium with the initial conditions given in (2) can be expressed using (5) and the d'Alembert's formula for lossless wave equation [2], [4]:

$$\psi(x; t) = \left\langle \frac{f(x + vt) + f(x - vt)}{2} + \frac{1}{2v} \int_{x-v\tilde{t}}^{x+v\tilde{t}} g(\xi) d\xi \right\rangle \quad (6)$$

Kac [1] only considered the case with zero velocity (i.e., with $g(x) \equiv 0$), but (6) generalizes his result. We will first use the 1D case to generate some useful results for the various moments of the random time \tilde{t} . Equation (6) can be put in a more suitable form if the initial data are expressed in terms of their Fourier transforms. The function $f(x)$ and its Fourier transform $F(k_x)$ are related by the usual transform relationship

$$f(x) = \frac{1}{2\pi} \int_{-\infty}^{\infty} F(k_x) e^{ik_x x} dk_x. \quad (7)$$

Using a similar definition for $g(x)$ and substituting into (6) we arrive at

$$\begin{aligned}\psi(x; t) &= \frac{1}{2\pi} \int_{-\infty}^{\infty} F(k_x) e^{ik_x x} \langle \cos(k_x v \tilde{t}) \rangle dk_x + \\ &+ \frac{1}{2\pi} \int_{-\infty}^{\infty} G(k_x) e^{ik_x x} \frac{\langle \sin(k_x v \tilde{t}) \rangle}{k_x v} dk_x.\end{aligned}\quad (8)$$

This alternate form is advantageous because the averaging operation has been transferred to known functions. One needs to know the n th moment $\gamma_n(t) = \langle \tilde{t}^n \rangle$ of the random time \tilde{t} in order to perform these averages. The Laplace transform $\Upsilon_n(s)$ of the n th moment is given in [1]:

$$\Upsilon(s) = \int_0^\infty \gamma_n(t) e^{-st} dt = \begin{cases} \frac{n!}{[s(s+1/\tau)]^{(n+1)/2}}, & n \text{ odd}, \\ \frac{n!}{s[s(s+1/\tau)]^{n/2}}, & n \text{ even}, \end{cases}\quad (9)$$

which can be inverted easily to find $\gamma_n(t)$. The results for $n = 1$ and $n = 2$ are

$$\gamma_1(t) = 2\tau e^{-t/2\tau} \sinh(t/2\tau), \quad \gamma_2(t) = 2\tau t \left(1 - \frac{\gamma_1(t)}{t}\right).\quad (10)$$

The explicit solution for the lossy wave equation in 1D is given in [4]

$$\begin{aligned}\psi(x; t) &= e^{-t/2\tau} \left\{ \frac{f(x+vt) + f(x-vt)}{2} \right. \\ &+ \frac{1}{2v} \int_{x-vt}^{x+vt} \left[f(\xi) \left(\frac{1}{2\tau} + \frac{\partial}{\partial t} \right) + g(\xi) \right] \\ &\left. \cdot I_0 \left(\frac{1}{2v\tau} \sqrt{v^2 t^2 - (x-\xi)^2} \right) \right\} d\xi,\end{aligned}\quad (11)$$

where $I_0(\cdot)$ is the modified Bessel function of order zero. Equations (6), (8) and (11) may be equated to each other to yield a number of interesting results. For instance using $x = 0$ and $f(x) \equiv 0$, we get

$$\left\langle \int_{-v\tilde{t}}^{v\tilde{t}} g(\xi) d\xi \right\rangle = e^{-t/2\tau} \int_{-vt}^{vt} g(\xi) I_0 \left(\frac{t}{2\tau} \sqrt{1 - \frac{\xi^2}{v^2 t^2}} \right) d\xi.\quad (12)$$

Note as already indicated that the quantity $v\tilde{t}$ could be positive or negative even if t is positive.

Choice-1: $g(\xi) = e^{-\lambda\xi/vt}$

Evaluating the left and right sides of (12) by using [5, formula 6.616-5, p. 690] we get

$$\begin{aligned}\left\langle \sinh \left(\frac{\lambda\tilde{t}}{t} \right) \right\rangle &= \frac{\lambda e^{-t/2\tau}}{\sqrt{\lambda^2 + (t/2\tau)^2}} \sinh \left(\sqrt{\lambda^2 + (t/2\tau)^2} \right) \\ &= e^{-t/2\tau} \frac{d}{d\lambda} \left[\cosh \left(\sqrt{\lambda^2 + (t/2\tau)^2} \right) \right]\end{aligned}\quad (13)$$

This identity could be used to find $\gamma_n(t)$ for any n . For example, differentiating both sides of (13) with respect to λ and

evaluating at $\lambda = 0$ yields $\gamma_1(t) = 2\tau \exp(-t/2\tau) \sinh(t/2\tau)$ which agrees with that given in (10).

Choice-2: $g(\xi) = e^{ib\xi}$

In this case one gets the useful result

$$\langle \sin(bv\tilde{t}) \rangle = \frac{be^{-t/2\tau}}{2} \int_{-vt}^{vt} e^{ib\xi} I_0 \left(\frac{t}{2\tau} \sqrt{1 - \frac{\xi^2}{v^2 t^2}} \right) d\xi\quad (14)$$

Using (5) and the explicit representation given in [2], the solution for the lossy wave equation in 2D with zero initial condition is

$$\psi(x, y; t) = \frac{1}{2\pi v} \iint_{S_0} \left\langle \frac{H(v\tilde{t} - R)}{\sqrt{v^2 t^2 - R^2}} \right\rangle g(\mathbf{r}_0) d\mathbf{r}_0,\quad (15)$$

$$\begin{aligned}&= \frac{e^{-t/2\tau}}{2\pi v} \iint_{S_0} H(vt - R) g(\mathbf{r}_0) \\ &\times \frac{\cosh \left(\frac{1}{2v\tau} \sqrt{v^2 t^2 - R^2} \right)}{\sqrt{v^2 t^2 - R^2}} d\mathbf{r}_0,\end{aligned}\quad (16)$$

where $H(\cdot)$ is the Heavyside step function, $\mathbf{r}_0 = (x_0, y_0)$, $R^2 = (x - x_0)^2 + (y - y_0)^2$ and $g(\mathbf{r})$ is non-zero over the spatial domain defined by S_0 . The presence of the step function ensures that the domain of dependence is $R \leq vt$. One may use the identities [5, 6.671-1], [4, §5.9, (75)], and (14) to yield

$$\begin{aligned}\psi(x, y; t) &= \frac{e^{-t/2\tau}}{2\pi v} \iint_{S_0} H(vt - R) g(\mathbf{r}_0) \int_0^\infty \kappa J_0(\kappa R) \\ &\times \frac{\sin \left(vt \sqrt{\kappa^2 - \left(\frac{1}{2v\tau} \right)^2} \right)}{\sqrt{\kappa^2 - \left(\frac{1}{2v\tau} \right)^2}} d\kappa d\mathbf{r}_0\end{aligned}\quad (17)$$

Comparing (17) and (16) we obtain a new identity (the zeroth order Hankel transform) which is not available in [5]:

$$\int_0^\infty \frac{\sin \left(vt \sqrt{\kappa^2 - \left(\frac{1}{2v\tau} \right)^2} \right)}{\sqrt{\kappa^2 - \left(\frac{1}{2v\tau} \right)^2}} \kappa J_0(\kappa R) d\kappa = \frac{\cosh \left(\frac{\sqrt{v^2 t^2 - R^2}}{2v\tau} \right)}{\sqrt{v^2 t^2 - R^2}}\quad (18)$$

ACKNOWLEDGEMENT

The above work was supported by the Army Research Office under grant ARO W911NF-10-1-0305.

REFERENCES

- [1] M. Kac, "A stochastic model related to the telegrapher's equation," *Rocky Mountain Journal of Mathematics*, vol. 43, no. 3, pp. 479–509, Summer 1974.
- [2] P. M. Morse and H. Feshbach, *Methods of Theoretical Physics, vol. I*. New York: McGraw-Hill, 1953.
- [3] A. Papoulis and S. Unnikrishnan, *Probability, Random Variables and Stochastic Processes*. New York: McGraw-Hill, 2002.
- [4] J. A. Stratton, *Electromagnetic Theory*. New York: McGraw-Hill, 1941.
- [5] L. S. Gradshteyn and I. S. Ryzhik, *Table of Integrals, Series, and Products*. New York: Academic Press, VI Ed., 2000.

Quantification of High Dimensional Uncertainty in Propagation over Random Terrain

Selman Özbayat and Ramakrishna Janaswamy

Electrical & Computer Engineering Department

University of Massachusetts Amherst, 100 Natural Resources Rd., Amherst, MA, 01003

E-mail: ozbayat@ecs.umass.edu, janaswamy@ecs.umass.edu

Abstract—Efficient calculation of expected (mean) propagation factor for wave propagation above a random long-range terrain is achieved. An adaptive sparse grid collocation algorithm (ASGC) is applied for interpolating each component function from an adaptive high dimensional model representations (HDMR) decomposition. The decomposition reveals significant elimination of redundant sampling. The obtained results are compared with the reference solution obtained with a large set of samples simulated with Monte-Carlo method.

I. INTRODUCTION

There are several sampling based interpolation tools for uncertainty quantification (UQ) in propagation environments of our interest, where the environment would have random sources, boundaries or domain parameters. Monte-Carlo (MC) simulation is the most common method to perform UQ, whereas recent developments have emerged with the effort of improving the low MC convergence rate of $1/\sqrt{Q}$, where Q is the number of samples out of an N -dimensional parameter space. Here we assume that randomness is present in N independent random variables (RVs). The stochastic collocation (SC) method [1] samples from a predetermined sparse grid irrespective of the target function that is interpolated, whereas variations of an adaptive sparse grid collocation (ASGC) were developed for discarding redundant samples out of the SC sparse grid [2]. Although ASGC can resolve non-smooth behavior of the target function, its performance worsens as N gets high. The high dimensional model representations (HDMR) [3] allow us to exactly decompose the high dimensional target function into lower dimensional components and interpolate each component with ASGC. For the decompose-and-solve strategy we follow an approach similar to [4]. The propagation problem is introduced in the next section, whereas a sample result is depicted and compared to that with MC sampling in Section III.

II. LOW-GRAZING ANGLE PROPAGATION OVER A RANDOM ROUGH SURFACE

The low-grazing angle propagation over a 1-D random surface in the 2-D free-space has been governed by the parabolic equation (PE) approximation to the 2-D Helmholtz equation, whereas an efficient numerical solver is in the form of a Volterra integral equation of 2nd kind [5]. The model geometry is depicted in Figure 1, where a source function $s(z)$ is excited from $x = 0$ plane, and the expected (mean) propagation factor (PF) is sought at a long-range plane $x = x_o$. PF is the ratio

of the total field to the incident field, $PF = |\psi_{tot}(z)/\psi_{inc}(z)|$, where $\psi_{inc}(z)$ is the field observed in Figure 1 without the presence of surface $g(x)$. We here assume the surface to be perfectly conducting (PEC). We will not go into details of the numerical solver, but mention how the random surface $g(x)$ is formed. Since it is our interest to utilize emerging tools for UQ for increasing N rather than start with a problem of very high N , we do not generate a rough surface from a large number of RVs, but instead control N by forming $g(x)$ from a series of non-overlapping Gaussian hills along x , where b^{th} hill is randomized by 3 uniform RVs: $\mu_b = U[\mu_b^{min}, \mu_b^{max}]$ controls the mean position of the hill, $\sigma_b = U[\sigma_b^{min}, \sigma_b^{max}]$ controls the width of the hill and $A_b = U[A_b^{min}, A_b^{max}]$ controls the peak height of the hill. The overall surface is determined by $g(x) = g_b(x) = A_b \exp[-(x - \mu_b)^2/2\sigma_b^2]$, $\frac{x_o}{B}(b-1) < x < \frac{x_o}{B}b$, $b = 1, 2, \dots, B$. Therefore, the dimensionality for above problem is $N = 3B$, where the applied UQ methods and concerns about applicability of this scattering problem are detailed in [6].

With each realization of the $3B$ RVs a surface profile $g(x)$ is initiated and the resultant deterministic scattering problem is solved by the integral equation solver. Since it is the deterministic solver that exploits most of the used memory in long-range propagation rather than the memory for storage, indexing and search of the samples in SC, ASGC and HDMR routines, the computational cost of each method in our case is highly proportional to the number of samples each method takes. It is therefore our goal to come up with the optimal interpolation method that will converge to the desired accuracy in the expected field with as small sample size Q as possible.

III. SAMPLE RESULT AND DISCUSSION

In the sample problem we compute the expected PF at an observation range of $x_o = 420$ m. The range is partitioned into seven regions each with a Gauss hill, thus the dimensionality is $N = 3B = 21$. The excitation from $x = 0$ is a distributed source: $s(z) = A_s \exp[-ik_0 z \sin \alpha - (z - z_t)^2/\sigma_s^2]$, where k_0 is the free-space wavenumber. The excitation is centered at an elevation of $z_t = 3$ m, has a width parameter $\sigma_s = 0.3$ m, and is steered with respect to range axis (x) by $\alpha = 5^\circ$. The frequency of operation is 1 GHz.

Figure 2 depicts the error in PF calculated with different methods, whereas the reference solution was obtained from a set of 10^6 MC samples. The normalized mean-squared error (NMSE) error is defined with respect to the reference solution

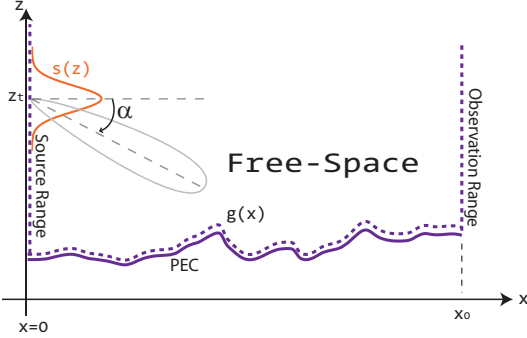


Fig. 1. The computation domain for the scattering problem, denoted with the dashed lines.

as:

$$NMSE = \frac{\int_0^{z_{max}} \left| \widetilde{PF}(x_o, z) - PF^{ref}(x_o, z) \right|^2 dz}{\int_0^{z_{max}} |PF^{ref}(x_o, z)|^2 dz}, \quad (1)$$

where $\widetilde{PF}(x_o, z)$ is the mean PF calculated obtained with each method and z_{max} is a finite elevation that truncates the domain, $(z_{max} - z_t)/\sigma_t \gg 1$.

Since the above error definition is in squared sense, one expects the MC error convergence be $\mathcal{O}(Q^{-1})$. Due to its dimensionality-dependent error convergence nature, the convergence error with SC method in Figure 2 is $Q^{-0.523}$. Although the ASGC in general represents a much better convergence than SC up to moderate dimensionality, the non-smooth nature of PF in the domain of RVs in this problem prevents ASGC to converge better than MC. In the case of HDMR decomposition on the other hand, the error convergence has a rate $Q^{-1.18}$. For instance, with roughly 1,000 samples, the HDMR allows more than one order of magnitude less error than the ASGC solution. The convergence rates were obtained by linear regression.

For the details of SC and ASGC methods we refer the reader to [1] and [2]. We will discuss how the dimensionality reduction performed by HDMR affects the overall target function behavior. A target function to interpolate in the N -dimensional random space is exactly decomposed as [3]:

$$\begin{aligned} f(y) = f_0 &+ \sum_{i=1}^N f_i(Y_i) + \sum_{1 \leq i_1 < i_2 \leq N} f_{i_1 i_2}(Y_{i_1}, Y_{i_2}) \\ &+ \dots + \sum_{1 \leq i_1 < \dots < i_p \leq N} f_{i_1 \dots i_p}(Y_{i_1}, \dots, Y_{i_p}) \\ &+ \dots + f_{12 \dots N}(Y_1, \dots, Y_N), \end{aligned} \quad (2)$$

where $y = (Y_1, Y_2, \dots, Y_N)$ is the set of N RVs. In the cases of SC and ASGC, the target function $f(y)$ is interpolated directly, whereas in HDMR (2) represents f in terms of components $f_{\mathbf{i}}$, $\mathbf{i} = (i_1, i_2, \dots, i_p)$, p is the “order” of the corresponding component. Most components in (2) are eliminated depending on their contribution to the statistics of the N -dimensional target function f [4]. For the 21-dimensional problem the HDMR

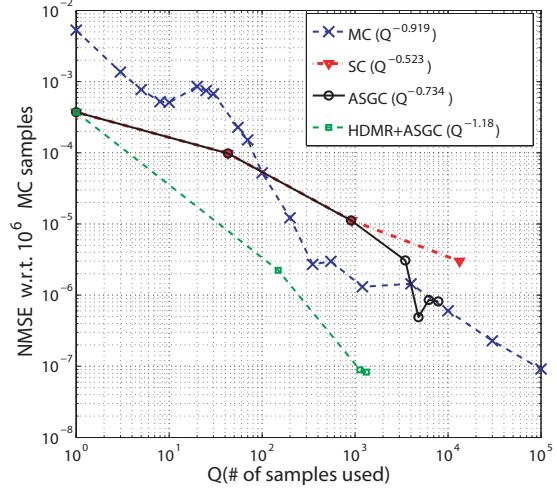


Fig. 2. Normalized mean-squared error convergence with respect to Q . The convergence rate of each method is displayed in parentheses.

routine terminated after order three, therefore in Figure 2 the curve that corresponds to HDMR decomposition (green-dashed) depicts four markers including order 0, where each marker corresponds to NMSE obtained with corresponding maximum order. The markers in the other curves have different meanings, but all correspond to the error at respective sample sizes.

IV. CONCLUSION

We have applied the HDMR for dimensionality reduction in a propagation over random terrain problem, where each reduced-dimensional component is interpolated with ASGC. The NMSE in expected PF revealed best convergence when HDMR is used. Higher order cases where the terrain is a rough surface generated by a large set of RVs, e.g. with Gaussian statistics, will be considered in the future.

ACKNOWLEDGEMENT

This work was supported by Army Research Office under grant W911NF-10-1-0305.

REFERENCES

- [1] D. Xiu and J. Hesthaven, “High-order collocation methods for differential equations with random inputs,” *SIAM J. Sci. Comput.*, vol. 27, no. 3, pp. 1118–1139, 2005.
- [2] S. Sankaran and A. Marsden, “A stochastic collocation method for uncertainty quantification and propagation in cardiovascular simulations,” *J. Biomech. Eng.*, vol. 133, no. 031001, 2011.
- [3] H. Rabitz and Ö. Alış, “General foundations of high-dimensional model representations,” *J. Math. Chem.*, vol. 25, pp. 197–233, 1999.
- [4] X. Ma and N. Zabaras, “An adaptive high-dimensional stochastic model representation technique for the solution of stochastic partial differential equations,” *J. Comput. Phys.*, vol. 229, pp. 3884–3915, 2010.
- [5] Z. Lai and R. Janaswamy, “Specular propagation over rough surfaces: numerical assessment of Uscinski and Stanek’s mean Green’s function technique,” *Waves in Random and Complex Media*, vol. 16, pp. 137–150, May 2006.
- [6] S. Özbayat and R. Janaswamy, “Sparse grid collocation methods for uncertainty quantification in benchmark EM scattering problems,” *unpublished, submitted to IEEE Trans. on Antennas and Propagation*, January 2013.

On Random Time and on the Relation Between Wave and Telegraph Equations

Ramakrishna Janaswamy, *Fellow, IEEE*

Abstract—Kac’s conjecture relating the solution of wave and telegraph equations in higher dimensions through a Poisson-process-driven random time is established through the concepts of stochastic calculus. New expression is derived for the probability density function of the random time. We demonstrate how the relationship between the solution of a lossy wave and that of a lossless wave equation can be exploited to derive some statistical identities. Relevance of the results presented to the study of pulse propagation in a dispersive medium characterized by a Lorentz or Drude model is discussed and new evolution equations for 2-D Maxwell’s equations are presented for the Drude medium. It is shown that the computational time required for updating the electric field using the stochastic technique is expected to go up as $O(\sqrt{t})$.

Index Terms—Dispersive media, finite-difference time domain (FDTD), Poisson processes, random time, stochastic differential equations, telegrapher’s equation.

I. INTRODUCTION

HERE has been an interest lately in developing probabilistic, stochastic, or Monte Carlo methods for field computation [1]. The basic idea is to formulate a stochastic process, producing an appropriate random variable, whose expected value is the solution of a certain deterministic problem. Among the computational advantages of the stochastic method that various researchers have advanced are 1) the method is local in that the field can be calculated at a desired point only without having to obtain the global solution by solving a linear system of equations, 2) the method needs no meshing, 3) the degree of accuracy can be controlled by varying the sample size (or number of realizations), 4) the method is inherently parallel because the intermediate results generated by each random realization are independent of each other. The resurgence of interest in the method is likely triggered by the last feature. Garcia and Sadiku [2] applied the random walk method with a variable step-size to solve Poisson’s equation. Le Coz *et al.* [3] determined the frequency-dependent capacitance and inductance of high-speed computer interconnects using the random walk method and quasi-static approximations. Subsequent researchers have developed random walk method for the

Helmholtz and wave equations [4], [5], and [6]. Budaev and Bogy [7] applied the stochastic differential equation technique to solve the complete transport equation pertaining to the amplitude part of the solution of the scalar Helmholtz equation in an inhomogeneous medium. The same technique was used in [8] and [9] to address the problem of wedge diffraction with impedance boundary conditions. The basic differential equations that form the subject matter of the present paper are the 3-D version of the telegrapher’s equation and the wave equation and certain stochastic quantities that relate the two.

The connection between partial differential equations (PDE) and random dispersion of particles in space-time has a long history; see [10]–[13] for some of the initial work. Majority of the works that followed these papers concentrated on random walks tied to the Brownian motion. The research has been documented in a number of books and research monographs such as [14]–[17]. It has previously been shown by Kac [18] (demonstrated for 1-D with zero initial velocity conditions and conjectured for higher dimensions) that the solution of a lossy wave equation (which is a modified telegrapher’s equation) can be obtained from that of a corresponding lossless wave equation by simply changing the time variable t in the latter by a randomized time variable $\zeta(t)$ that depends on a Poisson process and then performing an averaging operation with respect to the underlying Poisson process. The statistics of the Poisson process are governed by the loss present in the medium. This resulted in a very interesting stochastic representation for the solution of telegrapher equation, which could be conveniently implemented on a parallel type of computing machine. The link between wave and telegrapher’s equations via random time is very interesting and implies that macroscopic loss mechanisms can be thought of as arising from randomized time and an averaging process. Following Kac’s work, a number of researchers advanced the idea further and attempted to build random walk models for the telegrapher’s equation in higher dimensions. Some of this latter work is nicely summarized in [19] as well as in the recent paper [20].

Unlike some of the recent work, the present paper is not concerned with building random walk models for the telegrapher’s equations. Rather, the contributions of the present paper are 1) presenting a mathematical proof of Kac’s conjecture in higher space dimensions (Section II-C) using concepts from stochastic calculus [21]; no such formal proof currently exists in the literature to the best knowledge of the present author, 2) given the important role played by the random time in such stochastic representations, presenting a new expression for the first order statistics of the random time (II-D), and 3) demonstrating how the stochastic representation can be utilized to arrive at some

Manuscript received March 14, 2012; revised October 15, 2012; accepted December 26, 2012. Date of publication January 03, 2013; date of current version May 01, 2013. This work was supported by the Army Research Office under Grant ARO W911NF-10-1-0305.

The author is with the Department of Electrical and Computer Engineering, University of Massachusetts, Amherst, MA 01003 USA (e-mail: janaswamy@ecs.umass.edu).

Digital Object Identifier 10.1109/TAP.2013.2237739

useful schemes for computing multidimensional fields in dispersive media (Subsection II-E). In particular, the Lorentz and Drude media are considered in Subsection II-E. Hence, apart from being pedagogical in nature, the paper contains new results that are of interest to researchers working in the area of wave propagation. If the idea of random time can be extended to more complicated dispersive media than the ones considered in the paper, the concept could provide an alternate means to computing the time-instantaneous field in those media where analytical expressions are not available. For the benefit of readers unfamiliar with the techniques of stochastic processes and the associated calculus, we first present some basic properties of Poisson processes and preliminaries of stochastic calculus in Section II-A. The relevance of the stochastic model presented here to the study of pulse propagation in a causal dispersive media, such as the Lorentz- or Drude-model medium is discussed in Section II-E.

II. THEORY

A. Poisson Process and Preliminaries of Stochastic Calculus

A Poisson random process $N(t)$ is constructed from a sequence of independent and identically distributed exponential random variables τ_1, τ_2, \dots known as *inter-arrival times*, each with mean τ [22]. Starting from a value of zero at time $t = 0$, the process $N(t)$ jumps by unit value at the *arrival times* given by

$$t_n = \sum_{i=1}^n \tau_i, \quad n = 1, 2, \dots \quad (1)$$

The function $N(t)$ is assumed to be *right-continuous* in that $N(t) = \lim_{s \downarrow t} N(s)$ ($s \downarrow t$ means $s \rightarrow t$ from $s > t$; likewise $s \uparrow t$ means $s \rightarrow t$ from $s < t$) and can be expressed as

$$N(t) = \sum_{n=1}^{\infty} \Theta(t - t_n) \quad (2)$$

where $\Theta(t)$ is the unit-step function equal to 0 for $t < 0$ and equal to 1 for $t > 0$. Fig. 1(a) shows one sample path of a Poisson process. Because the expected time between jumps is τ , the jumps arrive at an average rate of $\lambda := 1/\tau$ and the process itself has the distribution

$$\mathbb{P}\{N(t) = k\} = \frac{(\lambda t)^k}{k!} e^{-\lambda t}, \quad k = 0, 1, \dots \quad (3)$$

where \mathbb{P} denotes probability. This last result can be derived from the fact that t_n given in (1) has a gamma distribution [21].

In addition, $N(t)$ satisfies the following properties:

- P1) Independence of Increments—for all $0 \leq t_0 < t_1 < t_2 < \dots < t_n, n \geq 1$, the random variables $N(t_1) - N(t_0), N(t_2) - N(t_1), \dots, N(t_n) - N(t_{n-1})$ are independent of each other.
- P2) Stationarity of Increments— $N(t + h) - N(s + h)$ has the same distribution as $N(t) - N(s)$ for all $h > 0$ and $0 \leq s < t$, i.e., $\mathbb{P}\{N(t + h) - N(s + h) = k\}$ is independent of $h > 0$ and equals $e^{-\lambda(t-s)}[\lambda(t-s)]^k/k!$.

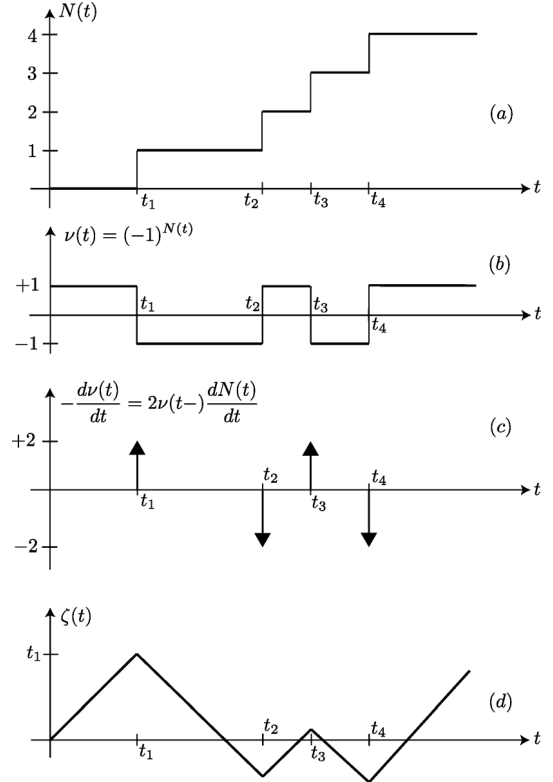


Fig. 1. Poisson processes and the functions generated from it. (a) Sample Poisson process, (b) the Telegraph signal, (c) increment of the Telegraph signal, and (d) Random time.

Using Property P2 it is easy to establish that the expected increment, which is equal to the average number of jumps between times s and t for $t \geq s$ is

$$\mathbb{E}[N(t) - N(s)] = \lambda(t - s) \quad (4)$$

where \mathbb{E} denotes expectation operator and it is assumed that the right-hand side of (4) will be rounded to the nearest integer. Hence, the expected number of jumps between s and t is only dependent on the elapsed time $(t - s)$, but not on the epoch s . A stochastic integral equation of the form

$$X(t) = X(0) + \int_0^t f[X(\sigma); \sigma] d\sigma + \int_0^t g[X(\sigma); \sigma] dN(\sigma) \quad (5)$$

will admit a solution in the Itô sense if, on an interval where $N(t)$ is constant, X satisfies $\dot{X} = f[X(t), t]$ and if $N(t)$ jumps at t_n , X behaves in the neighborhood of t_n according to the rule [23]

$$X(t_n+) = X(t_n-) + g \left[\lim_{t \uparrow t_n} X(t), t_n \right] \quad (6)$$

where $\dot{X} = dX/dt$. Note that the jump of $X(t)$ at time t_n depends on the value of $g(X(t); t)$ evaluated at a time just before the jump of $N(t)$. In such a case we say that the coefficient function $g[X(t); t]$ in (5) is *left continuous* in contrast to the process $N(t)$ that is right continuous. The increment $dN(\sigma)$ is to be interpreted as being equal to $N(\sigma + d\sigma) - N(\sigma)$. With this

understanding, the stochastic differential equation (SDE) corresponding to (5) is then written as

$$dX(t) = f(X(t); t)dt + g(X(t); t)dN(t) \quad (7)$$

where $dX(t)$ represents the change in $X(t)$ when t changes infinitesimally, i.e., $dX(t) = X(t+dt) - X(t)$.

Given (7) and a function $\psi(x, t)$ with continuous first derivatives in both x and t , we have the following Itô-Doeblin rule for the jump process $\psi[X(t); t]$ ([21], Ch. 11), [23]:

$$\begin{aligned} d\psi(X(t); t) &= \left[\frac{\partial\psi(X(t); t)}{\partial t} + \frac{\partial\psi(X(t); t)}{\partial x} f(X(t); t) \right] dt \\ &\quad + \{\psi(X(t-)) + g[X(t-); t]\} \\ &\quad - \{\psi(X(t-); t)\}dN(t). \end{aligned} \quad (8)$$

When the Poisson process jumps at $t = t_n$, there will be jump in the function $X(t)$ according to (6). We would expect $\psi(X(t); t)$ to jump too and the coefficient of dN in (8) governs the size of this jump. Again, it is important to observe that the jump size is governed entirely by the values of $X(t)$ and $g[X(t); t]$ evaluated at the left limit t_n- . Thus, there is statistical independence between the jump in $N(t)$ and the jump it causes in its multiplying factor. At times when there is no jump in $N(t)$, the term involving dN would vanish and one obtains the usual chain rule formula from calculus given by the term proportional to dt in (8). Keeping these in mind and using (4), the expectation of an incremental process of the type $dY(t) = h(X(t); t)dN(t)$ is interpreted as

$$\begin{aligned} \mathbb{E}[dY(t)] &= \mathbb{E}[h(X(t); t)dN(t)] \\ &= \mathbb{E}[h(X(t); t)]\mathbb{E}[dN(t)] \\ &= \lambda\mathbb{E}[h(X(t); t)]dt \end{aligned} \quad (9)$$

because the function $h(X(t); t)$ is assumed to be left continuous and dN is right continuous. As already stated, the jump in $N(t)$ is assumed to take place first independent of $h(X(t); t)$ and the corresponding jump in $h(X(t); t)$ occurs *momentarily* later. Some sort of causality and finite speed of signal propagation is thus inherently assumed in processes defined by $dY(t) = h(X(t); t)dN(t)$. This has very important implications in further analysis as we will show in Section II-C.

B. Random Time

Consider a random velocity¹ $\nu(t)$ (unitless) and a corresponding “position” $\zeta(t)$ (with units of time) defined with respect to the Poisson process $N(t)$ as

$$\nu(t) = (-1)^{N(t)}; \quad (10)$$

$$\zeta(t) = \int_0^t \nu(\sigma) d\sigma. \quad (11)$$

Note that $\nu(0) = 1$ and $\zeta(0) = 0$. Even though it is physically appealing to think of $\zeta(t)$ as the position of a particle whose velocity flips randomly between -1 and $+1$, the fact that it has units of time render it to be termed more appropriately as

¹In the literature $\nu(t)$ is referred to as the *semi-random telegraph signal* [24].

random time. Fig. 1(b) and (d), respectively, show sample waveforms of $\nu(t)$ and $\zeta(t)$. The velocity jumps at the same instants t_n when $N(t)$ jumps and takes values of ± 1 . The random time $\zeta(t)$ is continuous, but has slope discontinuities at t_n . If there are no jumps in the interval $(0, t)$, then $\zeta(t) = t$, otherwise $\zeta(t) \in (-t, t]$. It is clear that in an infinitesimal interval dt

$$\begin{aligned} d\nu &= \nu(t+dt) - \nu(t) \\ &= (-1)^{N(t)}[(-1)^{dN(t)} - 1] = -2\nu(t)dN(t). \end{aligned} \quad (12)$$

It is evident from Fig. 1(c) that the coefficient of $dN(t)$, viz., $\nu(t)$ is to be evaluated at $t-$, which confirms the rules laid out in Section II-A in relation to (7). Furthermore,

$$\begin{aligned} d\zeta &= \zeta(t+dt) - \zeta(t) = \int_t^{t+dt} \nu(\sigma) d\sigma = \int_0^{dt} \nu(t+\sigma) d\sigma \\ &= (-1)^{N(t)} \int_0^{dt} (-1)^{N(t+\sigma)-N(t)} d\sigma = \pm \nu(t)dt \end{aligned} \quad (13)$$

where the $+$ sign in (13) pertains to the case when no collisions occur in the time interval dt and the $-$ sign corresponds to the case when there is exactly one collision in the infinitesimal time interval dt . The relation between $d\zeta$ and $\nu(t)$ is also clear from Fig. 1(b) and (d). The following properties of the telegraph signal can be established from the definitions of the corresponding quantities and the properties of the Poisson process [24]:

$$\mathbb{E}[\nu(t)] = e^{-2\lambda t}, \quad (14)$$

$$\mathbb{E}[\nu(t+\Delta t)\nu(t)] = e^{-2\lambda|\Delta t|}. \quad (15)$$

Using these we can show that

$$\gamma_1(t) = \mathbb{E}[\zeta(t)] = e^{-\lambda t} \sinh(\lambda t)/\lambda, \quad (16)$$

$$\lambda\mathbb{E}[\zeta(t+\Delta t)\zeta(t)] = t - e^{-\lambda\Delta t} \cosh(\lambda\Delta t)\mathbb{E}[\zeta(t)]. \quad (17)$$

Both $\nu(t)$ and $\zeta(t)$ are therefore nonstationary random processes. For large times, $\gamma_1(t) \sim 0.5/\lambda$ and $\lambda\mathbb{E}[\zeta^2(t)] \sim t$. Hence, the standard deviation of random time increases as $\sqrt{t/\lambda}$ for large times.

C. Relation Between Wave and Telegrapher’s Equations

Consider now a function $\psi(t)$ and define the deterministic function $\varphi(t) = \mathbb{E}[\psi(\zeta(t))]$, i.e., $\varphi(t)$ is obtained from $\psi(t)$ by replacing the actual time variable t with the random time $\zeta(t)$ and then performing an averaging operation with respect to the underlying jump process. Using (8), (9), (12), (13), and the commutation of the expectation and differential operators

$$\begin{aligned} d\varphi(t) &= \mathbb{E}[d\psi(\zeta)] = \mathbb{E}[\nu(t)\psi'(\zeta)]dt \\ d^2\varphi(t) &= \mathbb{E}[d\nu(t)\psi'(\zeta) + \nu(t)d(\psi'(\zeta))]dt \\ &= -2\mathbb{E}[\nu(t)\psi'(\zeta)dN]dt + \mathbb{E}[\nu^2(t)\psi''(\zeta)](dt)^2 \\ &= \{-2\lambda\mathbb{E}[\nu(t)\psi'(\zeta)] + \mathbb{E}[\psi''(\zeta)]\}(dt)^2 \\ &= -2\lambda d\varphi(t)dt + \mathbb{E}[\psi''(\zeta)](dt)^2. \end{aligned} \quad (18)$$

In other words,

$$\frac{d^2\varphi(t)}{dt^2} + 2\lambda \frac{d\varphi(t)}{dt} = \mathbb{E}[\psi''(\zeta)] = \mathbb{E}\left[\frac{d^2\psi(t)}{dt^2}\Big|_{t=\zeta(t)}\right] \quad (19)$$

where $\psi'(\zeta) = d\psi(t)/dt|_{t=\zeta(t)}$ denotes the derivative with respect to its argument. The first line in the expansion for $d^2\varphi$ above is valid for terms up to order dt^2 ; higher order terms vanish in the limit of $dt \rightarrow 0$ in the eventual quantity of interest $d^2\varphi/dt^2$. If ψ and φ depend additionally on the spatial coordinates $\mathbf{r} = (x, y, z)$, i.e., if $\psi = \psi(\mathbf{r}; t)$ and ψ is a solution of the partial differential equation (PDE)

$$\frac{\partial^2\psi}{\partial t^2} = L_{\mathbf{r}}\psi \quad (20)$$

where $L_{\mathbf{r}}$ is some linear operator with respect to the spatial coordinates, subject to the initial conditions $\psi(\mathbf{r}; 0) = f(\mathbf{r})$ (this can be thought of as the specification of an *initial position*) and $\partial\psi(\mathbf{r}; t=0)/\partial t = g(\mathbf{r})$ (this can be thought of as the specification of an *initial velocity*), then the term inside the expectation operator on the right-hand-side of (19) will be of the form $\partial^2\psi/\partial t^2|_{t=\zeta(t)}$, which is equal to $L_{\mathbf{r}}\psi|_{t=\zeta(t)}$. Hence,

$$\varphi(\mathbf{r}; t) = \mathbb{E}[\psi(\mathbf{r}; t = \zeta(t))] \quad (21)$$

with $\psi(\mathbf{r}; t)$ given by (20) satisfies the PDE

$$\frac{\partial^2\varphi}{\partial t^2} + 2\lambda \frac{\partial\varphi}{\partial t} = L_{\mathbf{r}}\varphi \quad (22)$$

with the same initial conditions, *viz.*,

$$\varphi(\mathbf{r}; t=0) = f(\mathbf{r}) \text{ and } \frac{\partial\varphi(\mathbf{r}; t=0)}{\partial t} = g(\mathbf{r}) \quad (23)$$

where we have used $\zeta(0) = 0$ and $\nu(0) = 1$ in $\varphi(\mathbf{r}; 0) = \mathbb{E}[\psi(\mathbf{r}; \zeta(0))] = f(\mathbf{r})$ and $\partial\varphi(\mathbf{r}; t=0)/\partial t = \mathbb{E}[d\zeta/dt \partial\psi(\mathbf{r}; \zeta)/\partial\zeta|_{t=0}] = \mathbb{E}[\nu(0)\partial\psi(\mathbf{r}; t=0)/\partial t] = g(\mathbf{r})$ in establishing (23). It is seen that when a field quantity satisfies an operator equation that involves a second-order time derivative term, the effect of replacing the time variable in the original field quantity with the random time, followed by averaging with respect to the underlying Poisson process, has the effect of introducing a new field variable that satisfies a modified operator equation containing an additional first-order time derivative term. The coefficient of the first-derivative term is proportional to the average arrival rate of the Poisson process. The initial conditions for the modified field remain the same as the initial conditions for the original field. As a special case, if the original field ψ satisfies the scalar wave equation with $L_{\mathbf{r}} = v^2\nabla^2$, where v is the propagation speed, then the new field φ satisfies the *reduced Telegrapher's equation* (or the lossy wave equation)

$$\frac{\partial^2\varphi}{\partial t^2} + 2\lambda \frac{\partial\varphi}{\partial t} = v^2\nabla^2\varphi. \quad (24)$$

This remarkable result was first demonstrated in 1-D by Kac in [18] using an entirely different mathematical machinery. His conjecture that it continues to be valid for higher dimensions has been formally proven here using concepts from stochastic

calculus. An elementary application of Kac's result is that the solution for the current in a series linear RLC circuit can be obtained in terms of the current of a the lossless LC circuit when the time variable is replaced with random time having parameter $\lambda = R/2L$.

What is even more interesting is that this kind of correspondence is not limited to wave equation alone, as is clearly evident from (22). In most literature (24) is itself referred to as the telegrapher's equation although a clarification is in order. The telegrapher's equation was originally derived for a lossy transmission line having parameters R, G, L , and C ; respectively, the series resistance, the shunt conductance, the series inductance, and the shunt capacitance per unit length, all being nonnegative. With $\alpha = G/C, \beta = R/L$ and $v = 1/\sqrt{LC}$, the *telegrapher's equation* for the voltage $V(z; t)$ along the line reads

$$\frac{\partial^2V}{\partial t^2} + (\alpha + \beta) \frac{\partial V}{\partial t} + \alpha\beta V = v^2 \frac{\partial^2V}{\partial z^2} \quad (25)$$

where z is the space variable. With the change of variable $V = e^{-kt}\varphi$, where $k = \min(\alpha, \beta)$, one gets the equation

$$\frac{\partial^2\varphi}{\partial t^2} + |\alpha - \beta| \frac{\partial\varphi}{\partial t} = v^2 \frac{\partial^2\varphi}{\partial z^2} \quad (26)$$

which is seen to be the reduced telegrapher's equation in 1-D with the parameter $2\lambda = |\alpha - \beta|$. In the case of $\alpha = \beta$, (26) reduces to the wave equation. Equation (26) is also the equation satisfied by a wave propagating in a linear, homogeneous conducting medium characterized by the usual electrical parameters (ϵ, μ, σ) [25]. The quantity $v = 1/\sqrt{\mu\epsilon}$ is the speed of light in a lossless medium with parameters (ϵ, μ) , and $T = 1/2\lambda = \epsilon/\sigma$ is the relaxation time of charges in the conducting medium.

Using the d'Alembert's formula for the solution of a wave equation in 1-D [25], [26], the solution of the corresponding lossy wave equation in an unbounded medium with the initial conditions given in (23) can be expressed from the stochastic representation (21) as

$$\varphi(z; t) = \mathbb{E} \left[\frac{f(z + v\zeta(t)) + f(z - v\zeta(t))}{2} + \frac{1}{2v} \int_{z-v\zeta(t)}^{z+v\zeta(t)} g(\xi) d\xi \right]. \quad (27)$$

Equation (27), with the random time $\zeta(t)$ replaced by the deterministic time variable t and the expectation operator removed, is simply the d'Alembert's formula given in [25], [26] for the solution of a wave equation in 1-D. Kac [18] only considered the case with zero velocity (i.e., with $g(x) \equiv 0$), but (27) generalizes his result. We may use (21) and (27) to establish some useful stochastic identities. Equation (27) can be put in a more suitable form if the initial data are expressed in terms of their Fourier transforms. The function $f(z)$ and its Fourier transform $F(k_z)$ are related by the usual transform relationship

$$f(z) = \frac{1}{2\pi} \int_{-\infty}^{\infty} F(k_z) e^{ik_z z} dk_z. \quad (28)$$

Using a similar definition for $g(z)$ and substituting into (27) we arrive at

$$\begin{aligned} 2\pi\varphi(z; t) &= \int_{-\infty}^{\infty} F(k_z) e^{ik_z z} \mathbb{E}[\cos(k_z v \zeta(t))] dk_z \\ &\quad + \int_{-\infty}^{\infty} G(k_z) \frac{\mathbb{E}[\sin(k_z v \zeta(t))]}{k_z v} e^{ik_z z} dk_z. \end{aligned} \quad (29)$$

This alternate form is sometimes advantageous because the averaging operation has been transferred to known functions. The explicit solution for the lossy wave equation in 1-D is given in [26]

$$\begin{aligned} \varphi(z; t) &= e^{-\lambda t} \left\{ \frac{f(z+vt) + f(z-vt)}{2} \right. \\ &\quad + \frac{1}{2v} \int_{z-vt}^{z+vt} \left[f(\xi) \left(\lambda + \frac{\partial}{\partial t} \right) + g(\xi) \right] \\ &\quad \cdot I_0 \left(\frac{\lambda}{v} \sqrt{v^2 t^2 - (z-\xi)^2} \right) \left. \right\} d\xi \end{aligned} \quad (30)$$

where $I_0(\cdot)$ is the modified Bessel function of the first kind of order 0. Equations (27), (29), and (30) may be equated to each other to yield a number of interesting results. For instance using $z = 0$ and $f(z) \equiv 0$, we get

$$\mathbb{E} \left[\int_{-v\zeta(t)}^{v\zeta(t)} g(\xi) d\xi \right] = e^{-\lambda t} \int_{-vt}^{vt} g(\xi) I_0 \left(\lambda t \sqrt{1 - \frac{\xi^2}{v^2 t^2}} \right) d\xi. \quad (31)$$

Note as already indicated that the quantity $v\zeta(t)$ could be positive or negative even if t is positive. If $g(\xi)$ is chosen such that the left-hand side and the right-hand side integrals in (31) could be evaluated in a closed form, certain useful relations could be obtained. As an example, with $g(\xi) = e^{-a\xi/vt}$, we can show that [27]

$$\begin{aligned} \mathbb{E} \left[\sinh \left(\frac{a\zeta(t)}{t} \right) \right] &= \frac{ae^{-\lambda t}}{\sqrt{a^2 + \lambda^2 t^2}} \sinh \left(\sqrt{a^2 + \lambda^2 t^2} \right) \\ &= e^{-\lambda t} \frac{d}{da} \left[\cosh \left(\sqrt{a^2 + \lambda^2 t^2} \right) \right]. \end{aligned} \quad (32)$$

This identity could be used to find the n th moment $\gamma_n(t) = \mathbb{E}[\zeta^n]$ for any n . For example, differentiating both sides of (32) with respect to a and evaluating at $a = 0$ yields $\gamma_1(t) = \exp(-\lambda t) \sinh(\lambda t)/\lambda$ for the first moment of $\zeta(t)$, which agrees with that given in (16). The 2-D version of the main result in (21) was also used in [27] to derived some useful integral identities encountered in wave propagation area.

D. First-Order Statistics of the Random Time

In view of the central role played by random time in the stochastic representation of the solution of the telegrapher's equation such as in (27), it is of interest to determine the distribution of the random variable $\zeta(t)$ for a fixed t on the probability space (Ω, \mathbb{P}) , where Ω denotes sample space. Consequently, we

wish to determine the probability density function (pdf) $p(r; t)$ defined by $\mathbb{P}[\omega \in \Omega; \zeta(t; \omega) \in (r, r+dr)] = p(r; t)dr$, $r \in (-t, t]$. It will be demonstrated later in this section that the pdf $p(r; t)$ itself satisfies the reduced telegrapher's equation in 1-D with r taking the place of the spatial variable. As it is more convenient to first generate the transform of $p(r; t)$, we define the transform function $P(\kappa; s)$ which is obtained from $p(r; t)$ by taking the Laplace transform, \mathbf{L} , with respect to t and Fourier transform, \mathbf{F} , with respect to r :

$$\begin{aligned} P(\kappa; s) &= \int_{t=0}^{\infty} e^{-st} \int_{r=-\infty}^{\infty} p(r; t) e^{-i\kappa r} dr dt \\ &= \mathbf{L}(\mathbf{F}[p(r; t)]) = \mathbf{L}\left(\mathbb{E}\left[e^{-i\kappa\zeta(t)}\right]\right) \end{aligned} \quad (33)$$

where $i = \sqrt{-1}$. The use of Fourier-Laplace transform in the solution of linear PDEs with constant coefficients is a standard procedure and documented in a number of books, including [28]. From (8), (12), (13), and using the fact that $\nu^2(t) = 1$, we get

$$d\left(e^{-i\kappa\zeta(t)}\right) = -i\kappa\nu(t)e^{-i\kappa\zeta(t)}dt, \quad (34)$$

and

$$d\left(\nu(t)e^{-i\kappa\zeta(t)}\right) = -[i\kappa dt + 2\nu(t)dN(t)]e^{-i\kappa\zeta(t)}. \quad (35)$$

To facilitate further analysis we let $u_1(\kappa; t) = \mathbb{E}[e^{-i\kappa\zeta(t)}]$ and $u_2(\kappa; t) = \mathbb{E}[\nu(t)e^{-i\kappa\zeta(t)}]$. Then taking expectation on both sides of (34) we have

$$\frac{du_1(\kappa; t)}{dt} = -i\kappa u_2(\kappa; t). \quad (36)$$

Similarly, taking the expectation on both sides of (35) and making use of (9) we get

$$-\frac{du_2(\kappa; t)}{dt} = i\kappa u_1(\kappa; t) + 2\lambda u_2(\kappa; t). \quad (37)$$

Equations (36) and (37) constitute a system of coupled, linear first-order ordinary differential equations. Using $\mathbb{E}[\nu(0)] = 1$ and $\kappa = 0$ in (37) and solving for $u_2(0; t)$ recovers (14). If we now take Laplace transform with respect to t on both sides of (36) and (37) and use the usual properties of the Laplace transform of the derivative of a function, we arrive at

$$sP = -i\kappa Q + u_1(\kappa; 0) \quad (38)$$

$$sQ = -i\kappa P - 2\lambda Q + u_2(\kappa; 0) \quad (39)$$

where $Q(\kappa; s) = \mathbf{L}[u_2(\kappa; t)]$ and $P(\kappa; s)$ is defined in (33). Using $u_1(\kappa; 0) = \mathbb{E}[1] = 1$ and $u_2(\kappa; 0) = \mathbb{E}[\nu(0) \cdot 1] = \mathbb{E}[1] = 1$ and solving the simultaneous equations (38) and (39) we finally get

$$P(\kappa; s) = \frac{(s+2\lambda) - i\kappa}{s^2 + 2\lambda s + \kappa^2} \quad (40)$$

$$Q(\kappa; s) = \frac{s - i\kappa}{s^2 + 2\lambda s + \kappa^2}. \quad (41)$$

Equation (40) is also derived in [29], but using the expressions of the Laplace transform of the various moments provided in

[18]. However, the approach taken in this paper is more straightforward and as a bonus one can derive expressions for other quantities of interest such as $Q(\kappa; s)$. If $P(\kappa; s)$ is evaluated at $\kappa = 0$ and the inverse Laplace transform taken, one gets

$$\int_{-\infty}^{\infty} p(r; t) dr = \Theta(t) = 1, \quad t > 0 \quad (42)$$

verifying that $p(r; t)$ is a valid candidate for pdf for $t > 0$. It is also interesting to note from (40) that the pdf $p(r; t)$ itself satisfies the reduced telegrapher's equation. Indeed, for a function $w(r; t)$ satisfying the reduced telegrapher's equation $\partial^2 w / \partial t^2 + 2\lambda \partial w / \partial t = v^2 \partial^2 w / \partial r^2$ with initial conditions $p(r; 0) = p_0(r)$ and $\partial p(r; t) / \partial t|_{t=0} = v_0(r)$, the Fourier-Laplace transform $W(\kappa; s)$ satisfies

$$W(\kappa; s) = \frac{(s + 2\lambda)\tilde{p}_0(\kappa) + \tilde{v}_0(\kappa)}{s^2 + 2\lambda s + \kappa^2 v^2} \quad (43)$$

where $\tilde{p}_0(\kappa) = \mathbf{F}[p_0(r)]$ and $\tilde{v}_0(\kappa) = \mathbf{F}[v_0(r)]$. Comparing (43) with (40), we see that $p(r; t)$ satisfies the reduced telegrapher's equation in 1-D with the speed $v = 1$, $\tilde{p}_0(\kappa) = 1$, $\tilde{v}_0(\kappa) = -i\kappa$, the latter translating to the initial conditions $p_0(r) = \delta(r)$ and $v_0(r) = \delta'(r) = dp_0(r)/dr$. These initial conditions make perfect sense in view of the fact that $\zeta(0) = 0$ deterministically. Likewise, the inverse transform of $Q(\kappa; s)$ satisfies the same reduced telegrapher's equation, but with initial conditions $q(r; 0) = \delta(r)$ and $\partial q(r; t) / \partial t|_{t=0} = \delta'(r) - 2\lambda\delta(r)$.

The pdf $p(r; t)$ is obtained from the inverse relation

$$p(r; t) = \frac{1}{2\pi} \int_{-\infty}^{\infty} \frac{1}{2\pi i} \int_{\Gamma} \frac{s + 2\lambda - i\kappa}{s^2 + 2\lambda s + \kappa^2} e^{st} e^{i\kappa r} ds d\kappa \quad (44)$$

where the contour Γ is a straight line parallel to imaginary axis in the complex s -plane such that all singularities lie to the left of it. The integrand has simple poles at $s_{\pm} = -\lambda \pm i\sqrt{\kappa^2 - \lambda^2}$ in the complex s -plane. The Laplace inversion may be carried out by elementary means and the result is

$$p(r; t) = \frac{e^{-\lambda t}}{2\pi} \int_{-\infty}^{\infty} \left[\cos(\sqrt{\kappa^2 - \lambda^2} t) + (\lambda - i\kappa) \frac{\sin(\sqrt{\kappa^2 - \lambda^2} t)}{\sqrt{\kappa^2 - \lambda^2}} \right] e^{i\kappa r} d\kappa. \quad (45)$$

Along the same lines, the functions $u_{1,2}(\kappa; t)$, which relate to the mean of the stochastic processes $e^{-i\kappa\zeta(t)}$ and $\nu(t)e^{-i\kappa\zeta(t)}$ can be shown to be

$$u_1(\kappa; t) = e^{-\lambda t} \left[\cos \sqrt{\kappa^2 - \lambda^2} t \right. \\ \left. \pm \frac{\lambda \mp i\kappa}{\sqrt{\kappa^2 - \lambda^2}} \sin \sqrt{\kappa^2 - \lambda^2} t \right]. \quad (46)$$

Defining

$$p_1(r; t) = \frac{1}{2\pi} \int_{-\infty}^{\infty} \frac{\sin(\sqrt{\kappa^2 - \lambda^2} t)}{\sqrt{\kappa^2 - \lambda^2}} e^{i\kappa r} d\kappa \quad (47)$$

the pdf in (45) could be expressed as

$$e^{\lambda t} p(r; t) = \left(\lambda - \frac{\partial}{\partial r} + \frac{\partial}{\partial t} \right) p_1(r; t). \quad (48)$$

To evaluate the integral in (47) we use the identity [26, p. 303]

$$\frac{\sin(\sqrt{\kappa^2 - \lambda^2} t)}{\sqrt{\kappa^2 - \lambda^2}} = \frac{1}{2} \int_{-t}^t J_0(\lambda \sqrt{r^2 - t^2}) e^{\pm i\kappa r} dr \quad (49)$$

where $J_0(\cdot)$ is the Bessel function of the first kind of order 0. This equation demonstrates a Fourier transform relationship between the function $\sin(\cdot)/(\cdot)$ and the Bessel function $J_0(\cdot)$. The Fourier inverse desired in (47) is then equal to

$$p_1(r; t) = \frac{1}{2} I_0(\lambda \sqrt{t^2 - r^2}) R_t(r) \quad (50)$$

where $R_t(r)$ is a unit-valued rectangular pulse function centered at the origin and of support $r \in (-t, t]$, and we have used the fact that $I_0(x) = J_0(ix)$. Using this in (48), the pdf is finally obtained as

$$p(r; t) = e^{-\lambda t} \left\{ \delta(t - r) + \frac{\lambda}{2} \left[I_0(\lambda \sqrt{t^2 - r^2}) \right. \right. \\ \left. \left. + (r + t) \frac{I_1(\lambda \sqrt{t^2 - r^2})}{\sqrt{t^2 - r^2}} \right] \right\}, \\ \text{for } r \in (-t, t], t \geq 0. \quad (51)$$

This is a new result for the pdf of the random time and has not been derived before, although an expression for the even part of it, *viz.*, $h(r; t) = p(r; t) + p(-r; t)$ without the delta function term is available in [29]. It is also different from the expression given in [13] and [19], because these works assume different initial conditions that do not pertain to the random time $\zeta(t)$ that we are considering in the paper. It is seen that the pdf in (51) is asymmetric in r as it should be because $\zeta(t) = +t$ until the time first jump occurs, indicating that the random time is skewed towards positive times. Furthermore, the mean value, $\gamma_1(t)$, of $\zeta(t)$ per (16) is $\gamma_1(t) = \exp(-\lambda t) \sinh(\lambda t)/\lambda$, implying that the pdf cannot be symmetric about $r = 0$. The expression given in [19] is symmetric and even though it is a solution to the reduced telegrapher's equation, the pdf does not correspond to $\zeta(t)$. The delta function contribution in (51) arises from the event when there are no jumps in the interval $(0, t)$ and this, we know, happens for the Poisson process with a probability $e^{-\lambda t}$. The remaining terms are due to various jumps happening between $(0, t)$. Fig. 2 shows a plot of $p(r; t)$ for $\lambda = 0.1 \text{ s}^{-1}$, $t = 60 \text{ s}$, compared with numerical simulations generated with $N_r = 10^6$ realizations for the random time $\zeta(t)$. For the parameters chosen, the expected number of jumps in the interval $(0, t)$ is $\lambda t = 6$. The delta function has been excluded in the analytical data shown in Fig. 2. The asymmetry in r and the spike

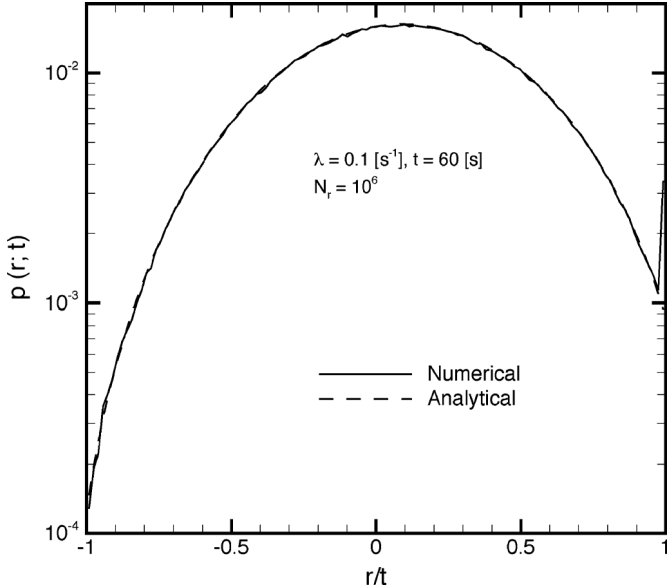


Fig. 2. PDF $p(r; t)$ of the random time for $t = 60$ s.

emerging at $r = t$ in the numerical results are clearly seen from the plot.

E. Application to Pulse Propagation in Dispersive Media

In this subsection, we will demonstrate how the stochastic model developed in the foregoing sections can be applied to derive some useful field relations in pulse propagation in causal dispersive media. We will consider 2-D Maxwell's equations, together with the commonly used dielectric dispersion models of Lorentz and Drude [30]. Extension to 3-D and other dispersion models can be proceeded along the same lines. Recall that the permittivity expression for a Lorentz model is derived by treating the interaction of a bound electron, itself represented as a damped harmonic oscillator, under the influence of a harmonic electric field [31]. Assuming an $e^{-i\omega t}$ time convention, where ω is the radian frequency, the complex dielectric permittivity of a single resonance Lorentz model is

$$\epsilon_{rc} = 1 - \frac{\omega_p^2}{(\omega^2 + i\gamma\omega - \omega_0^2)} := 1 + \chi_e(\omega) \quad (52)$$

where ω_p is the plasma frequency, γ is the damping constant resulting from collisions of electrons in the medium, ω_0 is the resonant frequency of the oscillator, and $\chi_e(\omega)$ is the electric susceptibility. When $\omega_0 = 0$, the model is known as the Drude model and is used in optical propagation in conductors as well as in radiowave propagation in the ionosphere [32]. For many practical media, including ionosphere and seawater, $\gamma < \omega_p$.

Consider 2-D ($\partial/\partial y = 0$) electromagnetic fields (E_z, H_y) that evolve in a semi-infinite Lorentz or Drude medium ($x > 0$). The field components are related through Maxwell's equations by

$$\frac{\partial E_z}{\partial x} = \mu_0 \frac{\partial H_y}{\partial t}, \quad (53)$$

$$\frac{\partial H_y}{\partial x} = \epsilon_0 \frac{\partial E_z}{\partial t} + \frac{\partial P_z}{\partial t} \quad (54)$$

where the electric polarization P_z is related to the electric field E_z via

$$\frac{\partial^2 P_z}{\partial t^2} + \gamma \frac{\partial P_z}{\partial t} = \epsilon_0 \omega_p^2 E_z - \omega_0^2 P_z. \quad (55)$$

The left-hand side of (55) is similar to that of (26), thus permitting stochastic formulation. It may be interesting to note that the average rate, λ , of the Poisson process determining the random time $\zeta(t)$ has a physical interpretation here in that it is directly proportional to the collision frequency, γ , of electrons within the medium comprising the model. Indeed $2\lambda = \gamma$ for the Lorentz/Drude media. By considering the particular solution

$$Q_z(x; t) = \epsilon_0 \omega_p^2 \int_{-\infty}^t E_z(x; \tau_1) \frac{\sin \omega_0(t - \tau_1)}{\omega_0} d\tau_1 \quad (56)$$

of the inhomogeneous wave equation corresponding to (55):

$$\frac{\partial^2 Q_z}{\partial t^2} + \omega_0^2 Q_z = \epsilon_0 \omega_p^2 E_z \quad (57)$$

the stochastic representation of P_z can be obtained as

$$P_z(x; t) = \epsilon_0 \omega_p^2 \mathbb{E} \left[\int_{-\infty}^{\zeta(t)} E_z(x; \tau_1) \frac{\sin \omega_0(\zeta(t) - \tau_1)}{\omega_0} d\tau_1 \right] \quad (58)$$

which could be substituted back into (54) to yield

$$\frac{1}{\epsilon_0} \frac{\partial H_y}{\partial x} = \frac{\partial E_z}{\partial t} + \omega_p^2 F(x; t) \quad (59)$$

where

$$F(x; t) = \Re \left\{ \mathbb{E} \left[\nu(t) e^{i\omega_0 \zeta(t)} \int_{-\infty}^{\zeta(t)} E_z(x; \tau_1) e^{-i\omega_0 \tau_1} d\tau_1 \right] \right\} \quad (60)$$

and $\Re(\cdot)$ denotes real part of. The system comprised of (53) and (59) can then be solved for (E_z, H_y) subject to boundary conditions specified at $x = 0$. The system may also be implemented using numerical schemes such as finite-difference time domain (FDTD) [33] to update (E_z, H_y) in time and space. In numerical implementations it would be necessary to examine how the quantity $F(x; t)$ evolves in time. Using properties (P1) and (P2) of the Poisson process, we can establish the following exact relation valid for any $\Delta t > 0$:

$$F(x; t + \Delta t) = \Re \left\{ g(t, \Delta t) F(x; t) + \mathbb{E} \left[\nu(t + \Delta t) e^{i\omega_0 \zeta(t + \Delta t)} \times \int_{\zeta(t)}^{\zeta(t + \Delta t)} E_z(x; \tau_1) e^{-i\omega_0 \tau_1} d\tau_1 \right] \right\} \quad (61)$$

where

$$g(t, \Delta t) = \mathbb{E} \left(\nu(t) \nu(t + \Delta t) e^{i\omega_0 [\zeta(t + \Delta t) - \zeta(t)]} \right). \quad (62)$$

Hence, it is seen that a knowledge of the correlation function of the complex-valued random process $\nu(t) \exp[i\omega_0 \zeta(t)]$ is required to update the field $F(x; t)$. The mean of this random process is given by the function $u_2(\kappa = -\omega_0; t)$ considered in Subsection II-D and its correlation function is given by (76) in the Appendix.

Owing to simplicity, we will henceforth consider the Drude medium ($\omega_0 = 0$) and derive some useful relations for the evolution of the field $F(x; t)$. However, the more general case with $\omega_0 \neq 0$ can be treated in a similar manner. From the second-order statistics given in (15), we see that the exact evolution equation for the Drude medium is

$$F(x; t + \Delta t) = e^{-\gamma \Delta t} F(x; t) + \mathbb{E} \left[\nu(t + \Delta t) \times \int_{\zeta(t)}^{\zeta(t + \Delta t)} E_z(x; \tau_1) d\tau_1 \right]. \quad (63)$$

It is seen from (63) that the future value of $F(x; t)$ depends on its present value, on the statistics of the jump process in the time interval $(t, t + \Delta t)$, on the telegraph signal $\nu(t + \Delta t)$ and on the electric field values in the interval $(\zeta(t), \zeta(t + \Delta t))$. Equation (59) together with (63) may be compared to the corresponding equation that appears in the recursive convolution method of FDTD formulations that is used to treat propagation in linear, dispersive media [33]. The convolutional integral there involving $d\chi_e(t)/dt$ and $E_z(x; t)$ is replaced in the stochastic formulation with the last term on the right-hand side of (59). The benefit of not having a convolutional integral is somewhat offset by the appearance of the expectation operator and the random upper limit of the inner integral in (60) in the stochastic formulation. If $\gamma \Delta t \ll 1$ as used in many FDTD calculations [34], [35] ([35] uses $\gamma/\omega_p = 6.732 \times 10^{-3}$, $\gamma \Delta t = 2.61 \times 10^{-4}$, [33] uses $\gamma \Delta t = 2.564 \times 10^{-2}$), the expected number of collisions in an interval Δt as given by (4) is equal to 0. In such a case $N(t + \Delta t) - N(t) \approx 0$, $\nu(t + \Delta t) \approx \nu(t)$, $\zeta(t + \Delta t) - \zeta(t) \approx \nu(t) \Delta t$ (see (13), and we get from (63) on using $\nu^2(t) = 1$ the approximate evolution equation

$$F(x; t + \Delta t) \approx e^{-\gamma \Delta t} F(x; t) + \Delta t \mathbb{E}[E_z(x; \zeta(t))] \quad (64)$$

on assuming the electric field to remain constant in the interval $|\zeta(t + \Delta t) - \zeta(t)| \leq \Delta t$. Thus, the updated field $F(x; t + \Delta t)$ depends on the current field $F(x; t)$ and the expected value of $E_z(x; t)$ at the random time $t = \zeta(t)$. It is safe to say that (64) will continue to hold for larger Δt such that $\gamma \Delta t \leq 0.1$. In fact, the probability of having no collisions in an interval Δt from (3) is $e^{-\lambda \Delta t} > 0.95$ for $\gamma \Delta t = 0.1$. In numerical computations, the field is normally evaluated over a uniform temporal grid. So, some sort of interpolation will be involved in computing the last term in (64). Furthermore, since the standard deviation of $\zeta(t)$ increases as \sqrt{t} for large t [see (16) and (17)],

more computations will be required at longer times to implement the expectation operator in (64) and the computation time involving (54) and (64) will approximately increase as $O(\sqrt{t})$ in time. This increase in computations at long times is also true for numerical schemes employing the traditional convolutional integral. It remains to be seen whether the representation (59) together with the approximate evolution equation (64) will result in more accurate or more stable numerical schemes than the ones currently used in FDTD. In this regard, one has to weigh in the operation count of the entire algorithm as well.

There is an alternative viewpoint in which the random time manifests in frequency-dependent dispersive media. The second-order equation satisfied by a Cartesian component of the electromagnetic field, E , in a homogeneous, isotropic, locally linear, temporally dispersive medium with no externally supplied sources is the Helmholtz equation $v^2 \nabla^2 E + \omega^2 \epsilon_{rc} E = 0$, where $v = 1/\sqrt{\mu_0 \epsilon_0}$ is the speed of light in free-space. The exact (pseudo) differential equation for the time-dependent field component \mathcal{E} , keeping in mind that a factor $-i\omega$ in the frequency domain translates to the operator $\partial/\partial t$ in time-domain, for the Drude medium is

$$v^2 \nabla^2 \mathcal{E} - \frac{\partial^2 \mathcal{E}}{\partial t^2} - \frac{\omega_p^2 \frac{\partial}{\partial t}}{(\gamma + \frac{\partial}{\partial t})} \mathcal{E} = 0. \quad (65)$$

This equation is not directly amenable to treatment by the stochastic model presented in this paper. However, in the low-frequency regime where $\omega \ll \gamma < \omega_p$, the complex dielectric constant approximates to $\epsilon_{rc} \omega^2 \sim \omega^2 + i\omega/\tau_0$, where $\tau_0 = \gamma/\omega_p^2$ and the exact equation (65) approximates to

$$v^2 \nabla^2 \mathcal{E} - \frac{\partial^2 \mathcal{E}}{\partial t^2} - \frac{1}{\tau_0} \frac{\partial \mathcal{E}}{\partial t} = 0 \quad (66)$$

which is identical to the modified Telegraphers's equation (24) considered in this paper. At these low frequencies, the statistics of the Poisson process in the stochastic model are governed by the damping constant as well as the plasma frequency. On the other hand, at high frequencies where $\omega \gg \gamma$, the dielectric constant approximates to $\epsilon_{rc} \omega^2 \sim \omega^2 - \omega_p^2$ and (65) reduces to the Klein-Gordon equation [25], [36] (which is a relativistic version of the time-dependent Schrödinger equation)

$$v^2 \nabla^2 \mathcal{E} - \frac{\partial^2 \mathcal{E}}{\partial t^2} - \omega_p^2 \mathcal{E} = 0. \quad (67)$$

It is not uncommon in electromagnetic pulse propagation studies to consider limiting cases such as these to facilitate asymptotic analysis [37]. Notwithstanding this, it is still of interest to develop a stochastic model for the exact equation (65) valid at all frequencies.

III. CONCLUSION

Using stochastic calculus pertaining to jump processes, we have in this paper, established Kac's conjecture that the solution of a modified telegrapher's equation can be expressed in terms of the solution of a wave equation by simply replacing the time variable with random time generated from a Poisson process. We are able to demonstrate this for arbitrary initial conditions and for linear PDEs more general than the wave equation that contain second-order time derivatives. An expression has

been derived for the probability density function of the random time and it is shown that the pdf itself satisfies the modified telegrapher's equation. This expression is more general than the currently available expression in the literature that is applicable only to the even part of the random time.

The theory presented in the paper is applicable to waves propagating in a conducting medium, including the case where the conductivity (or more generally where the complex relative permittivity) is frequency dependent. Accordingly, the concept of random time was applied to pulse propagation in dispersive media in Subsection II-E and new update equations for the field components have been derived that should find utility in numerical implementations such as FDTD. In particular Lorentz and Drude media were considered in the paper and we have shown that the computation time for field evaluation goes up in time as $O(\sqrt{t})$. Application to more complicated media such as those characterized by multiple resonant Lorentz model is underway and will be reported in a future paper. It would also be interesting to derive higher order evolution approximations to the field $F(x; t)$ by equating the probability of having fewer than k collisions in an interval Δt to a given number and then determining k from it. This should facilitate development of numerical schemes with some sort of error control. For instance approximation (64) has been derived under the assumption of having no collisions in an interval Δt , but the probability of no collisions in an interval Δt is $e^{-\lambda \Delta t}$. By setting this probability to a given number less than unity, one should be able to determine the maximum permissible Δt for this approximation. Such studies will be taken up in the future.

The concept of random could be utilized to extend the analytical solution of wave propagation problems that are available only for lossless media. For instance, the Cagniard-de Hoop method [38] has been applied in the past to treat transient radiation arising in certain nonconducting, boundary value problems [39], [40]. It should be possible to extend the expressions provided in these works to the corresponding lossy media by simply replacing the time variable with the random time and performing an expectation with respect to the Poisson process, thereby increasing the utility of the Cagniard-de Hoop method.

APPENDIX

CORRELATION FUNCTION OF $\nu(t)e^{i\omega_0\zeta(t)}$

Define

$$g(\eta, \xi) = \mathbb{E} \left\{ \nu(\eta) \nu(\eta + \xi) e^{i\omega_0 [\zeta(\eta+\xi) - \zeta(\eta)]} \right\}, \quad (68)$$

and

$$h_1(\eta, \xi) = \mathbb{E} \left\{ \nu(\eta) e^{i\omega_0 [\zeta(\eta+\xi) - \zeta(\eta)]} \right\}. \quad (69)$$

Then it is clear from using (14) and (15) that

$$g(\eta, 0) = 1, \quad (70)$$

$$h_1(\eta, 0) = e^{-2\lambda\eta}. \quad (71)$$

Using (9), (12), and (13), it can be established that for $\xi > 0$

$$\frac{\partial g}{\partial \xi} = -2\lambda g + i\omega_0 h_1, \quad (72)$$

and

$$\frac{\partial h_1}{\partial \xi} = i\omega_0 g. \quad (73)$$

From (70), (71) and (72), we see that

$$\frac{\partial g}{\partial \xi} \Big|_{\xi=0} = -2\lambda + i\omega_0 e^{-2\lambda\eta}. \quad (74)$$

A second-order equation for g can be obtained on combining (72) and (73):

$$\frac{\partial^2 g}{\partial \xi^2} + 2\lambda \frac{\partial g}{\partial \xi} + \omega_0^2 g = 0 \quad (75)$$

which can be solved by standard means for the initial conditions specified in (70) and (74) to yield

$$g(\eta, \xi) = \left[\cosh(p\xi) - \frac{\lambda - i\omega_0 e^{-2\lambda\eta}}{p} \sinh(p\xi) \right] e^{-\lambda\xi} \quad (76)$$

where $p = \sqrt{\lambda^2 - \omega_0^2}$. As a quick check, $g(\eta, \xi) = e^{-2\lambda\xi}$ when $\omega_0 = 0$, a result that agrees with (15).

REFERENCES

- [1] K. K. Sabelfeld, *Monte Carlo Methods in Boundary Value Problems*. New York, NY, USA: Springer-Verlag, 1991.
- [2] R. C. Garcia and M. N. O. Sadiku, "Monte Carlo fixed-radius floating random walk solution for potential problems," in *Proc. IEEE Southeastcon '96: Bringing Together Educat., Sci., Technol.*, Tampa, FL, USA, 1996, pp. 88–91, no. DOI: 10.1109/SECON.1996.510032.
- [3] Y. L. L. Coz, H. J. Greub, and R. B. Iverson, "Performance of random walk capacitance extractors for IC interconnects: A numerical study," *Solid-State Electron.*, vol. 42, pp. 581–588, 1998.
- [4] M. K. Chati, M. D. Grigoriu, S. S. Kulkarni, and S. Mukherjee, "Random walk method for the two- and three-dimensional Laplace, Poisson and Helmholtz's equations," *Int. J. Numer. Meth. Eng.*, vol. 51, pp. 1133–1156, 2001, no. DOI: 10.1002/nme.178.
- [5] K. Chatterjee, P. Matos, and Y. L. L. Coz, "A novel Dirichlet-Neumann random walk algorithm for the solution of time-harmonic Helmholtz equation at multiple wavelength length scales: 1D and 2D verifications," *Appl. Comput. Electromagn. Soc. J.*, vol. 19, no. 16, pp. 127–132, Mar. 2004.
- [6] K. Chatterjee, C. Yu, H. Yue, and J. Poggie, "A parallelized Monte Carlo algorithm for the one-dimensional wave equation: Validation with analytical benchmark solutions," *WSEAS Trans. Math.*, vol. 6, no. 3, pp. 487–493, Mar. 2007.
- [7] B. V. Budaev and D. B. Bogy, "A probabilistic approach to wave propagation and scattering," *Radio Sci.*, vol. 40, no. RS6S07, 2005, p. doi: 10.1029/2004RS003176.
- [8] B. V. Budaev and D. B. Bogy, "Two-dimensional diffraction by a wedge with impedance boundary conditions," *IEEE Trans. Antennas Propag.*, vol. 53, no. 6, pp. 2073–2080, Jun. 2005.
- [9] B. V. Budaev and D. B. Bogy, "Diffraction of plane skew electromagnetic wave by a wedge with general anisotropic impedance boundary conditions," *IEEE Trans. Antennas Propag.*, vol. 54, no. 5, pp. 1559–1567, May 2006.
- [10] G. I. Taylor, "Diffusion by continuous movements," *Proc. Lond. Math. Soc. (2)*, vol. 20, pp. 196–212, 1921/2.
- [11] R. Courant, K. Friedrichs, and H. Lewy, "On the partial difference equations of mathematical physics," *IBM Journal*, pp. 215–234, Mar. 1967, (This is a republication of the original paper that appeared in *Mathematische Annalen* 100, 32–74, 1928).
- [12] M. Kac, "Random walk and the theory of Brownian motion," *Amer. Math. Month.*, vol. 54, no. 7, pt. 1, pp. 369–391, Aug.–Sep. 1947.

- [13] S. Goldstein, "On diffusion by discontinuous movements, and on the Telegraph equation," *Quart. J. Mech. Appl. Math.*, vol. IV, pt. 2, pp. 129–156, 1951.
- [14] J. L. Doob, *Stochastic Processes*, ser. Wiley Classic Library. New York, NY, USA: Wiley, 1953.
- [15] E. B. Dynkin and A. A. Yuskevich, *Markov Processes: Theorems and Problems*. New York, NY, USA: Plenum, 1969.
- [16] M. Freidlin, *Functional Integration and Partial Differential Equations*, ser. Annals of Mathematical Studies. Princeton, NJ, USA: Princeton Univ. Press, 1985, no. 109.
- [17] G. H. Weiss, *Aspects and Applications of the Random Walk*. New York, NY, USA: North-Holland, 1994.
- [18] M. Kac, "A stochastic model related to the telegrapher's equation," *Rocky Mountain J. Math.*, vol. 43, no. 3, pp. 479–509, Summer 1974.
- [19] G. H. Weiss, "Some applications of persistent random walks and the telegrapher's equation," *Physica A*, vol. 311, pp. 381–410, 2002.
- [20] A. V. Plyukhin, "Stochastic processes leading to wave equations in dimensions higher than one," *Phys. Rev. E*, vol. 81, pp. 021 113-1–021 113-5, 2010, no. DOI: 10.1103/PhysRevE.81.021113.
- [21] S. E. Shreve, *Stochastic Calculus for Finance II: Continuous-Time Models*. New York, NY, USA: Springer, 2004.
- [22] W. Feller, *An Introduction to Probability Theory and Its Applications*, 3rd ed. New York, NY, USA: Wiley, 1957, vol. 1.
- [23] R. W. Brockett, W. Gong, and Y. Guo, "Stochastic analysis for fluid queueing systems," in *Proc. 38th IEEE Conf. Dec. Control*, Phoenix, AZ, USA, Dec. 1999, pp. 3077–3082.
- [24] A. Papoulis and S. Unnikrishnan, *Probability, Random Variables and Stochastic Processes*. New York, NY, USA: McGraw-Hill, 2002.
- [25] P. M. Morse and H. Feshbach, *Methods of Theoretical Physics, Vol. I*. New York, NY, USA: McGraw-Hill, 1953.
- [26] J. A. Stratton, *Electromagnetic Theory*. New York, NY, USA: McGraw-Hill, 1941.
- [27] R. Janaswamy, "Evaluation of certain integrals using stochastic formulation of the lossy wave equation," in *Proc. IEEE Antennas Propag. Soc. Int. Symp.*, Chicago, IL, USA, Jul. 8–14, 2012, Paper No. 563.7.
- [28] A. Debnath, *Integral Transforms and Their Applications*. New York, NY, USA: CRC, 2000.
- [29] C. DeWitt-Morette and S. K. Foong, "Path-integral solutions of wave equations with dissipation," *Phys. Rev. Lett.*, vol. 62, no. 19, pp. 2201–2204, May 8, 1989.
- [30] K. E. Oughstun, *Electromagnetic and Optical Pulse Propagation-I: Spectral Representations in Temporally Dispersive Media*. New York, NY, USA: Springer, 2006.
- [31] R. E. Hummel, *Electronic Properties of Materials: An Introduction to Engineers*. New York, NY, USA: Springer-Verlag, 1985.
- [32] K. G. Budden, *The Propagation of Radio Waves: The Theory of Radio Waves of Low Power in the Ionosphere and Magnetosphere*. New York, NY, USA: Cambridge Univ. Press, 1985.
- [33] A. Taflove and S. Hagness, *Computational Electrodynamics: The Finite Difference Time Domain Method*, 3rd ed. Boston, MA, USA: Artech House, 2005.
- [34] Y. Takayama and W. Klaus, "Reinterpretation of the auxiliary differential equation method for FDTD," *IEEE Microw. Wireless Compon. Lett.*, vol. 12, no. 3, pp. 102–104, Mar. 2002.
- [35] M. Okoniewski and E. Okoniewska, "Drude dispersion in ADE FDTD revisited," *IEE Electron. Lett.*, vol. 42, no. 9, pp. 503–504, Apr. 27, 2006.
- [36] G. B. Whitham, *Linear and Nonlinear Waves*, ser. Wiley Interscience Publication. New York, NY, USA: Wiley, 1974.
- [37] K. E. Oughstun, *Electromagnetic and Optical Pulse Propagation-II: Temporal Pulse Dynamics in Dispersive, Attenuative Media*. New York, NY, USA: Springer, 2009.
- [38] A. T. de Hoop, "A modification of Cagniard's method for solving seismic pulse problems," *Appl. Sci. Res.*, vol. 8, pp. 349–356, 1960, no. Sec. B.
- [39] A. T. de Hoop, "Pulsed electromagnetic field radiation from a line source in a two-media configuration," *Radio Sci.*, vol. 14, no. 2, pp. 253–268, Mar.–Apr. 1979.
- [40] A. T. de Hoop, M. Stumpf, and I. E. Lager, "Pulsed electromagnetic field radiation from a wide slot antenna with a dielectric layer," *IEEE Trans. Antennas Propag.*, vol. 59, no. 8, pp. 2789–2798, Aug. 2011.
- [41] R. Griego and R. Hersh, "Theory of random evolutions with applications to partial differential equations," *Trans. Amer. Math. Soc.*, vol. 156, pp. 405–418, May 1971.



Ramakrishna Janaswamy (F'03) received the B.S. degree in electronics and communications engineering from REC-Warangal (now NIT Warangal), Warangal, India, in 1981, the M.S. degree in microwave and radar engineering from IIT-Kharagpur, Kharagpur, India, in 1983, and the Ph.D. degree in electrical engineering from the University of Massachusetts, Amherst, MA, USA, in 1986.

From August 1986 to May 1987, he was an Assistant Professor of electrical engineering at Wilkes University, Wilkes Barre, PA, USA. From August 1987 to August 2001, he was on the faculty of the Department of Electrical and Computer Engineering, Naval Postgraduate School, Monterey, CA, USA. In September 2001, he joined the Department of Electrical and Computer Engineering, University of Massachusetts, Amherst, where he is currently a Professor. His research interests include deterministic and stochastic radio wave propagation modeling, analytical, and computational electromagnetics, antenna theory and design, wireless communications, and mathematical physics.

Prof. Janaswamy was the recipient of the R. W. P. King Prize Paper Award of the IEEE TRANSACTIONS ON ANTENNAS AND PROPAGATION in 1995. For his services to the IEEE Monterey Bay Subsection, he received the IEEE 3rd Millennium Medal from the Santa Clara Valley Section in 2000. He is an elected member of the U.S. National Committee of International Union of Radio Science, Commissions B and F. He served as an Associate Editor of Radio Science from January 1999 to January 2004 and an Associate Editor of the IEEE TRANSACTIONS ON VEHICULAR TECHNOLOGY from 2003 to 2006. He is currently an Associate Editor of the IEEE TRANSACTIONS ON ANTENNAS AND PROPAGATION and an Editor of *IETE Technical Reviews*. He is the author of the book *Radiowave Propagation and Smart Antennas for Wireless Communications* (Kluwer Academic, 2000) and a contributing author in *Handbook of Antennas in Wireless Communications* (CRC Press, 2001) and *Encyclopedia of RF and Microwave Engineering* (Wiley, 2005).

Errata

Errata to “On random time and on the relation between wave and telegraph equations”

Ramakrishna Janaswamy

In [1], an acknowledgment was overlooked. It should have appeared as follows. The IEEE regrets the omission.

Manuscript received May 03, 2013. Date of current version May 29, 2013.
The author is with the Department of Electrical and Computer Engineering, University of Massachusetts, Amherst, MA 01003 USA (e-mail: janaswamy@ecs.umass.edu).

Digital Object Identifier 10.1109/TAP.2013.2262155

ACKNOWLEDGMENT

After this paper was accepted, the author became aware of a mathematical proof of Kac’s conjecture given in reference [41]¹ using group theory.

REFERENCES

- [1] R. Janaswamy, “On random time and on the relation between wave and telegraph equations,” *IEEE Trans. Antennas Propag.*, vol. 61, no. 5, pp. 2735–2744, May 2013.
- [2] R. Griego and R. Hersh, “Theory of random evolutions with applications to partial differential equations,” *Trans. Amer. Math. Soc.*, vol. 156, pp. 405–418, May 1971.

¹Reference [41] appears here as reference [2].

Direct Solution of Current Density Induced on a Rough Surface by Forward Propagating Waves

Ramakrishna Janaswamy, *Fellow, IEEE*

Abstract—A new Volterra integral equation of the second kind with square integrable kernel is derived for paraxial propagation of radiowaves over a gently varying, perfectly conducting rough surface. The integral equation is solved exactly in terms of a infinite series and the necessary and sufficient conditions for the solution to exist and converge are established. Super exponential convergence of the Neumann series for arbitrary surface slope is established through asymptotic analysis. Expressions are derived for the determination of the number of terms needed to achieve a given accuracy, the latter depending on the parameters of the rough surface, the frequency of operation and the maximum range. Numerical results with truncated series are compared with that obtained by solving the integral equation numerically for a sinusoidal surface, Gaussian hill, and a random rough surface with Pierson–Moskowitz spectrum.

Index Terms—Irregular terrain, parabolic equation, rough sea, rough surface, small slopes, Volterra integral equation.

I. INTRODUCTION

WAVE propagation over a rough surface is a classical problem and is important in a number of areas including radar detection [1], [2], remote sensing [3], [4], wireless communications [5], [6], underwater acoustics [7], and optics [8], [9]. By rough surface we mean either a deterministic surface as in the case of an irregular terrain or a statistical one as in the case of a sea surface. Various methods such as physical optics (also known as the Kirchhoff's approximation) [10], small perturbation [9], integral equation [11]–[15], modal series [16], [17], partial differential equation [18]–[20], etc. are used to study scattering and propagation of waves over rough surfaces, with each offering its own niche advantage under certain situations.

When the normal distances of the source and receiving points relative to the mean surface are a small fraction of the separation between the source and observation points, and the rough surface is gently varying (meaning that its slope angles are small), propagation is primarily governed by forward traveling waves which make small angles with respect to the mean surface. Such cases are encountered, for example, in ship-ship radar/communications over a rough sea or long distance communications over irregular terrain with ground-based antennas. In such a case the Helmholtz equation, which the electromagnetic fields satisfy, may be replaced with the parabolic equation [21], wherein

paraxial waves travel in a unidirectional direction with respect to one coordinate (usually range) direction. Parabolic equation and its variants has been successfully used in many propagation and bistatic scattering problems in the electromagnetics [22], acoustics [7], and optics [7] areas. The present paper is concerned with determining the current density induced on a rough surface when the fields in a semi-infinite region bounded by the rough surface satisfy the parabolic equation under time-harmonic excitation.

Integral equation methods, that make use of the Green's function for the problem at hand, are attractive owing to their ability to automatically incorporate the boundary condition at infinity with the added advantage that unknowns are distributed only on the boundary of the region of interest. In our case the boundary is simply the rough surface. Because the parabolic equation has only a first-order derivative along the range axis, the relevant integral equation will be of Volterra type as opposed to the Fredholm type [13] for the Helmholtz equation. Previous formulations of the integral equations for the parabolic equation [24]–[27] or for low-grazing angle formulations [28] concentrated on obtaining the solution numerically using a variety of approaches. That the Volterra integral equation can be solved exactly appears to have escaped the attention of previous researchers and it is the purpose of the present paper to provide such a solution. By *exact* we mean a solution that does not involve matrix inversion, in the same sense that the infinite series solution of scattering of a perfectly conducting sphere is considered exact.

Using the Green's function for the parabolic equation, we first derive a new Volterra integral equation of the second kind in Section II-A for the induced current density assuming a perfectly conducting rough surface and horizontal polarization. Extension to other surface types and polarizations can be carried out in a similar fashion. The kernel of the integral equation as well as the initial fields are both shown to belong to the space of square integrable functions [29]. The resulting second-kind integral equation is solved in Section II-B exactly using Picard's method of iteration, resulting in an infinite series with iterated kernels. The necessary and sufficient conditions for the series to converge are established. An expression is found in Section II-C for the integrated mean square error bound in terms of the maximum range, the frequency of operation and the parameters of the rough surface when the infinite series is truncated. While the exact series solution stands on its own merit, we do not claim that it will result in a numerically efficient solution for long distance propagation without further optimization of the various algorithmic steps. However, we believe that it will open the door to obtaining various analytical approximations under specialized situations. For instance, the zeroth

Manuscript received July 23, 2012; revised February 13, 2013; accepted March 09, 2013. Date of publication March 26, 2013; date of current version July 01, 2013. This work was supported by the Army Research Office under Grant ARO W911NF-10-1-0305.

The author is with the Department of Electrical and Computer Engineering, University of Massachusetts, Amherst, MA 01003 USA (e-mail: janaswamy@ecs.umass.edu).

Digital Object Identifier 10.1109/TAP.2013.2254692

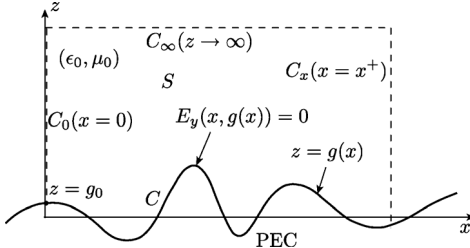


Fig. 1. Perfectly conducting rough surface bounding the region S .

order approximation comprised of the right-hand side of the original integral equation is shown in Section II-D to be accurate when the slope angles and/or the range parameters are sufficiently small. Numerical results for the current density and propagation factor obtained with a truncated series are compared in Section III with those obtained on solving the integral equation numerically for a surfaces with both small and large slope angles (but still small enough so that parabolic approximation still holds). Finally, conclusions and future directions are presented in Section IV. The deterministic results presented in the paper will form the starting point for the treatment of a *random* rough surface. Still, the results should have a value of their own right in areas such as wireless communication, where one is concerned with the propagation of radiowaves over a deterministic irregular terrain [30], [31], [22].

II. THEORY

We consider time-harmonic propagation of two-dimensional radio waves over a 1-D rough surface (a surface varying only in one direction). For simplicity, the surface is assumed to be perfectly conducting, although a similar formulation could be carried out for the more general case of an impedance surface. Fig. 1 shows the geometry of the problem along with the coordinate system assumed. All field quantities are assumed to be invariant of the y -axis and an $e^{-i\omega\tau}$ time dependence at the radian frequency $\omega = 2\pi f$ in the time variable τ is assumed and suppressed throughout. The fields are assumed to be generated by a vertically polarized magnetic source placed in the plane $x = 0$, resulting in a TE_z mode with nonzero field components of E_y , H_x , and H_z , where E denotes electric field and H denotes magnetic field. The rough surface is described by $z = g(x)$ and the medium above it is assumed to be vacuum with constitutive parameters (ϵ_0, μ_0) . Vacuum is treated as the limiting case of a lossy medium having wavenumber $k_0 = \omega\sqrt{\epsilon_0\mu_0}(1 + i\epsilon)$, $\epsilon > 0$, in the limit of $\epsilon \rightarrow 0$.

We assume that the slopes of the rough surface are small enough so that back scattering can be ignored and that waves travel predominantly in the paraxial direction. In practice, waves traveling roughly within $\pm(15^\circ - 20^\circ)$ relative to the horizontal axis are correctly modeled by the formulation we are considering. The reduced field $U = e^{-ik_0x}E_y$ then satisfies the standard parabolic equation (PE) [32], [33]

$$\frac{\partial U}{\partial x} = \frac{i}{2k_0} \frac{\partial^2 U}{\partial z^2} \quad (1)$$

together with the initial condition $U(x = 0, z) = U_0(z)$ and the boundary condition $U(x, z = g(x)) = 0$. The derivation of an

integral equation for the unknown surface current residing on the rough surface is facilitated by the availability of a Green's function. The Green's function, G_0 , in free-space for the PE satisfies the equation

$$\frac{\partial G_0}{\partial x} = \frac{i}{2k_0} \frac{\partial^2 G_0}{\partial z^2} + \delta(x - \xi)\delta(z - \eta) \quad (2)$$

where $\delta(x)$ is the unit impulse function at $x = 0$. This linear partial differential equation with constant coefficients can be solved by employing either a Fourier transformation with respect to z [34] or a Laplace transformation with respect to x and carrying out standard manipulations. The solution is

$$G_0(x, z; \xi, \eta) = \frac{\gamma\Theta(x - \xi)}{\sqrt{x - \xi}} \exp \left[i \frac{k_0}{2} \frac{(z - \eta)^2}{(x - \xi)} \right] \quad (3)$$

where $\gamma = \sqrt{k_0/2\pi i}$ and $\Theta(x)$ is the unit step function. For later purposes the following integral representation of G_0 will become useful:

$$G_0(x, z; \xi, \eta) = \frac{\Theta(x - \xi)}{2\pi} \int_{-\infty}^{\infty} e^{ik_z(z - \eta)} e^{-i\frac{k_z^2}{2k_0}(x - \xi)} dk_z. \quad (4)$$

The Green's function G_0 satisfies the following basic properties:

- I $\frac{\partial G_0}{\partial x} = -\frac{\partial G_0}{\partial \xi}, \frac{\partial G_0}{\partial z} = -\frac{\partial G_0}{\partial \eta}$
- II $\lim_{|z| \rightarrow \infty} |G_0| = 0, \lim_{|z| \rightarrow \infty} |\partial G_0 / \partial z| = 0$
- III $\lim_{x \rightarrow \xi} G_0(x, z; \xi, \eta) = \delta(z - \eta)$
- IV $\lim_{z \rightarrow \eta} \frac{i}{2k_0} \frac{\partial G_0}{\partial z} = -\text{Sign}(z - \eta) \frac{1}{2} \delta(x - \xi)$

as can be easily verified by keeping in mind that k_0 has a vanishingly small positive imaginary part.

A. Volterra Integral Equation of the Second Kind

Consider a region S bounded by $C_0 + C + C_x + C_\infty$ as shown in Fig. 1. The contour C_0 is defined by the vertical line $x = 0$, C_x is defined by the line $x = x^+$, C_∞ is defined by the horizontal line $z \rightarrow \infty$ and C corresponds to the rough surface. Integrating the null quantity $\{G_0 \cdot [\partial U / \partial z - (i/2k_0) \partial^2 U / \partial z^2] + U \cdot [\partial G_0 / \partial z + (i/2k_0) \partial^2 G_0 / \partial z^2 + \delta(x - \xi)\delta(z - \eta)]\}$ over S and assuming that U and $\partial U / \partial z$ are bounded at infinity, it can be shown by making use of the properties (I)-(IV) of the Green's function that

$$U(x, z) = \int_{g_0}^{\infty} U_0(\eta) G_0(x, z; 0, \eta) d\eta - \frac{i}{2k_0} \int_0^x J(\xi) G_0[x, z; \xi, g(\xi)] d\xi =: U_i(x, z) + U_s(x, z) \quad (5)$$

where $g_0 = g(x = 0)$ and $J(\xi) := (\partial U)/(\partial \eta)[\xi, \eta = g(\xi)]$ is referred to as the *current density*.¹ The first integral on the right-hand side of (5) constitutes the field in free-space, $U_i(x, z)$, that arises from the initial field $U_0(\eta)$, and the second term corresponds to the scattered field, $U_s(x, z)$, that is generated by the vertical derivative, $\partial U/\partial z$, of the reduced field residing on C .

An integral equation of the first kind can be derived as in [27] by taking the limit as $z \rightarrow g(x)$ along a vertical line and making use of the fact that $U(x, g(x)) = 0$. However, we are interested in deriving an integral equation of the second kind so that an analytical solution in terms of an infinite series is possible. To this end, we take the vertical derivative on both sides of (5) and take the limit as $z \rightarrow g(x)$ on a vertical line. The following limit relation is encountered, which can be easily derived based on property (IV) of G_0 :

$$\lim_{z \rightarrow g(x)} \frac{1}{ik_0} \frac{\partial G_0}{\partial z}[x, z; \xi, g(\xi)] = \delta(x - \xi) + g_d(x; \xi) \cdot G_0[x, g(x); \xi, g(\xi)] \quad (7)$$

where

$$g_d(x; \xi) := \frac{g(x) - g(\xi)}{x - \xi}. \quad (8)$$

The function $g_d(x; \xi)$ is bounded when the slopes of the rough surface are finite. Using (7), the following Volterra integral equation of the second kind in the unknown $J(x)$ is obtained from (6):

$$J(x) - \gamma \int_0^x \frac{K_0(x; \xi)}{\sqrt{x - \xi}} J(\xi) d\xi = J_i(x) \quad (9)$$

where

$$K_0(x; \xi) := g_d(x; \xi) e^{ik_0(x - \xi) g_d^2(x; \xi)/2} = K_0^*(\xi; x) \quad (10)$$

with superscript * denoting complex conjugate and

$$J_i(x) := -2 \int_{g_0}^{\infty} U_0(\eta) \frac{\partial G_0(x, g(x); 0, \eta)}{\partial \eta} d\eta \quad (11)$$

$$= 2 \int_{g_0}^{\infty} \frac{\partial U_0}{\partial \eta} G_0(x, g(x); 0, \eta) d\eta \quad (12)$$

is the incident current density defined entirely in terms of the initial data. The latter equality in (12) assumes that the initial data is differentiable. Equation (9) was used in [26] and [35] and solved numerically, although its derivation was not shown there. The auxiliary kernel $K_0(x; \xi)$ will be bounded if Lipschitz conditions are imposed on the function $g(x)$ describing the rough surface. This will be clarified in Section II-B. Note that for a differentiable rough surface, $g_d(x; x) = g_d(x; x^-) = g'(x)$ and $K_0(x; x) = g'(x)$. A Volterra integral equation of the second kind based on the parabolic approximation and different from (9) was also given in [24], [25] for the attenuation function over

¹It may be noted that the traditional current density for 2-D propagation defined as $\mathbf{y} \cdot (\mathbf{n} \times \mathbf{H})$ can be approximately related to the vertical derivative for surfaces having small slopes by noting that $\mathbf{y} \cdot (\mathbf{n} \times \mathbf{H}) = (i/\omega\mu_0)\mathbf{n} \cdot \nabla E_y = (i/\omega\mu_0)[\partial E_y/\partial z - g'(x)\partial E_y/\partial x]/\sqrt{1 + (g'(x))^2} \approx (i/\omega\mu_0)\partial E_y/\partial z/\sqrt{1 + (g'(x))^2} = (i/\omega\mu_0)e^{ik_0 x} J(x)/\sqrt{1 + (g'(x))^2}$, where $g'(x)$ is the derivative of $g(x)$.

a lossy irregular terrain. Most previous works in radiowave and acoustic propagation, including [26], [27] and [25], were concerned with obtaining a numerical solution of the derived integral equations. Our goal, however, is to obtain a direct solution that will not involve matrix inversions.

The kernel of the integral equation in (9) has a weak singularity as evidenced by the presence of $\sqrt{x - \xi}$ in the denominator of the integrand. This will prevent a direct application of the theory for $\mathcal{L}_2(0, X)$ kernels (i.e., square integrable over a finite range $x = X$) available in standard references such as [36]. We will first transform it to another integral equation with a square integrable kernel using the device suggested in [36]. We rewrite (9) as

$$\gamma \int_{t=0}^{x'} \frac{K_0(x'; t)}{\sqrt{x' - t}} J(t) dt = J(x') - J_i(x') \quad (13)$$

multiply both sides with $\gamma K_0(x; x')/\sqrt{x - x'}$ and integrate over $x' = (0, x)$. The two integrals on the left-hand side may be interchanged by noting that

$$\int_{x'=0}^x dx' \int_{t=0}^{x'} dt = \int_{t=0}^x dt \int_{x'=t}^x dx'. \quad (14)$$

Equation (13) is again utilized on the right-hand side of the resulting equation to finally yield the following Volterra integral equation of the second kind with a square integrable kernel K_1 :

$$J(x) - \gamma^2 \int_{t=0}^x K_1(x; t) J(t) dt = J^{(0)}(x) \quad (15)$$

where

$$J^{(0)}(x) := J_i(x) + \gamma \int_{x'=0}^x J_i(x') \frac{K_0(x; x')}{\sqrt{x - x'}} dx', \quad (16)$$

and

$$K_1(x; t) := \int_{x'=t}^x \frac{K_0(x; x') K_0(x'; t)}{\sqrt{(x - x')(x' - t)}} dx'. \quad (17)$$

The kernel K_1 is actually bounded in addition to being in $\mathcal{L}_2(0, X)$ space. The weak singularity in the integrand of (17) is removable as can be seen by making the change of variable $x' = x \sin^2 \theta + t \cos^2 \theta$ to result in

$$K_1(x; t) = 2 \int_{\theta=0}^{\pi/2} K_0(x; x \sin^2 \theta + t \cos^2 \theta) \times K_0(x \sin^2 \theta + t \cos^2 \theta; t) d\theta \quad (18)$$

which shows that K_1 is bounded if $K_0(x; x')$ is bounded. Equation (18) also shows that $K_1(x, x) = \pi K_0^2(x; x) = \pi[g'(x)]^2$. The transformation $x' = x \sin^2 \theta$ in (16) yields the expression

$$J^{(0)}(x) = J_i(x) + 2\gamma \sqrt{x} \times \int_{\theta=0}^{\pi/2} J_i(x \sin^2 \theta) K_0(x; x \sin^2 \theta) \sin \theta d\theta \quad (19)$$

which reveals that $J^{(0)}(x)$ is bounded and square integrable in $(0, X)$ if $J_i(x)$ is bounded.

B. Exact Current Distribution

Under certain conditions, the integral equation (15) can be readily solved by the Picard's method of successive approximation to result in an infinite series, also known as the *Neumann series* [36]. We assume at the outset that the initial data is such that the incident current density $J_i(x)$ is bounded. A *sufficient condition* for $|J_i(x)|$ to be bounded can be established by making use of (11) and (4). Using the Fourier representation (4) of the Green's function in (11), we see that

$$\begin{aligned} J_i(x) &= \frac{i}{\pi} \int_{g_0}^{\infty} \int_{-\infty}^{\infty} U_0(\eta) k_z e^{ik_z(g(x)-\eta)} e^{-ik_z^2 x / 2k_0} dk_z d\eta \\ &= \frac{i}{\pi} \int_{-\infty}^{\infty} k_z \bar{U}_0(k_z) e^{ik_z g(x)} e^{-ik_z^2 x / 2k_0} dk_z, \end{aligned} \quad (20)$$

where $\bar{U}_0(k_z) = \int_{g_0}^{\infty} U_0(\eta) \exp(-ik_z\eta) d\eta$ is the Fourier transform of $U_0(\eta)$. Therefore,

$$\pi |J_i(x)| \leq \int_{-\infty}^{\infty} |k_z \bar{U}_0(k_z)| dk_z. \quad (21)$$

The integrand of the right-hand side is recognized as the modulus of the Fourier spectrum of $dU_0(\eta)/d\eta$. Thus, (21) implies that a sufficient condition for $J_i(x)$ to be bounded is the existence of the first derivative of $U_0(\eta)$ in the entire interval (g_0, ∞) . However, $J_i(x)$ can remain finite even if $U_0(\eta)$ is discontinuous at finite number of isolated points. This is certainly true for a truncated Gaussian type of source that is commonly used in propagation studies [18]. Indeed, for a Gaussian source of amplitude A , centered at H_t with a standard deviation σ_z and truncated to zero below $\eta = g_0$

$$U_0(\eta) = \frac{A}{\sqrt{2\pi}\sigma_z} e^{-(\eta-H_t)^2/2\sigma_z^2}, \quad \eta = (g_0^+, \infty) \quad (22)$$

and we get

$$J_i(x) = \frac{A[H_t - g(x)]}{(\sigma_z^2 + ix/k_0)^{3/2}} \sqrt{\frac{2}{\pi}} f_i \exp \left[-\frac{(H_t - g(x))^2}{2(\sigma_z^2 + ix/k_0)} \right] \quad (23)$$

where

$$\begin{aligned} f_i &= 1 - \frac{1}{2} \operatorname{erfc} \left(\gamma_g \sqrt{\beta} + \frac{u_0}{2\sqrt{\beta}} \right) \\ &\quad + \frac{\exp \left[- \left(\gamma_g \sqrt{\beta} + \frac{u_0}{2\sqrt{\beta}} \right)^2 \right]}{2\gamma\sqrt{\pi\beta}} \end{aligned} \quad (24)$$

$$\sim 1, \quad u_0 \gg 1 \quad (25)$$

with $u_0 = (H_t - g_0)/\sigma_z$, $\gamma_g = ik_0(H_t - g(x))\sigma_z/x$, $(2\beta)^{-1} = (1 - ik_0\sigma_z^2/x)$ and $\operatorname{erfc}(\cdot)$ denotes complementary error function [37]. Hence, $J_i(x)$ is bounded for any x in a finite range $(0, X)$ even though $U_0(g_0^+) \neq 0$ and $U_0(g_0)$ is set to zero.

We next assume that the function defining the rough surface satisfies the Lipschitz's condition [29] on $(0, X)$, i.e., for a positive constant α_g

$$|g(x) - g(\xi)| \leq \alpha_g |x - \xi|. \quad (26)$$

Lipschitz requirement is stronger than continuity, but weaker than differentiability. For differentiable functions, α_g is simply the maximum absolute derivative, but the Lipschitz condition is satisfied also by non-differentiable functions. For instance, a continuous, piecewise linear rough surface satisfies the Lipschitz condition with $\alpha_g = \max(\text{absolute slope})$. Thus, the function in (8) satisfies $|g_d(x; \xi)| \leq \alpha_g$ and the kernel in (10) remains bounded: $|K_0(x; \xi)| \leq \alpha_g$. As already pointed out in Section II-A, the kernel $K_1(x; t)$ and the function $J^{(0)}(x)$ are both bounded and hence belong to the $\mathcal{L}_2(0, X)$ space if $K_0(x; x')$ and $J_i(x)$ are, respectively, bounded. In view of these results, the following theorem [36], [38] immediately applies to our situation:

Theorem (Volterra Integral Equation of the Second Kind): The Volterra integral equation of the second kind (15), where the kernel $K_1(x; t)$ and the function $J^{(0)}(x)$ belong to the class $\mathcal{L}_2(0, X)$, has a unique nontrivial solution in $\mathcal{L}_2(0, X)$ for arbitrary $\gamma \in \mathbb{C}$. This solution is given by the formula

$$J(x) = J^{(0)}(x) + \sum_{n=1}^{\infty} \gamma^{2n} \int_0^x K_n(x; t) J^{(0)}(t) dt \quad (27)$$

where the kernels $K_n(x; t)$ satisfy the recurrence relation

$$K_n(x; t) = \int_{\xi=t}^x K_1(x; \xi) K_{n-1}(\xi; t) d\xi, \text{ for } n \geq 2. \quad (28)$$

It is important to bear in mind that for any $n = 1, 2, \dots, K_n(x; t) = 0$ for $t > x$. Computation of the solution from (27) requires i) determining the zeroth order current density $J^{(0)}(x)$ from (16), ii) determining the kernels $K_n(x; t)$ by evaluating the integrals (28), and iii) evaluating the integrals on the right-hand side of (27). The amount of computational labor depends on the number of terms used in the series, the nature of the rough surface, the maximum range X , and the integration scheme employed.

C. Truncated Series and Error Estimates

In practice one would like to truncate the series in (27) to some finite upper limit to aid computation. Our main goal in this subsection is to investigate the rate at which the truncated series solution approaches the exact solution as the number of terms is increased. Using asymptotic theory we show that the truncation limit can be chosen appropriately so that the error with respect to the exact solution can be made as small as desired for *any* slope (of course within the constraints imposed by the validity of the parabolic approximation). We also derive an expression for the integrated root mean square error as a function of the physical parameters of the problem as well as expressions for the determination of the number of terms needed to achieve a given accuracy. We make repeated use of the Schwartz inequality [29],

which states for two complex valued functions $f_1(x)$ and $f_2(x)$ and in $x \in (a, b)$ that

$$\left| \int_a^b f_1(x) f_2(x) dx \right|^2 \leq \int_a^b |f_1(x)|^2 dx \int_a^b |f_2(x)|^2 dx. \quad (29)$$

The \mathcal{L}_2 norm of the n th iterate, $\|J^{(n)}\|$, over the domain $x \in (0, X)$ is defined as

$$\|J^{(n)}(x)\|^2 = \int_0^X |J^{(n)}(x)|^2 dx. \quad (30)$$

The N th iterate of the current density is that which is obtained by truncating the upper limit in the right-hand side of (27) to N :

$$\begin{aligned} J^{(N)}(x) &= J^{(0)}(x) + \sum_{n=1}^N \gamma^{2n} \int_0^x K_n(x; t) J^{(0)}(t) dt \\ &\equiv J^{(0)}(x) + \sum_{n=1}^N [J^{(n)}(x) - J^{(n-1)}(x)] \end{aligned} \quad (31)$$

where the incremental contribution of the n th term in the summation is

$$J^{(n)}(x) - J^{(n-1)}(x) = \left(\frac{-i}{\lambda} \right)^n \int_0^x K_n(x; t) J^{(0)}(t) dt \quad (32)$$

on recognizing that $\gamma^2 = -i/\lambda$, where λ is the free-space wavelength. For N sufficiently large, $J^{(N)}(x)$ will be close to the exact solution $J(x) \equiv J^{(\infty)}(x)$. For a given accuracy, that value of N depends on the maximum range $x = X$, the nature of the rough surface, frequency of operation, etc.

We will first provide worst case estimates for the error incurred in employing the N th iterate by performing an analysis along the lines of Tricomi [36]. From Sections II-A and II-B we can conclude that

$$|K_0(x; t)| \leq \alpha_g, \text{ and} \quad (33)$$

$$|K_1(x; t)| \leq \pi \alpha_g^2. \quad (34)$$

It is also clear from observing the phase of K_0 in (10) that the maximum effective wavenumber of oscillation along the terrain is $k_x = k_0 \alpha_g^2 / 2$ and the corresponding minimum wavelength of oscillation is $\lambda_x = 2\pi/k_x = 2\lambda/\alpha_g^2$. Hence, if the maximum slope angle of the terrain is 10° , the minimum wavelength of oscillation is $\lambda_x \approx 64\lambda$. The squared norm of the kernel $K_n(x; t)$ is defined as

$$\|K_n\|^2 = \int_{x=0}^X \int_{t=0}^x |K_n(x; t)|^2 dt dx. \quad (35)$$

Let us designate

$$\begin{aligned} A^2(x) &= \int_{t=0}^x |K_1(x; t)|^2 dt, \quad 0 \leq x \leq X \\ &= \int_{t=0}^x |K_1(x; t)|^2 dt \leq (\pi \alpha_g^2)^2 x \end{aligned} \quad (36)$$

$$\begin{aligned} B^2(t) &= \int_{x=0}^X |K_1(x; t)|^2 dx, \quad 0 \leq t \leq X \\ &= \int_{x=t}^X |K_1(x; t)|^2 dx \leq (\pi \alpha_g^2)^2 (X - t) \end{aligned} \quad (37)$$

where the last inequalities in (36) and (37) follow from (33) and (34) respectively. Using these it is easy to see that

$$\|K_1\|^2 = \int_{x=0}^X A^2(x) dx = \int_{t=0}^X B^2(t) dt \quad (38)$$

$$\leq (\pi \alpha_g^2 X)^2 / 2. \quad (39)$$

From the upper bound in (39) one can conclude that $\|K_1\|$ increases linearly with X and quadratically with α_g . It is straightforward to show that all the higher order kernels are also bounded. Schwartz inequality applied to (28) yields the inequalities

$$\|K_n\| \leq \|K_1\| \cdot \|K_{n-1}\| \implies \|K_n\| \leq \|K_1\|^n, \quad n \geq 1. \quad (40)$$

However, it is possible to get tighter bounds on the norms using the procedure outlined in [36] so that the convergence of the series (27) can be established for arbitrary surface slope and maximum range. Now

$$\begin{aligned} |K_2(x; t)|^2 &= \left| \int_{\xi=t}^x K_1(x; \xi) K_1(\xi; t) d\xi \right|^2 \\ &\leq \int_{\xi=0}^X |K_1(x; \xi)|^2 d\xi \cdot \int_{\xi=0}^X |K_1(\xi; t)|^2 d\xi \\ &\leq A^2(x) B^2(t). \end{aligned} \quad (41)$$

Similarly, it can be shown that

$$|K_{n+2}(x; t)|^2 \leq A^2(x) B^2(t) F_n(x; t), \quad n = 0, 1, \dots \quad (42)$$

where $F_0(x; t) := 1$ and

$$F_n(x; t) = \int_{\xi=t}^x A^2(\xi) F_{n-1}(\xi; t) d\xi, \quad n = 1, 2, \dots \quad (43)$$

On realizing that $A^2(x) = \partial F_1(x; t) / \partial x$, one can show that

$$F_n(x; t) = \frac{F_1^n(x; t)}{n!}. \quad (44)$$

Now

$$F_1(x; t) = \int_{\xi=t}^x A^2(\xi) d\xi \leq \int_{\xi=0}^X A^2(\xi) d\xi = \|K_1\|^2. \quad (45)$$

Using (45) and (44) in (42), we arrive at

$$|K_{n+2}(x; t)|^2 \leq A^2(x)B^2(t) \frac{\|K_1\|^{2n}}{n!}, \quad n = 0, 1, \dots, \quad (46)$$

which implies that for $n \geq 2$

$$\|K_n\| \leq \frac{\|K_1\|^n}{\sqrt{(n-2)!}} \quad (47)$$

which is a substantial improvement over the bounds expressed by (40). Consider the local mean square error incurred in truncating the series to $N = M + 1$ terms, $M \geq 0$:

$$\begin{aligned} I_\epsilon^2(x) &= \left| J^{(\infty)}(x) - J^{(N)}(x) \right|^2 \\ &= \left| \sum_{n=N+1}^{\infty} \left(\frac{-i}{\lambda} \right)^n \int_{t=0}^x K_n(x; t) J^{(0)}(t) dt \right|^2 \\ &\leq \sum_{n=N+1}^{\infty} \frac{1}{\lambda^{2n}} \int_{t=0}^x |K_n(x; t)|^2 dt \int_{t=0}^x \left| J^{(0)}(t) \right|^2 dt \\ &= \|J^{(0)}\|^2 \sum_{n=N+1}^{\infty} \frac{1}{\lambda^{2n}} \int_{t=0}^x |K_n(x; t)|^2 dt. \end{aligned} \quad (48)$$

Defining $\rho = (\|K_1\|/\lambda)^2$, the relative integrated mean square error is

$$\begin{aligned} \epsilon^2(N) &= \frac{1}{\|J^{(0)}\|^2} \int_{x=0}^X I_\epsilon^2(x) dx \\ &\leq \sum_{n=N+1}^{\infty} \frac{1}{\lambda^{2n}} \int_{x=0}^X \int_{t=0}^x |K_n(x; t)|^2 dt dx \\ &= \sum_{n=N+1}^{\infty} \frac{\|K_n\|^2}{\lambda^{2n}} \end{aligned} \quad (49)$$

$$\leq \sum_{n=N+1}^{\infty} \frac{1}{\lambda^{2n}} \frac{\|K_1\|^{2n}}{(n-2)!} \quad (50)$$

$$= \rho^2 \sum_{m=M}^{\infty} \frac{\rho^m}{m!} = \rho^2 e^\rho P(M, \rho) \quad (51)$$

where the function $P(M, \rho)$ is related to the lower incomplete gamma function $\gamma(M, \rho)$ [37] as $P(M, \rho) = \gamma(M, \rho)/\Gamma(M)$. It is clear from (51) that the error tends to zero as $M \rightarrow \infty$ for any finite ρ . However, to gain more insight into the convergence process such as the rate of decay at infinity, it is necessary to examine how the error behaves for large M . A uniform asymptotic form of the function P for large M is available in [39]:

$$P(M, \rho) \sim \frac{1}{2} \operatorname{erfc}(-\eta \sqrt{M/2}), \quad M \gg 1 \quad (52)$$

where $\eta^2 = 2(a - \ln(ae))$, $\operatorname{sign}(\eta) = \operatorname{sign}(a - 1)$ and $a = \rho/M$. For $M \gg \rho$, $a \rightarrow 0$ and $\eta \sim -\sqrt{2 \ln(M/e\rho)}$. Using the asymptotic form of the complementary error function, $\operatorname{erfc}(z) \sim \exp(-z^2)/\sqrt{2\pi}z$ for large $|z|$, we can conclude that

$\operatorname{erfc}(-\eta \sqrt{M/2}) < (e\rho/M)^M / \sqrt{2\pi M \log(M/e\rho)}$. Inserting this in (52) we get

$$\epsilon^2(N) < \frac{\rho^2 e^\rho}{2\sqrt{\pi M \ln(M/e\rho)}} \left(\frac{e\rho}{M} \right)^M, \quad M > e\rho, M \gg 1 \quad (53)$$

which clearly decays to zero *super-exponentially* as $M \rightarrow \infty$ for *any* finite ρ . The same right-hand side as in (53) is obtained if one starts from (50) and makes use of $(m+M)! > m! M!$ and the lower bound for $M!$ (see formula (6.1.38) of [37]).

Having established that the Neumann series converges to the exact solution for any slope and range, it is of interest to determine the order N for which the current density achieves a given accuracy. To this end, we first note from (31) and (32) that

$$\begin{aligned} \|J^{(N)}\|^2 &\leq \|J^{(0)}\|^2 + \sum_{n=1}^N \int_0^X \left| J^{(n)}(x) - J^{(n-1)}(x) \right|^2 dx \\ &\leq \|J^{(0)}\|^2 \left[1 + \sum_{n=1}^N \frac{\|K_n\|^2}{\lambda^{2n}} \right]. \end{aligned} \quad (54)$$

Similarly,

$$\|J^{(\infty)}\|^2 \leq \|J^{(0)}\|^2 \left[1 + \sum_{n=1}^{\infty} \frac{\|K_n\|^2}{\lambda^{2n}} \right]. \quad (55)$$

To achieve a relative accuracy of $(1 - \delta)$ (or a relative error of δ), where $\delta \ll 1$, in the current distribution, we set $\|J^{(N)}\|^2 = (1 - \delta)^2 \|J^{(\infty)}\|^2 \approx (1 - 2\delta) \|J^{(\infty)}\|^2$. It is reasonable to use upper limits for $\|J^{(N)}\|$ and $\|J^{(\infty)}\|$ as given by (54) and (55) as both are based on the same kind of approximations. Hence, we get

$$\sum_{n=N+1}^{\infty} \frac{\|K_n\|^2}{\lambda^{2n}} = 2\delta \left(1 + \sum_{n=1}^{\infty} \frac{\|K_n\|^2}{\lambda^{2n}} \right). \quad (56)$$

The upper limit in both summations may be replaced with a large integer N_{\max} without causing too much error. We then get a form more suitable for numerical computations as

$$\begin{aligned} F(N, N_{\max}) &:= \sum_{n=N+1}^{N_{\max}} \frac{\|K_n\|^2}{\lambda^{2n}} = 2\delta \left(1 + \sum_{n=1}^{N_{\max}} \frac{\|K_n\|^2}{\lambda^{2n}} \right) \\ &=: G. \end{aligned} \quad (57)$$

When the current density is accurately represented by the N th iterate, the left-hand side of (56) may be approximated by the first term in the series to result in the following useful formula for determining N :

$$F(N, N + 1) = \frac{\|K_{N+1}\|^2}{\lambda^{2(N+1)}} \approx G. \quad (58)$$

For a given rough surface, maximum range, and frequency of operation, the various $\|K_n\|$ may be computed and N determined from (57) or (58) to achieve a specified relative error δ . From (47) and (39), it is clear that all of the norms can increase linearly with maximum range and quadratically with the maximum absolute slope angle. Hence, the number of terms N is expected to increase with the maximum absolute slope angle of the surface, the maximum range and the frequency of operation.

Conversely, for a shallow rough surface, or small ranges or low frequencies, few terms in the series should be adequate.

D. Accuracy of the Zeroth-Order Approximation

The zeroth order approximation to the current density, $J^{(0)}(x)$, given in (16), itself may be adequate when the range and/or the terrain slopes are small so that $\rho \ll 1$. Note that the zeroth-order approximation is dependent on the initial field $U_0(z)$ via the incident current density, $J_i(x)$, as well as on the properties of the rough surface. Indeed, it is itself the first-order iterate of the original integral equation (9). This is in contrast to the normal physical optics approximation [10], [12] wherein the zeroth-order term primarily involves evaluation of the tangential component of the incident magnetic field along the rough surface. Using the upper bound for $\|K_1\|$ from (39) and by arbitrarily setting $\rho \leq 1/\pi^3$, one may conclude that if $\alpha_g^2 X/\lambda \leq \sqrt{2}/\pi^{5/2}$, the current density will be dominated by the zeroth-order approximation. In other words, the zeroth-order approximation is good for a maximum range up to about

$$X = X_0 = \frac{\sqrt{2}\lambda}{\alpha_g^2 \pi^{5/2}} \quad (59)$$

which varies inversely with α_g^2 . If the slope angle is doubled, the corresponding maximum range up to which the zeroth-order approximation is accurate decreases by a factor of four. The maximum range is also seen to increase linearly with wavelength of operation. All else being equal, a decrease in frequency of operation by a factor of two increases the maximum range by a factor of two. The zeroth-order approximation should consequently be very good for low frequencies and small slope angles.

III. NUMERICAL RESULTS FOR TRUNCATED SERIES

The exact solution for the current density $J(x)$ is given in (27) with the iterated kernels defined by (28) and the zeroth-order current density given in (16). The substitution $\xi = x \sin^2 \theta + t \cos^2 \theta$ reveals that the n th iterated kernel $K_n(x; t)$ is a smooth function of both arguments and behaves as $(x - t)^{n-1}$ near the boundaries. It may be noted that the purpose of the paper is not to offer the exact solution as a numerically efficient solution for long ranges and no effort was spent on numerically optimizing the series solution. Notwithstanding this, the numerical computation of the various kernels can be carried out using any of the standard integration routines. As remarked in Section II-C, the relative error in the truncated series for a given N depends on the wavelength λ , Lipschitz constant α_g , the maximum range X . We compare the performance of the approximate solution (31) with that obtained by solving the integral (9) numerically following the procedure outlined in [26]. The latter solution was obtained with a range discretization of Δx and we label it as J_{num} in the plots. We also compute the total field on a vertical line at $x = X$ using (6) and plot the propagation factor $\text{PF} = |U(X, z)/U^i(X, z)| = |1 + U_s(X, z)/U_i(X, z)|$ obtained by using both the numerical solution $J_{\text{num}}(x)$ and $J^{(N)}(x)$. Two extreme examples are considered first, one having a relatively large slope angle and a second having a relatively long range. Even though the Neumann series solution converges for any slope angle, one has to keep in mind that the parabolic equation approximation itself will break down if the absolute slope

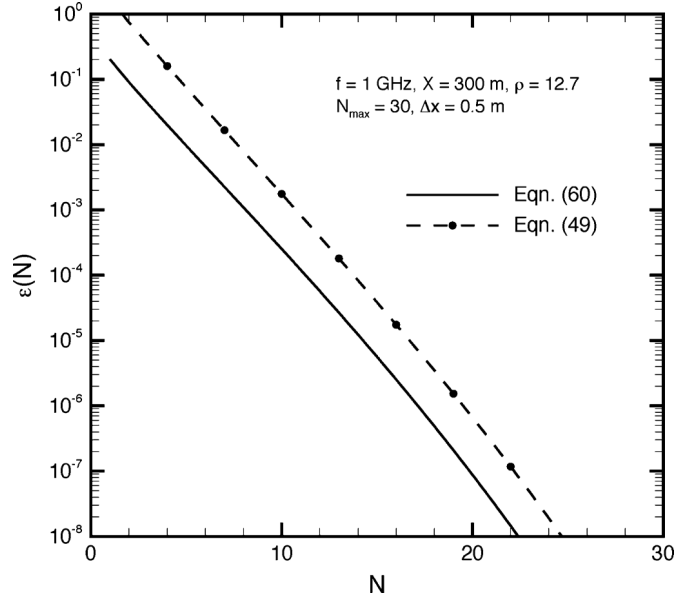


Fig. 2. Upper bound to the RMS error versus N for a sinusoidal rough surface $g(x) = A_{pp} \sin^2(\pi x/L)$.

angles are greater than roughly 7.5° or so. We also show results for propagation of low-grazing angles waves over one realization of random sea surface, whose roughness spectrum is modeled by the Pierson–Moskowitz spectrum [40].

The first example we consider is a rough surface characterized by $g(x) = A_{pp} \sin^2(\pi x/L)$. The slope of this surface is $(A_{pp}\pi/L) \sin(2\pi x/L)$ yielding $\alpha_g = \pi A_{pp}/L$. We use $A_{pp} = 1$ m, $L = 30$ m to result in $\alpha_g = 0.1051$. The maximum absolute slope angle with these parameters is 6° . A Gaussian source of the form (22) with $\sigma_z = 4\lambda/3$, $H_t = 5$ m and operating at a frequency $f = 1$ GHz ($\lambda = 0.3$ m) was used for the initial source and the current density was calculated until a range $X = 300$ m. For these parameters, $\|K_1\|/\lambda \approx 3.56$, $\rho \approx 12.7$, and $X_0 \approx 2.2$ m. The numerical solution $J_{\text{num}}(x)$ was obtained using $\Delta x = 0.5$ m = $5\lambda/3$. Recall from Section II-C that the minimum effective wavelength along the surface is $\lambda_x = 2\lambda/\alpha_g^2 \approx 181\lambda$ here. Hence, the step size of $\Delta x = 5\lambda/3$ is a small fraction of this minimum wavelength and should be more than adequate to sample the current density along the surface. Fig. 2 shows the upper bound to the root mean square (RMS) error $\epsilon(N)$ as given by (49), versus N . The RMS error computed directly by using the various iterates of the current density

$$\epsilon_{\text{num}}(N) = \sqrt{\frac{\int_0^X |J^{(N)}(x) - J^{(N_{\max})}(x)|^2 dx}{\int_0^X |J^{(0)}(x)|^2 dx}} \quad (60)$$

is also shown in the figure for $N_{\max} = 30$, where $J^{(N_{\max})}(x)$ may be roughly regarded as the exact current distribution. Both curves are seen to have nearly the same asymptotic slope and suggest that with $N \approx 5$ –8 terms, the relative error will be less than 10^{-2} . Fig. 3 shows the curves $F(N, N_{\max})$ and $F(N, N+1)$ in (57) and (58), respectively, versus N and their intersection with the quantity G for an accuracy of $(1 - \delta) = 99.99\%$. It is seen that $N \approx 5$ in agreement with the estimate obtained from Fig. 2. Fig. 4 shows the magnitude of current density $J^{(N)}(x)$ for $N = 0, N = 5$ together with

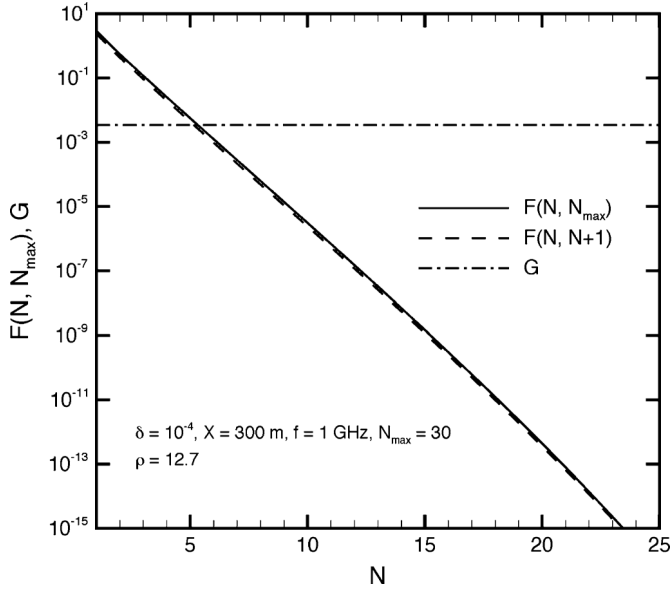


Fig. 3. Curves for the determination of number of terms needed for a specified accuracy for a sinusoidal rough surface $g(x) = A_{pp} \sin^2(\pi x/L)$.

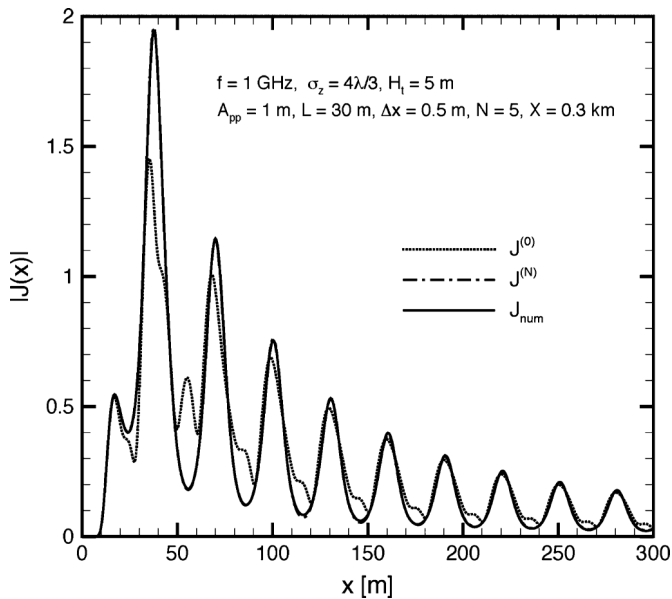


Fig. 4. Modulus of current density on a sinusoidal rough surface $g(x) = A_{pp} \sin^2(\pi x/L)$.

$J_{\text{num}}(x)$. Clearly, the zeroth-order approximation is inadequate for these parameters and the $N = 5$ solution remains very close to $J_{\text{num}}(x)$. Fig. 5 shows that the propagation factor calculated with $J^{(5)}(x)$ agrees very well with that obtained with $J_{\text{num}}(x)$.

Equation (57) predicts that for a given relative accuracy, frequency of operation and maximum slope, the number of terms increases with the maximum range X . The increase with X is, however, not linear. We have confirmed this through numerical computations. For instance, for a sinusoidal surface with a maximum slope angle of 6° and $L = 3$ m, we observed that $N = 1$ terms as calculated from (57) gave accurate results for the current distribution when $X = 30$ m, whereas $N = 2$ terms were required for $X = 300$ m to achieve the same relative accuracy.

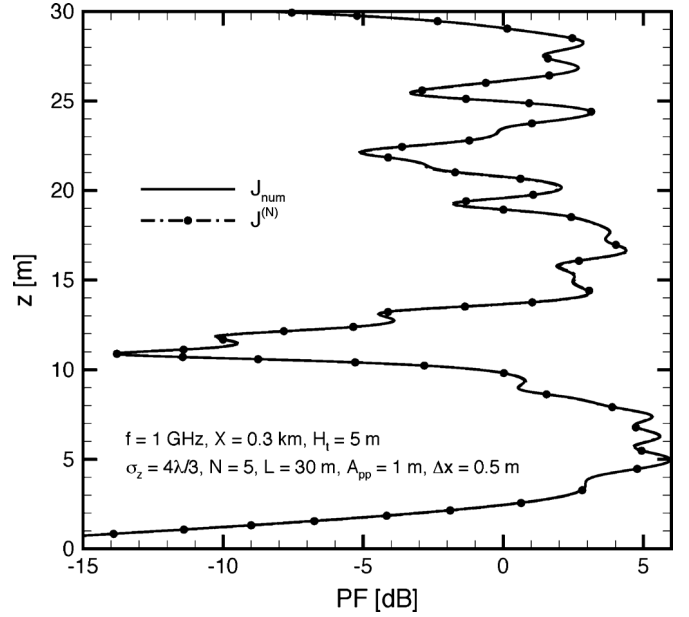


Fig. 5. Propagation factor at $X = 300$ m for the sinusoidal rough surface $g(x) = A_{pp} \sin^2(\pi x/L)$.

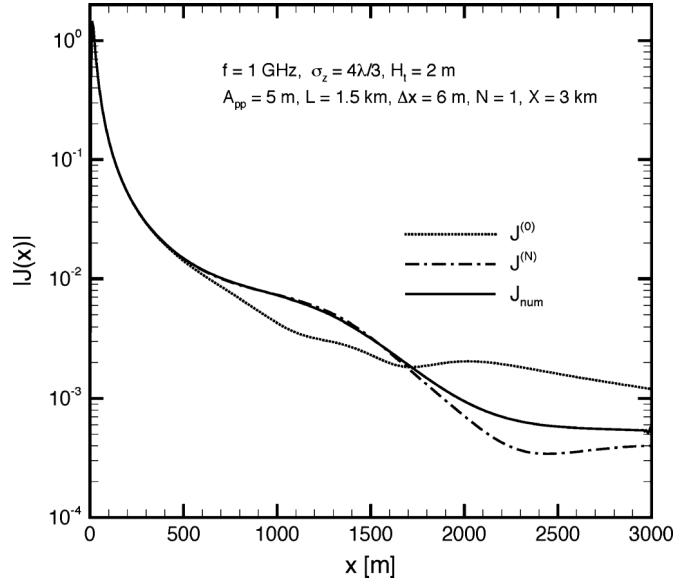


Fig. 6. Modulus of current density on a Gaussian hill $g(x) = A_{pp} \exp(-(x-L)/\sigma_x^2)$.

The second example we choose is that of propagation over a Gaussian hill defined by $g(x) = A_{pp} \exp(-(x-L)^2/\sigma_x^2)$. The maximum absolute slope of the Gaussian hill appears at $x = L \pm \sigma_x$ and takes the value $\sqrt{e} A_{pp}/\sigma_x = \alpha_g$. We choose $A_{pp} = 5$ m, $L = 1.5$ km, $\sigma_x = 0.5$ km. The source parameters were the same as in the previous example except that $H_t = 2$ m. For these parameters, $\alpha_g = 6.0653 \times 10^{-3}$, $\|K_1\|/\lambda \approx 0.2952$, $\rho \approx 0.087$, and $X_0 \approx 660$ m. The maximum absolute slope angle in this case equals 0.35° . The numerical solution was computed with $\Delta x = 6$ m. The modulus of the current density is shown in Fig. 6 for $N = 0$ and $N = 1$ along with the numerical solution. The $N = 2$ solution, not shown here, was virtually indistinguishable from the numerical solution over the four

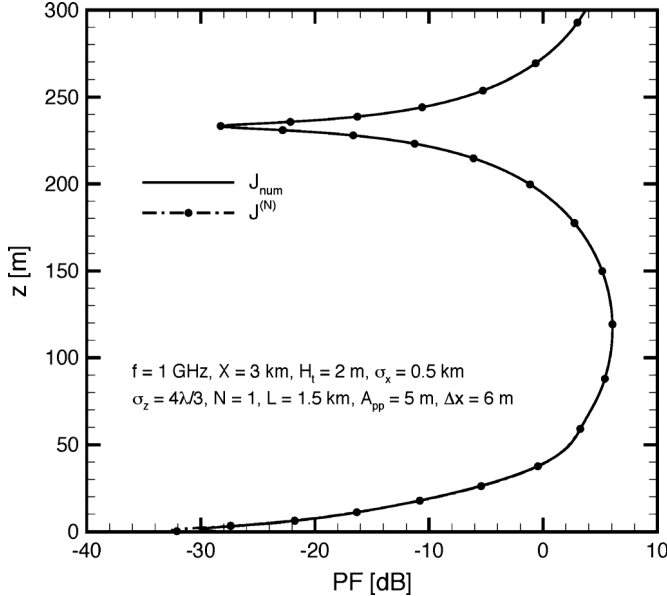


Fig. 7. Propagation factor at $X = 3 \text{ km}$ for a Gaussian hill $g(x) = A_{\text{pp}} \exp(-(x - L)/\sigma_x^2)$.

orders of magnitude shown in Fig. 6. It is also seen that the zeroth-order solution is indistinguishable from the numerical solution for ranges up to about 700 m, which roughly agrees with the estimate of $X_0 = 660 \text{ m}$ from (59). The first-order solution is virtually indistinguishable from the numerical solution over three orders of magnitude occurring for ranges up to about 1.6 km, that lies beyond the peak of the Gaussian hill. The disagreement between the $N = 1$ series solution and the numerical solution is apparent only for small values of the current density. Even then, the propagation factor calculated with $J^{(1)}(x)$ as shown in Fig. 7 agrees very well with that obtained with the numerical solution.

We next consider the propagation of low-grazing angle waves over one realization of a fully-developed random sea surface. The surface is assumed to be zero mean and having Gaussian height statistics. As in [41], we model the roughness spectrum of the sea surface by the Pierson–Moskowitz (PM) spectrum, which is completely determined by the wind speed U flowing at a height of 19.5 m above the mean surface. The power spectral density $W(\kappa)$ for the PM spectrum as a function of the surface wavenumber κ is given by

$$W(\kappa) = \frac{\alpha}{4|\kappa|^3} e^{-3\kappa_p^2/2\kappa^2} \quad (61)$$

where $\kappa_p = \sqrt{2\beta/3}g/U^2$ is the wave number at which the spectrum has a peak and $\alpha = 8.1 \times 10^{-3}$, $\beta = 0.74$, $g = 9.81 \text{ m/sec}^2$. The PM model provides a useful test of surface scattering theory with a range of roughness scales. Some useful parameters can be derived for the spectrum given in (61): the RMS surface height deviation, $\sigma_h = \sqrt{\alpha}/\sqrt{6}\kappa_p$ and the RMS correlation length of the surface $\rho_c = 5/2\sqrt{2}\kappa_p$. If the upper spatial wavenumber is truncated to κ_c , then the RMS slope of the surface $\sigma_{\text{sl}} = \sqrt{\alpha E_1(y_c)/2}$, where $y_c = 3\kappa_p^2/2\kappa_c^2$ and $E_1(\cdot)$ is the exponential integral [37]. We generate a rough surface using the spectral approach as outlined in [40], [42] for $U = 10 \text{ m/s}$ and $\kappa_c = 51\kappa_p$ using a 512-point FFT. For this wind speed,

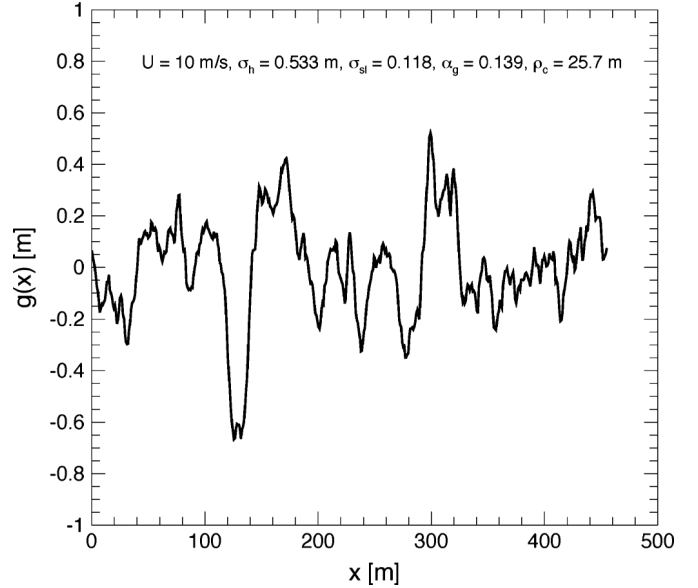


Fig. 8. Pierson–Moskowitz sea surface for a wind speed of $U = 10 \text{ m/s}$.

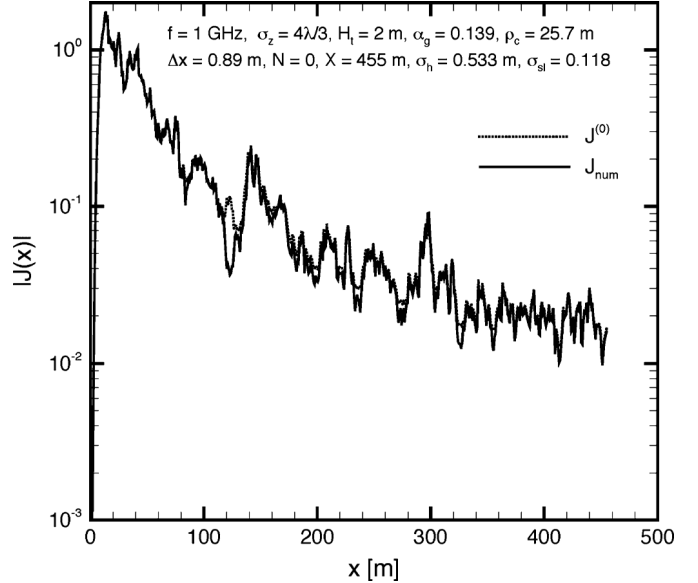


Fig. 9. Modulus of current density on a Pierson–Moskowitz rough surface.

$\sigma_h = 0.533 \text{ m}$, $\rho_c = 25.7 \text{ m}$. We generate a surface having an overall length of $X = 455 \text{ m}$, so that $X/\rho_c \approx 17.7$. For the upper cutoff wavenumber chosen, $\sigma_{\text{sl}} = 0.118$, while the maximum absolute slope of the surface is $\alpha_g = 0.139$, corresponding to a slope angle of 7.9° . The generated surface is shown in Fig. 8. We compute the zeroth-order current density induced on this surface at a frequency of 1 GHz for the Gaussian source at a height of $H_t = 2 \text{ m}$ by (16) and compare it to the one generated numerically from solving (9). Fig. 9 shows the comparison along with the other parameters used. It is seen that while the zeroth-order approximation does not agree perfectly with the numerically generated one, it does follow the trends in various excursions rather accurately. Fig. 10 shows a comparison of the corresponding propagation factors at the maximum range of 455 m. Very good agreement between the two is observed, despite the slight disagreement in the current distribution. It may be worth noting that the accuracy for the current

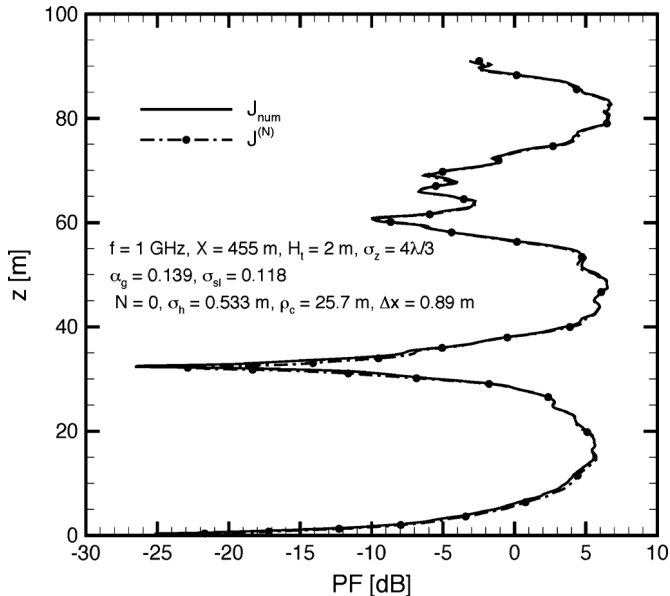


Fig. 10. Propagation factor at $X = 455$ m for a Pierson–Moskowitz sea surface.

TABLE I
COMPUTATIONAL TIME (SEC) IN MATLAB

Current Density	Fig. 4	Fig. 6
$J^{(0)}$	0.1	0.2
$J^{(N)}$	101	48
J_{num}	73	50

distribution greatly improved by the use of the first-order iterate $J^{(1)}(x)$ (not shown in the figures).

It is of interest to look at the computational times incurred in computing various approximations of the current density. Table I shows the CPU times involved in computing $J^{(0)}$, $J^{(N)}$, and J_{num} using MATLAB. We have made no attempt to optimize the various algorithmic steps involved in computing the current density by the Neumann series. The times shown for $J^{(N)}$ includes those spent in computing all of the previous orders $J^{(i)}$, $i = 1, \dots, N - 1$. Obviously, the time required to compute $J^{(0)}$ is a very small fraction of that required to compute J_{num} , because the former involves the computation of one integral. A good part of the time incurred in computing $J^{(N)}$ goes towards computing the kernel $K_1(x; t)$ in (17). Recall that $N = 5$ in Fig. 4, while $N = 1$ in Fig. 6. It is clear that the Neumann series solution will be very competitive in cases where only a few orders are adequate to accurately represent the current density. This, in turn, is dictated by the maximum slope of the surface and the maximum range involved.

IV. CONCLUSION

A new Volterra integral equation of the second kind, (15), was derived for 2-D wave propagation over a perfectly conducting rough surface and an exact expression, (27), was presented for the current density. The necessary and sufficient conditions for the exact series solution to converge were established: the rough surface should satisfy the uniform Lipschitz condition, (26), and the field at zero range should have finite first derivative with respect to height, (21). Because the formulation was based on the

parabolic approximation to the Helmholtz equation, the exact solution presented is valid for low-grazing angle waves propagating over rough surfaces having gentle slopes when backscattering can be ignored. In practice, the solution should be valid for surfaces with absolute slope angles $\leq 10^\circ$. For a specified accuracy δ , (57) or (58) may be used to determine the number of terms needed in Neumann series representation. The number of terms used in the series is expected to increase with increasing range, increasing frequency of operation, and increasing slope angles. In order to keep the number of terms needed in the series to low values, the range should be restricted. However, this is not a serious limitation of the method. For, if propagation prediction is desired over long ranges, one can always employ the multiple-section strategy explored in [26], wherein the field calculated on a vertical line at the end of one short section serves as the initial field for the next section. An advantage of the series solution is that it provides complete error control, in that the number of terms can be chosen appropriately to achieve a certain relative error for the current distribution.

To make the series solution a viable and efficient numerical approach for studying wave propagation over rough surfaces, several algorithmic steps considered in the paper must be optimized. However, it is believed that the theory presented in the paper will lay the groundwork for obtaining approximate analytical solutions in a variety of situations. For instance, in low-grazing angle propagation over a sea surface, one is interested in the mean field at certain distance from the transmitter [1], [35], and [43]. This problem is also of interest to underwater acoustic propagation [27]. The importance of shadowing in low-grazing angle propagation has long been recognized, but is still an unresolved issue [44]. The current method incorporates all orders of shadowing interaction subject to the forward propagation approximation. The zeroth-order approximation, (16), could be used in (5), as we have done in Fig. 9, and the expectation performed with respect to the randomness of the sea surface to possibly yield an analytical solution for the total mean field when the maximum range encompasses several correlation lengths of the random surface. The first term by itself, $J_i(x)$, in the zeroth-order approximation will yield the well known Ament roughness reduction factor [10] for determining the mean field. This term will only incorporate the variance and mean of the rough surface. Correlation function of the rough surface will enter through the second term of $J^{(0)}(x)$ as well as through the higher order terms in the Neumann series. It is hoped that availability of such analytical expressions for the mean field will be useful in propagation modeling for radar detection [45] as well as wireless communications [42]. This will be explored in the future. Extension of the theory to surfaces modeled by the impedance boundary condition and to 3-D propagation over 2-D rough surfaces are worth exploring and these will be also be considered in the future.

REFERENCES

- [1] W. S. Ament, "Towards a theory of reflection by a rough surface," *Proc. IRE*, vol. 41, no. 1, pp. 142–146, 1953.
- [2] H. V. Hitney, J. H. Richter, R. A. Pappert, K. D. Anderson, and J. G. B. Baumgartner, "Tropospheric radio propagation assessment," *Proc. IEEE*, vol. 73, no. 2, pp. 265–283, Feb. 1985.
- [3] F. T. Ulaby, R. K. Moore, and A. K. Fung, *Microwave Remote Sensing: Active and Passive*. Norwood, MA, USA: Artech House, 1986, vol. II.

- [4] L. Tsang, J. A. Kong, and K.-H. Ding, *Scattering of Electromagnetic Waves: Theories and Applications*. New York, NY, USA: Wiley, 2000.
- [5] J. J. Egli, "Radio propagation above 40 mc over irregular terrain," *Proc. IRE*, vol. 45, no. 10, pp. 1383–1391, Oct. 1957.
- [6] A. G. Longley and P. L. Rice, "Prediction of Tropospheric radio transmission loss over irregular terrain: A computer method—1968," Inst. for Telecomm. Services, Boulder, CO, USA, Tech. Rept. AD0676874, Jul. 1968.
- [7] F. B. Jensen, W. A. Kuperman, M. B. Porter, and H. Schmidt, *Comput. Ocean Acoust.*. New York, NY, USA: Springer-Verlag, 2000.
- [8] J. M. Elson, "Theory of light scattering from a rough surface with an inhomogeneous dielectric permittivity," *Phys. Rev. B*, vol. 30, no. 10, pp. 5460–5480, Nov. 1984.
- [9] A. Ishimaru, *Wave Propagation and Scattering in Random Media*. Piscataway, NJ, USA: IEEE Press, 1997.
- [10] P. Beckmann and A. Spizzichino, *The Scattering of Electromagnetic Waves From Rough Surfaces*. New York, NY, USA: Pergamon, 1963.
- [11] G. S. Brown, "Application of the integral equation method of smoothing to random surface scattering," *IEEE Trans. Antennas Propag.*, vol. 32, no. 12, pp. 1308–12 312, Dec. 1984.
- [12] D. Holliday, "Resolution of a controversy surrounding the Kirchoff approach and the small perturbation method in rough surface scattering," *IEEE Trans. Antennas Propag.*, vol. AP-35, no. 1, pp. 120–122, Jan. 1987.
- [13] R. Janaswamy, "A Fredholm integral equation method for propagation predictions over small terrain irregularities," *IEEE Trans. Antennas Propag.*, vol. 40, no. 11, pp. 1416–1422, Nov. 1992.
- [14] J. T. Hvistid, J. B. Andersen, J. Toftgard, and J. Bojer, "Terrain-based propagation model for rural area—An integral equation approach," *IEEE Trans. Antennas Propag.*, vol. 43, no. 1, pp. 41–46, Jan. 1995.
- [15] L. Tsang, J. A. Kong, and K.-H. Ding, *Scattering of Electromagnetic Waves: Advanced Topics*. New York, NY, USA: Wiley, 2001.
- [16] R. Petit, *Electromagnetic Theory of Gratings*, ser. Topics in current physics. New York, NY, USA: Springer-Verlag, 1980, vol. 22.
- [17] D. E. Barrick, "Grazing behavior of scatter and propagation above any rough surface," *IEEE Trans. Antennas Propag.*, vol. 46, no. 1, pp. 73–83, Jan. 1998.
- [18] A. E. Barrios, "A terrain parabolic equation model for propagation in the troposphere," *IEEE Trans. Antennas Propag.*, vol. 42, no. 1, pp. 90–98, Jan. 1994.
- [19] S. W. Marcus, "A hybrid (finite-difference-surface Green's function) method for computing transmission losses in an inhomogeneous atmosphere over irregular terrain," *IEEE Trans. Antennas Propag.*, vol. 40, no. 12, pp. 1451–1459, Dec. 1002.
- [20] R. Janaswamy, "A fast finite difference method for propagation predictions over irregular, inhomogeneous terrain," *IEEE Trans. Antennas Propag.*, vol. 42, no. 9, pp. 1257–1267, Sep. 1994.
- [21] V. A. Fock, *Electromagnetic Diffraction and Propagation Problems*. New York, NY, USA: Pergamon, 1965.
- [22] M. F. Levy, *Parabolic Equation Methods for Electromagnetic Wave Propagation*, ser. Electromagnetic Wave Series. London, U.K.: IEE Press, 2000, vol. 45.
- [23] J. V. Roey, J. van der Donk, and P. E. Lagasse, "Beam-propagation method: Analysis and assessment," *J. Opt. Soc. Amer.*, vol. 71, no. 7, pp. 803–810, 1981.
- [24] G. A. Hufford, "An integral equation approach to the problem of wave propagation over an irregular surface," *Quart. Appl. Math.*, vol. 9, no. 4, pp. 391–404, 1952.
- [25] R. H. Ott, "An alternative integral equation for propagation over irregular terrain, 2," *Radio Sci.*, vol. 6, no. 4, pp. 429–435, Apr. 1971.
- [26] M. J. Motta, "Equivalent impedance of rough surface at low grazing angles," M.S. thesis, Naval Postgraduate School, Monterey, CA, USA, Sep. 1999 [Online]. Available: <http://www.dtic.mil/cgi-bin/GetTRDoc?AD=ADA369420>
- [27] B. J. Uscinski and C. J. Stanek, "Acoustic scattering from a rough sea surface: The mean field by the integral equation method," *Waves in Random Media*, vol. 12, pp. 247–263, 2002.
- [28] D. Holliday, J. L. L. DeRaad, and G. J. St-Cyr, "Volterra approximation for low grazing angle shadowing on smooth ocean-like surfaces," *IEEE Trans. Antennas Propag.*, vol. 43, no. 11, pp. 1199–1207, Nov. 1995.
- [29] E. Kreyszig, *Introductory Functional Analysis With Applications*, ser. Wiley Classics Library. New York, NY, USA: Wiley, 1978.
- [30] *Microwave Mobile Communications*, W. C. Jakes, Ed. Piscataway, NJ, USA: IEEE Press, 1974.
- [31] D. Parsons, *The Mobile Radio Propagation Channel*, D. Parsons, London, U.K.: Pentech Press, 1992. London, U.K.: Pentech, 1992.
- [32] J. R. Kuttler and G. D. Dockery, "Theoretical description of the parabolic approximation/Fourier split-step method of representing electromagnetic propagation in the troposphere," *Radio Sci.*, vol. 26, no. 2, pp. 381–393, Mar.–Apr. 1991.
- [33] R. Janaswamy, "Roadiowave propagation over a nonconstant impedance plane," *Radio Sci.*, vol. 36, no. 3, pp. 387–405, May–Jun. 2001.
- [34] B. Davies, *Integral Transforms and Their Applications*, 3rd ed. New York, NY, USA: Springer-Verlag, 2002.
- [35] Z. Lai and R. Janaswamy, "Specular propagation over rough surfaces: Numerical assessment of Uscinski and Stanek's mean Green's function technique," *Waves in Random and Complex Media*, vol. 16, no. 2, pp. 137–150, May 2006.
- [36] F. G. Tricomi, *Integral Equations*, ser. Wiley Interscience. New York, NY, USA: Wiley, 1957.
- [37] M. Abramowitz and I. A. Stegun, Eds., *Handbook of Mathematical Functions: With Formulas, Graphs, and Mathematical Tables*. New York, NY, USA: Dover, 1964.
- [38] L. Debnath and P. Mikusinski, *Introduction to Hilbert Spaces With Applications*, 2nd ed. New York, NY, USA: Academic, 1999.
- [39] N. M. Temme, "Uniform asymptotics for the incomplete gamma functions starting from negative values of the parameters," *Meth. Applicat. Anal.*, vol. 3, no. 3, pp. 335–344, 1996.
- [40] E. I. Thorsos, "The validity of the Kirchoff approximation for a rough surface scattering using a Gaussian roughness spectrum," *J. Acoust. Soc. Amer.*, vol. 83, no. 1, pp. 78–92, Jan. 1988.
- [41] E. I. Thorsos, "Acoustic scattering from a "Pierson-Moskowitz" sea surface," *J. Acoust. Soc. Amer.*, vol. 88, no. 1, pp. 335–349, Jul. 1990.
- [42] R. Janaswamy, *Radiowave Propagation and Smart Antennas for Wireless Communications*. Norwell, MA, USA: Kluwer, 2001.
- [43] D. E. Freund, N. E. Woods, H.-C. Ku, and R. S. Awadallah, "Forward radar propagation over a rough sea surface: A numerical assessment of the Miller-Brown approximation using a horizontally polarized 3-GHz line source," *IEEE Trans. Antennas Propag.*, vol. 54, no. 4, pp. 1292–1304, Apr. 2006.
- [44] D. E. Freund, N. E. Woods, H.-C. Ku, and R. S. Awadallah, "The effect of shadowing on modelling forward radar propagation over a rough sea surface," *Waves Random Complex Media*, vol. 18, no. 3, pp. 387–408, Aug. 2008.
- [45] A. Karimian, C. Yardim, P. Gerstoft, W. S. Hodgkiss, and A. E. Barrios, "Multiple grazing angle sea clutter modeling," *IEEE Trans. Antennas Propag.*, vol. 60, no. 9, pp. 4408–4417, Sep. 2012.



Ramakrishna Janaswamy (M'83–SM'93–F'03) received the bachelor's degree in electronics and communications engineering from REC-Warangal (now NIT-Warangal), Warangal, India, in 1981, the master's degree in microwave and radar engineering from IIT-Kharagpur, Kharagpur, India, in 1983, and the Ph.D. degree in electrical engineering from the University of Massachusetts, Amherst, MA, USA, in 1986.

From August 1986 to May 1987, he was an Assistant Professor of electrical engineering at Wilkes University, Wilkes Barre, PA, USA. From August 1987 to August 2001, he was on the faculty of the Department of Electrical and Computer Engineering, Naval Postgraduate School, Monterey, CA, USA. In September 2001, he joined the Department of Electrical and Computer Engineering, University of Massachusetts, Amherst, where he is currently a Professor. He was a Visiting Researcher at the Center for PersonKommunikation, Aalborg, Denmark, from September 1997 to June 1998 and spent the Summers of 1994 and 1995 at SPAWARSCEN, San Diego, CA, and NASA Ames Research Center, Moffett Field, CA, respectively. His research interests include deterministic and stochastic radio wave propagation modeling, analytical and computational electromagnetics, antenna theory and design, and wireless communications. His research is/was funded by several agencies such as NSF, ONR, ARO, and several Department of Navy laboratories. He is the author of the book *Radiowave Propagation and Smart Antennas for Wireless Communications* (Kluwer, 2000) and a contributing author in *Handbook of Antennas in Wireless Communications*, L. Godara (Ed.) (CRC, 2001) and *Encyclopedia of RF and Microwave Engineering*, K. Chang (Ed.) (Wiley, 2005).

Prof. Janaswamy is a Fellow of IEEE and was the recipient of the R. W. P. King Prize Paper Award of the IEEE TRANSACTIONS ON ANTENNAS AND PROPAGATION in 1995. For his services to the IEEE Monterey Bay Subsection, he received the IEEE 3rd Millennium Medal from the Santa Clara Valley Section in 2000. He is an elected member of U.S. National Committee of International Union of Radio Science, Commissions B and F. He served as an Associate Editor of *Radio Science* from January 1999 to January 2004 and Associate Editor of IEEE TRANSACTIONS ON VEHICULAR TECHNOLOGY from 2003 to 2006. He is currently an Associate Editor of IEEE TRANSACTIONS ON ANTENNAS AND PROPAGATION and of the IETE (India) Technical Reviews.

Efficiency of Adaptive Sparse Grid Collocation Methods in Wave Propagation Environments with Uncertainty

Selman Özbayat, *Student Member, IEEE* and Ramakrishna Janaswamy, *Fellow, IEEE*

Electrical and Computer Engineering Department
 University of Massachusetts Amherst
 100 Natural Resources Rd Amherst, MA 01003, USA
 E-mail: ozbayat@ecs.umass.edu, janaswamy@ecs.umass.edu

Abstract—Sparse grid collocation methods are used for uncertainty quantification in electromagnetic propagation problems. Two applications are considered. The first application involves waves propagating in dielectric media with uncertain permittivities and permeabilities, in which several cases with increasing random-space dimensionality are exemplified. The objective in the second application is to compute expected signal strength above flat Earth surface at ranges far from transmitter location, where randomness is present due to uncertain refractive index of the atmosphere. The uncertainty is extracted from published measurements and constitutes for long-term variation. Two different sparse grid algorithms are demonstrated throughout the paper, and the deterministic evaluators are accessed as a black box by the sparse grid algorithms. Through the results considered, strengths of the two algorithms are differentiated depending on the characteristics of the randomness.

Index Terms—Radiowave propagation, Random Media, Inhomogeneous Atmosphere, Parabolic Equation Method, Split-Step Fourier Propagator, Uncertainty Quantification, Sparse Grid Collocation.

I. INTRODUCTION

Expectation, or the mean-value integration, is the most fundamental operator to apply in a statistical problem, where any higher moment calculation basically involves the mean-value integration. Research topics in electromagnetics with such interest include but not limited to propagation in random media [1], [2], [3], statistical variability of components [4]–[6], electromagnetic field interaction in biological tissues [7], [8] and random walk models of waves [9]–[11].

The source of uncertainties in electromagnetics may be due to random radiating sources (excitation), random boundaries or random domain parameters. The uncertainties are in the most general sense represented as random processes, in which case pre-processing of the given randomness may be required. For instance one may decompose a given random process to finite number of random variables (RV) through Karhunen-Loëve transform [12]. This decomposition is not necessary for problems involving finite number of independent RVs, which will also be the case throughout this study.

The most common sampling method to perform mean value integrations is the Monte-Carlo (MC) sampling. MC sampling has a convergence rate of $O(1/\sqrt{Q})$ [13], where Q is the sample size (number of realizations). One should keep in mind the nice

feature of MC sampling that the convergence rate is independent of dimensionality (d), i.e. one would get the same convergence rate however big d is. Nevertheless, this is a rather slow rate and there has always been interest for improvement. Several alternatives to MC sampling have been developed by researchers until last decade, and these techniques are often referred to as “variance reduction techniques”. These include Importance Sampling [14], Latin Hypercube Sampling (LHS) [15], [16] and Markov Chain Monte Carlo (MCMC) [17]. Another series of techniques based on sampling of low-discrepancy sequences are the Quasi Monte Carlo (QMC) methods that were shown to achieve up to $O(Q^{-1})$ convergence depending on d and variations in random space [18]. All of the above techniques offer size reductions of up to an order, but may become worse than MC sampling for problems with very high dimensionality, often termed as “the curse of dimensionality”. In this work, among the sequences available for QMC methods we will demonstrate results only with the Sobol [19] and Halton [20] sequences.

A more recent development was achieved by Xiu [21]–[23], where they generalized Wiener’s homogeneous chaos of Gaussian processes [24] to arbitrary processes each with a choice of orthogonal basis. This is termed generalized polynomial chaos (gPC) technique. In this technique, the inputs and outputs of the model problem with randomness are projected onto a complete space spanned by the basis of orthogonal polynomials. A Galerkin projection carried out in the spanned space transforms the stochastic problem into a system of coupled differential equations with deterministic unknowns. Such a weak formulation was termed Stochastic Galerkin (SG), and any finite moment of the originally desired random output (target) can be computed from the coupled system without any sampling, unless the original stochastic system have highly non-linear terms that do not allow closed form expressions of the target function’s moments. The dependence on RVs are highly nonlinear for great majority of the numerical solutions in electromagnetics, therefore sampling based methods are inevitable. In this regard, the sparse grid collocation (SGC) method avoids coupled nature of SG, where the mean value integration (or any higher moment computation) is performed via independent calls of the function on a set of cubature points (sparse grid nodes). The sparse grid formation is independent of the target function, *viz.*, the function under uncertainty for which we seek the moments in a random domain.

In cases where the target function is highly non-smooth, e.g. when the field is highly sensitive to certain RVs, SGC does not

offer superiority over conventional MC methods, and adaptive algorithms for sparse grid construction in SGC become attractive. The fast convergence of SGC in interpolation of the target function depends on the smoothness, and it is not unreasonable to assume that the target function under uncertainty meets the smoothness condition of Smolyak algorithm, derived in [25]. It is thus crucial to refine the sparse grid around regions of non-smooth target function output, and sample less the smooth regions of the random domain. From a mathematical point of view non-smoothness may appear as discontinuities or regions of the random domain where there is rapid fluctuation in the target function output.

In cases of high dimensional problems, ($d \gg 1$), even the adaptive sparse grids suffer the curse of dimensionality. The high dimensional model representations (HDMR) [26], [27] provide an exact representation for high dimensional functions in terms of lower dimensional sub-functions, which we will refer to as “components”. Each component in the HDMR represents collective contribution of the RVs it includes on the target function interpolation, thus allows measure of to what extent each RV, or combination of RVs, dominate the target function behavior. Use of HDMR for dimensionality reduction has recently attracted attention of various authors [28], [29], [30]. Although the published literature reveals acceptable convergence rates for up to 500 dimensions in some partial differential equations with random input data, it is a question if electromagnetic propagation and scattering will be subject to such an enhancement over existing performance with sparse grids. The authors in [31] have applied this technique for electromagnetic compatibility and interference (EMC/EMI) analysis, and obtained desired characterization at 240 dimensions. Ma and Zabaras [29] have merged their adaptive sparse grid method with HDMR, and given a thorough interface algorithm between HDMR and their method. We introduce some modifications to their interface algorithm, and make use of it in our problems, which will be referred to as HDMR+ASGC. Lately, Jakeman and Roberts introduced another improved scheme, h -GSG, which can also be attractive for certain applications [32]. Throughout this work, we will use HDMR+ASGC and h -GSG methods, and assess their performance compared to the conventional MC sampling and QMC methods.

Regarding the use of sparse grids for propagation problems with uncertainty, there are several applications to be addressed, which have conventionally been tackled with MC sampling. However, given the fact that the performance of these methods are limited for non-smooth behavior and for high- d , we are interested in tackling problems of where the dimensionality can controllably be increased, and the smoothness of the target function can favor adaptive methods via rendering certain RVs more important than the rest of the RVs. In this respect, we choose to begin with a simple 1-D (in space) scattering application, yet the target function behavior in the random space can become highly non-smooth. Through such an example we intend to compare the state-of-the-art SGC methods in their performance in EM scattering and propagation with uncertainty in intrinsic domain parameters, where we have the flexibility to assume as high d as desired, and assume each RV having as large support as desired.

The focus of our motivation with SGC methods extend to their

application in long-range tropospheric propagation phenomena with narrow-angle parabolic equation (PE) solvers [33]. Inhomogeneous atmospheric refractive index has been investigated thoroughly for decades, where conventional analytical models exist based on measurements [34]–[37]. Although the refractive index in the most general sense varies as a function of all dimensions in real-time due to atmospheric pressure, water-vapor pressure and temperature variations [38], [39], in PE research spatial variation only along the elevation direction out from Earth surface is given a significant role. This variation usually results in ducting layers around certain elevation, and has been given analytical expressions derived from measurements. A review of different ducting formations observed in various coastal middle latitude locations were given in [40]. Through extraction of an uncertainty model from published measurements, we solve the expected PF in the presence of uncertain ducting formations.

The inverse problem of predicting refractive index profile from measured data has been an active research area, where popular prediction tools include evolutionary-type optimization algorithms and Markov-Chain-Monte-Carlo (MCMC) method [41]–[43]. Recently Grabner, et. al. have published their measured data that set a validated uncertainty model in terms of several random variables (RVs) [43]–[45], [46, Chapter 7]. Joint distribution of 5 RVs are validated and depicted in [46, Chapter 7], where it is assumed that each of these RVs is independent in moderate perturbations around locations of high probability in the probability distribution functions. Such an uncertainty in ducting model enables one to tackle field estimation problem, e.g. compute the mean-power available at desired receiver end. This estimation has conventionally been carried out for the propagation loss as a function of range using Monte Carlo (MC) sampling [47]. In this work we perform this estimation with sparse grid methods, and obtain expected field and power distributions by exploiting much less resources (computation time) than the MC sampling and QMC methods.

The paper is organised as follows: in Section II we briefly mention the construction of the sparse grid in SGC, and the two adaptive algorithms that we use. Section III-A introduces the 1-D scattering application in which the random dimensionality is varied from $d = 6$ up to $d = 100$. The tropospheric long-range propagation (2-D) is studied in Section III-B, where the uncertainty model of the ducting has a fixed dimensionality of $d = 5$. The details of this work can be found in [48].

II. EVALUATION OF EXPECTATION

It should be re-stressed that our goal in this work is to compute expectation of quantities $E[f(r, y)]$, where $E[\cdot]$ is the expectation operator, $y = (Y_1, \dots, Y_d)$ is the vector of d independent RVs, and r is the vector of any spatial/temporal variables. The target function, f , will be in the first application a reflection coefficient, and in the last two applications the field distribution at the observation range along the direction transverse to propagation axis. We refer to the d -dimensional space of RVs as Γ . If we drop the deterministic arguments r for brevity,

$$\begin{aligned} E[f(y)] &= \int_{Y_1} \dots \int_{Y_d} f(y) \rho_1(Y_1) \dots \rho_d(Y_d) dY_d \dots dY_1 \\ &\approx \sum_{q=1}^Q f(y_q) \alpha_q, \end{aligned} \quad (1)$$

where ρ_k is the probability distribution function of the k th RV, $k = 1, 2, \dots, d$. If one uses MC sampling, each sample is equally weighted, i.e. $\alpha_q = 1/Q$ and y_q are drawn totally randomly from Γ . As stated before, MC sampling will constitute the reference method that we will compare our results to. Next, the Sparse Grid Collocation (SGC) method and its enhancements are introduced.

The SGC method is based on Smolyak's cubature formula for numerical computation of multi-dimensional integrals [49], where the same formula was later generalized to the broader problem of multi-dimensional function interpolation [50]–[52] in the below form:

$$\mathcal{A}_{(d,s)}(f) = \mathcal{A}_{(d,s-1)}(f) + \Delta\mathcal{A}_{(d,s)}(f), \quad (2)$$

where $s \geq 0$ is referred to as the “level” of the Smolyak algorithm, with which both number of samples used, Q , and interpolation accuracy is expected to increase. $\mathcal{A}_{(d,s)}(f)$ is the s th level sparse grid approximation to the d -dimensional function f . $\Delta\mathcal{A}_{(d,s)}(f)$ is a hierarchical interpolation difference, which can be regarded as the functional change from level $s-1$ to level s :

$$\Delta\mathcal{A}_{(d,s)}(f) = \sum_{|\mathbf{i}|_1=d+s} \sum_{\mathbf{n} \in B_{\mathbf{i}}} \Xi_{\mathbf{n}}^{\mathbf{i}} w_{\mathbf{n}}^{\mathbf{i}}. \quad (3)$$

We name $\mathbf{i} = (i_1, \dots, i_d)$ as the super-index levels (or super-indices) in uni-dimensional interpolations along each RV, $|\mathbf{i}|_1 = i_1 + i_2 + \dots + i_d$, and $\mathbf{n} = (n_1, n_2, \dots, n_d)$ as the sub-indices, respectively. Each super-index level $i_k \in \mathbb{N}^+$ determines the number of nodes that appear in the uni-dimensional interpolation formula associated with Y_k , whereas the value of $n_k \in \mathbb{N}^+$ follows a convention according to the set $B_{\mathbf{i}}$. $w_{\mathbf{n}}^{\mathbf{i}}$ is a surplus value associated with index pair (\mathbf{i}, \mathbf{n}) . Together, each index pair (\mathbf{i}, \mathbf{n}) corresponds to a particular node y_q from Γ . We skip further discussions with $B_{\mathbf{i}}$ and $w_{\mathbf{n}}^{\mathbf{i}}$, and encourage the reader to see the thorough derivation in [52]. Lastly, $\Xi_{\mathbf{n}}^{\mathbf{i}}$ is the d -tensor product of uni-dimensional basis functions $\Xi_{\mathbf{n}}^{\mathbf{i}}(y) := \xi_{n_1}^{i_1}(Y_1) \otimes \dots \otimes \xi_{n_d}^{i_d}(Y_d)$, where \otimes is the tensor product symbol. As uni-dimensional basis functions ξ_n^i we interchangeably choose local triangular functions or Lagrange characteristic polynomials. When we use local triangular functions, the corresponding nodes are equi-distant, also known as Newton-Cotes nodes, also chosen in [53]. When we use Lagrange characteristic polynomial interpolation, we use Chebyshev nodes of the second kind, also known as Clenshaw-Curtis nodes [54]. Unless otherwise stated, we keep local triangular function interpolation and equi-distant node selection as standard.

Once the sparse grid for d -dimensional function interpolation is constructed according to (2), (3), $E[f]$ can now be computed as

superposition of expectations of hierarchical differences, which is obtained by substituting (3) in (1):

$$E[\Delta\mathcal{A}_{(d,s)}(f)] = \sum_{|\mathbf{i}|_1=d+s} r_{\mathbf{i}}, \quad (4)$$

$$\begin{aligned} r_{\mathbf{i}} &= \sum_{\mathbf{n} \in B_{\mathbf{i}}} w_{\mathbf{n}}^{\mathbf{i}} \left[\int_{Y_1} \dots \int_{Y_d} \xi_{n_1}^{i_1}(Y_1) \otimes \right. \\ &\quad \left. \otimes \dots \otimes \xi_{n_d}^{i_d}(Y_d) \rho_1(Y_1) \dots \rho_d(Y_d) dY_d \dots dY_1 \right]. \end{aligned} \quad (5)$$

So far, the SGC construction above is deterministic in the sense that all nodes in the sparse grid and their corresponding basis tensor products are a-priori known without the knowledge of how smooth f is in Γ . Therefore, the SGC often suffers accuracy for non-smooth f , e.g. with singularities/discontinuities, and may result in redundant sampling. For $d \gg 1$, the SGC employs $Q \sim (2d)^s/s!$ predetermined nodes (samples) from Γ [22]. Therefore, adaptive strategies are inevitable especially for high- d spaces, which reduce the number of samples used in sparse grid construction through sampling of important subspaces rather than a pre-determined sampling. Next, we briefly present the two adaptive construction methods we used in this work.

A. Adaptive Sparse Grid Collocation Method

Among several adaptive construction enhancements to SGC, in this section we present the Adaptive Sparse Grid Collocation (ASGC) method [55], which resulted in one of the best performances for interpolating wave propagation problems we are interested in. Although the hierarchical construction we follow was detailed and the term “ASGC” was coined in [53], the algorithm in [55] presents slight differences and we follow the latter.

Suppose s_{max} is a maximum level, beyond which the sparse grid construction terminates. For each node y_q considered in the sparse grid, a percentage surplus error is defined as:

$$\gamma_{\mathbf{n}}^{\mathbf{i}} = 100 \times w_{\mathbf{n}}^{\mathbf{i}} / f(y_q). \quad (6)$$

In cases the function behavior is smooth with respect to a node, i.e. the surplus $w_{\mathbf{n}}^{\mathbf{i}}$ for the specific node is not significant with respect to the exact function value evaluated at that node, $f(y_q)$, then simply the specific node under investigation is discarded from further neighbor refinement in the sparse grid. This way, the sparse grid is adaptively refined towards the singular, if not non-smooth regions in Γ . (e.g. see [53], Fig.7). The error threshold for adaptivity can be assumed in different means. We use a constant mean percentage error threshold t_e , where the error is defined as in (6).

The ASGC method has recently been applied to several problems [55], [56]. Although it introduced a hyper-cube refinement strategy to sample only important subspaces of Γ , it

can still suffer the “curse of dimensionality” for moderate-to-high- d problems, depending on smoothness of f . In [29], decomposition of the target function f into lower dimensional component functions, and tackling each component function with ASGC was established. This decomposition is based on the high dimensional model representations (HDMR) of [26], [27]:

$$\begin{aligned} f(y) = f_0 + \sum_{i=1}^d f_i(Y_i) + \sum_{1 \leq i_1 < i_2 \leq d} f_{i_1 i_2}(Y_{i_1}, Y_{i_2}) \\ + \dots + \sum_{1 \leq i_1 < \dots < i_p \leq d} f_{i_1 \dots i_p}(Y_{i_1}, \dots, Y_{i_p}) \\ + \dots + f_{12\dots d}(Y_1, \dots, Y_d), \end{aligned} \quad (7)$$

where f_0 is a constant term and is equal to the evaluation at the origin of Γ , $f(y_{\text{origin}})$, and $f_{i_1 i_2 \dots i_p}$ are p th order component functions, that account for the contribution of p -tuple RVs (Y_1, Y_2, \dots, Y_p) into f . The component index $\mathbf{u} = \{i_1, i_2, \dots, i_p\}$ is used to represent the RVs that are included in the component $f_{\mathbf{u}}(Y_{\mathbf{u}})$. For several physical systems it has been shown that the first few order components in (7) dominate the overall behavior of f , thus majority of the components can be eliminated, or adaptive selection among them are allowed. It should be stressed that the expansion in (7) is nested, in the sense that even if no adaptive elimination of components is applied, no extra nodes are introduced to the sparse grid when (7) is utilized prior to interpolation with ASGC. Henceforth, we refer to this technique as HDMR+ASGC. The procedure we use, which follows [29] except for a sub-routine, is summarized below:

- 1) Let θ denote a threshold value, which will be used as an indicator for an elimination to be explained later. For example, $\theta = 0.01$ means that the elimination will be based on 1% error.
- 2) Let $p_{\max} \in \mathbb{N}^+$ denote the maximum order at which HDMR in (7) will be truncated, i.e. it represents the highest dimensionality a component in (7) can have.
- 3) Pre-determine parameters of the ASGC method to be accessed: determine s_{\max} and t_e of Section II-A.
- 4) Now define four sets that hold component vectors (\mathbf{u}),
 - \mathcal{R}_u : set of “admissible” components, which are order $p+1$ each. The set is redefined at each order p , $p = 0, 1, \dots, p_{\max} - 1$.
 - \mathcal{T}_u : set of “selected” components, redefined at each order according to θ criterion.
 - \mathcal{C}_u : set of “all” components considered in the coarse of HDMR. This set will monotonically enlarge, where the cardinality of this set can never exceed 2^d according to (7).
 - \mathcal{I} : set of “important dimensions”, i.e. important order-1 components out of the N order-1 components in (7).
- 5) Set $\mathcal{R}_u = \emptyset$, $\mathcal{T}_u = \emptyset$, $\mathcal{C}_u = \emptyset$, $\mathcal{I} = \emptyset$. Compute $f_0 = f(y_{\text{origin}})$. Set $p = 1$.
- 6) Interpolate each of the d order-1 components using ASGC with parameters s_{\max} and t_e , and compute $E[f_j]$, $j = 1, 2, \dots, N$. Add each order-1 component $\{j\}$ in \mathcal{C}_u . Those order-1 components that satisfy $\eta_j > \theta$ are labelled as being “important”, and only these components $\{j\}$ are

put in both \mathcal{I} and \mathcal{T}_u , where

$$\eta_j = \frac{|E[f_j]|_{L_1(D)}}{|f_0|_{L_1(D)}}, \quad (8)$$

where as the first norm $| \cdot |_{L_1(D)}$, we use the sum of absolute values of the evaluated function at each spatial/temporal variable r ($f(y) \equiv f(y, r)$).

7) while $p < p_{\max}$

- Components to be considered (at order- $(p+1)$) are obtained by the routine $\text{CompAdmit}(\cdot, \cdot)$, which is detailed later in this section, and these components are put in the admissible set: $\mathcal{R}_u \leftarrow \text{CompAdmit}(\mathcal{T}_u, \mathcal{I})$.
- $\mathcal{T}_u = \emptyset$.
- If $\mathcal{R}_u \neq \emptyset$, for each component \mathbf{u} from \mathcal{R}_u use ASGC with parameters s_{\max} and t_e to get $E[f_{\mathbf{u}}(y_{\mathbf{u}})]$.
 - for each \mathbf{u} from \mathcal{R}_u compute error $\eta_{\mathbf{u}}$, where

$$\eta_{\mathbf{u}} = \frac{|E[f_{\mathbf{u}}]|_{L_1(D)}}{\left| \sum_{\mathbf{v} \in \mathcal{C}_u, |\mathbf{v}| < |\mathbf{u}|} E[f_{\mathbf{v}}] \right|_{L_1(D)}}. \quad (9)$$

8) endwhile

Next, we discuss how the order- $(p+1)$ components are admitted, given the set of “important” dimensions (\mathcal{I}) and order- p components already computed (\mathcal{T}_u).

CompAdmit($\mathcal{T}_u, \mathcal{I}$)

This routine is the main difference we have with respect to the procedure in [29], where they use a more conservative component admission strategy than ours. We have experienced in general better results with our selection. Below routine returns the components to be admitted at order- $(p+1)$. The assumption is that all components in the input \mathcal{T}_u are order- p .

- $\mathcal{R}_u = \emptyset$
- for $n = 1, n \leq \mathcal{I}.\text{size}()$, $n++$
 - for $m = 1, m \leq \mathcal{T}_u.\text{size}()$; $m++$
 - * if $n \notin \mathcal{T}_u(m)$, then $\mathcal{R}_u = \mathcal{R}_u \cup \text{Concatenate}\{\mathcal{T}_u(m), n\}$.
 - endfor
 - endfor
 - return \mathcal{R}_u .

The concatenation of component vectors restricts ascending order, and a component vector can contain unique integers only. For instance, $\text{Concatenate}\{\{1, 2, 3\}, \{1, 4\}\} = \{1, 2, 3, 4\}$. Finally, we demonstrate a sample adaptive component elimination in Table I, for a $d = 5$ -dimensional system that will be

studied in Section III-B. This elimination was performed with $\theta = 10^{-4}$. Note that the first RV, that corresponds to the component f_1 from (7) and component vector $\{1\}$ in Table I, produces an indicator of 10^{-11} , and is the only unimportant dimension according to $\theta = 10^{-4}$. Out of the 31 components (other than f_0) present for this 5-dimensional system, 14 of them were considered and interpolated with an ASGC solver with parameters $t_e = 0.5$ and $s_{max} = 6$. Indeed, the elimination in Table I resulted in use of 1,777 nodes (samples) to evaluate f at, whereas the SGC method (non-adaptive) of $s_{max} = 6$ in a 5-dimensional space requires 6,993 evaluations irrespective of f .

TABLE I
THE ERRORS η_u , FOR A SAMPLE HDMR+ASGC COMPONENT ELIMINATION
PERFORMED FOR THE APPLICATION IN SECTION III-B ($d = 5$).

u	η_u	u	η_u
$\{1\}$	10^{-11}	$\{3,4\}$	1.03×10^{-3}
$\{2\}$	0.0160	$\{3,5\}$	5.31×10^{-4}
$\{3\}$	0.0761	$\{4,5\}$	3.20×10^{-3}
$\{4\}$	9.21×10^{-3}	$\{2,3,4\}$	4.01×10^{-5}
$\{5\}$	0.0206	$\{2,3,5\}$	7.04×10^{-6}
$\{2,3\}$	1.89×10^{-4}	$\{3,4,5\}$	9.10×10^{-5}
$\{2,4\}$	5.18×10^{-5}		
$\{2,5\}$	1.56×10^{-6}		

B. h-Adaptive Generalized Sparse Grid Method

The second adaptive strategy we will apply for computing $E[f]$ is the h -Adaptive Generalized Sparse Grid (h -GSG) method [32]. Different from ASGC, this method creates an adaptive refinement not only in the nodes of the sparse grid, but also in the super-indices i . The method dates back to [57], where in the original work only super-indices i are adaptively selected, and all nodes entailed with i according to the node set B_i , are included in the sparse grid. In h -GSG however, adaptive refinement in between the nodes in B_i of a selected index i is also present. As it was the case with ASGC method, we can either use equi-distant nodes or Chebyshev nodes. The reader is referred to [32] for the details of the algorithm.

While both HDMR+ASGC and h -GSG have different strengths, it is in general easier to optimize the parameters of h -GSG, as it only uses a single parameter: ϵ_{tol} . However, in HDMR+ASGC, there are a total of 3 parameters to optimize for best convergence, thus this method suffers from lack of easiness of optimization compared to h -GSG. To perform indexing and node search operations present in sparse grid methods in a fast way we used the standard *set* library of C++, and as an efficient linear algebra package the *Eigen* library [58].

III. NUMERICAL APPLICATIONS

A. First Scattering Example: Reflection from multi-layered slabs

A test case to study performance of sparse grid methods is the problem of plane wave normally incident on a series of

infinite (in the transverse plane) planar dielectric slabs of finite thicknesses as shown in Figure 1, where the K slabs are assumed to exist between two open half-infinite free space regions. The parameters of the k th slab are the thickness h_k , permittivity ϵ_k , permeability μ_k , conductivity σ_k , and thus complex wave number γ_k , $k = 1, 2, \dots, K$. This example is instructive because it will explain how sparse grids may be applied to more complicated scattering problems, such as rough surface scattering. The target in this example is to compute expected value of the reflection coefficient, $|E[R]|$, where R is the reflection coefficient for the normally incident wave, as depicted in Figure 1.

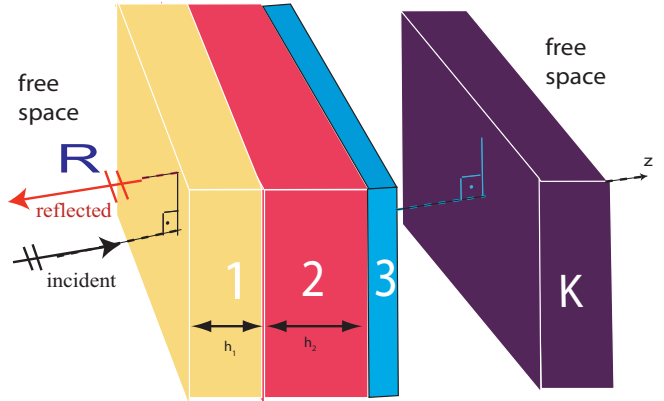


Fig. 1. Normal-incidence reflection from multi-layered media.

The analytical solution for R is straightforward to derive utilizing oppositely directed plane wave pair-solutions in each slab and enforcing field continuities at interfaces, for which we refer the reader to [59, Chapter 5]. The series of examples that will be considered next will shed light on the convergence performance of the sparse grid methods applied to the canonical reflection problem discussed above. In all the results, we seek the mean value $|E[R]|$ of the reflection coefficient. These examples are listed in Table II along with the reference solution (exact $|E[R]|$), at the operating frequency of 300 MHz.

TABLE II
LIST OF EXAMPLES CONSIDERED IN SECTION III-A.

Example	K	d	RV List	$ E[R] $ (reference)	Fixed Values
1	3	6	$\epsilon_1, \epsilon_2, \epsilon_3,$ μ_1, μ_2, μ_3	0.010320	$\sigma_k = 1mS/m,$ $h_k = 0.5m,$ $k=1,2,3.$
2	10	20	$\epsilon_1, \dots, \epsilon_{10},$ μ_1, \dots, μ_{10}	0.60437	$\sigma_1 = 1.67mS/m,$ $\sigma_k = 0, k \neq 1.$ $h_1 = 2m,$ $h_k = 0.5m,$ $k \neq 1.$
3	50	100	$\epsilon_1, \dots, \epsilon_{50},$ μ_1, \dots, μ_{50}	0.63423	$\sigma_1 = 1.67mS/m$ $\sigma_k = 0, k \neq 1.$ $h_1 = 2m,$ $h_k = 0.1m,$ $k \neq 1.$

The series of examples that will be considered next will shed light on the convergence performance of the sparse grid methods applied to the reflection problem. In all the results, we seek the

mean value $|E[R]|$ of the reflection coefficient. These examples are listed in Table II along with the reference solution (exact $|E[R]|$), at the operating frequency of 300 MHz.

The first example is the case of a three infinite slabs inserted in free space, with 6 RVs ($d = 6$): relative permittivity and relative permeability of each slab are uniform RVs $\epsilon = U[1, 2]$, $\mu = U[1, 2]$. Each slab is 0.5 m thick, and each has conductivity 1 mS/meters. The magnitude of the mean reflection coefficient is $|E[R]| = 0.010320$, which is obtained from 10^7 MC samples, where the convergence results are shown in Figure 2, in which the first-norm errors are defined as:

$$Err_{L_1} = \frac{|h_{tar} - h_{ref}|}{|h_{ref}|}, \quad (10)$$

where h_{tar} and h_{ref} are the estimate and exact (reference) $E[R]$, respectively. In this particular example we consider a case where each individual RV and p -tuple combinations of RVs contribute significantly to the target function R , where p corresponds to the component orders in (7). In Figure 2 the error convergence for MC sampling, ASGC and HDMR+ASGC are depicted. The ASGC solution was applied with Chebyshev nodes, with a threshold parameter $t_e = 0$, therefore it is indeed a non-adaptive solution (SGC). The markers on the ASGC curve denote errors for increasing levels s , as a function of the nodes (Q) used in the sparse grid. Note that the error attained at level $s = 5$, using 4,865 samples, is much lower than the MC sampling would attain with 10^6 samples. The HDMR+ASGC curve on the other hand depicts the errors with increasing component orders p , while keeping $s_{max} = 5$ in the algorithm in Section II-A, as a function of Q . The HDMR error indicator was selected with $\theta = 0$, and $p_{max} = N = 6$, so that the decomposition in (7) does not make any component elimination, and at order $p_{max} = N = 6$ completely recovers the ASGC solution it was applied upon. In Figure 3, component importance indicators η_u are depicted as a function of the index of the components u . Note that for this example there are a total of 2^6 components in (7), and all η_u except for the 0th order term are depicted ($\eta_0 = 1$ always). It is obvious in Figure 3 that unlike the general use of HDMR+ASGC algorithm for dimensionality reduction, this example reveals a case where all components up to $p = 5$ th order are quite important, and cannot be eliminated. This is also obvious in Figure 2 that the HDMR+ASGC error is quite high unless all components are included. Through Example 1, we have considered a case where the physics of the geometry and the RVs assumed therein do not allow adaptation along certain reduced dimensional subspaces of the 6-dimensional space (Γ). It is in general the case in the K-Slabs problem in this section, that unless some RVs are deliberately made less-important, all permittivities and permeabilities are comparably important in the input reflection coefficient R . The convergence rates listed in the legend are obtained from the slopes of the best-fit lines for each curve. Note that MC sampling curve has a rate of $Q^{-0.412}$, which is in the asymptotic case expected as $O(1/\sqrt{Q})$. It is an indication that the target function, R , has a large dynamic range in Γ and a sample size bigger than 10^7 would be required to achieve $1/\sqrt{Q}$ rate.

Example 2 is the case of 10 dielectric slabs, thus the problem is $d = 20$ -dimensional. In this example, the thickness of the first slab is $h_1 = 2$ meters, whereas the other nine slabs have

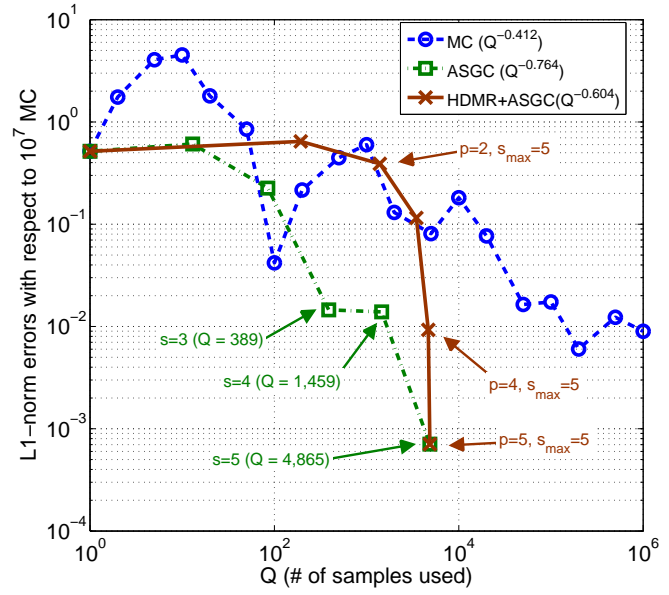


Fig. 2. Error convergence for Example 1 of Section III-A for MC sampling, ASGC method for increasing levels s , and HDMR+ASGC for increasing component orders p .

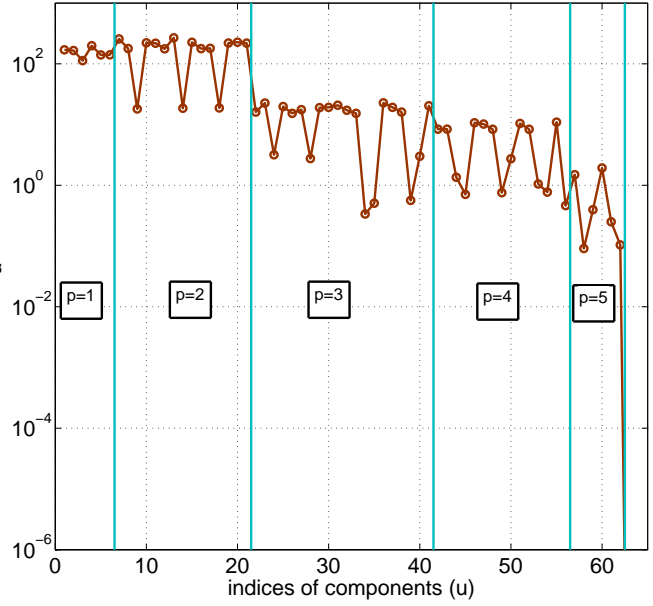


Fig. 3. η_u corresponding to the components of the HDMR expansion (HDMR+ASGC curve) in Figure 2.

thicknesses $h_2 = h_3 = \dots = h_{10} = 0.5$ meters. Accordingly, for the purpose of creating a high-impedance first slab compared to the remaining nine slabs, all RVs are identical and uniform, except that the permeability of the first slab is much higher than other permeabilities: $\epsilon_1, \epsilon_2, \dots, \epsilon_{10}, \mu_2, \mu_3, \dots, \mu_{10} \sim U[1, 1.5]$, and $\mu_1 \sim U[20, 21]$. With such distinction of μ_1 from other RVs, and the first slab being four times thicker than the other slabs, the random problem becomes more fluctuating due to the uncertainty in μ_1 than other RVs. Figure 4 depicts the first norm errors for Example 2 with respect to 10^7 MC samples, which gives the reference value of $|E[R]| = 0.60437$. For this example we also include QMC results with Sobol and Halton sequences. Note that both sequences attained a lower error than MC, Sobol has a convergence of $Q^{-0.637}$ and Halton has a convergence of $Q^{-0.653}$. On the other hand, both HDMR+ASGC and h -GSG have significantly improved convergence with respect to MC and QMC. The h -GSG sparse grid construction terminated after having used $Q = 855$ samples, where the tolerable error level parameter of h -GSG was $\epsilon_{tol} = 10^{-4}$. For the HDMR+ASGC, the parameter set was $\theta = 10^{-4}$, $s_{max} = 6$, and $t_e = 0.2\%$. The HDMR algorithm terminated after order $p = 2$, which used $Q = 692$ nodes and attained more than two orders of magnitude less error than the MC sampling with the similar Q . The error that h -GSG attained with 855 samples is even lower, and represents a lower error than MC sampling with 10^6 samples has.

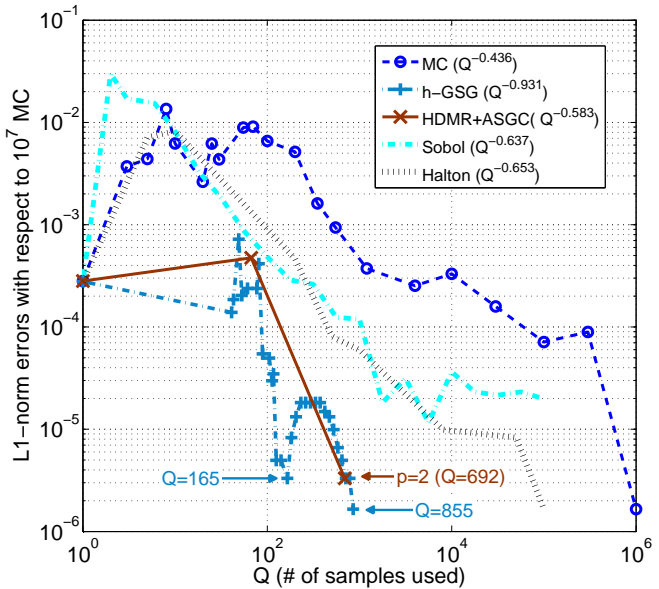


Fig. 4. Error convergence for Example 2 of Section III-A

Example 3, the last example of this section, is a 50 dielectric slabs problem, which makes Γ 100-dimensional. Through this example we intend to demonstrate a high-dimensional case ($d = 100$) where the randomness in Γ is highly along a specific RV, which we expect to be ideal for interpolating with h -GSG. Our experience and related literature shows that the methods based on SGC, which is ASGC and HDMR+ASGC in our case, fail to attain better convergence than the MC and QMC with such high-dimensional examples. The difference of thicknesses of

slabs is made very severe: $h_1 = 2$ meters, $h_2 = h_3 = \dots = h_{50} = 0.1$ meters. Similar to Example 2, only the permeability of the first slab (μ_1) is assigned a large support and all other 99 RVs have much more restricted variation. This time we assume normal RVs, where the two arguments of a normal variable $N[., .]$ stand for the mean and the standard deviation. The 99 restricted RVs are $\epsilon_1, \epsilon_2, \dots, \epsilon_{50}, \mu_2, \mu_3, \dots, \mu_{50} \sim N[1, 0.05]$, and $\mu_1 \sim N[20, 0.5]$. Figure 5 depicts the performance of QMC and sparse grid methods in Example 3 with respect to the reference solution. The reference solution in this case was obtained with 4×10^8 samples. Note in Figure 5 that the performance of both QMC sequences are slightly better than MC sampling, yet are not worse than the 20-dimensional case in Example 2. This is an indication that although we have a 100-dimensional problem in Example 4, the randomness in Γ is not significantly higher than in Example 2. As expected, in Figure 5 the performance of h -GSG method is the best of all methods considered, and terminated at $Q = 2,029$ with $\epsilon_{tol} = 10^{-6}$. The fast decaying pattern in the error of h -GSG curve represent a super-index search along the axis of the μ_1 RV, for this example basically only that axis is very densely discretized due to its importance. The HDMR+ASGC on the other hand, terminates after order $p = 2$, and cannot draw nearer to the reference solution in a decent sparse grid size. This is mainly due to the fact, as explained earlier in Section II-A, that the ASGC method at level s considers admissibility of all indices altogether, that satisfy $|\mathbf{i}|_1 = d + s$, thus unlike h -GSG cannot perform adaptivity along a single axis of Γ .

The HDMR+ASGC method, as depicted in Figure 5, terminated after order $p = 2$ with a sample size of $Q = 1,091$. The peak physical memory taken during this execution was monitored as 5.3 MB and the method elapsed 170 seconds before termination. On the other hand, the h -GSG execution, which terminated after $Q = 2,029$, took 14 MB of peak physical memory and a total of 70 seconds. These are tabulated in Table III. Note that above values reflect the cost of sparse grid methods, since an analytical solver is used in this section. For both sparse grid codes, it is a general trend that as Q monotonically increases, so does the memory in a linear fashion. We think this is due to the dynamic sized sets of objects that we store sparse grid nodes' attributes in. Each object in the set has attributes for its position in Γ , its super-index \mathbf{i} , and its sub-index \mathbf{n} . For holding these objects the standard *set* library of C++ is used. As a linear algebra package we used the *Eigen* library [58]. Similarly, for the MC sampling, the memory usage increases almost linearly with Q , and for the above considered problem, each of MC sampling and QMC methods with $Q = 2,000$ samples took 2.4 MB of physical memory. Although the memory usage of sparse grid methods depend on how the operations with the nodes in Γ are performed, the above numbers suggest that for a $d = 100$ -dimensional problem, the sparse grid methods take memories in the order of megabytes. In cases where the deterministic solver is a very heavy numerical solver, e.g. that involves inversion of large dense matrices, above values of memory and time in Table III will be negligible compared to those taken by the solver. This will be verified in the next section through demonstration of error evolution with total elapsed time.

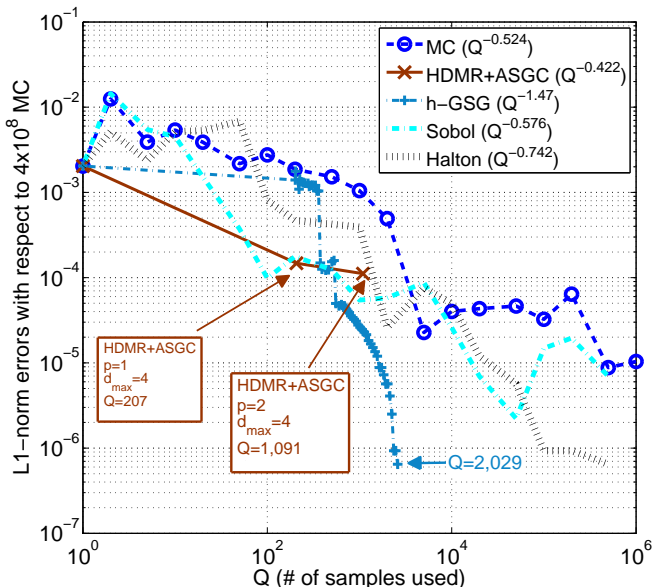


Fig. 5. Error convergence for Example 3 of Section III-A

TABLE III
MEMORY AND TIME USAGES IN EXAMPLE 3 OF SECTION III-A.

Method	Samples Used (Q)	Peak Physical Memory	Total Time
MC&QMC	2,000	2.4 MB	0.54 sec.
HDMR+ASGC	1,091	5.3 MB	170 sec.
h-GSG	2,029	14 MB	77 sec.

B. Application in Tropospheric Propagation: Field Estimation in Long-Range Uncertain Ducting Environments

This section is reserved for the above $d = 5$ -dimensional application which will demonstrate strength of sparse grid methods through a more realistic propagation scenario. The objective is to compute expected signal strength over flat Earth surface at ranges far from the transmitter location, where randomness is present due to uncertain refractive index of the atmosphere. This is a far-range propagation problem that one has to take the effective radius of the Earth into account, where the Helmholtz equation needs to be modified accordingly. This scenario is depicted in Figure 6 for waves propagating long distances in shallow angles with respect to the main propagation axis, x , that is tangential to the Earth surface everywhere. The z axis is normal to the surface, and a_e is the effective radius of the Earth. The standard parabolic equation in the atmosphere is approximated from the modified Helmholtz equation as [60]:

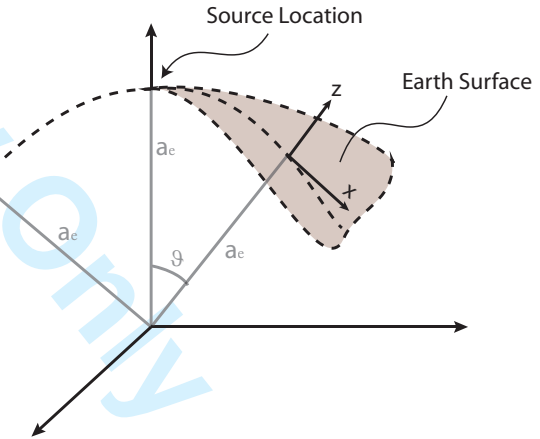
$$\frac{\partial \psi}{\partial x} = \left[\frac{i}{2k_o} \frac{\partial^2}{\partial z^2} + ik_o \left(n(z) + \frac{z}{a_e} - 1 \right) \right] \psi, \quad (11)$$

where k_o is the wavenumber in free-space, $i = \sqrt{-1}$. The quantity $\psi(x, z)$ is a reduced field that constitutes as a one-way approximation to the full-wave solution in atmosphere. The refractive index of the atmosphere, n , is assumed to smoothly deviate from the homogeneous case as a function of

elevation (z) only. This is a valid assumption, and has mostly been modeled as having a slight negative gradient in z at lower elevations. A more general “ducting” phenomenon, which appears up to few hundred meters elevation mostly in coastal locations, has been observed [37], whereas in this work we use the following duct model from [46, Chapter 7]:

$$N(z) = N_o + G_N z + \frac{dN}{2} \tanh \frac{2.96(z - h_o)}{dh}, \quad (12)$$

where N_o (N-units) is the nominal refractivity, G_N (N-units) is the gradient, dN (N-units) is the duct depth, h_o (meters) is the duct height, dh (meters) is the duct height and N-units is a measure of small changes in the true refractive index, $N = (n - 1) \times 10^6$. The refractivity N is related to the often-used modified refractivity M through $N = M - 10^6 z/a_e$. To give a demonstration, a realization of N, M according to (12) is depicted in Figure 7. The slopes of N at small and large heights are shown as dotted lines and are seen to be similar. From the joint cumulative distribution functions in [46, Chapter 7], we choose to assume supports of each of the 5 RVs to be independent and uniform. The nominal refractivity is a uniform RV $U[300, 340]$ N-units, G_N is $U[-0.057, -0.017]$ N-units/m, dN is $U[-7.5, 2.5]$ N-units, h_o is $U[20, 70]$ meters, and dh is $U[10, 60]$ meters. These supports were selected from where each probability distribution have their maxima in, out of the measured data in [46, Chapter 7], and where the cumulative distributions roughly increase linearly, so that uniform RV assumption makes sense and the assumed randomness constitutes the majority of the randomness present in the measured data.

Fig. 6. The 2-D (x, z) environment at every range (x) on the Earth surface, defined with respect to the source location.

Equation (11) has conventionally been solved with the split-step parabolic equation (SSPE) propagator [60]. Among other computational advantages of this propagator, a march-along-range computation that is performed every range step Δx makes it advantageous for propagation far ranges from the transmitter. With the assumption of perfectly conducting smooth Earth surface, the SSPE makes use of sine-transforms to update the field quantity along x :

$$\psi(x_o + \Delta x, z) = e^{ik_o(\bar{m}-1)\Delta x} \int_0^\infty e^{-ip^2 \frac{\Delta x}{2k_o}} \tilde{\psi}(x_o, p) \sin pz dp, \quad (13)$$

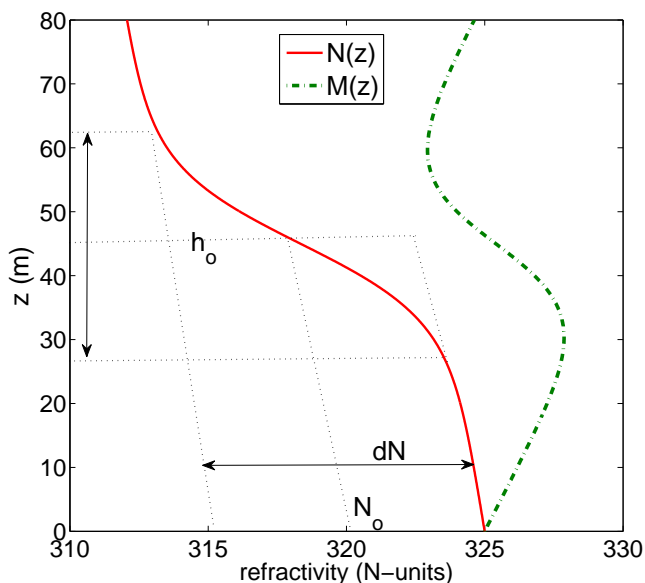


Fig. 7. Refractive index profile according to (12), where $N_o = 320$ N-units, $G_N = -0.037$ N-units/m, $dN = -10$ N-units, $h_o = 45$ meters and $dh = 35$ meters.

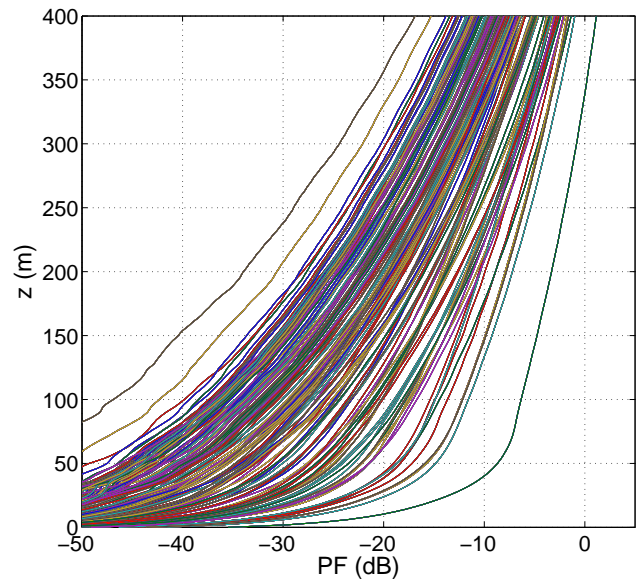


Fig. 8. PF (in dB scale) corresponding to the 2,000 realizations of N at $t_{obs} = 100$ km.

where \bar{m} is an average modified refractive index in the range step $(x_o, x_o + \Delta x)$ which can tolerate only smooth variation in refractive index along height. The modified refractive index is $m = n + z/a_e$. The forward sine-transform that transforms z -varying field into the spectral p -domain is:

$$\tilde{\psi}(x, p) = \frac{2}{\pi} \int_0^{\infty} \psi(x, z) \sin pz dz. \quad (14)$$

Note that the Dirichlet boundary condition on Earth surface, *viz.*, $\psi(x, 0) = 0$ is already satisfied in (13). Before each of forward and backward transforms in the course of the propagator above, the nonzero field quantity at a designated truncation height z_{max} however needs to be smoothly tapered to prevent numerical reflections incurred in numerical transforms. For this, at each step we pre-multiply spatial and spectral quantities with a Hanning window as suggested in [60]. To give an idea of the dynamic range of propagated fields in the presence of the above uncertainty, 2,000 independent realizations of the propagation factor (PF) variation at the observation range, $x_{obs} = 100$ km, is shown in Figure 8. The PF is defined as the total observed field in the presence of inhomogeneous atmosphere, ψ , normalized by the free-space field:

$$PF = \left| \frac{\psi(x_{obs}, z)}{\psi_{FS}(x_{obs}, z)} \right|. \quad (15)$$

The source function that we use in this section, that is excited at $x = 0$, is a Gaussian aperture distribution with height z_t and width σ_t :

$$\psi(0, z) = Ae^{-(z-z_t)^2/2\sigma_t^2}, \quad (16)$$

which leads to the following free-space field received at (x, z)

[61]:

$$\psi_{FS}(x, z) = \frac{A\sigma_t}{\sqrt{\sigma_t^2 + ix/k_o}} e^{-(z-z_t)^2/2(\sigma_t^2 + ix/k_o)}. \quad (17)$$

We will demonstrate three case examples, where in all of them the operating frequency is 300 MHz. For the first two examples $z_t = 50$ meters, $\sigma_t = 2$ meters and $x_{obs} = 100$ km, whereas for the third example $z_t = 100$ meters, $\sigma_t = 1$ meters and $x_{obs} = 150$ km. These source widths correspond to less than 15° elevation beamwidth with respect to x -axis [62], which creates a fairly moderate spectral content span that is accurately propagated with SSPE. The observation of field along elevation is between the Earth surface $z = 0$, and $z_{max} = 375$ meters. This height is safely above the elevations around which ducting phenomena occur, therefore does not lack generality in including uncertainty of the whole ducting regime. In Example 1 the PF is the target function, i.e. we are interested in estimating $E[PF(100 \text{ km}, z; y)]$. The complex field is the target function in Example 2, i.e. estimate of $E[\psi(100 \text{ km}, z; y)]$. Lastly in Example 3, for the sake of investigating the effect of observation range on sparse grid performances, the PF at 150 km range is chosen as the target function, i.e. estimate of $E[PF(150 \text{ km}, z; y)]$.

Figure 9 depicts the error convergence with respect to a reference solution for Example 1. The reference solution for comparing all $E[PF(x_{obs}, z; y)]$ estimates is obtained from MC simulation with $Q = 2 \times 10^6$ random samples. Since we are interested in estimating distributions in this section, the first

norm error, in the vertical axes is defined as:

$$Err_{L_1} = \frac{\int_0^{z_{max}} |h_{tar}(z) - h_{ref}(z)| dz}{\int_0^{z_{max}} |h_{ref}(z)| dz}, \quad (18)$$

where h_{tar} and h_{ref} are the computed target and the reference solutions, respectively. For the HDMR+ASGC method, with only $Q = 135$ samples the error attained is lower than the error MC sampling would attain with 10^6 samples. On the other hand, the h -GSG method terminated after using 167 samples, and attained less error than with 10^5 MC samples. On the other hand, the convergence of QMC methods with Sobol and Halton sequences in Figure 9 attained $O(Q^{-0.638})$ and $O(Q^{-0.803})$ rates, respectively. For instance, the HDMR+ASGC, with 135 samples, attained less error than the Halton sequence with 5,000 samples. In Figure 10 sparse grid estimates for PF are compared to the reference solution and to MC sampling estimate with comparable Q . Note that the HDMR+ASGC estimate ($Q = 135$) and h -GSG estimate ($Q = 167$) are indistinguishable from the reference, whereas the MC sampling with $Q = 200$ samples results in discrepancy of 2 dB at 50m and 0.9 dB at 200m elevation.

Example 2 targets the complex field estimate at $x_{obs} = 100$ km $-E[\psi(100\text{km}, z; y)]$. The error convergence and field estimate magnitudes are depicted in Figures 11 and 12, respectively. In this example, both sparse grid methods resulted in taking more samples compared to previous case in general. This can be assessed as the power quantity being statistically less fluctuating than the real and imaginary parts of the complex field. Nevertheless, the HDMR+ASGC is still much steeper in convergence compared to MC, and at $p = 3$ component order, using $Q = 728$ samples, attains less error than the MC sampling estimate of 10^6 samples. The h -GSG in this case however takes much more samples than in Example 1 for converging to the reference solution. From the statistical point of view this can be explained with the fact that as the important hyper-cubic regions of Γ are separated from the individual axes, dimension-adaptive methods like h -GSG render less accurate in such cases. This is where methods based on ASGC are favorable, as we witness in this problem. Although h -GSG uses orders of more samples than the HDMR+ASGC, it attains less error than the MC sampling estimate with 10^6 samples. In Figure 12, it is clear that a MC estimate with $Q = 20,000$ samples is much more inaccurate than both sparse grid methods, whereas the best accuracy is attained with HDMR+ASGC with only 728 samples.

In Example 3, the effect of range on the uncertainty is investigated by observation at $x_{obs} = 150$ km. Figures 13 and 14 depict the error convergence and PF estimate comparisons, respectively. As expected, the received power levels at this range are weaker than in Example 1. The h -GSG and HDMR+ASGC methods terminated at $Q = 924$ and $Q = 541$ samples, respectively. In comparison to Figure 9, Figure 13 clearly reveals that the sparse grid methods' performances worsen with increased x_{obs} , and they become comparably accurate as the Sobol and Halton sequences. This is mainly due to increased uncertainty with more interaction of waves with uncertain media. On the other hand, the MC sampling applied with a sample size similar

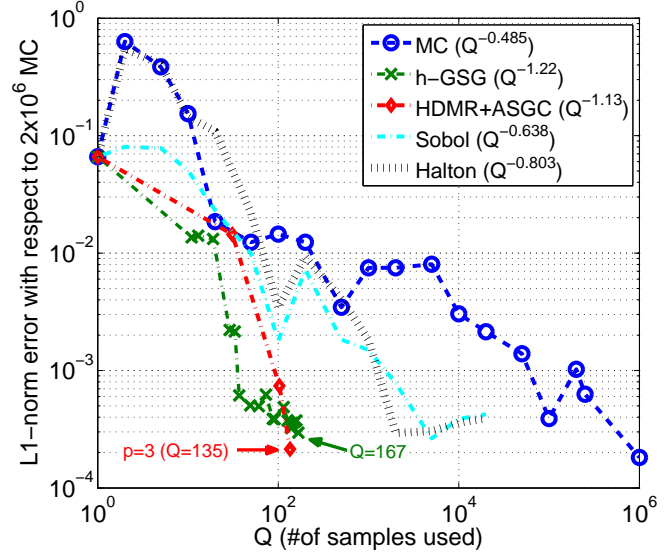


Fig. 9. Error convergence in Example 1 of Section III-B.

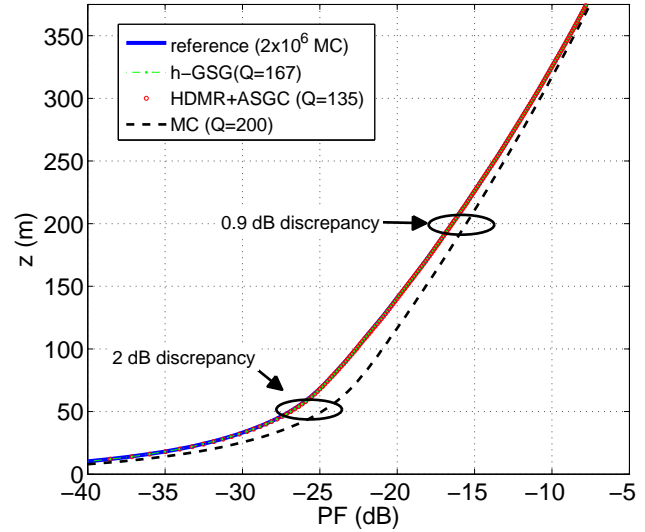


Fig. 10. PF estimates for Example 1, $|E[PF(100\text{km}, z; y)]|$, corresponding to the convergence results in Figure 9.

to that of the depicted sparse grids ($Q = 1,000$) revealed 2.8 dB and 1.8 dB reception discrepancies at 100 meters and 200 meters elevations, respectively. However the h -GSG solution with $Q = 924$ samples, and HDMR+ASGC solution with $Q = 541$ samples very accurately matched the reference solution, as depicted in Figure 14.

Finally, the error convergence as a function of total elapsed time for Example 1 is depicted in Figure 15. The average computation time that SSPE solver takes to evaluate each sample was monitored as 54 milliseconds, running on a computer with Intel Core i7 3.4 GHz processor and 4GB memory. We demonstrate this only with MC sampling, but the QMC methods have the

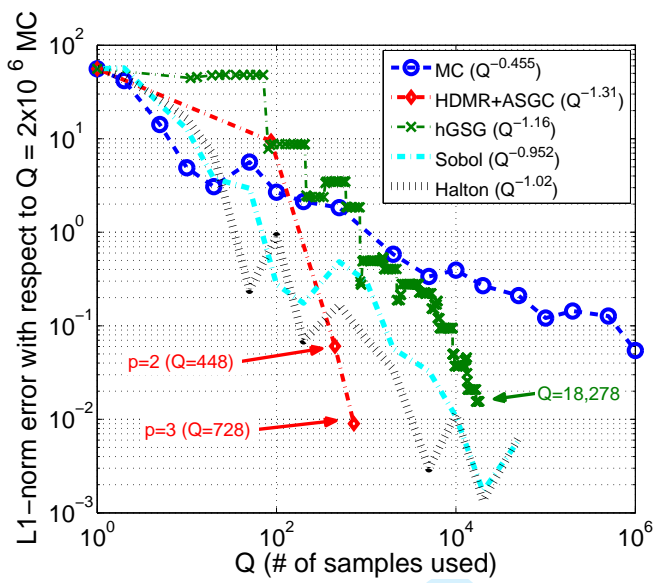


Fig. 11. Error convergence in Example 2 of Section III-B.

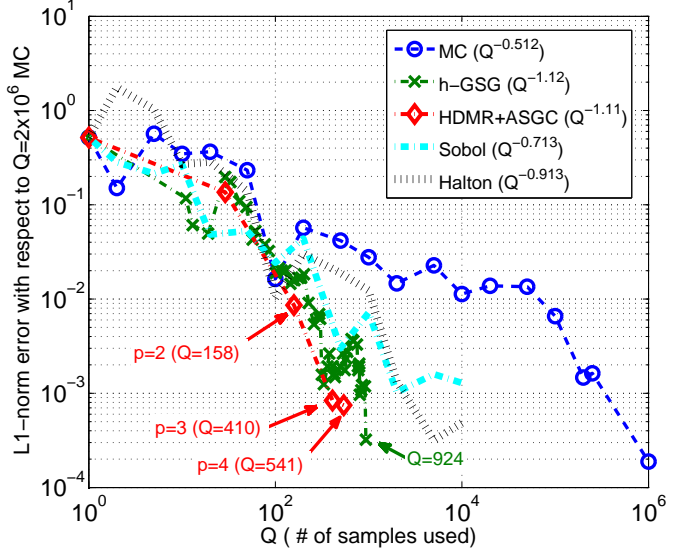
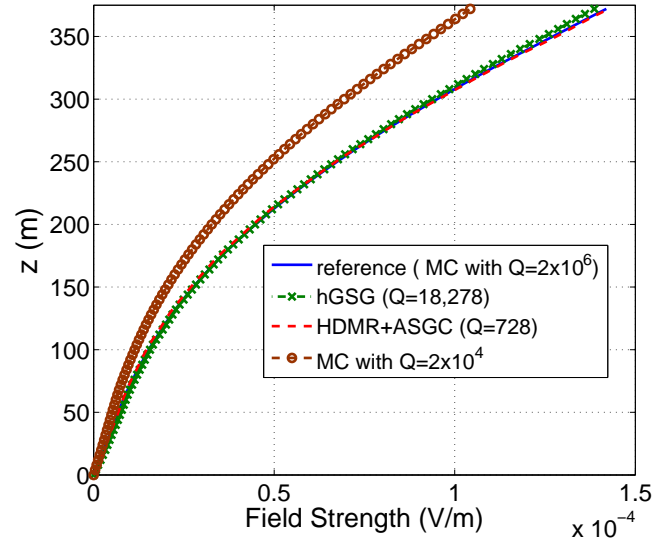
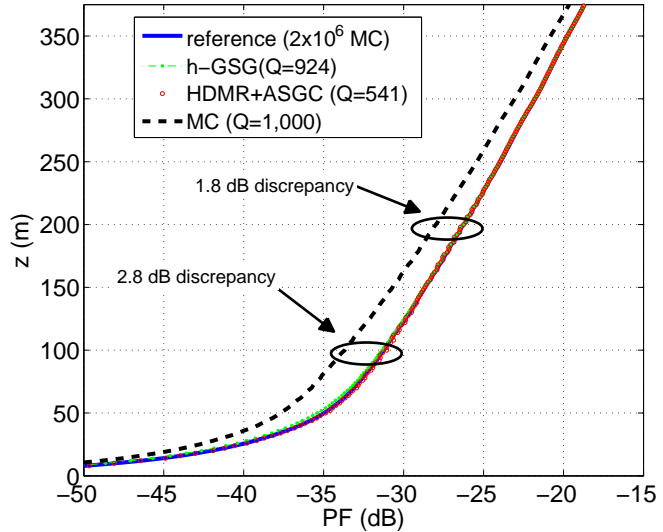


Fig. 13. Error convergence in Example 3 of Section III-B.

Fig. 12. Field estimates for Example 2, $|E[\psi(100\text{km}, z; y)]|$, corresponding to the convergence results in Figure 11.

same computational cost. In accordance with the discussion on time in Section III-A, comparison between Figures 9 and 15 reveals that total computation time is dominated by the number of samples the SSPE solver evaluates. Therefore, the computational cost other than that of evaluating the samples is minor. As the deterministic solver gets more time consuming, the extra cost incurred in sparse grids will be relatively less significant.

Fig. 14. Field estimates for Example 3, $|E[PF(150\text{km}, z; y)]|$, corresponding to the convergence results in Figure 13.

IV. CONCLUSIONS

We have considered two canonical examples for assessing the strength of the sparse grid methods in electromagnetic propagation environments. For the interface of dimensionality reduction method (HDMR) with the adaptive SGC (ASGC), HDMR+ASGC, we have introduced and used *CompAdmit*, which has a less conservative “component admission” rule than the original rule given in [29]. For *h*-GSG method, we have followed [32].

The first application, reflection from *K*-Slabs is a 1-D scat-

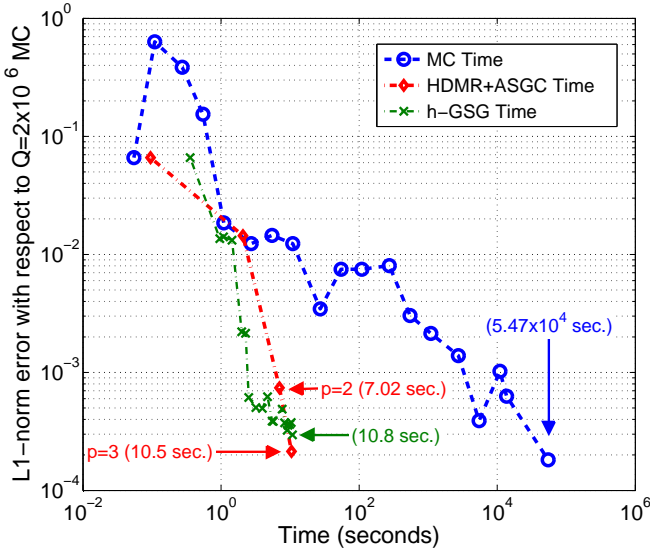


Fig. 15. Error convergence for MC sampling, h -GSG and HDMR+ASGC as a function of total elapsed time in seconds, for Example 1.

tering problem. Through this application we tested the SGC methods' performance with increasing dimensionality and statistical variation. The 100-dimensional example in Section III-A revealed strength of the h -GSG for problems where randomness is cast along certain axes of the random space.

In Section III-B, we considered a more realistic propagation problem with uncertainty, where randomness is represented in $d = 5$ RVs that constitute uncertain ducting phenomena in the lower troposphere. The RVs are extracted from published measured data, and represents randomness observed during a season-long atmospheric monitoring [46]. We have showed that both HDMR+ASGC and h -GSG offered much steeper convergence than the MC sampling and QMC methods in this problem. The advantage of using sparse grids were more significant in the case where the target function is the complex field, than is the PF (normalized power). The sparse grids have proven better convergence than MC sampling and QMC methods up to 150 km range.

Another application that is common in long-range propagation phenomena is the scattering from rough surfaces. A forward scattering approach in computing PF far from the transmitter location, whereas the randomness is in the generation of the randomly shaped perfectly conducting (PEC) surface, has conventionally been tackled with MC sampling [61], [63]. We have considered this application with sparse grids in [64]. There, due to highly non-smooth behavior in the random space and high- d feature of existing random surface generation tools, the sparse grid performances are poorer than that of QMC methods in general.

V. ACKNOWLEDGEMENT

This work was funded by the Army Research Office under grant W911NF-10-1-0305.

REFERENCES

- [1] A. Ishimaru, *Wave Propagation and Scattering in Random Media*. New York: IEEE Press, 1999.
- [2] J. Xu and R. Janaswamy, "Electromagnetic degrees of freedom in 2-d scattering environments," *IEEE Trans. on Antennas and Propagat.*, vol. 54, pp. 3882–3894, December 2006.
- [3] R. Wagner, J. Song, and C. W.C., "Monte Carlo simulation of electromagnetic scattering from two-dimensional random rough surfaces," *IEEE Trans. on Antennas and Propagat.*, vol. 45, pp. 235–245, February 1996.
- [4] P. Sumant, A. Cangellaris, and N. Aluru, "Reduced-order models of finite element approximations of electromagnetic devices exhibiting statistical variability," *IEEE Trans. Antennas Propagat.*, vol. 60, January 2012.
- [5] P. Sumant, H. Wu, A. Cangellaris, and N. Aluru, "A sparse grid based collocation method for model order reduction of finite element approximations of passive electromagnetic devices under uncertainty," (Anaheim, CA), pp. 1652–1655, 2010., IEEE Int. Microwave Symp. Digest, May 2010.
- [6] P. Li, F. Liu, X. Li, L. Pileggi, and S. Nassif, "Modeling interconnect variability using efficient parametric model order reduction," vol. 2, (Munich, Germany), Proc. of the Design, Automation and Test in Europe Conference and Exhibition (DATE05), May 2005.
- [7] S. Gangnus, S. Matcher, and I. Meglinski, "Monte Carlo modeling of polarized light propagation in biological tissues..." 2004.
- [8] Y.-G. Lv, Z.-S. Deng, and J. Liu, "3-d numerical study on the induced heating effects of embedded micro/nanoparticles on human body subject to external medical electromagnetic field," *NanoBioscience, IEEE Transactions on*, vol. 4, no. 4, pp. 284–294, 2005.
- [9] M. Franceschetti, "A random walk model of wave propagation," *IEEE Trans. on Antennas and Propagat.*, vol. 49, pp. 1304–1317, May 2004.
- [10] R. Janaswamy, "Transitional probabilities for the 4-state random walk on a lattice," *J. Phys. A: Math. Theor.*, vol. 41, p. 155306(11pp), 2008.
- [11] R. Dashen, "Path integrals for waves in random media," *J. Math. Phys.*, vol. 20, no. 894, pp. 894–920, 1979.
- [12] M. Loeve, *Probability Theory*. New Jersey: Van Nostrand, 1963.
- [13] G. Fishman, *Monte Carlo: Concepts, Algorithms and Applications*. New York: Springer, 1999.
- [14] C. Clark, "Importance sampling in Monte Carlo analyses," *Operations Research*, vol. 9, pp. 603–620, September-October 1961.
- [15] M. D. McKay, R. Beckman, and W. Conover, "A comparison of three methods for selecting values of input variables in the analysis of output from a computer code," *Technometrics*, vol. 21, pp. 239–245, May 1979.
- [16] M. Stein, "Large sample properties of simulations using latin hypercube sampling," *Technometrics*, vol. 29, pp. 143–151, May 1987.
- [17] F. Liang, C. Liu, and R. Carroll, *Advanced Markov Chain Monte Carlo Methods*. Chichester, West Sussex, U.K.: Wiley, 2010.
- [18] R. Schürer, "A comparison between (quasi-)Monte Carlo and cubature rule based methods for solving high-dimensional integration problems," *Mathematics and Computers in Simulation*, vol. 62, pp. 50–517, 2003.
- [19] I. Sobol, "On the distribution of points in a cube and the approximate evaluation of integrals," *USSR Comput. Math. Math. Phys.*, vol. 7, pp. 86–112, 1967.
- [20] J. Halton and G. Smith, "Radical-inverse quasi-random point sequence," *Communications of the ACM*, vol. 7, pp. 701–702, Dec. 1964.
- [21] D. Xiu and G. Karniadakis, "The Wiener-Askey polynomial chaos for stochastic differential equations," *SIAM J. Sci. Comput.*, vol. 24, no. 2, pp. 619–644, 2002.
- [22] D. Xiu and J. Hesthaven, "High-order collocation methods for differential equations with random inputs," *SIAM J. Sci. Comput.*, vol. 27, no. 3, pp. 1118–1139, 2005.
- [23] D. Xiu, "Fast numerical methods for stochastic computations: A review," *Commun. Comput. Phys.*, vol. 5, pp. 242–272, February 2009.
- [24] N. Wiener, "The homogeneous chaos," *Amer. J. Math.*, vol. 60, pp. 897–936, 1938.
- [25] E. Novak and K. Ritter, "High dimensional integration of smooth functions," *Numer. Math.*, vol. 75, pp. 79–97, 1996.
- [26] H. Rabitz and Ö. Alış, "General foundations of high-dimensional model representations," *J. Math. Chem.*, vol. 25, pp. 197–233, 1999.
- [27] H. Rabitz, Ö. Alış, J. Shorter, and K. Shim, "Efficient input-output model representations," *Computer Physics Communications*, vol. 117, pp. 11–20, 1999.
- [28] J. Foo and G. Karniadakis, "Multi-element probabilistic collocation method in high dimensions," *J. Comput. Phys.*, vol. 229, pp. 1536–1557, 2010.

- [29] X. Ma and N. Zabaras, "An adaptive high-dimensional stochastic model representation technique for the solution of stochastic partial differential equations," *J. Comput. Phys.*, vol. 229, pp. 3884–3915, 2010.
- [30] M. Griebel and M. Holtz, "Dimension-wise integration of high-dimensional functions with applications to finance," *J. Complexity*, vol. 26, pp. 455–489, 2010.
- [31] A. Yücel, H. Bağci, and E. Michielssen, "Efficient stochastic EMC/EMI analysis using HDMR-generated surrogate models," (Istanbul, Turkey), URSI General Assembly, 2011., August 2011.
- [32] J. D. Jakeman and S. G. Roberts, "Local and dimension adaptive stochastic collocation for uncertainty quantification," in *Sparse Grids and Applications*, pp. 181–203, Springer, 2013.
- [33] M. Levy, *Parabolic Equation Methods for Electromagnetic Wave Propagation*. London: IEE, 2000.
- [34] S. M. Babin, G. S. Young, and J. A. Carton, "A new model of the oceanic evaporation duct," *Journal of applied meteorology*, vol. 36, no. 3, pp. 193–204, 1997.
- [35] T. Tsuda, P. May, T. Sato, S. Kato, and S. Fukao, "Simultaneous observations of reflection echoes and refractive index gradient in the troposphere and lower stratosphere," *Radio science*, vol. 23, no. 4, pp. 655–665, 1988.
- [36] E. E. Gossard, "Refractive index variance and its height distribution in different air masses," *Radio Science*, vol. 12, no. 1, pp. 89–105, 1977.
- [37] A. Webster, "Raypath parameters in tropospheric multipath propagation," *Antennas and Propagation, IEEE Transactions on*, vol. 30, no. 4, pp. 796–800, 1982.
- [38] B. R. Bean and G. D. Thayer, "Models of the atmospheric radio refractive index," *Proceedings of the IRE*, pp. 740–755, May 1959.
- [39] G. D. Thayer, "An improved equation for the radio refractive index of air," *Radio Science*, vol. 9, no. 10, pp. 803–807, 1974.
- [40] C. Yardim, *Statistical estimation and tracking of refractivity from radar clutter*. PhD thesis, University of California, San Diego, La Jolla, CA, 2007.
- [41] C. Yardim, P. Gerstoft, and W. S. Hodgkiss, "Estimation of radio refractivity from radar clutter using Bayesian Monte Carlo analysis," *Antennas and Propagation, IEEE Transactions on*, vol. 54, no. 4, pp. 1318–1327, 2006.
- [42] C. Yardim, P. Gerstoft, and W. S. Hodgkiss, "Statistical maritime radar duct estimation using hybrid genetic algorithm–Markov chain Monte Carlo method," *Radio Science*, vol. 42, no. 3, 2007.
- [43] P. Valtr, P. Pechac, V. Kvicerá, and M. Grabner, "A terrestrial multiple-receiver radio link experiment at 10.7 GHz—comparisons of results with parabolic equation calculations," *Radioengineering*, vol. 19, no. 1, pp. 117–121, 2010.
- [44] O. Jicha, P. Pechac, V. Kvicerá, and M. Grabner, "On the uncertainty of refractivity height profile measurements," *Antennas and Wireless Propagation Letters, IEEE*, vol. 10, pp. 983–986, 2011.
- [45] O. Jicha, P. Pechac, V. Kvicerá, and M. Grabner, "Estimation of the radio refractivity gradient from diffraction loss measurements," 2013.
- [46] V. Zhurbenko, ed., *Electromagnetic Waves*. Shanghai: InTech, 2011.
- [47] P. Gerstoft, W. S. Hodgkiss, L. T. Rogers, and M. Jablecki, "Probability distribution of low-altitude propagation loss from radar sea clutter data," *Radio science*, vol. 39, no. 6, 2004.
- [48] S. Özbayat, *Techniques to Increase Computational Efficiency in Some Deterministic and Random Electromagnetic Propagation Problems*. PhD thesis, University of Massachusetts Amherst, Amherst, MA, 01003 USA, 2013.
- [49] S. Smolyak, "Quadrature and interpolation formulas for tensor products of certain classes of functions," *Soviet Math. Dokl.*, vol. 4, pp. 240–243, 1963.
- [50] H.-J. Bungartz and M. Griebel, "Sparse grids," *Acta numerica*, vol. 13, no. 1, pp. 147–269, 2004.
- [51] W. Klimke, *Uncertainty Modeling Using Fuzzy Arithmetic and Sparse Grids*. PhD thesis, Universität Stuttgart, Germany, 2006.
- [52] A. Klimke and B. Wohlmuth, "Algorithm 847: SPINTERP: Piecewise multilinear hierarchical sparse grid interpolation in matlab," *ACM Trans. Math. Software*, vol. 31, pp. 561–579, December 2005.
- [53] X. Ma and N. Zabaras, "An adaptive hierarchical sparse grid collocation algorithm for the solution of stochastic differential equations," *J. Comput. Phys.*, no. 228, pp. 3084–3113, 2009.
- [54] C. Clenshaw and A. Curtis, "A method for numerical integration on an automatic computer," *Numerische Mathematik*, vol. 2, pp. 197–205, 1960.
- [55] S. Sankaran and A. Marsden, "A stochastic collocation method for uncertainty quantification and propagation in cardiovascular simulations," *J. Biomech. Eng.*, vol. 133, no. 031001, 2011.
- [56] B. Ganapathysubramanian and N. Zabaras, "A stochastic multiscale framework for modeling flow through random heterogeneous porous media," *Journal of Computational Physics*, vol. 228, no. 2, pp. 591–618, 2009.
- [57] T. Gerstner and M. Griebel, "Dimension-adaptive tensor-product quadrature," *Computing*, vol. 71, no. 1, pp. 65–87, 2003.
- [58] B. Jacob and G. Guennebaud, *Eigen : C++ template library for linear algebra*. <http://eigen.tuxfamily.org/>, 3.1.1 ed.
- [59] C. Balanis, *Advanced Engineering Electromagnetics*. New York: Wiley, 1989.
- [60] J. R. Kuttler and G. D. Dockery, "Theoretical description of the parabolic approximation/Fourier split-step method of representing electromagnetic propagation in the troposphere," *Radio Science*, vol. 26, no. 2, pp. 381–393, 1991.
- [61] M. Motta, "Equivalent impedance of rough surface at low grazing angles," Master's thesis, Naval Postgraduate School, Monterey, CA, 1999.
- [62] R. Janaswamy, "Radio wave propagation over a nonconstant impedance plane," *Radio Sci.*, vol. 36, pp. 387–405, May-June 2001.
- [63] Z. Lai and R. Janaswamy, "Specular propagation over rough surfaces: numerical assessment of Uscinski and Staneks mean Greens function technique," *Waves in Random and Complex Media*, vol. 16, pp. 137–150, May 2006.
- [64] S. Özbayat and R. Janaswamy, "Quantification of high dimensional uncertainty in propagation over random terrain," (Orlando, FL), IEEE Symp. on Antennas and Propagat. 2013., July 2013.

On the EM Degrees of Freedom in Scattering Environments

Ramakrishna Janaswamy, *Fellow, IEEE*

Abstract—By considering the 2D problem of electrical line sources radiating in the presence of perfectly conducting cylinders and decomposing the real power flow on a circumscribing observation circle separating the transmit nodes from the receive nodes, simple formulas are derived for the electromagnetic degrees of freedom in scattering environments for a network of nodes communicating with each other. The locations, magnitudes, and phases of the line sources are assumed to be independent and identically distributed (i.i.d.) random variables. Similarly, the locations of the scatterers in the region outside the observation circle are assumed to be i.i.d. random variables. The exact scattering problem is cast in the form of an integral equation, where the Fourier coefficients of the scatter current density are the unknowns. Based on the Born approximation that is valid for mild scatter densities and asymptotic analysis, a closed form expression is derived for the number of degrees of freedom in scattering environments. The benefit of observing near-fields in the determination of degrees of freedom is included in the numerical examples considered. If the power per source and/or the number of sources within the circumscribing circle are made to increase algebraically with the size of the circle, it is shown that scattering environments can offer much higher degrees of freedom than what are available in free-space.

Index Terms—Born approximation, electromagnetic degrees of freedom, electromagnetic scattering, integral equations, random discrete scatterers.

I. INTRODUCTION

OVER the last few decades, wireless systems have pervaded many areas including consumer electronics, military electronics systems, electronic health systems, navigational systems, imaging systems, electro-optical systems etc., to name a few. In the area of wireless communications, the focus has been shifting steadily from a point-point based system to systems comprised of distributed, communicating nodes. AdHoc [1], body area [2], [3], and cognitive wireless networks [4] have thus evolved over the last few years. In the efficient design of many of these systems, it becomes imperative to understand the intrinsic limits set by the sizes of radiating and receiving volumes, distribution of nodes and the architecture of system in the case of wireless networks, the electromagnetic environment in which the systems operate, the inevitable noise present in the detecting systems, etc. This leads one to the notion of degrees

Manuscript received October 18, 2010; revised March 14, 2011; accepted April 04, 2011. Date of publication August 04, 2011; date of current version October 05, 2011. This work was funded in part by the Army Research Office under Grant ARO W911NF-10-1-0305.

The author is with the Department of Electrical & Computer Engineering, University of Massachusetts, Amherst, MA 01003 USA (e-mail: janaswamy@ecs.umass.edu).

Digital Object Identifier 10.1109/TAP.2011.2163776

of freedom (DOF), whose study has been undertaken by many researchers in the past. Qualitatively, the number of independent parameters needed to represent the output field or signal within a given precision is known as DOF.

One of the earliest investigations on the degrees of freedom was carried out by Toraldo di Francia [5], who showed that the number of degrees of freedom (NDOF) that are available in an optical image formed by any real instrument is finite even if that contained in the object is infinite; further the NDOF along each spatial direction for monochromatic or incoherent images detected by *far-field* receivers subject to limited aperture is proportional to the product of the numerical aperture and the spatial extent of the object, a result that is known as diffraction limit in optics. The spatial bandwidth of scattered electromagnetic fields introduced by Bucci and Franceschetti [6] is proportional to the DOF. In a series of papers [7], [8], Bucci and coworkers showed that the electromagnetic field radiated or scattered by bounded sources can be represented over a substantially arbitrary surface by a finite number of samples even when the observation domain is unbounded. Treating the optical system as a communication system where electromagnetic waves communicate in a three-dimensional space, Piestun and Miller [9] and Miller [10] showed that the optimum transmitting and receiving functions and the NDOF are solutions of well-defined eigenvalue equations.

With the advent of multiple-input multiple-output (MIMO) wireless communication systems [11], [12], there has been a renewed interest in the notion of DOF. The issue of interest there is how the system capacity scales under rich multipath scattering with the number of elements under a variety of constraints: fixed transmitting and receiving volumes, fixed amount of scattering, fixed signal to noise ratio (SNR), fixed transmit power, etc. The answer to these questions is intimately tied to the available NDOF of the MIMO system and has been studied by a number of authors. Poon, *et al.* [13], [14] evaluated the effective degrees of freedom (EDOF) for clustered scattering environments, where the space between the transmit array and receive array of a MIMO system is partially filled with scattering clusters. They showed that the number of spatial degrees of freedom is equal to the product of angular spread as seen from a far-zone receive array and the electrical size of the array; a result reminiscent of the earlier result obtained by Toraldo di Francia. Migliore [15] related these EDOF to the NDOF of the electromagnetic field itself. Using a plane-wave representation of receiving multipath fields, Kennedy, *et al.* [16] show the familiar result that the degrees of freedom in 2-D spatial regions is linearly proportional to the size of the circle that circumscribes the receive array. In order to study the dependence of the DOF on the amount of scattering present, Xu and Janaswamy [17]

studied the full-wave electromagnetic problem having fixed size transmit and receive antennas in the presence of an intervening scatter cluster. Their simulation results indicate that the DOF number generally increases with both the transmit volume and the receive volume before it saturates. The scattering environment together with the sizes of the transmit and receive antenna volumes were shown to be the key factors that influence the DOF number.

In wireless networks, it is of interest to know how the system throughput scales with the number of nodes N_i as $N_i \rightarrow \infty$ [18], [19]. A number of studies have been conducted lately in this regard [20]–[23]. Ozgur, *et al.* considered both dense networks (node density increases with the number of nodes) and extended networks (coverage area increases with the number of nodes) and obtained scaling law results for information-theoretic capacity by considering a particular fading model and a non-free-space path loss model. Their results were built upon those of Xie and Kumar [20], [21] and Xue and Kumar [24]. However, Franceschetti *et al.* [23] considered an extended wireless network with N_i users located within a ball of radius proportional to $\sqrt{N_i}$ and communicating with an equal number of exterior users. They showed that the capacity scaling for $N_i \rightarrow \infty$ is subject to a fundamental limitation that is independent of power attenuation and fading models; instead, it was the electromagnetic degrees of freedom that determine the scaling laws.

Subsequent research [25] has also recognized the importance of NDOF in determining the throughput capacity of wireless networks. It is clear from [26] that the degrees of freedom also play a central role in determining the capacity of cognitive networks. What is not clear from many of these later studies is whether the degrees of freedom, as measured by the significant number of modes present on a closed observation surface separating the transmit nodes from the receive ones, depend on scatterers present *outside* it. The asymptotic studies carried out in [23] for $N_i \rightarrow \infty$ assume that they do not. While, the asymptotic results of [20] and [23] yield the order magnitude behavior for the DOF, they are not very useful when applied to the practical case of small sized networks. Further, they shed no light on the proportionality constant, which could be an important parameter in an actual system design. There is reason to believe that external scatterers, acting as secondary sources of radiation and causing back-scattering, can redistribute power in the available modes and consequently change the NDOF. Furthermore, the benefits provided by observing the *near-fields* [27] must be included in any estimation of the degrees of freedom.

The main purpose of the present paper is to examine whether scatterers external to the closed observation surface separating the transmit and receive nodes play any role in the determination of the degrees of freedom. We demonstrate by considering 2D situation with line sources and perfectly conducting circular cylinders that external scatterers actually provide opportunities for significantly increasing the NDOF over what are possible in free-space. The electrical size of the problem for conducting the initial exact numerical studies to validate the Born approximation employed later in the paper is chosen based on computational constraints and may/may-not necessarily correspond to a physical wireless network. Nevertheless, despite this short-

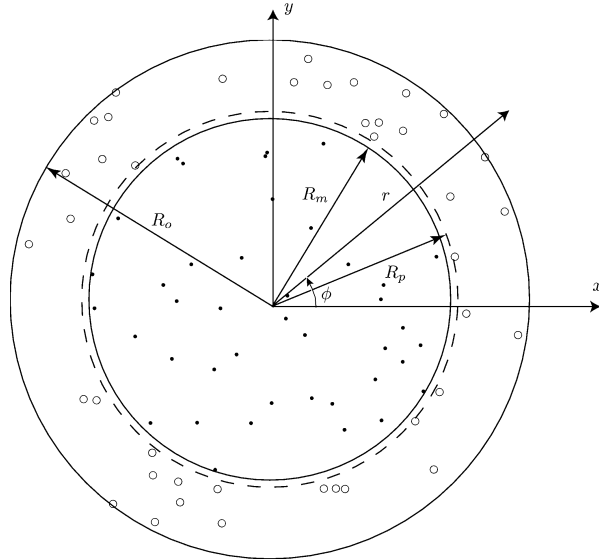


Fig. 1. Sources randomly located within an circle of radius $r \leq R_m$ and scatterers located in the annular region $R_p \leq r \leq R_o$. The buffer layer $R_m < r < R_p$ is of fixed thickness $\Delta \ll b$ and is free of scatterers and sources. The observation circle has radius $b = (R_m + R_p)/2 \approx R_m$.

coming, we believe that the role of external scatterers as delineated in the present paper and the Born-approximation analytical results presented do carry-over to an actual network. It may be noted that the scatterers present inside the surface need not be accounted for separately as they are equivalent to secondary interior sources that behave similar to primary interior sources. The connection between the NDOF and the wireless system capacity is established in a number of works (see [23] and [22], for example) and will not be pursued here.

II. THEORY

Fig. 1 shows N_i electric current sources (will also be referred to as nodes or users) randomly distributed within a circular region of radius R_m . The usual cylindrical coordinates (\mathbf{r}, z) are employed in the paper, where $\mathbf{r} = (r, \phi)$ denotes the polar coordinates in the plane. It is assumed that these nodes are communicating with some exterior nodes and the wireless links between them intersect the imaginary surface $r = b > R_m$. Together, all of these nodes constitute a wireless network. One of the key system performance metrics is the network throughput capacity between the interior and exterior cluster of users, which depends on the NDOF observed on the surface $r = b$ [23].

The magnitude α_n and the phase β_n , $n = 1, 2, \dots, N_i$ of the individual node source currents $I_n = \alpha_n e^{j\beta_n}$ are assumed to be independent and identically distributed random variables. In particular, we assume that β_n are uniformly distributed in the range $(0, 2\pi)$ and that the magnitudes are restricted by $\langle \alpha_n^2 \rangle = 2P_o/\eta_0$, where angle brackets denote expectation, η_0 is the intrinsic impedance of free-space, and P_o is the power per node. Upper bounding the mean square current magnitude of these individual line sources automatically prevents the excitation of antenna superdirectivity, an issue whose importance was also underscored in the studies of [28] and [23]. Perfectly conducting scatterers, each of radius a and Q in number, are assumed to be randomly located in the annular region $R_p \leq r \leq R_o$. A

thin buffer layer $R_m < r < R_p$ of vanishing thickness excludes sources and scatterers. The fields are observed on the circle with radius $b = (R_p + R_m)/2 \approx R_m$ within this buffer layer. The scatterers are assumed to be uniformly distributed in space and their locations are assumed independent of each other. The fractional area density of scatterers, ρ_a , is given by $\rho_a = Qa^2/(R_o^2 - R_p^2)$. The assumptions on independent scatter position make sense provided that the area density is low enough. Otherwise the statistics will be governed by the pair-distribution functions [29], [30].

The observation circle $r = b$ corresponds to the cut-set or simply the cut that divides the communicating region into two parts—the source region and the destination region. According to the *Max-Flow-Min-Cut* bound theorem [31], [20], the total rates achievable from the nodes in the source set to those in the destination set depends on the mutual information or distribution of power observed on the cut. This result has been used in [23] in determining the degrees of freedom and we will also determine the degrees of freedom by observing the power flow on the cut. As stated previously, it is not necessary to include scatterers in the region $r \leq R_m$ as these will tantamount to secondary sources whose influence on NDOF will be the same as the primary source currents.

The assumed sources generate a TM_z wave comprised of the field (E_z, H_r, H_ϕ) . We will be concerned with the normal component of the Poynting vector on the observation circle, which will depend only on the field components (E_z, H_ϕ) ; we will consequently relabel these as simply (E, H) . A time harmonic variation of the form $e^{j\omega\tau}$, where ω is the radian frequency and τ is the time variable is assumed of all source and field quantities. The wavenumber in free-space is denoted by k_0 and the location of the n th source is denoted by $\mathbf{r}_n = (r_n, \phi_n)$. The total incident field (E_i, H_i) caused by all of the interior sources acting in free-space is given by

$$E_i(\mathbf{r}) = -\frac{k_0\eta_0}{4} \sum_{n=1}^{N_i} I_n H_0^{(2)}(k_0|\mathbf{r} - \mathbf{r}_n|) \quad (1)$$

where $H_m^{(2)}(x)$ is the Hankel function of second kind of order m and argument x . Using the addition theorem for Hankel functions [32], the incident field could be decomposed in terms of orthogonal modes on any observation circle of radius $r > R_m$ as

$$E_i = \frac{-k_0\eta_0}{4} \sum_{n=1}^{N_i} I_n \sum_{m=-\infty}^{\infty} H_m^{(2)}(k_0r) J_m(k_0r_n) e^{jm(\phi - \phi_n)} \quad (2)$$

where $J_m(x)$ is the Bessel function of the first kind of order m and argument x . The magnetic field $H_i = (jk_0\eta_0)^{-1} \partial E_i / \partial r$ is similarly given by

$$H_i = \frac{jk_0}{4} \sum_{n=1}^{N_i} I_n \sum_{m=-\infty}^{\infty} H_m^{(2)'}(k_0r) J_m(k_0r_n) e^{jm(\phi - \phi_n)} \quad (3)$$

where the superscript prime denotes differentiation with respect to the argument. Each term with a fixed m in the above summa-

tions will represent an orthogonal mode, in terms of which the fields are expanded. The mode impedance (ratio of the mode electric field to the mode magnetic field) for the interior source is a complex quantity of the form $j\eta_0 H_m^{(2)}(k_0r)/H_m^{(2)'}(k_0r) \sim \eta_0$, as $r \rightarrow \infty$. The real part of the average power flow $P_t = \Re\langle -E_i H_i^* \rangle$, [Watts/m²], where the expectation is performed with respect to all random variables (locations, magnitudes and phases of sources), $\Re(z)$ denotes the real part of z , and superscript * denotes complex conjugation, can be readily obtained by using the Wronskian property of the Bessel functions $H_m^{(2)'}(x)J_m(x) - H_m^{(2)}(x)J_m'(x) = -2j/\pi x$ [32], the expectation result $\langle e^{j(\beta_n - \beta_m)} \rangle = \delta_m^n$, where δ_m^n is the Kronecker's delta, and the identity $\sum_{m=-\infty}^{\infty} J_m^2(x) = 1$, as

$$P_t = \frac{k_0 P_o(b)}{4\pi b} \sum_{n=1}^{N_i} \sum_{m=-\infty}^{\infty} \langle J_m^2(k_0r_n) \rangle \\ := \sum_{m=-\infty}^{\infty} P_m^i = \frac{k_0 N_i P_o(b)}{4\pi b}. \quad (4)$$

The argument b is included in P_o to indicate the possibility that the power per node can depend on the radius b separating the interior sources from the exterior ones. The quantity P_m^i is the power carried by the m th mode in free-space due to all of the interior nodes and will appear later in the asymptotic analysis. As expected, P_t decays with distance in free-space as $O(1/b)$ when $P_0(b)$ is a constant.

In the presence of scatterers, we express the total field as $(E, H) = (E_i, H_i) + (E_s, H_s)$, where the scattered field (E_s, H_s) is set up by the currents \mathbf{J}_s induced on the surface of the scattering objects. For the TM_z polarization, the induced currents are in the z -direction, *viz.*, $\mathbf{J}_s = \mathbf{z}J_s$. The scattered electric field is related to the surface current densities through [33]

$$E_s(\mathbf{r}) = \frac{-k_0\eta_0}{4} \sum_{q=1}^Q \int_{\Gamma_q} J_s(\mathbf{r}_q) H_0^{(2)}(k_0|\mathbf{r} - \mathbf{r}_q|) d\gamma_q \quad (5)$$

where Γ_q denotes the surface of the q th cylinder and \mathbf{r}_q denotes a point on it. To determine the surface current densities, we set up an electric field integral equation by requiring that the total field on the p th cylindrical surface be identically zero: $E(\mathbf{r}_p) = E_i(\mathbf{r}_p) + E_s(\mathbf{r}_p) = 0, p = 1, 2, \dots, Q$. For circular cylinders, it is convenient to expand the surface currents in a finite Fourier series of the form

$$J_s(\mathbf{r}_q) \simeq \frac{1}{2\pi a} \sum_{\ell=-L}^L K_\ell^{(q)} e^{j\ell\vartheta_q} \quad (6)$$

where ϑ_q denotes the polar angle on the q th cylinder with respect to a coordinate system erected at its center and $K_\ell^{(q)}$ [Amps], $q = 1, 2, \dots, Q, \ell = -L, \dots, L$ are the unknown current coefficients to be solved. The total number $L_0 = (2L+1)$ of Fourier modes required to accurately represent the current on a cylinder depends on its electrical size k_0a . For a circular cylinder excited by a plane wave or a line source, the mode coefficients decay as $J_\ell(k_0a)/H_\ell^{(2)}(k_0a)$ [33]. For example, with $k_0a = 0.1$, $|K_1^{(q)}/K_0^{(q)}| \simeq 1.42 \times 10^{-2}$ and it may be sufficient to use $L =$

0. A good rule of thumb is to use $L = \max(0, \lfloor 5k_0a - 0.5 \rfloor)$, where $\lfloor x \rfloor$ denotes nearest integer value of x . If the coordinates of the observation point with respect to the center of the q th cylinder are (τ_q, ξ_q) , substitution of (6) in (5) together with the addition theorem for Bessel functions results in

$$E_s = \frac{-k_0\eta_0}{4} \sum_{q=1}^Q \sum_{\ell=-L}^L K_\ell^{(q)} J_\ell(k_0a) H_\ell^{(2)}(k_0\tau_q) e^{j\ell\xi_q}. \quad (7)$$

To set up the integral equation, it is necessary to express the coordinates (τ_q, ξ_q) in terms of the centralized coordinates (r, ϕ) and the coordinates of the center of each cylinder. To accomplish this, the addition theorem is once again invoked for the function $H_\ell^{(2)}(k_0\tau_q)$. The orthogonal expansion of (6) enables the enforcement of the boundary condition $E = 0$ on the surface of each cylinder on a mode by mode basis. When these steps are carried out, the following linear equations for the unknowns $K_\ell^{(q)}$ are obtained:

$$\begin{aligned} & K_{\ell'}^{(q)} H_{\ell'}^{(2)}(k_0a) + \sum_{\substack{p=1 \\ p \neq q}}^Q \sum_{\ell=-L}^L K_\ell^{(p)} J_\ell(k_0a) e^{j(\ell-\ell')\beta_{qp}} \\ & \times H_{\ell-\ell'}^{(2)}(k_0r_{pq}) \\ & = - \sum_{n=1}^{N_u} I_n H_{\ell'}^{(2)}(k_0R_{nq}) e^{-j\ell'\gamma_{nq}} \\ & q = 1, 2, \dots, Q, \ell' = -L, \dots, L \end{aligned} \quad (8)$$

where r_{pq} is the distance between the centers of the p th and q th cylinders, β_{qp} is the polar angle of the center of q th cylinder with respect to the center of the p th cylinder, R_{nq} is the distance between the n th line source and the center of the q th cylinder, and γ_{nq} is the polar angle of the n th line source with respect to the center of the q th cylinder. Equation (8) is a system of $N_u = L_0 Q$ equations for the N_u unknowns $K_{\ell'}^{(q)}$. The first term on the left hand side of (8) arises from the scattering of incident waves by the q th cylinder and the double summations terms arise from the multiple scattering of waves by other cylinders. Equation (8) constitutes what we call as the *full-wave* case and determination of the unknowns will involve inverting an $N_u \times N_u$ matrix. Denoting $\mathbf{K} = [K_{-L}^{(1)}, K_{-L+1}^{(1)}, \dots, K_L^{(1)}, K_{-L}^{(2)}, K_{-L+1}^{(2)}, \dots, K_L^{(2)}, \dots, K_{-L}^{(Q)}, K_{-L+1}^{(Q)}, \dots, K_L^{(Q)}]^t$, where the superscript ‘ t ’ denotes matrix transpose, $\mathbf{V} = V_{-L}^{(1)}, V_{-L+1}^{(1)}, \dots, V_L^{(1)}, V_{-L}^{(2)}, V_{-L+1}^{(2)}, \dots, V_L^{(2)}, \dots, V_{-L}^{(Q)}, V_{-L+1}^{(Q)}, \dots, V_L^{(Q)}]^t$, where

$$V_\ell^{(q)} = - \sum_{n=1}^{N_u} I_n H_\ell^{(2)}(k_0R_{nq}) e^{-j\ell\gamma_{nq}} \quad (9)$$

Equation (8) can be cast in the form of a matrix equation

$$\mathbf{K} = \mathbf{Y}\mathbf{V} \quad (10)$$

where the elements of the admittance matrix \mathbf{Y} will only depend on the location and electrical size of the scatterers, and the order ℓ of the current expansion. For subsequent analysis, it is convenient to express the quantity \mathbf{V} as $\mathbf{V} = \mathbf{U}\mathbf{I}$, where the matrix element of \mathbf{U} is

$$U_{tn} = -H_\ell^{(2)}(k_0R_{nq}) e^{-j\ell\gamma_{nq}} \quad (11)$$

with the single index

$$t = qL_0 - L + \ell, \quad t = 1, 2, \dots, N_u \quad (12)$$

taking the place of the pair (q, ℓ) and $\mathbf{I} = [I_1, I_2, \dots, I_{N_u}]^t$ is the vector of source currents.

When the density of scatterers ρ_a is low enough, the multiple scattering terms in (8) can be ignored and an explicit solution for the unknowns is possible:

$$K_\ell^{(q)} \approx \frac{1}{H_\ell^{(2)}(k_0a)} \sum_{n=1}^{N_u} I_n U_{tn}. \quad (13)$$

This is known as the *Born approximation* [34] and is extremely useful in getting physical insight into the role of various scattering parameters as will be demonstrated shortly. If, in addition, the cylinders are electrically small ($k_0a \ll 1$), only the $\ell = 0$ term is significant.

If the coordinates of the center of the q th cylinder are denoted by (μ_q, θ_q) , the scattered fields at any point $\mathbf{r} = (r < \mu_q, \phi)$, after a recourse to the addition theorem, are given by

$$\begin{aligned} E_s(\mathbf{r}) &= \frac{-k_0\eta_0}{4} \sum_{q=1}^Q \sum_{\ell=-L}^L K_\ell^{(q)} e^{j\ell\theta_q} J_\ell(k_0a) \\ &\times \sum_{m=-\infty}^{\infty} H_{m-\ell}^{(2)}(k_0\mu_q) J_m(k_0r) e^{jm(\phi-\theta_q)} \end{aligned} \quad (14)$$

$$\begin{aligned} H_s(\mathbf{r}) &= \frac{jk_0}{4} \sum_{q=1}^Q \sum_{\ell=-L}^L K_\ell^{(q)} e^{j\ell\theta_q} J_\ell(k_0a) \\ &\times \sum_{m=-\infty}^{\infty} H_{m-\ell}^{(2)}(k_0\mu_q) J'_m(k_0r) e^{jm(\phi-\theta_q)}. \end{aligned} \quad (15)$$

It is seen that for the exterior (actual or induced) sources, the mode impedance E_m^s/H_m^s is $j\eta_0 J_m(k_0r)/J'_m(k_0r)$, which is always purely imaginary. The induced sources due to exterior scatterers will not contribute to real power flow on the observation circle $r = b$. But the interference of incident and scattered fields can contribute to real power flow as the next section shows.

A. Power Flow in Orthogonal Modes

In [28] and [23], the authors performed a singular value decomposition of the fields on the observation surface assuming volume current densities of sources that belong to the \mathcal{L}_2 (square integrable function) space. However, as shown in [35], [36], requiring the field intensities to belong to the \mathcal{L}_2 space (so that energy in a finite space is finite) does not imply that the current densities belong to this space. Simple counter examples are singular point sources and surface current densities on perfectly conducting surfaces. Instead, we will look at the real power carried by orthogonal modes on the observational surface, which will then take the place of singular values in the study of [23].

Even though real part of Poynting vector is used here, the important contribution of near fields is manifest through the inherent coupling present between the incident and scattered fields. The power, P_m , carried by the m th orthogonal mode on the observation circle $r = b$ is defined as $\Re[\langle -E_m(b)H_m^*(b) \rangle]$, where (E_m, H_m) is the total field contained in the m th mode. The incident and scattered fields in the m th mode are given in (2), (3) and (14), (15). As already indicated in (4), the contribution of the line sources in free-space to P_m is denoted by P_m^i and equals

$$P_m^i = P_t \langle J_m^2(k_0 r_n) \rangle. \quad (16)$$

Using (14) and (15) for the scattered fields and carrying out some algebraic manipulations, the power P_m can be expressed as

$$P_m = P_m^i + \frac{k_0 \eta_0}{8\pi b} \sum_{q=1}^Q \sum_{\ell=-L}^L \sum_{n=1}^{N_i} \Re \left\langle I_n K_\ell^{(q)*} e^{j(m-\ell)\theta_q} \times e^{-jm\phi_n} J_\ell(k_0 a) J_m(k_0 r_n) H_{m-\ell}^{(1)}(k_0 \mu_q) \right\rangle. \quad (17)$$

As stated in the previous subsection, the scattered fields alone yield reactive power on the circle $r = b$ and do not contribute to P_m . The additional terms contained in (17) are due to the interaction of the scattered field with the incident field and depend on the non-zero correlation between the source currents I_n and the induced scattering currents $K_\ell^{(q)}$. If the induced currents $K_\ell^{(q)}$ were replaced with primary source currents $I_k^{(e)}$, $k = 1, 2, \dots$, of exterior users that are *statistically uncorrelated* to I_n , one would get a value of zero, as expected, for the additional terms in (17), resulting in $P_m = P_m^i$. Hence uncorrelated exterior sources do not contribute to the power flow on the observation surface.

Averages with respect to the fluctuations in the source currents in (17) can be performed by invoking (10). Carrying out the expectations with respect to the magnitude, phase and location of source currents and simplifying, the following exact expression is obtained for the power carried by the m th mode on $r = b$:

$$P_m = P_m^i \left[1 - \sum_t \sum_{t'} \Re \left\langle Y_{tt'}^* e^{j[(m-\ell)\theta_q - (m-\ell')\theta_{q'}]} \times J_\ell(k_0 a) H_{m-\ell}^{(1)}(k_0 \mu_q) H_{m-\ell'}^{(1)}(k_0 \mu_{q'}) \right\rangle \right] \quad (18)$$

where the indices t and t' are defined as in (12). Thus the power P_m depends in a highly non-linear fashion on the source and scatter coordinates. Also, the exact solution needs the inversion of the linear equations given in (8) to obtain the admittance matrix \mathbf{Y} .

Under the Born approximation, it is clear from (13) that $Y_{tt'} = \delta_{tt'}^s / H_\ell^{(2)}(k_0 a)$, a result that is independent of the scatterer q . Furthermore, because the position distribution of all scatterers is assumed identical, the averaging in (18) needs to be done only for one typical cylinder. In that case one gets

$$P_m \approx P_m^i \left[1 - \Re \sum_{\ell=-L}^L \frac{Q J_\ell(k_0 a)}{H_\ell^{(1)}(k_0 a)} \left\langle \left(H_{m-\ell}^{(1)}(k_0 \mu_q) \right)^2 \right\rangle \right]. \quad (19)$$

As expected, the Born approximation result (19) is independent of the scatterer azimuthal position θ_q . If, in addition to mild scattering, the scatterer radius $k_0 a \ll 1$, then only the $\ell = 0$ Fourier mode on the scatterer is significant and one gets the simpler expression

$$P_m \approx P_m^i \left[1 - \Re \left(\frac{Q J_0(k_0 a)}{H_0^{(1)}(k_0 a)} \left\langle \left(H_m^{(1)}(k_0 \mu_q) \right)^2 \right\rangle \right) \right]. \quad (20)$$

The averages present in (16) and (19) can be evaluated in a closed form for a uniform distribution of sources and scatterers. The probability density function in the radial position for a uniform distribution of a point in the annular region $r_1 \leq r \leq r_2$ is $p(r) = 2\pi r/A$, where $A = \pi(r_2^2 - r_1^2)$ is the area of the annular region. The averages can be evaluated using the identity [37]

$$\langle \mathcal{Z}_m^2 \rangle = \frac{2\pi}{A} \int r \mathcal{Z}_m^2(r) dr \quad (21)$$

$$= \frac{\pi r^2}{A} [\mathcal{Z}_m^2(r) - \mathcal{Z}_{m-1}(r) \mathcal{Z}_{m+1}(r)] \quad (22)$$

where $\mathcal{Z}_m(r)$ is any integer ordered Bessel function.

B. Asymptotic Analysis

Expressions (20), (19), and (18) are valid for any order m . To estimate the DOFs in free-space and in scattering environments and for effectively evaluating these expressions for large m , it is necessary, however, to carry out an asymptotic analysis valid for large m . For fixed argument and large orders with $m > z$, we employ the following asymptotic formulas for the Bessel functions [32]

$$H_m^{(1)}(z) \sim i Y_m(z) \sim -i \sqrt{\frac{2}{\pi m}} \left(\frac{2m}{ez} \right)^m \quad (23)$$

$$J_m(z) \sim \sqrt{\frac{1}{2\pi m}} \left(\frac{ez}{2m} \right)^m. \quad (24)$$

Using these in (16), (20), and (21) we get

$$P_m^i \sim \frac{P_t}{2\pi m(m+1)} \left(\frac{ex_1}{2m} \right)^{2m} \quad (25)$$

$$\left\langle \left[H_m^{(1)}(k_0 \mu_q) \right]^2 \right\rangle \sim -\frac{2x_2^2}{m(m-1)A_s} \left(\frac{2m}{ex_2} \right)^{2m} \times \left[1 - \left(\frac{R_p}{R_o} \right)^{2(m-1)} \right] \quad (26)$$

where $x_1 = k_0 R_m$, $x_2 = k_0 R_p$, $x_3 = k_0 R_o$, $A_s = \pi(x_3^2 - x_2^2)$. It is clear from (25) that for large m , the power carried by the m th mode in free-space decays faster than any exponential. For

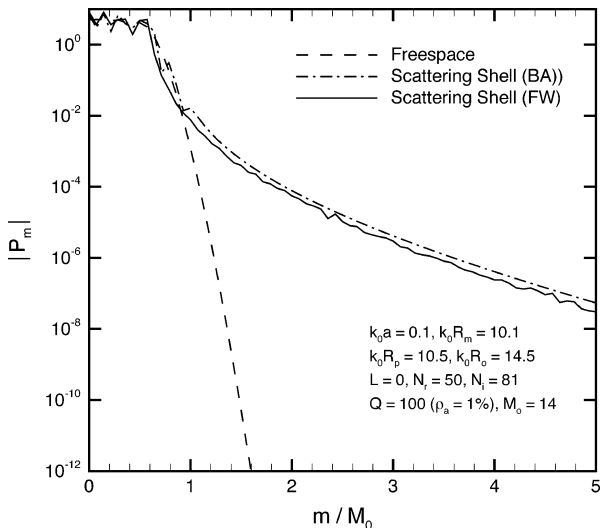


Fig. 2. Power contained in the orthogonal modes versus mode number.

electrically small scatterers operating under low scatter density (i.e., under the Born approximation), (20) and (26) give

$$\begin{aligned} P_m &\sim \frac{P_t \gamma \rho_a}{(\pi m k_0 a)^2 (m^2 - 1)} \left(\frac{R_m}{R_p} \right)^{2m}, \quad m > x_3 \\ &\sim \frac{P_t \gamma \rho_a}{(\pi m^2 k_0 a)^2}, \quad m > x_3 \end{aligned} \quad (27)$$

where we have assumed in the latter that $x_3 \gg 1$, $R_m/R_p \approx 1$, and set $\gamma = J_0^2(k_0 a)/|H_0^{(1)}(k_0 a)|^2$. Hence in the presence of scatterers, it is seen that the higher-order mode power decays only algebraically. This will have a direct bearing on the NDOF as we will see shortly.

The NDOF is defined as the smallest number of modes M such that the power P_ϵ contained in the tail from $[M+1, \infty)$ is a small fraction of the total power P_t contained in all of the modes. Such a *self-referral* definition for NDOF avoids direct comparison of received power with noise and yields the same value, irrespective of pathloss, at any range $r > b$, as long as the fractional power is kept constant above some threshold. Of course the threshold chosen will depend on noise power. The power contained in the tail in free-space, P_ϵ^i , and in the presence of scattering, P_ϵ , can be evaluated in a closed form using (25) and (27) and are obtained as

$$P_\epsilon^i = 2 \sum_{M+1}^{\infty} P_m^i < \frac{P_t}{\pi(M^2 - M_o^2)} \left(\frac{M_o}{M} \right)^{2(M+1)} \quad (28)$$

$$\begin{aligned} P_\epsilon &= 2 \sum_{M+1}^{\infty} P_m \\ &= \frac{P_t \gamma \rho_a}{3} \left(\frac{2M_o}{\pi e k_0 a} \right)^2 \psi^{(3)}(M+1) \\ &\sim \frac{2P_t \gamma \rho_a}{3M_o} \left(\frac{2}{\pi e k_0 a} \right)^2 \left(\frac{M_o}{M} \right)^3 \end{aligned} \quad (29)$$

where the factor of 2 is included to add the contribution from negative indices, $\psi^{(3)}(z)$ is the polygamma function [32], and $M_o = \lceil e k_0 b / 2 \rceil \sim \lceil e k_0 R_m / 2 \rceil$. The inequality in (28) follows from the fact that [38]

$$\begin{aligned} \sum_{m=M+1}^{\infty} \left(\frac{M_o}{m} \right)^{2m} \frac{1}{m(m+1)} &< \sum_{m=M+1}^{\infty} \left(\frac{M_o}{M} \right)^{2m} \frac{1}{m^2} \\ &\sim \frac{(M_o/M)^{2(M+1)}}{M^2 - M_o^2}. \end{aligned} \quad (30)$$

It is seen that the fractional power contained in the tail of the orthogonal modes decays faster than any exponential in free-space, but only algebraically in the presence of scattering. Also, under Born approximation, the power P_ϵ is linearly proportional to the area density ρ_a of scatterers. The power P_t is proportional to the product of N_i and P_o (see (4)) and will grow at least quadratically with M_o for an extended network. For a given error power density P_ϵ , (29) may be inverted to yield an expression for the degrees of freedom M

$$\frac{M}{M_o} = \frac{1}{\pi} \left[\frac{k_0^2 \gamma \rho_a N_i(M_o) P_o(M_o)}{3e(k_0 a)^2 M_o^2 P_\epsilon} \right]^{1/3}, \quad M > N_o \quad (31)$$

where we have changed the argument of P_o from b to M_o and added the argument to N_i to indicate the possibility that the number of nodes can increase with the size M_o of the observation circle. Hence if the product $P_o(M_o)N_i(M_o)$ can be made to increase at least quadratically with M_o , there is a potential for increasing M enormously relative to what is offered in free-space. This has positive implications in wireless network design provided that one can successfully address the simultaneous issue of higher adjacent node interference.

III. NUMERICAL RESULTS

We first establish the validity of Born approximation (labelled ‘BA’ in the figures) for mild scatter densities. The exact integral equation (labelled ‘FW’ for full-wave in the figures) will require the solution of an $N_u \times N_u$ matrix per realization. The number of realizations, N_r , and the problem sizes are chosen modestly so as not to inundate the computational resources. Thus, the relatively small areas chosen for the purpose of calculating the exact results should not detract the reader in the usefulness of the Born approximation approach. In Fig. 2, we show comparison between the exact integral equation solution, as per (18), and that by the Born approximation, as per (20), for $k_0 a = 0.1$, $x_1 = k_0 R_m = 10.1$, $x_2 = 10.5$, $x_3 = 14.5$, $N_i = 81$, $Q = 100$, $L = 0$, $N_u = 100$, $\rho_a = 1\%$ and $N_r = 50$. Because the scatter sizes are electrically small, it was found that convergent solution was obtained with $L = 0$ itself. The power contained in the m th mode is plotted against the mode number normalized to $M_o = \lceil ex_1/2 \rceil = 14$. For comparison, the power in free-space is also shown. It is seen that the Born approximation accurately captures the proper slopes of P_m with m both for $m < M_o$ and for $m > M_o$. The high-frequency oscillations seen in the exact solution is due to the inadequacy of the number of realizations ($N_r = 50$) used for averaging and can be eliminated by using a significantly larger number.

Fig. 3 shows the comparison for larger scatterers with $k_0 a = 0.1\pi$. The current density on each cylinder was expanded using 5 modes ($L = 2$) as well as using 3 modes ($L = 1$). Very little difference in the results was found between the two choices. Also, larger domain size with $x_1 = 16.5\pi$, $x_3 = 23.5\pi$ which

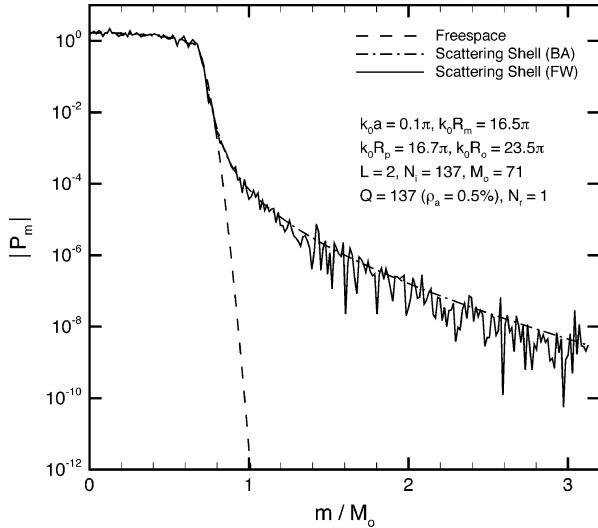


Fig. 3. Power contained in the orthogonal modes versus mode number.

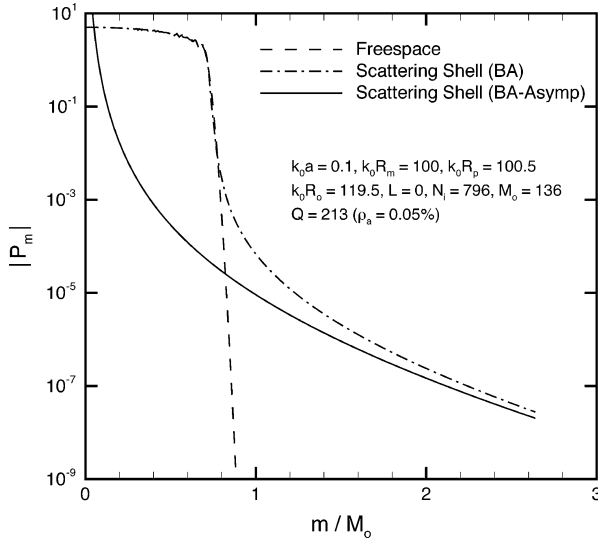


Fig. 4. Asymptotic expression for the mode power P_m versus m .

result in larger number of source currents $N_i = 137$ and scatterers ($Q = 137$) have been considered. The exact solution involving $N_u = 685$ unknowns for each realization took 19 hours on a laptop using MATLAB and is compared with the Born approximation that uses $L = 0$. The exact solution requires the inversion of a 685×685 complex-valued matrix for each realization followed by $m \times N_u$ matrix multiplications for each summation sign in (18). There were a total of 270 values of m for which P_m was computed in Fig. 3. Once again, it is seen that the Born approximation reasonably models the mode power both for $m < M_o$ and $m > M_o$.

The direct expression contained in (20) is not suitable for an accurate evaluation for large m , because it would involve the difference of extremely large numbers that are close to each other. The asymptotic expressions available in (25) and (27) are more suitable for that purpose. Fig. 4 shows the appropriateness of the asymptotic expressions for large m . The parameters used in the computation are $k_0a = 0.1$, $x_1 = 100$, $x_3 =$

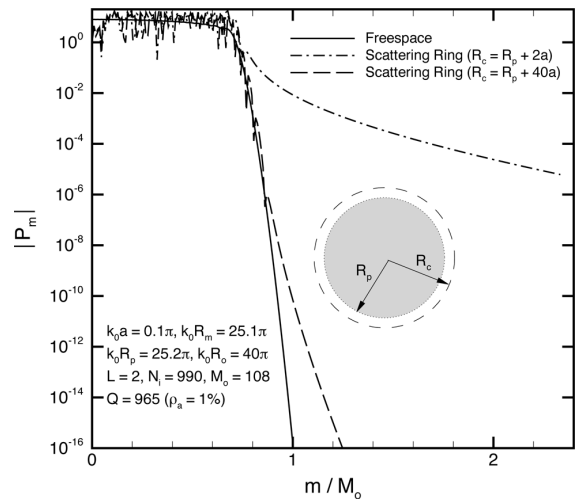


Fig. 5. Mode power for scatterers distributed uniformly on a ring of radius $R_c > R_p$.

119.5, $M_o = 136$, $N_i = 796$, and $\rho_a = 0.05\%$. The direct expression (19) involves Hankel functions of order exceeding 250 for argument of around 100 and diverge beyond $m > 2.6M_o \approx 354$. However, the asymptotic expression (labelled 'BA-Asymp' in the figure) remain valid for any large $m > N_o = \lceil ex_3/2 \rceil \approx 1.2M_o$ and get better as $m \rightarrow \infty$, as can be clearly seen from the figure. Of course the asymptotic formula is not valid for smaller values of m as is also evident from the figure.

The rapid decay of higher order mode power observed in free-space is halted when scatterers are present. This is particularly true when the power is observed in the reactive region of scattered fields. To appreciate this point better, we consider scatterers distributed uniformly on a ring of radius $R_c > R_p$ around the interior sources. The sources are still considered uncorrelated and uniformly distributed inside the circle of radius $R_m < R_p$. Under the Born approximation, equation (19) is once again obtained with $\mu_q = R_c$, but without the averaging operator. We locate scatterers very close to the boundary ($R_c = R_p + 2a$) and contrast that with a situation where scatterers are away from it ($R_c = R_p + 40a$). Fig. 5 shows the mode power decay in both cases. It is seen that while scatterers slow the decaying rate of higher mode power in both cases, the slowing is more dramatic when the scatterers are closer to the observation circle than when they are away from it. The higher power available in these higher order modes will increase the degrees of freedom offered by the electromagnetic field when their power exceeds the noise power. Such an increase in the degrees of freedom due to near-field coupling has previously been reported by other researchers [27], [39] and generally referred to as super-resolution. In a practical situation, scatterers may neither be close to receiver nor far from it, and the benefits will be between the two extremes.

Fig. 6 shows a plot of the fractional power ratio P_ϵ/P_t for $\rho_a = 1\%$ and $R_o/R_m \approx 1.36$. Other parameters chosen are shown in the figure legend. The ratio P_ϵ/P_t may be roughly interpreted as inverse of the signal-to-noise ratio (SNR). In free-space, the power ratio rolls off faster than any exponential for $M > M_o$ indicating that the NDOF in free-space is M_o even

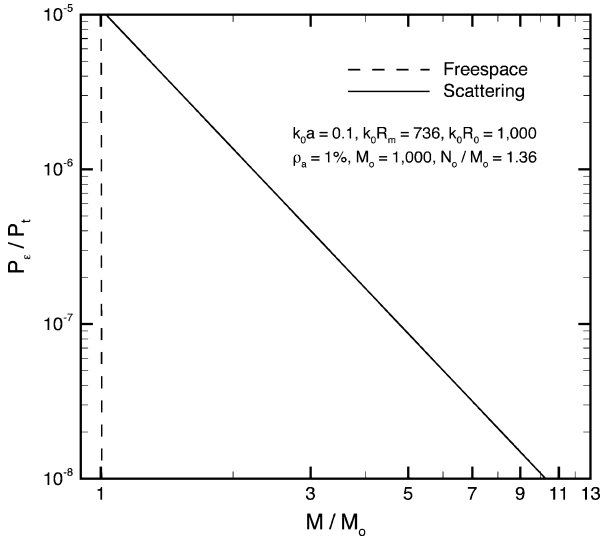


Fig. 6. Power P_ϵ contained in the tail $[M + 1, \infty)$ as a fraction of the total power versus the M .

if other competing quantities (such as number of sources N_i , power per source $P_o(b)$, etc.) are made to increase algebraically with M_o . In other words, the NDOF is essentially independent of SNR. Identical results were obtained using analyses based on singular value decomposition of fields as carried out in [23]. Benefits of near-zone fields of sources alone are not experienced here because we are looking at the real part of the Poynting vector. This applies both to interior and exterior sources. However, the interference terms in the total power arising from the incident and scattered fields do contribute to the real part. Hence in the presence of exterior scatterers, the power ratio rolls off much more gradually (only as a power law), thereby indicating increased NDOF with scattering. Fig. 6 also shows that one needs to have high a SNR in order to reap the benefits of increased NDOF. If the SNR is low enough, $M \sim M_o$. However, if the noise floor is such that $P_\epsilon/P_t = 10^{-7}$, the NDOF with exterior scatterers is equal to $5M_o$. This is with a scatterer area density of only 1%. Higher densities and larger particle sizes could lead to higher values as it has been established by various researchers [40], [29] that higher scatter densities lead to enhanced backscattering. Furthermore, if the total power P_t is made to increase with b in the form of the power law $P_t \propto b^\alpha$, one gets significantly larger NDOF with scattering than in free-space when $\alpha > 1$. Such an increase in power could be achieved either by increasing the number of nodes at an appropriate rate, or by increasing power per node, or a by a combination of the two. This result contained in (29) is in contrast to what has been suggested in [23] for the limiting case of $N_i \rightarrow \infty$ and could lead to much higher transport capacities for finite sized wireless networks if proper power scaling and node density strategies are devised.

Much of the benefit of increased NDOF comes from the near fields contributed by the scatterers. In order to better understand the benefit arising out of the near-fields, we consider the extreme case of scatterers arranged uniformly on a ring of radius $R_c > R_p$. As remarked previously, one gets M_o degrees of freedom in freespace, which is rather independent on the SNR. Denoting the ratio of $P_\epsilon = \sum_{m=M+1}^{\infty} P_m$ to P_t as χ

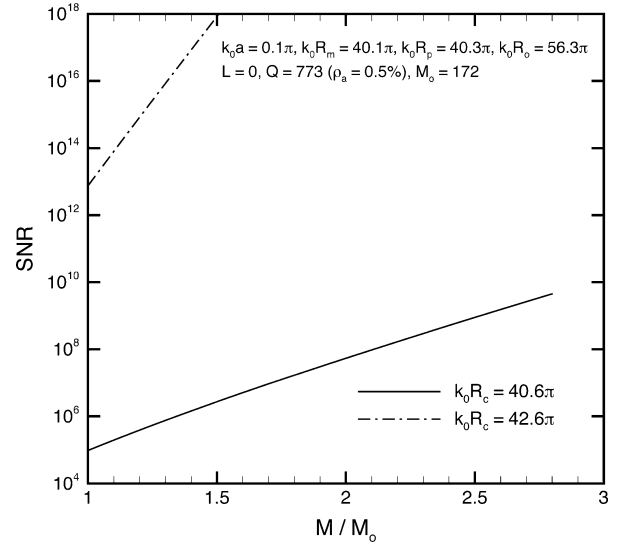


Fig. 7. SNR versus normalized degrees of freedom for a ring of scatterers placed in the near-zone.

and using the approximate expression (19) for P_m , one gets for $M > \lceil ek_0R_c/2 \rceil > M_o$ after ignoring the free-space contribution P_e^i that

$$\chi \sim \left| \frac{J_0(k_0a)}{\pi H_0^{(1)}(k_0a)} \right|^2 \left(\frac{R_m}{R_c} \right)^{2M} \frac{R_m^2}{R_c^2 - R_m^2} \frac{2Q}{(M+1)^3}. \quad (32)$$

Fig. 7 shows a plot of the SNR $1/\chi$ as a function of M/M_o . The other parameters considered in this example are shown in the figure legend. It is seen that higher NDOF is obtained when the ring of scatterers is closer to the observation circle (radius $b \approx R_m$) than when it is farther out. It may be noted that the term SNR, used only to represent the ratio P_t/P_ϵ , may not pertain to the actual SNR at a receiver node. Nevertheless, Fig. 7 indicates that a high SNR is needed in order to realize the increased degrees of freedom offered by scatterers, particularly for low scatter densities.

IV. CONCLUSION

By considering the problem of line sources radiating in the presence of exterior perfectly scattering cylinders and decomposing the real power flow on an observation circle $r = b$ in terms of orthogonal modes, we have shown that the NDOF in free-space is fixed at $M_o = \lceil ek_0b/2 \rceil$ even if the average power per line source $P_o(M_o)$ and/or the number of line sources $N_o(M_o)$ increases as a power law with M_o . This is due to the rapid drop-off of higher-order mode power as given in (25). In the presence of exterior scatterers (scatterers outside $r = b$) the higher order mode power decays only algebraically due to backscattering and near-field effects, thereby offering the potential of increased NDOF. In particular, we have derived a closed form expression (31) for the number of degrees of freedom assuming that the fractional area density ρ_a of scatterers is low enough (as a rule of thumb, $\rho_a < 0.1$) to neglect multiple scattering. The expression is applicable to large networks as well.

It has been demonstrated that the benefits offered by scattering will be most effectively realized at high SNRs.

Extension of the results to 3D should be straightforward, although the analysis is expected to be more cumbersome and the qualitative results may likely behave differently due to the faster decay of 3D fields with distance. Other scattering scenarios are also of interest and worthy of study-isolated scatter clusters surrounding transmit and receive nodes, large scatter cluster intervening an otherwise free-space region between transmit and receive nodes, transmit and receive nodes operating in the vicinity of half-space and an intervening scatter cluster, etc. For higher scatter density, more refined approximations such as the Rytov approximation or those based on diagrammatic techniques [41], [34], [42] are worth exploring and these will be undertaken in the future. The locations of the line sources and those of the scatterers were assumed to be independent and identically distributed (iid) random variables. These are expected to valid for electrically small sized sources and scatterers. For larger sized scatterers, the two-particle joint probability density function [30] is more appropriate and this will also be pursued in the future.

REFERENCES

- [1] K. Pahlavan and A. H. Levesque, *Wireless Inf. Networks*. New York: Wiley, 1995.
- [2] "Wearable technology," *IEEE Engrng. Med. Biol. Mag.*, vol. 22, no. 3, 2003.
- [3] R. S. H. Istepanian, E. Jovanov, and Y. Zhang, "Guest editorial introduction to the special section on m-health: Beyond seamless mobility and global wireless health-care connectivity," *IEEE Trans. Inf. Tech. in Biomed.*, vol. 8, no. 4, pp. 405–414, 2004.
- [4] S. Haykin, "Cognitive radio: Brain empowered wireless communications," *IEEE J. Sel. Areas Commun.*, vol. 23, pp. 201–220, Feb. 2005.
- [5] G. Toraldo di Francia, "Resolving power and information," *J. Opt. Soc. Am.*, vol. 45, no. 7, pp. 497–501, Jul. 1955.
- [6] O. M. Bucci and G. Franceschetti, "On the spatial bandwidth of scattered fields," *IEEE Trans. Antennas Propag.*, vol. 35, no. 12, pp. 1445–1455, Dec. 1987.
- [7] O. M. Bucci and G. Franceschetti, "On the degrees of freedom of scattered fields," *IEEE Trans. Antennas Propag.*, vol. 35, no. 7, pp. 918–926, Jul. 1989.
- [8] O. M. Bucci, C. Gennarelli, and C. Savarese, "Representation of electromagnetic fields over arbitrary surfaces by a finite and nonredundant number of samples," *IEEE Trans. Antennas Propag.*, vol. 46, no. 3, pp. 351–359, Mar. 1998.
- [9] R. Piestun and D. A. B. Miller, "Electromagnetic degrees of freedom of an optical system," *J. Opt. Soc. Am. A*, vol. 17, no. 5, pp. 892–902, May 2000.
- [10] D. A. B. Miller, "Communicating with waves between volumes: Evaluating orthogonal spatial channels and limits on coupling strengths," *Appl. Opt.*, vol. 39, no. 11, pp. 1681–1699, Apr. 2000.
- [11] G. J. Foschini and M. J. Gans, "On limits of wireless communications in a fading environment when using multiple antennas," *Wireless Pers. Commun.*, no. 6, pp. 311–335, Mar. 1998.
- [12] E. Telatar, "Capacity of multiantenna Gaussian channels," *Europ. Trans. Telecomm.*, vol. 10, pp. 585–596, Nov. 1999.
- [13] A. S. Y. Poon, R. W. Brodersen, and D. N. C. Tse, "Degrees of freedom in multiple-antenna channels: A signal space approach," *IEEE Trans. Inf. Theory*, vol. 51, no. 2, pp. 523–536, Feb. 2005.
- [14] A. S. Y. Poon, D. N. C. Tse, and R. W. Brodersen, "Impact of scattering on the capacity, diversity, and propagation range of multiple-antenna channels," *IEEE Trans. Inf. Theory*, vol. 52, no. 3, pp. 1087–1100, Mar. 2006.
- [15] M. D. Migliore, "On the role of the number of degrees of freedom of the field in MIMO channels," *IEEE Trans. Antennas Propag.*, vol. 54, no. 2, pp. 620–628, Feb. 2006.
- [16] R. A. Kennedy, P. Sadeghi, T. Abhayapala, and H. M. Jones, "Intrinsic limits of dimensionality and richness in random multipath fields," *IEEE Trans. Signal Process.*, vol. 55, no. 6, pp. 2542–2556, Jun. 2007.
- [17] J. Xu and R. Janaswamy, "Electromagnetic degrees of freedom in 2-D scattering environments," *IEEE Trans. Antennas Propag.*, vol. 54, no. 12, pp. 3882–3894, Dec. 2006.
- [18] P. Gupta and P. R. Kumar, "The capacity of wireless networks," *IEEE Trans. Inf. Theory*, vol. 46, no. 2, pp. 388–404, Mar. 2000.
- [19] N. Vu, M. Devroye, and V. Tarokh, "An overview of scaling laws in adhoc and cognitive radio networks," *Wireless Pers. Commun.*, vol. 45, pp. 343–354, 2008.
- [20] L.-L. Xie and P. R. Kumar, "A network information theory for wireless communications: Scaling laws and optimal operation," *IEEE Trans. Inf. Theory*, vol. 53, no. 10, pp. 3549–3572, May 2004.
- [21] L.-L. Xie and P. R. Kumar, "On the path-loss attenuation regime for positive cost and linear scaling of transport capacity in wireless networks," *IEEE Trans. Inf. Theory*, vol. 52, no. 6, pp. 2313–2328, Jun. 2006.
- [22] A. Özgür, O. Leveque, and D. N. C. Tse, "Hierarchical cooperation achieves optimal capacity scaling in AdHoc networks," *IEEE Trans. Inf. Theory*, vol. 53, no. 10, pp. 3549–3572, Oct. 2007.
- [23] M. Franceschetti, M. D. Migliore, and P. Minero, "The capacity of wireless networks: Information-theoretic and physical limits," *IEEE Trans. Inf. Theory*, vol. 55, no. 8, pp. 3413–3424, Aug. 2009.
- [24] F. Xue, L.-L. Xie, and P. R. Kumar, "The transport capacity of wireless networks over fading channels," *IEEE Trans. Inf. Theory*, vol. 51, no. 3, pp. 834–847, Mar. 2005.
- [25] A. Ozgür, O. Leveque, and D. Tse, "Linear capacity scaling in wireless networks: Beyond physical limits arXiv:1002.3065v1 [cs.IT], Feb. 2010.
- [26] A. Goldsmith, S. Jafar, I. Maric, and S. Srinivasa, "Breaking spectrum gridlock with cognitive radios: An information theoretic perspective," *Proc. IEEE*, vol. 97, no. 5, pp. 894–914, May 2009.
- [27] O. M. Bucci, L. Crocco, and T. Isernia, "Improving the reconstruction capabilities in inverse scattering problems by exploitation of close-proximity setups," *J. Opt. Soc. Am. A*, vol. 16, no. 7, pp. 1788–1798, Jul. 1999.
- [28] F. K. Gubert and E. A. Marengo, "New aspects of electromagnetic information theory for wireless and antenna systems," *IEEE Trans. Antennas Propag.*, vol. 56, no. 11, pp. 1470–1484, Nov. 2008.
- [29] C. E. Mandt, L. Kuga, Y. Tsang, and A. Ishimaru, "Microwave propagation and scattering in a dense distribution of non-tenuous spheres: experiment and theory," *Waves Random Media*, vol. 2, pp. 225–234, 1992.
- [30] L. Tsang and J. A. Kong, *Scattering of Electromagnetic Waves*. New York: Wiley, 2001.
- [31] T. M. Cover and J. A. Thomas, *Elements of Inf. Theory*. New York: Wiley, 1991.
- [32] M. Abramowitz and I. A. Stegun, *Handbook of Mathematical Functions*. New York: Dover, 1972.
- [33] R. F. Harrington, *Time-Harmonic Electromagnetic Fields*. New York: McGraw-Hill, 1965.
- [34] A. Ishimaru, *Electromagnetic Wave Propagation, Radiation, and Scattering*. Englewood Cliffs, NJ: Prentice Hall, 1991, 07632.
- [35] G. C. Hsiao and R. E. Kleinman, "Mathematical foundations for error estimation in numerical solutions of integral equations in electromagnetics," *IEEE Trans. Antennas Propag.*, vol. 45, no. 3, pp. 316–328, Mar. 1997.
- [36] J.-C. Nedelec, *Acoustic and Electromagnetic Equations*, ser. Applied Mathematical Sciences. New York: Springer Verlag, 2001, vol. 144.
- [37] L. S. Gradshteyn and I. S. Ryzhik, *Table of Integrals, Series, and Products*, 6th ed. New York: Academic Press, 2000.
- [38] C. Ferreira and J. L. Lopez, "Asymptotic expansions of the hurwitz-lerch zeta function," *J. Math Anal. Appl.*, vol. 298, pp. 210–224, 2004.
- [39] M. D. Migliore, "On electromagnetics and information theory," *IEEE Trans. Antennas Propag.*, vol. 56, no. 10, pp. 3188–3200, Oct. 2008.
- [40] Y. Kuga and A. Ishimaru, "Retroreflectance from a dense distribution of spherical particles," *J. Opt. Soc. Am. A*, vol. 1, no. 8, pp. 831–835, Aug. 1984.
- [41] J. B. Keller, "Accuracy and validity of the Born and Rytov approximations," *J. Opt. Soc. Am.*, vol. 59, no. 1, pp. 1003–1004, Aug. 1969.
- [42] U. Frisch, *Wave Propagation in Random Media in Probabilistic Methods in Appl. Mathematics*, A. T. Bharucha-Reid, Ed. New York: Academic Press, 1968, vol. 1.



Ramakrishna Janaswamy (F'03) received the Ph.D. degree in electrical engineering in 1986 from the University of Massachusetts, Amherst, the Master's degree in microwave and radar engineering from IIT-Kharagpur, India in 1983, and the Bachelor's degree in electronics and communications engineering from REC-Warangal (now NITWarangal), India in 1981.

From August 1986 to May 1987, he was an Assistant Professor of electrical engineering at Wilkes University, Wilkes Barre, PA. From August 1987–August 2001 he was on the faculty of the Department of Electrical and Computer Engineering, Naval Postgraduate School, Monterey, CA. In September 2001, he joined the Department of Electrical & Computer Engineering, University of Massachusetts, Amherst, where he is currently a Professor. His research interests include deterministic and stochastic radio

wave propagation modeling, analytical and computational electromagnetics, antenna theory and design, and wireless communications.

Prof. Janaswamy is a Fellow of IEEE and was the recipient of the R. W. P. King Prize Paper Award of the IEEE TRANSACTIONS ON ANTENNAS AND PROPAGATION in 1995. For his services to the IEEE Monterey Bay Subsection, he received the IEEE 3rd Millennium Medal from the Santa Clara Valley Section in 2000. He is an elected member of U.S. National Committee of International Union of Radio Science, Commissions B and F. He served as an Associate Editor of *Radio Science* from January 1999–January 2004 and Associate Editor of IEEE TRANSACTIONS ON VEHICULAR TECHNOLOGY from 2003–2006. He is currently an Associate Editor of IEEE TRANSACTIONS ON ANTENNAS AND PROPAGATION and an Editor of *IETE Technical Reviews*. He is the author of the book *Radiowave Propagation and Smart Antennas for Wireless Communications* (Kluwer Academic, November 2000) and a contributing author in *Handbook of Antennas in Wireless Communications* (CRC Press, August 2001) and *Encyclopedia of RF and Microwave Engineering* (Wiley, 2005).

Transitional probabilities for the 4-state random walk on a lattice

R Janaswamy

Department of Electrical and Computer Engineering, University of Massachusetts,
215-D Marcus Hall, 100 Natural Resources Road, Amherst, MA 01003, USA

E-mail: janaswamy@ecs.umass.edu

Received 27 October 2007, in final form 3 March 2008

Published 2 April 2008

Online at stacks.iop.org/JPhysA/41/155306

Abstract

The diffusion and Schrödinger propagators have been known to coexist on a lattice when a particle undergoing random walk is endowed with two states of spin in addition to the two states of direction in a 1+1 spacetime dimension. In this paper we derive explicit expressions for the various transitional probabilities by employing generating functions and transform methods. The transitional probabilities are all expressed in terms of a one-dimensional integral involving trigonometric functions and/or Chebyshev polynomials of the first and second kind from which the spacetime continuum limits of the diffusion equation and Schrödinger equation follow directly.

PACS numbers: 03.65.-w, 05.40.Fb

1. Introduction

There has been a lot of interest in the recent past to understand quantum mechanics in the context of classical statistical mechanics. On the one hand, Brownian motion provides a microscopic model of diffusion and provides an unambiguous interpretation of the diffusion equation. On the other hand, a similar physical interpretation is lacking for the Schrödinger equation, whose wave solution is a complex quantity without a physical reality. Because classical diffusion cannot account for the self-interference pattern that is so intrinsic to quantum behavior, several theories have been put forward recently to understand the microphysics of quantum behavior. Nelson [1] derived the Schrödinger equation starting from Newtonian mechanics and by assuming that a particle is subject to an underlying Brownian motion described by a combined forward-in-time and a backward-in-time Wiener processes. A detailed account of Nelson's original idea of stochastic mechanics and its subsequent refinement is given in [2–5]. Nottale [6] and Ord [7] advanced the idea that spacetime is not differentiable but is of a fractal nature, suggesting that an infinity of geodesics lie between any two points and, thereby, providing a fundamental and universal origin for the double

Wiener process of Nelson. These ideas are elaborated in the monograph [8]. El Naschie [9] too considered a fractal spacetime with a Cantorial structure and argued that quantum behavior could be mimicked by combining this fractal spacetime with a diffusion process. A totally different paradigm was recently introduced by Ord [10], who by considering a symmetric random walk on a lattice, showed that both the diffusion equation and the Schrödinger equation occur as approximate descriptions of different aspects of the same classical probabilistic system. By considering a 4-state random walk (4RW) on a discrete lattice, wherein a particle is endowed with two states of direction and two states of spin, Ord [10–12] has shown that both diffusion and Schrödinger propagators coexist on a lattice and that either can be obtained from a distinct projection of the same random walk. It is too early to speculate as to which of Nelson's or Ord's model will duplicate the true quantum behavior under a variety of situations. This can only be ascertained through additional work on both models. It may be mentioned that the combination of displacement and spin have also been used previously in [13, 14] to study dynamics of a quantum particle in spacetime. However, the important distinction between the Ord model and the one considered in [13, 14] is that the states describing the direction of motion are independent of those describing the spin states in the former model. There is also an intrinsic notion of *memory* embedded in the Ord's model.

The Schrödinger type of equation is encountered under the guise of *parabolic wave equation*, or simply parabolic equation in the solution of boundary-value problems in several branches of applied physics such as acoustics [15], optics and classical electromagnetic wave propagation [16]. In such boundary-value problems, inhomogeneities of the propagating medium caused by the varying index of refraction of the intervening material take the place of the potential field experienced by a quantum particle. The standard parabolic equation is resulted when one extracts paraxial propagation along a preferred direction from the full Helmholtz equation. In addition to providing a microscopic model for the Schrödinger equation, the 4RW model considered by Ord is also attractive in the solution of stochastic differential equations associated with these parabolic type of equations, carried out by employing only real random processes. Because walks modeling the Schrödinger equation in the 4RW model traverse only real space, no analytical continuation of boundary data into complex space is required that would otherwise be demanded [17, 18] when solving these boundary-value problems.

Ord does not provide explicit expressions for the various transitional probabilities, but, instead, discusses the continuum limits directly from the governing difference equations. For a variety of reasons, it is desirable to obtain closed-form expressions (or those involving integrals) for these transitional probabilities. In this paper, we provide analytical expressions for the transitional probabilities associated with the 4-state random walk in 1+1 dimension in spacetime by using a transform approach. Our work here is partly motivated by the desire to have expressions for the transitional probabilities while solving the aforementioned boundary-value problems using the parabolic equation in a homogeneous medium. Using these expressions, it is further shown that in the continuum limits as the mesh size shrinks to zero in both space and time, one directly recovers the diffusion equation and the Schrödinger equation. Thus, the main contributions of the paper are to (i) elucidate methodology for obtaining the closed-form expressions for the various transitional probabilities of the 4RW, and (ii) establish the continuum limits of the diffusion and Schrödinger equations describing the dynamics of particles obeying the 4RW. The methodology presented in this paper is most suitable for describing quantum dynamics of a free-particle, although the 4RW model itself has been extended in the presence of a potential field [19]. The paper is organized as follows: section 2 gives a brief introduction of the random walks considered in [10, 12]. Section 3 introduces the generating functions and the 2D transforms considered in this paper.

Table 1. Various states in random walk.

State	Direction	Spin
1	Right	+1
2	Left	+1
3	Right	-1
4	Left	-1

Section 4 provides expressions for the various transitional probabilities as well as discusses the derivation of the diffusion equation and the Schrödinger equation as continuum limits of these probabilities.

2. Multistate random walks

Consider the 4RW model proposed by Ord and Deakin [12], where a particle undergoes random motion in discrete spacetime ($x = m\Delta, t = s\epsilon$), with x denoting space and t denoting time, and Δ and ϵ denoting the spatial and temporal steps, respectively. At every point the particle is endowed with two independent binary properties, its direction of motion (right or left) and its spin or parity (± 1). The particle is assumed to change its direction with every collision, but change its spin only every other collision. The four states of the particle corresponding to the four combinations of direction and spin are indicated in table 1. Note that the particle can execute any direction of motion irrespective of the spin, in contrast to the model used in [13, 14]. However, there is an intrinsic assumption of *memory* in Ord's model that arises from keeping track of the parity of collisions. If $p_\mu(m\Delta, s\epsilon)\Delta, \mu = 1, \dots, 4$, is the probability that a particle is in state μ at the spacetime point $(m\Delta, s\epsilon)$, $m = 0, \pm 1, \pm 2, \dots, s = 0, 1, \dots$, then the transitional relations considered in [12] were of the form

$$\begin{aligned} p_1[m\Delta, (s+1)\epsilon] &= \alpha p_1[(m-1)\Delta, s\epsilon] + \beta p_4[(m+1)\Delta, s\epsilon] \\ p_2[m\Delta, (s+1)\epsilon] &= \alpha p_2[(m+1)\Delta, s\epsilon] + \beta p_1[(m-1)\Delta, s\epsilon] \\ p_3[m\Delta, (s+1)\epsilon] &= \alpha p_3[(m-1)\Delta, s\epsilon] + \beta p_2[(m+1)\Delta, s\epsilon] \\ p_4[m\Delta, (s+1)\epsilon] &= \alpha p_4[(m+1)\Delta, s\epsilon] + \beta p_3[(m-1)\Delta, s\epsilon], \end{aligned} \quad (1)$$

where $\alpha + \beta = 1$. Here, α is the probability that a particle maintains its direction at the next time step, whereas β is the probability that it will change its direction at the next time step. The Markov-chain character of the transitional probabilities is evident from definitions in (1). From the total probability theorem, the probability that a particle is somewhere on the lattice at a given time is equal to 1 and is represented mathematically by

$$\sum_{\mu=1}^4 \sum_{m=-\infty}^{\infty} p_\mu(m\Delta, s\epsilon)\Delta = 1. \quad (2)$$

Ord [10] has shown that the diffusion and Schrödinger propagators coexist on the lattice and that both behaviors are embedded in equations (1). To affect a separation of the diffusive behavior from the wave-like behavior, the following linear transformation is used: $q_1(m\Delta, s\epsilon) = 2^{s/2}[p_1(m\Delta, s\epsilon) - p_3(m\Delta, s\epsilon)]$, $q_2(m\Delta, s\epsilon) = 2^{s/2}[p_2(m\Delta, s\epsilon) - p_4(m\Delta, s\epsilon)]$, $w_1(m\Delta, s\epsilon) = [p_1(m\Delta, s\epsilon) + p_2(m\Delta, s\epsilon) + p_3(m\Delta, s\epsilon) + p_4(m\Delta, s\epsilon)]$, and $w_2(m\Delta, s\epsilon) = [p_1(m\Delta, s\epsilon) + p_3(m\Delta, s\epsilon)] - [p_2(m\Delta, s\epsilon) + p_4(m\Delta, s\epsilon)]$. The quantity $q_1\Delta$ (without the weight factor $2^{s/2}$) indicates the expected difference in the number of

particles of opposite spin arriving at $(m\Delta, s\epsilon)$ while moving to the right. Similarly, $q_2\Delta$ refers to the expected number of particles arriving at $(m\Delta, s\epsilon)$ while moving to the left. Also, $w_1(m\Delta, s\epsilon)\Delta$ is the probability that a particle leaves $(m\Delta, s\epsilon)$ in either direction and in any spin state, and $w_2(m\Delta, s\epsilon)\Delta$ is the difference in the probabilities that a particle leaves $(m\Delta, s\epsilon)$ to the right and the left. Introducing the shift operator $E_x^{\pm 1} p_\mu(m\Delta, s\epsilon) = p_\mu[(m \pm 1)\Delta, s\epsilon]$, a time-advancing operator $E_t p_\mu(m\Delta, s\epsilon) = p_\mu[m\Delta, (s+1)\epsilon]$, and the vector $\mathbf{p} = [p_1, p_2, p_3, p_4]^T$, where the superscript T denotes transpose, the transitional relations in (1), which are of the form $E_t \mathbf{p} = \mathbf{S}_x \mathbf{p}$, get transformed into

$$E_t \begin{pmatrix} w_1 \\ w_2 \end{pmatrix} = \frac{1}{2} \begin{pmatrix} (E_x + E_x^{-1}) & -(E_x - E_x^{-1}) \\ (\alpha - \beta)(E_x - E_x^{-1}) & (\alpha - \beta)(E_x + E_x^{-1}) \end{pmatrix} \begin{pmatrix} w_1 \\ w_2 \end{pmatrix}, \quad (3)$$

$$E_t \begin{pmatrix} q_1 \\ q_2 \end{pmatrix} = \frac{1}{\sqrt{2}} \begin{pmatrix} 2\alpha E_x^{-1} & -2\beta E_x \\ 2\beta E_x^{-1} & 2\alpha E_x \end{pmatrix} \begin{pmatrix} q_1 \\ q_2 \end{pmatrix}. \quad (4)$$

Thus the variables (w_1, w_2) get decoupled from (q_1, q_2) . Essentially, this decoupling results from block-diagonalizing the matrix \mathbf{S}_x and describing the system in terms of its eigenstates. The physical significance of this transformation is touched upon in [11, 12]. Note that w_j and q_j need not strictly be probabilistic quantities (meaning ≥ 0), but we will continue to describe them as ‘transitional probabilities’ with the understanding that the actual probabilistic quantities, namely, p_μ , can be easily recovered from these using the inverse relations.

3. Generating functions and transforms

We are interested in the solutions of (3) and (4) for the special case of a symmetric random walk with $\alpha = \beta = 0.5$. In this case we have a set of linear difference equations and the solution can be obtained conveniently using transform methods [20, 21] and appropriate generating functions. The key step here is to pick a suitable transform consistent with the nature and domain of definition of the problem. We denote the 2D transform \mathcal{L} , consisting of a Fourier transform in space (owing to the unbounded nature of the spatial coordinate) and the z -transform [22] in time (the z -transform can be arrived from the discretized version of a Laplace transform and is suitable for discrete functions defined on a half-line), of a discrete function $v(m\Delta, s\epsilon)$ as $V(k_x, z)$ and define

$$V(k_x, z) = \Delta \sum_{m=-\infty}^{\infty} \sum_{s=0}^{\infty} v(m\Delta, s\epsilon) z^s e^{-imk_x \Delta} \equiv \mathcal{L}v(m\Delta, s\epsilon). \quad (5)$$

The inverse relation can then be obtained as

$$v(m\Delta, s\epsilon) = \frac{1}{4\pi^2 i} \int_{k_x=-\pi/\Delta}^{\pi/\Delta} \oint_{C_z} \frac{V(k_x, z)}{z^{s+1}} e^{imk_x \Delta} dk_x dz \equiv \mathcal{L}^{-1} V(k_x, z), \quad (6)$$

where the identities

$$\int_{k_x=\Delta=-\pi}^{\pi} e^{i(n-m)k_x \Delta} dk_x \Delta = 2\pi \delta_m^n \quad (7)$$

$$\oint_{C_z} z^{r-s-1} dz = 2\pi i \delta_s^r \quad (8)$$

are used to derive (6). Here δ_m^n is the Kronecker’s delta and C_z is a closed contour around the origin in the complex z -plane that encloses only the singularities at the origin. The present

analysis, consisting of the z -transform along the time axis and Fourier transform along the spatial axis, is most suitable for studying linear difference equations with constant coefficients such as encountered in the study of free-Schrödinger equation by the 4RW model. Other suitable methods must be devised for studying particle motion in the presence of a potential field. Note that $V(k_x, z)$ is periodic in k_x with a period $2\pi/\Delta$. Using the definition in (5), it can also be shown that

$$\mathcal{L}v[m\Delta, (s+1)\epsilon] = z^{-1} [V(k_x, z) - V_0(k_x)] \quad (9)$$

$$\mathcal{L}v[(m \pm 1)\Delta, s\epsilon] = e^{\pm ik_x \Delta} V(k_x, z), \quad (10)$$

where $V_0(k_x)$ is the Fourier transform of the initial distribution $v(m\Delta, 0)$:

$$V_0(k_x) = \Delta \sum_{m=-\infty}^{\infty} v(m\Delta, 0) e^{-imk_x \Delta}. \quad (11)$$

Note that the periodicity property of $V_0(k_x)$ implies that $V_0(\pi/\Delta) = V_0(-\pi/\Delta)$.

4. Transitional probabilities

Having defined the required transforms, we will now derive expressions for the transitional probabilities w_1, w_2, q_1 and q_2 . Because of the decoupling afforded in (3) and (4), it is sufficient to consider the diffusive and wave-like behaviors separately.

4.1. Diffusive behaviour

The diffusive part of the particle motion is governed by the discrete functions w_1 and w_2 as will be evident shortly. Let $W_1(k_x, z)$ and $W_2(k_x, z)$ be the 2D transforms of $w_1(m\Delta, s\epsilon)$ and $w_2(m\Delta, s\epsilon)$ and $\Upsilon_1(k_x)$ and $\Upsilon_2(k_x)$ be the transforms of the initial distributions $w_1(m\Delta, 0)$ and $w_2(m\Delta, 0)$, respectively. From the definition of w_1 in terms of p_μ , $\mu = 1, \dots, 4$, and relation (2), it is seen that $\Upsilon_1(0) = 1$. On applying the transform \mathcal{L} to the set (3) and making use of the properties (9) and (10), it is easy to see that $W_2(k_x, z) = \Upsilon_2(k_x)$ and

$$W_1(k_x, z) = \frac{\Upsilon_1(k_x) - iz \sin(k_x \Delta) \Upsilon_2(k_x)}{1 - z \cos(k_x \Delta)} \quad (12)$$

$$= \sum_{n=0}^{\infty} z^n \cos^n(k_x \Delta) [\Upsilon_1(k_x) - iz \sin(k_x \Delta) \Upsilon_2(k_x)] \quad (13)$$

where (13) has been obtained by using the series expansion of $[1 - z \cos(k_x \Delta)]^{-1}$. Such a series converges uniformly provided that $|z \cos(k_x \Delta)| < 1$ and this can always be insured by choosing an appropriate C_z in (6). In other words, the contour C_z is chosen such that the zeroes of the function $1 - z \cos(k_x \Delta)$ lie outside it. Substituting this into (6) and making use of (8), we finally arrive at

$$w_1(m\Delta, s\epsilon) = \frac{1}{2\pi} \int_{-\pi/\Delta}^{\pi/\Delta} \cos^s(k_x \Delta) [\Upsilon_1(k_x) - i\Theta(s-1) \tan(k_x \Delta) \Upsilon_2(k_x)] e^{imk_x \Delta} dk_x, \quad (14)$$

where $\Theta(\cdot)$ is the Heaviside step function. For a given $\Upsilon_1(k_x)$ and $\Upsilon_2(k_x)$, integral (14) may be computed efficiently by the application of the inverse fast Fourier transform (iFFT) algorithm [22]. However, for special values of $\Upsilon_1(k_x)$ and $\Upsilon_2(k_x)$, the integral may be evaluated in

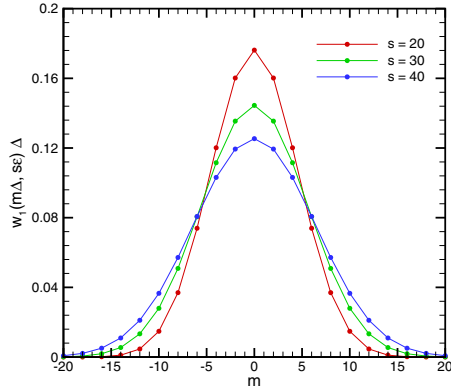


Figure 1. Calculated values of $w_1(m\Delta, s\epsilon)$ for $\Upsilon_1(k_x) = 1$, $\Upsilon_2(k_x) = 0$.

a closed form. For example, with $w_1(m\Delta, 0) = \frac{1}{\Delta} \delta_m^0$, $w_2(m\Delta, 0) = 0 (\implies \Upsilon_1(k_x) = 1, \Upsilon_2(k_x) = 0)$ and m and s even, (14) reduces to ([23], 3.631–17)

$$w_1(m\Delta, s\epsilon)\Delta = \frac{1}{2^s} \binom{s}{(s-m)/2}, \quad m \leq s. \quad (15)$$

The right-hand side of (15) gives the probability of finding a particle at m in s steps, given that it started at the origin at $s = 0$, in a symmetric, discrete-time, 1D random walk. The result can be obtained directly from combinatorial analysis and is available in standard texts ([24], p 75), ([25], p 16). Figure 1 shows a plot of $w_1(m\Delta, s\epsilon)\Delta$ for $s = 20, 30$ and 40 , where the data at discrete m has been connected by smooth lines for the sake of visual clarity. The plots clearly exhibit the diffusive behavior of w_1 , wherein w_1 spreads out in space with a diminishing peak value as s increases. Using the identity $\sum_{m=-\infty}^{\infty} \exp(\pm imx) = 2\pi \delta(x)$, $-\pi \leq x \leq \pi$, where $\delta(\cdot)$ is the delta function, it may be easily verified from (14) that $\sum_{m=-\infty}^{\infty} w_1(m\Delta, s\epsilon)\Delta = 1$. Also note that $w_1 > 0$. Hence $w_1\Delta$ behaves like a true probability mass function.

We are also interested in the continuum limits $\Delta \rightarrow 0$, $\epsilon \rightarrow 0$, $m \rightarrow \infty$, and $s \rightarrow \infty$ such that $\Delta^2/2\epsilon = D > 0$, $m\Delta \rightarrow x$, $s\epsilon \rightarrow t$. Using the results $\lim_{\substack{\Delta \rightarrow 0 \\ s \rightarrow \infty}} [\cos^s(k_x\Delta)] = \exp(-k_x^2 Dt)$, $\lim_{\substack{\Delta \rightarrow 0 \\ s \rightarrow \infty}} [\cos^s(k_x\Delta) \tan(k_x\Delta)] = 0$ in (14), we arrive at

$$w_1(x, t) = \frac{1}{2\pi} \int_{-\infty}^{\infty} \Upsilon_1(k_x) e^{-k_x^2 Dt} e^{ik_x x} dk_x. \quad (16)$$

This is the well-known solution of the diffusion equation $\partial w_1/\partial t = D \partial^2 w_1/\partial x^2$ in an unbounded medium with an initial spectral content $\Upsilon_1(k_x)$ (see, for example, [26]). For an impulsive initial condition, $\Upsilon_1(k_x) = 1$, and one recovers the Green's function $w_1(x, t) = \exp(-x^2/4Dt)/\sqrt{4\pi Dt}$. The function $w_1(m\Delta, s\epsilon)$ given in equation (14) is the discrete version of $w_1(x, t)$ and is seen to depend not only on $\Upsilon_1(k_x)$, but also on $\Upsilon_2(k_x)$. The latter contribution arises entirely from the discrete nature of space and vanishes in the continuum limit. To summarize, the quantity $w_1(m\Delta, s\epsilon)\Delta$ that describes the probability that a particle leaves $(m\Delta, s\epsilon)$ in either direction and in any spin state describes the diffusion process for a symmetric 4RW.

4.2. Wave-like behaviour

The wave-like behavior of the particle motion is governed by the discrete functions q_1 and q_2 . The governing equations in this case are repeated below from (4):

$$E_t \begin{pmatrix} q_1 \\ q_2 \end{pmatrix} = \frac{1}{\sqrt{2}} \begin{pmatrix} E_x^{-1} & -E_x \\ E_x^{-1} & E_x \end{pmatrix} \begin{pmatrix} q_1 \\ q_2 \end{pmatrix}. \quad (17)$$

Our objective here is to derive closed-form expressions for the transitional probabilities q_1 and q_2 . Let $Q_j(k_x, z)$ be the \mathcal{L} transforms of $q_j(m\Delta, s\epsilon)$, and let $\Gamma_j(k_x)$ be the Fourier transforms of the initial distribution $q_j(m\Delta, 0)$, $j = 1, 2$. On applying the \mathcal{L} transform to (17) and making use of properties (9) and (10) and carrying out some algebraic manipulations, we get

$$\begin{bmatrix} Q_1(k_x, z) \\ Q_2(k_x, z) \end{bmatrix} = \frac{1}{(1 - \sqrt{2}z \cos(k_x \Delta) + z^2)} \begin{bmatrix} 1 - \frac{z}{\sqrt{2}} e^{ik_x \Delta} & -\frac{z}{\sqrt{2}} e^{ik_x \Delta} \\ \frac{z}{\sqrt{2}} e^{-ik_x \Delta} & 1 - \frac{z}{\sqrt{2}} e^{-ik_x \Delta} \end{bmatrix} \begin{bmatrix} \Gamma_1(k_x) \\ \Gamma_2(k_x) \end{bmatrix}. \quad (18)$$

To permit evaluation of the integral with respect to z in the inverse transform, we need to express Q_1 and Q_2 in a separable form with respect to k_x and z . To this end, we make use of the identity ([23], 8.945.2)

$$\frac{1}{1 - 2tx + t^2} = \sum_0^\infty U_n(x)t^n, \quad (19)$$

where $U_n(\cdot)$ is the Chebyshev polynomial of the second kind of order n , in (18) to arrive at

$$Q_1(k_x, z) = \sum_{n=0}^\infty U_n \left(\frac{\cos k_x \Delta}{\sqrt{2}} \right) z^n \left[\left(1 - \frac{z}{\sqrt{2}} e^{ik_x \Delta} \right) \Gamma_1(k_x) - \frac{z}{\sqrt{2}} e^{ik_x \Delta} \Gamma_2(k_x) \right] \quad (20)$$

$$Q_2(k_x, z) = \sum_{n=0}^\infty U_n \left(\frac{\cos k_x \Delta}{\sqrt{2}} \right) z^n \left[\frac{z}{\sqrt{2}} e^{-ik_x \Delta} \Gamma_1(k_x) + \left(1 - \frac{z}{\sqrt{2}} e^{-ik_x \Delta} \right) \Gamma_2(k_x) \right]. \quad (21)$$

As with the diffusive case, the contour C_z in the inverse transform is chosen such that the zeroes of the denominator function $(1 - \sqrt{2}z \cos(k_x \Delta) + z^2)$ lie outside it. Equations (20) and (21) may be substituted into the definition of the inverse transform (6) and the integral with respect to z evaluated by making use of (8). For reasons that will become clear shortly, we are interested in the composite discrete function $\psi_d(m\Delta, s\epsilon) = q_2(m\Delta, s\epsilon) + i q_1(m\Delta, s\epsilon)$, which will be compared directly with the solution of the Schrödinger equation. The expression for ψ_d is

$$\begin{aligned} \psi_d(m\Delta, s\epsilon) = & \frac{1}{2\pi} \int_{-\pi/\Delta}^{\pi/\Delta} \left\{ U_s \left(\frac{\cos k_x \Delta}{\sqrt{2}} \right) [\Gamma_2 + i\Gamma_1(k_x)] \right. \\ & + U_{s-1} \left(\frac{\cos k_x \Delta}{\sqrt{2}} \right) [(e^{-i\pi/4}\Gamma_1(k_x) - e^{i\pi/4}\Gamma_2(k_x)) \cos(k_x \Delta) \\ & \left. + (e^{-i\pi/4}\Gamma_1(k_x) + e^{i\pi/4}\Gamma_2(k_x)) \sin(k_x \Delta)] \right\} e^{imk_x \Delta} dk_x. \end{aligned} \quad (22)$$

As in section 4.1, the integral in (22) may be evaluated efficiently by employing the iFFT algorithm. In the special case of $\Gamma_1(k_x) = 0, \Gamma_2(k_x) = K_2$, a constant, the expression provided in (22) can be further simplified. Making a change of variable $y = \cos(k_x \Delta)$

and using $dy/\sqrt{1-y^2} = -dk_x\Delta$, $\cos(m \cos^{-1} y) = T_m(y)$, where $T_m(\cdot)$ is the Chebyshev polynomial of the first kind of order m , we can show that

$$\begin{aligned} \psi_d(m\Delta, s\epsilon)\Delta &= \frac{K_2}{\pi} \int_{-1}^1 \frac{1}{\sqrt{1-y^2}} \left\{ U_s\left(\frac{y}{\sqrt{2}}\right) T_m(y) - \frac{1}{\sqrt{2}} U_{s-1}\left(\frac{y}{\sqrt{2}}\right) \right. \\ &\quad \left. \times [T_{m-1}(y) + i T_{m+1}(y)] \right\} dy. \end{aligned} \quad (23)$$

From the even and odd properties of Chebyshev polynomials, it can be deduced that for $s = 2r$ and $m = 2n - 1$ (or vice versa), the integral in (23) vanishes implying that $\psi_d[(2n-1)\Delta, 2r\epsilon] = 0$ in this special case.

Other interesting identities can be derived starting from (22). Using the relation $U_s(1/\sqrt{2}) = U_s[\cos(\pi/4)] = \sin(s\pi/4) + \cos(s\pi/4)$, one can readily see that

$$\sum_{m=-\infty}^{\infty} \psi_d(m\Delta, s\epsilon)\Delta = e^{-i\pi s/4} [\Gamma_2(0) + i\Gamma_1(0)]. \quad (24)$$

Hence, unlike $w_1\Delta$, the quantities $q_1\Delta$ and $q_2\Delta$ can be of alternating signs and do not represent true probability mass functions.

Ord [11] has shown that eight different continuous functions are embedded into the discrete functions q_1 and q_2 . We will focus on the continuous function that would result from choosing $x = 2n\Delta$, $n = 0, \pm 1, \pm 2, \dots$, and $t = 8r\epsilon$, $r = 0, 1, 2, \dots$, in the discrete functions q_1 and q_2 . We show that ψ_d satisfies the Schrödinger equation for $m = 2n$, $s = 8r$ in the limit as $\Delta \rightarrow 0$, $\epsilon \rightarrow 0$, $n \rightarrow \infty$, $r \rightarrow \infty$ such that $\Delta^2/2\epsilon = D$. The following identities [23, 27] involving Chebyshev polynomials will be utilized in subsequent development:

$$zU_{s-1}(z) = U_s(z) - T_s(z) \quad (25)$$

$$\frac{d}{dz} T_s(z) = sU_{s-1}(z) \quad (26)$$

$$T_s\left(\frac{1}{\sqrt{2}}\right) = \cos\left(\frac{\pi s}{4}\right), \quad (1-z^2)T_s''(z) - zT_s'(z) + s^2T_s(z) = 0 \quad (27)$$

$$U_{s-1}\left(\frac{1}{\sqrt{2}}\right) = \sqrt{2}\sin\left(\frac{\pi s}{4}\right), \quad (1-z^2)U_s''(z) - 3zU_s'(z) + s(s+2)U_s(z) = 0, \quad (28)$$

where a prime denotes differentiation with respect to the argument. For the purpose of investigating the continuum limits, we would like to cast (22) in a form more suitable for asymptotic analysis. The last term in (22) involving $U_{s-1}(\cdot)$ can be replaced with $dT_s(\cdot)/dk_x$ on using the second relation (26) to yield

$$\frac{\sin k_x\Delta}{\sqrt{2}} U_{s-1}\left(\frac{\cos k_x\Delta}{\sqrt{2}}\right) = \frac{-1}{s\Delta} \frac{d}{dk_x} T_s\left(\frac{\cos k_x\Delta}{\sqrt{2}}\right). \quad (29)$$

This term is then integrated by parts and simplified using the periodicity condition $\Gamma_j(\pi/\Delta) = \Gamma_j(-\pi/\Delta)$, $j = 1, 2$. A convenient expression for the evaluation of $\psi_d(m\Delta, s\epsilon)$ is then obtained as

$$\begin{aligned} \psi_d(m\Delta, s\epsilon) &= \frac{1}{2\pi} \int_{-\pi/\Delta}^{\pi/\Delta} e^{imk_x\Delta} \left\{ [\Gamma_1(k_x) - i\Gamma_2(k_x)] U_s\left(\frac{\cos k_x\Delta}{\sqrt{2}}\right) \right. \\ &\quad + (1+i) \left(\left[1 + i\frac{m}{s} \right] \Gamma_2(k_x) + \left[i + \frac{m}{s} \right] \Gamma_1(k_x) \right) T_s\left(\frac{\cos k_x\Delta}{\sqrt{2}}\right) \\ &\quad \left. + \frac{1+i}{s\Delta} [\Gamma'_2(k_x) - i\Gamma'_1(k_x)] T_s\left(\frac{\cos k_x\Delta}{\sqrt{2}}\right) \right\} dk_x, \end{aligned} \quad (30)$$

which is also more amenable to asymptotic analysis than (22). In the special case of $\Gamma_1(k_x) = 0, \Gamma_2(k_x) = K_2$ and for $m/s \rightarrow 0$ (small spatial locations and large times) we move on using (25) that

$$\psi_d(m\Delta, s\epsilon) = \frac{K_2}{2\pi} \int_{-\pi/\Delta}^{\pi/\Delta} e^{imk_x\Delta} \left[T_s \left(\frac{\cos k_x \Delta}{\sqrt{2}} \right) - i \frac{\cos k_x \Delta}{\sqrt{2}} U_{s-1} \left(\frac{\cos k_x \Delta}{\sqrt{2}} \right) \right] dk_x. \quad (31)$$

We now perform an asymptotic analysis for small $k_x \Delta$ in (31) and show that $\psi_d(2n\Delta, 8r\epsilon)$ satisfies the Schrödinger equation. To this end, we note the following Taylor series expansions which are obtained by making use of (26)–(28):

$$\cos k_x \Delta \sim 1 - \frac{k_x^2 \Delta^2}{2} + \frac{(k_x \Delta)^4}{4!} + \dots \quad (32)$$

$$\begin{aligned} T_s \left(\frac{\cos k_x \Delta}{\sqrt{2}} \right) &\sim \cos \left(\frac{\pi s}{4} \right) - \frac{k_x^2 \Delta^2 s}{2} \sin \left(\frac{\pi s}{4} \right) - \frac{(k_x \Delta)^4 s^2}{4!} \\ &\times \left[3 \cos \left(\frac{s\pi}{4} \right) - \frac{4}{s} \sin \left(\frac{s\pi}{4} \right) \right] + \dots \end{aligned} \quad (33)$$

$$\begin{aligned} \frac{1}{\sqrt{2}} U_{s-1} \left(\frac{\cos k_x \Delta}{\sqrt{2}} \right) &\sim \sin \left(\frac{\pi s}{4} \right) + \frac{k_x^2 \Delta^2 s}{2} \left[\cos \left(\frac{\pi s}{4} \right) - \frac{1}{s} \sin \left(\frac{\pi s}{4} \right) \right] \\ &+ \frac{(k_x \Delta)^4}{4!} \left[(10 - 3(s^2 - 1)) \sin \left(\frac{\pi s}{4} \right) - 10s \cos \left(\frac{\pi s}{4} \right) \right] + \dots \end{aligned} \quad (34)$$

Inserting (32)–(34) into (31) and choosing $s = 8r, \Delta^2 = 2D\epsilon, s\epsilon = t, m\Delta = x, s \rightarrow \infty, m \rightarrow \infty, \Delta \rightarrow 0, \epsilon \rightarrow 0$, we arrive at the desired result:

$$\begin{aligned} \psi_d(x, t) &= q_2(x, t) + iq_1(x, t) \sim \frac{K_2}{2\pi} \int_{-\infty}^{\infty} \left(1 - iDk_x^2 t - \frac{k_x^4 D^2 t^2}{2!} + \dots \right) e^{ik_x x} dk_x \\ &= \frac{K_2}{2\pi} \int_{-\infty}^{\infty} e^{-iDk_x^2 t} e^{ik_x x} dk_x. \end{aligned} \quad (35)$$

Equation (35) is the spectral representation of the Green's function corresponding to the Schrödinger equation $\partial\psi/\partial t = iD\partial^2\psi/\partial x^2$ with the impulsive initial condition $\psi(x, t = 0^+) = K_2\delta(x)$. It has the exact solution

$$\psi(x, t) = \frac{K_2}{\sqrt{4\pi iDt}} e^{ix^2/4Dt}. \quad (36)$$

To reinforce to the reader that the plots of the transitional probabilities (q_1, q_2) do resemble the solutions of the free Schrödinger equation, we show in figure 2a comparison of the real, \Re , and imaginary, \Im , parts of the exact solution (36) of the Schrödinger equation with the partial solution (q_1, q_2) of the 4RW. The numerical solutions shown in the figure for ψ_d are on a discrete spacetime ($x = m\Delta, t = s\epsilon$) and have been computed using (31) with the iFFT algorithm [22] with size $s = 2^{13} = 8192$. It is seen that the 4RW produces solutions of oscillatory type with both positive and negative excursions for the expectations q_1 and q_2 , which are in excellent agreement with the analytical results for small $\frac{m}{s}$. This is in contrast to the quantity w_1 shown in figure 1, which, behaving like the solution of the diffusion equation, decays exponentially in space and always remains positive.

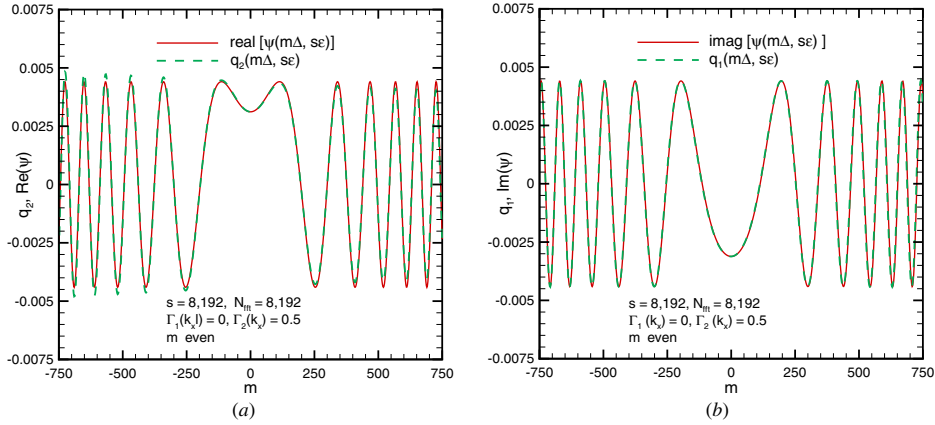


Figure 2. Comparison of the exact solution of Schrödinger equation with the discrete solution of a 4RW for an impulsive initial condition. (a) $q_2(m\Delta, s\epsilon)$, $\text{Re}\{\psi(m\Delta, s\epsilon)\}$ and (b) $q_1(m\Delta, s\epsilon)$, $\text{Im}\{\psi(m\Delta, s\epsilon)\}$.

5. Summary

By considering a multistate random walk on a discrete lattice, expressions have been derived for the various transitional probabilities using the concept of generating functions. A 2D transform involving Fourier transformation in space and the z -transformation in time is employed to accomplish this. The transitional probabilities governing particle motion are expressed in terms of integrals involving trigonometric functions in the case of the diffusion equation, and involving Chebyshev polynomials of the first and second kinds in the case of the Schrödinger equation. Closed-form expressions have been given for particular cases of the initial conditions. The continuum limits of the diffusion equation and Schrödinger equation have been shown to follow directly from these transitional probabilities through the performance of appropriate asymptotic analysis. The present analysis consisting of the z -transform along the time axis and Fourier transform along the spatial axis is most suitable for studying linear difference equations with constant coefficients. In the 4RW model, this would correspond to the free Schrödinger equation. The important extension of this analysis to higher dimensions is worth exploring and would be taken up in the future. The incorporation of a smooth potential field in the Schrödinger equation into the 4RW model has already been addressed by Ord in [19] and the study of its transitional probabilities will be taken up in a separate paper using a different approach.

Acknowledgments

This work was funded in part by the US Army Research Office under ARO grant W911NF-04-1-0228 and by the Center for Advanced Sensor and Communication Antennas, University of Massachusetts at Amherst, under the US Air Force Research Laboratory Contract FA8718-04-C-0057.

References

- [1] Nelson E 1966 Derivation of the Schrödinger equation from Newtonian mechanics *Phys. Rev.* **150** 1079–85

- [2] Nelson E 2001 *Dynamical Theories of Brownian Motion* 2nd edn (Princeton, NJ: Princeton University Press) web edition at <http://www.math.princeton.edu/nelson/books.html>
- [3] Nelson E 1985 *Quantum Fluctuations* (Princeton, NJ: Princeton University Press)
- [4] Nagasawa M 1993 *Schrödinger Equations and Diffusion Theory* (Boston: Birkhäuser)
- [5] Nagasawa M 2000 *Stochastic Processes in Quantum Physics* (Boston: Birkhäuser Verlag)
- [6] Nottale L and Schneider J 1984 Fractals and non-standard analysis *J. Math. Phys.* **25** 1296–300
- [7] Ord G N 1983 Fractal spacetime: a geometric analogue of relativistic quantum mechanics *J. Phys. A: Math. Gen.* **16** 1869–84
- [8] Nottale L 1995 Scale relativity, fractal space-time and quantum mechanics *Quantum Mechanics, Diffusion and Chaotic Fractals* ed M S El Naschie, O E Rossler and I Prigogine (New York: Elsevier)
- [9] El Naschie M S 1995 Quantum measurement, information, diffusion and cantorian geodesics *Quantum Mechanics, Diffusion and Chaotic Fractals* ed M S El Naschie, O E Rossler and I Prigogine (New York: Elsevier Science)
- [10] Ord G N 1996 The Schrödinger and diffusion propagators coexisting on a lattice *J. Phys. A: Math. Gen.* **29** L123–8
- [11] Ord G N and Deakin A S 1996 Random walks, continuum limits, and Schrödinger's equation *Phys. Rev. A* **154** 3772–78
- [12] Ord G N and Deakin A S 1997 Random walks and Schrödinger's equation in (2+1) dimensions *J. Phys. A: Math. Gen.* **30** 819–30
- [13] Aharonov Y, Davidovich L and Zagury N 1993 Quantum random walks *Phys. Rev. A* **48** 1687–90
- [14] Aslangul C 2005 Quantum dynamics of a particle with a spin-dependent velocity *J. Phys. A: Math. Gen.* **38** 1–16
- [15] Jensen F B, Kuperman W A, Porter M B and Schmidt H 1994 *Computational Ocean Acoustics* (New York: Springer)
- [16] Levy M F 2000 *Parabolic Equation Methods for Electromagnetic Wave Propagation* (London: IEE Press)
- [17] Budaev B V and Bogy D B 2002 Application of random walk methods to wave propagation *Quart. J. Mech. Appl. Math.* **55** 206–26
- [18] Janaswamy R 2007 Solution of BVPs in electrodynamics by stochastic methods *IEEE Applied Electromagnetics Conf.* vol 1 (*Kolkata, India, 19–20 Dec. 2007*)
- [19] Ord G N 1996 Schrödinger's equation and discrete random walks in a potential field *Ann. Phys.* **250** 63–8
- [20] Montroll E W 1965 Random walks on lattices-II *J. Math. Phys.* **6** 167–81
- [21] Barber M N and Ninham B W 1970 *Random and Restricted Walks* (New York: Gordon and Breach)
- [22] Rabiner R R and Gold B 1975 *Theory and Application of Digital Signal Processing* (Englewood Cliffs, NJ: Prentice-Hall)
- [23] Gradshteyn I S and Ryzhik I S 2000 *Table of Integrals, Series, and Products* 6th edn (New York: Academic)
- [24] Feller W 1970 *An Introduction to Probability Theory and Its Applications* vol II 2nd edn (New York: Wiley)
- [25] van Kampen N G 2007 *Stochastic Processes in Physics and Chemistry* 3rd edn (New York: North-Holland)
- [26] Barton G 1989 *Elements of Green's Functions and Propagation* (New York: Oxford University Press)
- [27] Abramowitz M and Stegun I A 1970 *Handbook of Mathematical Functions* (New York: Dover)

Transitional probabilities for the four-state random walk on a lattice in the presence of partially reflecting boundaries

R. Janaswamy^{a)}

*Department of Electrical and Computer Engineering, University of Massachusetts, 100
Natural Resources Road, 215-D Marcus Hall, Amherst, Massachusetts 01003, USA*

(Received 12 November 2008; accepted 24 March 2009; published online 5 May 2009)

The four-state random walk (4RW) model, wherein the particle is endowed with two states of spin and two states of directional motion in each space coordinate, permits a stochastic solution of the Schrödinger equation (or the equivalent parabolic equation) without resorting to the usual analytical continuation in complex space of the particle trajectories. Analytical expressions are derived here for the various transitional probabilities in a 4RW by employing generating functions and eigenfunction expansions when the particle moves on a 1+1 space-time lattice with two-point boundary conditions. The most general case of dissimilar boundaries with partially reflecting boundary conditions is treated in this paper. The transitional probabilities are all expressed in terms of a finite summation involving trigonometric functions and/or Chebyshev polynomials of the second kind that are characteristics of diffusion and Schrödinger equations, respectively, in the 4RW model. Results for the special case of perfectly absorbing boundaries are compared to numerical values obtained by directly counting paths in the random walk simulations. © 2009 American Institute of Physics. [DOI: [10.1063/1.3122768](https://doi.org/10.1063/1.3122768)]

I. INTRODUCTION

The four-state random walk (4RW) model, wherein a particle undergoing random walk is endowed with two states of direction (in a one-dimensional case) and two states of spin or parity, was considered by Ord and Deakin¹ to arrive at a macroscopic model for the Schrödinger equation and physically interpret its wavelike solutions. It was shown in that paper that both the traditional diffusion equation as well as the Schrödinger equation were embedded in the same physical model. The usual diffusion process is contained in the overall sum of all particle paths irrespective of their direction and parity, while the wavelike behavior of the Schrödinger equation is contained in the differences in densities of the right-going particles or left-going particles with opposite parity. The 4RW model owes its existence to the Feynman chessboard model as elaborated in Ref. 2 and is also useful in solving practical electromagnetic, acoustic, and optical boundary value problems for the complex field amplitude when a stochastic approach is used to treat the governing *parabolic equation*. (In the applied sciences area, the parabolic equation is sometimes referred to as the parabolic wave equation.) The standard parabolic equation used in such time-harmonic problems contains partial derivatives with respect to the spatial coordinates only, where the spatial coordinate along the axial direction takes the place of the time variable in the time-dependent Schrödinger equation. Furthermore, the potential function present in the Schrödinger equation is replaced by the medium refractive-index term in the parabolic equation. The parabolic equation is obtained when the Helmholtz equation describing the true field is subject to a one-way propagation with a subsequent application of the paraxial approximation.^{3,4} Normally one needs to resort to analytical continuation of boundary data, as is done in Ref. 5, when the parabolic equation is

^{a)}Electronic mail: janaswamy@ecs.umass.edu.

solved numerically using a stochastic approach. The resulting random walks will then traverse a complex-valued space, which, in turn, calls for analytical continuation of boundary data and the spatial geometry.⁶ However, the 4RW model permits a solution to these problems without such analytical continuations.

In a previous paper,⁷ the author developed expressions for the various transitional probabilities for the 4RW on a discrete lattice for spatially unbounded case. In addition to detailing a method for arriving at the transitional probabilities, the results presented therein could also be useful in determining other stochastic quantities of interest such as the first passage time probabilities, expected number of visits to a given site, and maximum excursions of a random walk on a line for various linear combinations of these probabilities. In developing numerical schemes for solving boundary value problems with complex geometries, it is desirable to have analytical solutions for simpler geometries to facilitate validation against benchmark problems.⁸ The traditional way to discretize the Schrödinger equation or the diffusion equation for numerical treatment by the finite difference method is to employ a central difference formula in the spatial coordinates. An example of this is the implicit Crank–Nicolson scheme, which, for the diffusion equation, can be identified with the traditional two-state random walk, where the particle is endowed with two directions of motion only. Analytical results for the traditional two-state random walk with perfectly absorbing and/or reflecting boundaries have been treated in number of works including Refs. 9 and 10. Separately, the case of the telegraph equation with partially reflecting boundaries is studied in Ref. 11. No such analytical results are yet available for the 4RW model and it is the purpose of the present paper to provide analytical results for a benchmark initial-boundary-value problem in 1 + 1 space-time dimension for the model. To this end, we extend the results in Ref. 7 by considering two-point boundary conditions for the 4RW model and derive analytical expressions for various transitional probabilities. Setting aside the fact that the 4RW model has a physical basis in the Feynman chessboard model and that various transitional probabilities are related to the solution of the continuous Schrödinger equation, it is not at all obvious at the outset from the governing difference equations that an analytical solution is possible for the said boundary value problem, particularly for the wavelike solutions. The transform approach utilized in this paper will reveal the presence of the discrete Laplacian operator that is embedded in these equations and will clearly demonstrate why such a solution is still possible, while paving the way for eigenfunction expansion. This will be elaborated in Secs. II and III. The most general case of partially absorbing and dissimilar boundaries is considered in this paper. Results for the special cases of perfectly absorbing and perfectly reflecting boundaries are also provided in the paper. The results presented here correspond to the solution of the discrete form of the diffusion equation as well as to the real and imaginary parts of the discrete Schrödinger equation.

In Sec. II, the 4RW model is briefly reviewed, and the problem under investigation is defined. In Sec. III, the solution to the 4RW model subject to the general boundary conditions is developed using the concept of generating functions and eigenfunction expansion. Expressions are provided for the special cases of perfectly reflecting and perfectly absorbing boundaries and the results for the latter are compared to numerical simulations obtained by directly counting paths. Finally, conclusions and topics of further research are given in Sec. IV. It may be noted parenthetically that it is not our purpose here to evaluate other various models that have been put forward to physically interpret the Schrödinger equation, a topic that is immensely interesting in its own right.

II. 4RW MODEL

For a particle moving on a discrete lattice and subject to random collisions, the transitional probabilities considered in Ref. 7 at the discrete space-time point ($x=m\Delta, t=s\epsilon$) are of the form

$$E_t \begin{pmatrix} w_1 \\ w_2 \end{pmatrix} = \frac{1}{2} \begin{pmatrix} (E_x + E_x^{-1}) & -(E_x - E_x^{-1}) \\ 0 & 0 \end{pmatrix} \begin{pmatrix} w_1 \\ w_2 \end{pmatrix}, \quad (1)$$

$$E_t \begin{pmatrix} q_1 \\ q_2 \end{pmatrix} = \frac{1}{\sqrt{2}} \begin{pmatrix} E_x^{-1} & -E_x \\ E_x^{-1} & E_x \end{pmatrix} \begin{pmatrix} q_1 \\ q_2 \end{pmatrix}, \quad (2)$$

where $q_1(m\Delta, s\epsilon) = 2^{s/2}[p_1(m\Delta, s\epsilon) - p_3(m\Delta, s\epsilon)]$, $q_2(m\Delta, s\epsilon) = 2^{s/2}[p_2(m\Delta, s\epsilon) - p_4(m\Delta, s\epsilon)]$, $w_1(m\Delta, s\epsilon) = [p_1(m\Delta, s\epsilon) + p_2(m\Delta, s\epsilon) + p_3(m\Delta, s\epsilon) + p_4(m\Delta, s\epsilon)]$, $w_2(m\Delta, s\epsilon) = [p_1(m\Delta, s\epsilon) + p_3(m\Delta, s\epsilon)] - [p_2(m\Delta, s\epsilon) + p_4(m\Delta, s\epsilon)]$, and $p_\mu(m\Delta, s\epsilon)\Delta$, $\mu=1, \dots, 4$, is the probability that a particle is in state μ at the space-time point $(m\Delta, s\epsilon)$, $m=0, \pm 1, \pm 2, \dots$, $s=0, 1, \dots$. The particle changes its direction of motion with every collision, but changes its parity or spin at every other collision. The combination of two directions of motion and two states of spin constitute the four states in the model. It has been shown in Refs. 1 and 12 that such a four-state random walk simultaneously encompasses the diffusion as well as Schrödinger equations. The quantities w_1 and w_2 pertain to the diffusion process, while q_2 and q_1 correspond to the real and imaginary parts of the Schrödinger wave function in the discrete case. We will refer to (1) as the diffusion equation and to (2) as the Schrödinger equation even though they are really the respective discrete counterparts of the traditional diffusion and Schrödinger equations. The operators E_x and E_t are, respectively, the spatial and temporal advancing operators and are defined mathematically as $E_x^{\pm 1} p_\mu(m\Delta, s\epsilon) = p_\mu[(m \pm 1)\Delta, s\epsilon]$ and $E_t p_\mu(m\Delta, s\epsilon) = p_\mu[m\Delta, (s+1)\epsilon]$. It is assumed in Eqs. (1) and (2) that the probability that a particle maintains its direction at the next time step remains the same as the probability that it will change its direction at the next time step and that the probability of remaining at the same location at the next time step is zero. If the number of right-going particles is the same as those going to the left at time $t=0$, then $w_2 \equiv 0$ and Eq. (1) reduces to the simpler equation

$$E_t w_1 = D_x w_1, \quad (3)$$

where $D_x = (E_x + E_x^{-1})/2$ is the discrete averaging operator. The averaging operator in (3) owes its existence to the presence of the Laplacian operator in the continuous diffusion equation $\partial w_1 / \partial t = D_1 \partial^2 w_1 / \partial x^2$ when the spatial and temporal step sizes are subject to the condition $\Delta = \sqrt{2\epsilon D_1}$. As such, most of the well-posed issues that pertain to the continuous case¹³ will be carried over to the discrete case. In particular, Eq. (3) will be well posed with two-point Robin type of boundary conditions and the solution will exist.

The difference equations (1) and (2) are assumed to be valid in the region $0 < m < \ell$ and $s > 0$ and they are supplemented by an initial condition at $s=0$ and boundary conditions at $m=0, \ell$. We will adopt the abbreviation $v(m, s)$ to denote the discrete function $v(m\Delta, s\epsilon)$. The boundary conditions we are interested in are of the form

$$p_j(0, s) - \alpha_1 p_j(1, s) = 0 \quad \text{and} \quad p_j(\ell, s) - \alpha_2 p_j(\ell - 1, s) = 0, \quad j = 1, \dots, 4, \quad (4)$$

where the constants α_1 and α_2 are assumed to be real and positive. These are the discrete versions of the general Robin type of boundary conditions for the continuous case. The case of purely absorbing boundaries at $m=0, \ell$ is characterized by $\alpha_i=0$, $i=1, 2$, while the purely reflecting case is characterized by $\alpha_i=1$, $i=1, 2$.^{9,14} The general case corresponds to partially absorbing and partially reflecting boundaries with different degrees of absorption at the two ends. Our interest is to obtain analytical solutions to (1) and (2) on a discrete space-time lattice $(m\Delta, s\epsilon)$ subject to the boundary conditions in (4). In contrast to the diffusion equation (3), it is not clear at the outset whether a solution will exist for (2) under the boundary condition (4), setting aside the fact that it is tied to the Schrödinger equation. This is because of the presence of the spatial shift operators that are neither symmetric (as in the operator D_x) nor asymmetric (as in an operator of the form $V_x = [E_x - E_x^{-1}]$). Recall, for instance, that the diffusion equation with a drift term, whose discrete counterpart will have neither a symmetric nor an asymmetric spatial operator, will not always have a solution even with Neumann type of boundary conditions. However, we will demonstrate in Sec. III that the temporally transformed equation corresponding to (2) will indeed contain the averaging operator and the existence question will be set to rest. Because of the linearity of Eqs. (1) and (2),

a convenient solution can be obtained by using generating function and integral transform techniques as outlined in Refs. 7 and 15.

III. SOLUTION BY GENERATING FUNCTIONS

In the following, we assume complete symmetry between the right-moving and left-moving particles so that $w_2 \equiv 0$. Consider a function $v(m\Delta, s\epsilon)$ and its temporal transform $\hat{v}(m\Delta, z)$ as defined in Ref. 7,

$$\hat{v}(m\Delta, z) = \sum_{s=0}^{\infty} v(m\Delta, s\epsilon) z^s \equiv \mathcal{T}v. \quad (5)$$

The quantity $\hat{v}(m\Delta, z)$ may be thought of as the discrete version of the Laplace transform of v and is simply referred to as the z -transform. The inverse relation is defined as

$$v(m\Delta, s\epsilon) = \frac{1}{2\pi i} \oint_{C_z} \frac{\hat{v}(m\Delta, z)}{z^{s+1}} dz \equiv \mathcal{T}^{-1}\hat{v}, \quad (6)$$

where C_z is a closed contour around the origin in the complex z -plane that encloses only the singularities at the origin, $i=\sqrt{-1}$, and the symbol \mathcal{T} denotes the temporal transform. The transformed variable $\hat{v}(m\Delta, z)$ is also referred to as the *generating function* within the random walk community.⁹ Applying the temporal transform to (2) and (3) and making use of the shift property of the \mathcal{T} transform ($\mathcal{T}[E_t v_1] = z^{-1}[\hat{v}_1(m\Delta, z) - v_1(m, 0)]$) and carrying out some simplifications, we arrive at the following equations for various generating functions in terms of the initial conditions:

$$[1 - zD_x]\hat{v}_1(m\Delta, z) = w_1(m, 0), \quad (7)$$

$$[1 - \sqrt{2}zD_x + z^2]\hat{q}_1(m\Delta, z) = q_1(m, 0) - \frac{z}{\sqrt{2}}E_x[q_2(m, 0) + q_1(m, 0)], \quad (8)$$

$$[1 - \sqrt{2}zD_x + z^2]\hat{q}_2(m\Delta, z) = q_2(m, 0) - \frac{z}{\sqrt{2}}E_x^{-1}[q_2(m, 0) - q_1(m, 0)]. \quad (9)$$

The characteristic operators that appear on the left hand sides of (7)–(9) are generic to the diffusion and the Schrödinger equations under the 4RW model and are seen to be completely independent of the boundary conditions. A remarkable feature of the spatial dependence of these operators, which is not entirely evident in the initial Eq. (2) describing the transitional probabilities, is that they all involve only the averaging operator D_x that is the discrete counterpart of the Laplacian operator in the continuous case. Such a relation has already been alluded to in Sec. II. Both the diffusion and the Schrödinger equations contain the Laplacian operator as far as the spatial variables are concerned, and the transformation from the continuous case to the discrete case for a given order of accuracy is not unique. Employing a central difference formula for the spatial operator will lead to Crank–Nicolson type of discrete equations,⁸ which, like the 4RW model, result in a spatially second order accurate schemes. The important point to note from (9) is that the unknown variable contains only the averaging operator D_x and that any other asymmetries that arise from E_x or E_x^{-1} alone are contained only on the right hand side, operating on the known initial conditions. A formal solution to Eqs. (7)–(9) can be affected by using the inverse relation (6) and evaluating the integrals in the complex z -plane after expanding the reciprocal of the characteristic operators in a Maclaurin series. [Recall that the contour integral in the inverse operator in (6) is a closed loop of vanishing size around the origin]. The procedure is similar to that outlined in Ref. 7 and will involve Chebyshev polynomials of the second kind for the wave functions q_1 and q_2 . The result is

$$w_1(m,s) = D_x^s w_1(m,0), \quad (10)$$

$$q_1(m,s) = U_s\left(\frac{D_x}{\sqrt{2}}\right)q_1(m,0) - \frac{1}{\sqrt{2}}U_{s-1}\left(\frac{D_x}{\sqrt{2}}\right)E_x[q_2(m,0) + q_1(m,0)], \quad (11)$$

$$q_2(m,s) = U_s\left(\frac{D_x}{\sqrt{2}}\right)q_2(m,0) - \frac{1}{\sqrt{2}}U_{s-1}\left(\frac{D_x}{\sqrt{2}}\right)E_x^{-1}[q_2(m,0) - q_1(m,0)], \quad (12)$$

where $U_s(x)$ is Chebyshev polynomial of the second kind of order s and argument x . The formal solution given in (10)–(12) are general enough and are valid for all appropriate boundary conditions. The presence of the operator D_x^s in the diffusion variable $w_1(m,s)$ is not surprising at all. Indeed, in free space, (10) directly generates the *characteristic function* $\cos^s \theta$ of the probability w_1 when $w_1(m,0)$ is expanded in a Fourier series with transform variable θ . By the same token, the appearance of the polynomials $U_s(\cdot)$ and $U_{s-1}(\cdot)$ is intrinsic to the Schrödinger equation in the 4RW model, as already indicated previously. Note that the operators D_x (or any power of it) and E_x commute and the order of these terms on the right hand sides of (11) and (12) is not important. To complete the solution, we must now expand the unknown functions in terms of eigenfunctions of the D_x operator that are consistent with the boundary conditions at $m=0,\ell$. In free space, the appropriate eigenfunctions are plane waves with a continuous wavenumber as adopted in Ref. 7 (or said in other words, the unknown function is represented in terms of its Fourier transform or series).

For the boundary conditions indicated as in (4), we seek an expansion of a spatial function $v(m)$ in terms of exponential and/or trigonometric functions. An exponential function of the form $v_0(m)=r^m$ is a valid eigenfunction provided that the base $r=\alpha_1^{-1}=\alpha_2$. Clearly this is only possible in the special case of $\sqrt{\alpha_1\alpha_2}:=\alpha_g=1$, where α_g denotes the geometric mean of α_1 and α_2 . In such a case, $D_x v_0(m)=0.5(\alpha_1+\alpha_2)v_0(m):=\alpha_a \cdot v_0(m)$, where α_a , being the arithmetic mean of α_1 and α_2 , is the eigenvalue pertaining to $v_0(m)$. When $\alpha_g \neq 1$, such an exponential function will not exist. We will denote the presence of this exponential function by employing the Kronecker symbol $\delta_{\alpha_g}^1$. A harmonic function of the form

$$u_j(m) = A_j \sin(k_j m) + B_j \cos(k_j m), \quad j = 1, 2, \dots \quad (13)$$

is also a valid eigenfunction provided that

$$B_j(1 - \alpha_1 \cos k_j) = A_j \alpha_1 \sin k_j \quad (14)$$

with the spatial frequency k_j given by

$$\sin(k_j \ell) - 2\alpha_a \sin[k_j(\ell - 1)] + \alpha_g^2 \sin[k_j(\ell - 2)] = 0. \quad (15)$$

Equations (14) and (15) are obtained by enforcing the boundary condition (4) at the two ends. A trivial solution of Eq. (15) is $k_j=0$. There will be a total of $(\ell-1)$ nontrivial solutions of (15), thus constituting a total of ℓ distinct eigenfunctions [including the function $v_0(m)$] to represent the solution of (9) and (12) at the points $m=0, \dots, \ell$. Making use of (14) in (13) allows us to extract a bare eigenfunction $v_j(m)$ (i.e., without the coefficient A_j and other common factors) in the form

$$v_j(m) = \sin(k_j m) - \alpha_1 \sin[k_j(m-1)], \quad (16)$$

with the spatial frequency set by (15) for a given α_1 , α_2 , and ℓ . It can be easily verified that $D_x v_j(m)=\cos k_j \cdot v_j(m)$ so that the eigenvalue of $v_j(m)$ with respect to the averaging operator is $\cos k_j$. Furthermore, the eigenfunctions $v_j(m)$ with distinct k_j as well as $v_j(m)$ and $v_0(m)$ are mutually orthogonal, i.e.,

$$\sum_{m=1}^{\ell-1} v_i(m)v_j(m) = 0, \quad i, j = 1, \dots, \ell-1, \quad i \neq j, \quad (17)$$

$$\sum_{m=1}^{\ell-1} v_j(m)v_0(m) = 0, \quad j = 1, \dots, \ell-1. \quad (18)$$

The following normalization results can also be readily established for the functions $v_0(m)$ and $v_j(m)$:

$$\sum_{m=1}^{\ell-1} v_0^2(m) = \frac{\alpha_1^{-2(\ell-1)} - 1}{1 - \alpha_1^2} := 1/a_0 \quad (19)$$

and

$$\begin{aligned} \sum_{m=1}^{\ell-1} v_j^2(m) &= \frac{\sin(k_j\ell)}{\sin k_j} \left[\alpha_1 \cos[k_j(\ell-2)] - \frac{1}{2}(1 + \alpha_1^2) \cos[k_j(\ell-1)] \right] + \frac{\ell(1 + \alpha_1^2)}{2} - \alpha_1 \ell \cos k_j \\ &\quad - \alpha_1^2 \sin^2[k_j(\ell-1)] := 1/a_j. \end{aligned} \quad (20)$$

Gathering all of the above results, an arbitrary function $v(m)$ satisfying the boundary condition (4) will admit a spectral representation of the form

$$v(m) = A_0 v_0(m) \delta_{\alpha_g}^l + \sum_{j=1}^{\ell-1} A_j v_j(m), \quad (21)$$

where the coefficients A_0 and A_j of the basis functions $v_0(m)$ and $v_j(m)$ can be obtained in terms of the function $v(m)$ via the orthogonality conditions and normalization relations (17)–(20),

$$A_0 = a_0 \sum_{m=1}^{\ell-1} v_0(m)v(m), \quad (22)$$

$$A_j = a_j \sum_{m=1}^{\ell-1} v_j(m)v(m), \quad j = 1, \dots, \ell-1. \quad (23)$$

With this spectral representation, it is clear that

$$D_x v(m) = A_0 \alpha_a \cdot v_0(m) \delta_{\alpha_g}^l + \sum_{j=1}^{\ell-1} A_j \cos k_j \cdot v_j(m). \quad (24)$$

Hence, the presence of D_x in the spatial domain is accounted for by multiplying the spectral basis function term by its respective eigenvalue. In particular,

$$D_x^s v(m) = A_0 \alpha_a^s \cdot v_0(m) \delta_{\alpha_g}^l + \sum_{j=1}^{\ell-1} A_j \cos^s k_j \cdot v_j(m) \quad (25)$$

and

$$U_s \left(\frac{D_x}{\sqrt{2}} \right) v(m) = A_0 U_s \left(\frac{\alpha_a}{\sqrt{2}} \right) \cdot v_0(m) \delta_{\alpha_g}^l + \sum_{j=1}^{\ell-1} A_j U_s \left(\frac{\cos k_j}{\sqrt{2}} \right) \cdot v_j(m). \quad (26)$$

Having laid out the formulation for the general case, we will now consider two interesting special cases which will merit a separate discussion.

A. Totally absorbing boundaries

In this case $\alpha_1=\alpha_2=0$, which precludes the exponential solution $v_0(m)$. Equation (15) implies a solution $k_j=\pi j/\ell$, $j=1, \dots, \ell-1$. The eigenfunctions $v_j(m)$ will be reduced to $\sin(\pi jm/\ell)$ and $a_j=2/\ell$ from (20). In this case, one gets the discrete sine transform¹⁶ representation for a function satisfying Dirichlet boundary conditions,

$$v(m) = \sum_{j=1}^{\ell-1} A_j \sin\left(\frac{j\pi m}{\ell}\right), \quad A_j = \frac{2}{\ell} \sum_{m=1}^{\ell-1} v(m) \sin\left(\frac{j\pi m}{\ell}\right), \quad j = 1, \dots, \ell-1. \quad (27)$$

B. Totally reflecting boundaries

For totally reflecting boundaries at both ends, $\alpha_1=\alpha_2=1$, which dictate that $\alpha_g=\alpha_a=1$. Equation (15) indicates a solution $k_j=j\pi/(\ell-1)$, $j=1, \dots, \ell-1$. The exponential function now reduces to a constant function $v_0(m)=1$. The normalization constants a_0 and a_j are obtained from (19) and (20) as

$$1/a_0 = (\ell-1), \quad 1/a_j = 2(\ell-1) \sin^2\left(\frac{\pi j}{2(\ell-1)}\right). \quad (28)$$

An unknown function $v(m)$ satisfying perfectly reflecting conditions at the two ends can then be expressed as

$$\begin{aligned} v(m) &= A_0 + \sum_{j=1}^{\ell-1} A_j \left[\sin\left(\frac{\pi jm}{\ell-1}\right) - \sin\left(\frac{\pi j(m-1)}{\ell-1}\right) \right] = A_0 + \sum_{j=1}^{\ell-1} 2A_j \sin\left(\frac{\pi j}{2(\ell-1)}\right) \cos\left(\frac{\pi j(m-\frac{1}{2})}{\ell-1}\right) \\ &:= A_0 + \sum_{j=1}^{\ell-1} C_j \cos\left(\frac{\pi j(m-\frac{1}{2})}{\ell-1}\right) \end{aligned} \quad (29)$$

with the coefficients given by

$$A_0 = \frac{2}{\ell-1} \sum_{m=1}^{\ell-1} v(m), \quad C_j = \frac{2}{\ell-1} \sum_{m=1}^{\ell-1} \cos\left(\frac{\pi j(m-\frac{1}{2})}{\ell-1}\right) v(m), \quad j = 1, \dots, \ell-1. \quad (30)$$

Equations (29) and (30) constitute the discrete-cosine-transform (Ref. 16) representation of a function satisfying Neumann type of boundary conditions at the end points.

C. Solution for general case

The results given in (25) and (26) will now be used to determine the Green's function¹³ of the diffusion equation (10) and the Schrödinger equations (11) and (12). The linearity of the governing equations with respect to the initial conditions enables the solution to arbitrary initial conditions in terms of this Green's function. To this end we consider initial conditions of the form $p_\mu(m, 0)\Delta = P_{\mu 0}\delta_m^{n_0}$, $1 \leq m_0 \leq \ell-1$, where $\sum_{\mu=1}^4 P_{\mu 0} = 1$. This initial condition corresponds to the case where the particles are released from the location m_0 in a state μ with probability $P_{\mu 0}$. Letting $\Gamma_1 = (P_{10} - P_{30})/\Delta$ and $\Gamma_2 = (P_{20} - P_{40})/\Delta$, it is clear from the definitions that $w_1(m, 0) = \delta_m^{n_0}$, $q_1(m, 0) = \Gamma_1 \delta_m^{n_0}$, and $q_2(m, 0) = \Gamma_2 \delta_m^{n_0}$. Using the spectral representation given in (21)–(23) for the functions $w_1(m, 0)$, $q_1(m, 0)$, and $q_2(m, 0)$, we arrive at

$$w_1(m, 0) = a_0 v_0(m_0) v_0(m) \delta_{\alpha_g}^1 + \sum_{j=1}^{\ell-1} a_j v_j(m_0) v_j(m), \quad (31)$$

$$q_1(m, 0) = a_0 \Gamma_1 v_0(m_0) v_0(m) \delta_{\alpha_g}^l + \Gamma_1 \sum_{j=1}^{\ell-1} a_j v_j(m_0) v_j(m), \quad (32)$$

$$q_2(m, 0) = a_0 \Gamma_2 v_0(m, 0) v_0(m) \delta_{\alpha_g}^l + \Gamma_2 \sum_{j=1}^{\ell-1} a_j v_j(m_0) v_j(m). \quad (33)$$

Substituting (31)–(33) into (10) and (11) and recalling relations (25) and (26), we arrive at the solution for the general boundary conditions as

$$w_1(m, s) = a_0 \alpha_d^s v_0(m_0) v_0(m) \delta_{\alpha_g}^l + \sum_{j=1}^{\ell-1} a_j \cos^s(k_j) v_j(m_0) v_j(m) \quad (34)$$

and

$$\begin{aligned} q_1(m, s) &= a_0 v_0(m_0) \delta_{\alpha_g}^l \left[\Gamma_1 U_s \left(\frac{\alpha_a}{\sqrt{2}} \right) v_0(m) - \frac{\Gamma_2 + \Gamma_1}{\sqrt{2}} U_{s-1} \left(\frac{\alpha_a}{\sqrt{2}} \right) v_0(m+1) \right] + \sum_{j=1}^{\ell-1} a_j v_j(m_0) \\ &\times \left[\Gamma_1 U_s \left(\frac{\cos k_j}{\sqrt{2}} \right) v_j(m) - \frac{\Gamma_2 + \Gamma_1}{\sqrt{2}} U_{s-1} \left(\frac{\cos k_j}{\sqrt{2}} \right) v_j(m+1) \right], \end{aligned} \quad (35)$$

$$\begin{aligned} q_2(m, s) &= a_0 v_0(m_0) \delta_{\alpha_g}^l \left[\Gamma_2 U_s \left(\frac{\alpha_a}{\sqrt{2}} \right) v_0(m) - \frac{\Gamma_2 - \Gamma_1}{\sqrt{2}} U_{s-1} \left(\frac{\alpha_a}{\sqrt{2}} \right) v_0(m-1) \right] + \sum_{j=1}^{\ell-1} a_j v_j(m_0) \\ &\times \left[\Gamma_2 U_s \left(\frac{\cos k_j}{\sqrt{2}} \right) v_j(m) - \frac{\Gamma_2 - \Gamma_1}{\sqrt{2}} U_{s-1} \left(\frac{\cos k_j}{\sqrt{2}} \right) v_j(m-1) \right]. \end{aligned} \quad (36)$$

D. Solution for totally absorbing case

We will now provide some numerical results for the special case of totally absorbing boundaries at the two ends. In this case, Eqs. (34)–(36) will be reduced to

$$w_1(m, s) = \frac{2}{\ell} \sum_{j=1}^{\ell-1} \sin \left(\frac{\pi j m_0}{\ell} \right) \sin \left(\frac{\pi j m}{\ell} \right) \cos^s \left(\frac{\pi j}{\ell} \right), \quad (37)$$

$$\begin{aligned} q_1(m, s) &= \frac{2}{\ell} \sum_{j=1}^{\ell-1} \sin \left(\frac{\pi j m_0}{\ell} \right) \left[\Gamma_1 U_s \left(\frac{\cos \left(\frac{\pi j}{\ell} \right)}{\sqrt{2}} \right) \sin \left(\frac{\pi j m}{\ell} \right) \right. \\ &\quad \left. - \frac{\Gamma_2 + \Gamma_1}{\sqrt{2}} U_{s-1} \left(\frac{\cos \left(\frac{\pi j}{\ell} \right)}{\sqrt{2}} \right) \sin \left(\frac{\pi j (m+1)}{\ell} \right) \right], \end{aligned} \quad (38)$$

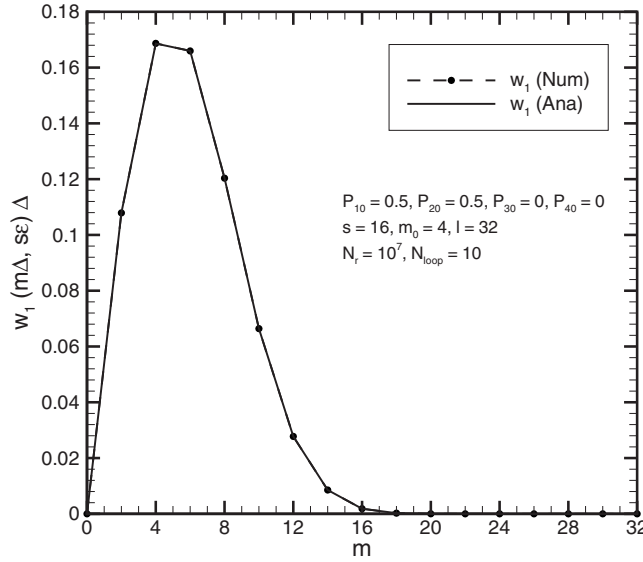


FIG. 1. Comparison of analytical solution for $w_1(m\Delta, s\epsilon)\Delta$ with that obtained from counting paths in random walk simulations for totally absorbing boundary conditions.

$$q_2(m, s) = \frac{2}{\ell} \sum_{j=1}^{\ell-1} \sin\left(\frac{\pi jm_0}{\ell}\right) \left[\Gamma_2 U_s \left(\frac{\cos\left(\frac{\pi j}{\ell}\right)}{\sqrt{2}} \right) \sin\left(\frac{\pi jm}{\ell}\right) - \frac{\Gamma_2 - \Gamma_1}{\sqrt{2}} U_{s-1} \left(\frac{\cos\left(\frac{\pi j}{\ell}\right)}{\sqrt{2}} \right) \sin\left(\frac{\pi j(m-1)}{\ell}\right) \right]. \quad (39)$$

Because the Green's functions satisfy reciprocity conditions, it is permissible to interchange m and m_0 in the above expressions without changing the field values. The solution for a continuous space can be obtained by carrying out the same limiting process as outlined in Ref. 7. For example, Eq. (37) reduces to the expression for the probability density function of the diffusion process with a diffusion constant D with two totally absorbing points at $x=0$ and $x=L$ and an impulsive initial condition at $x=x_0$,

$$p(x, t) = \frac{2}{L} \sum_{j=1}^{\infty} \sin\left(\frac{\pi j x_0}{L}\right) \sin\left(\frac{\pi j x}{L}\right) \exp\left(-\frac{\pi^2 j^2 D t}{2L^2}\right), \quad (40)$$

a result that is found in many texts including Ref. 9. The results given in (34)–(39) are exact, and as such, no validation is necessary. Nevertheless, it is interesting to compare the numerical data they generate with those generated through direct random walk simulations, as the latter will more likely be employed for more complicated time-dependent boundaries. In such cases, the analytical results developed here will serve more as a validation check for the numerical results generated through random walk simulations. The analytical results (labeled “Ana” in the figures) and the results obtained by counting the fractional number of paths (labeled “Num” in the figures) in the 4RW simulations with initial conditions set at $P_{10}=0.5=P_{20}$ from the location $m_0=4$ are shown in Figs. 1 and 2 at $s=16$ and for $\ell=32$. For reference, the solution for Schrödinger equation in free space is also shown in Fig. 2. For the parameters chosen in Fig. 2, the solution with boundaries will differ from the free-space case only for $0 \leq m \leq 12$, as is clearly seen in the figure. A large number of realizations (about 10^8) was needed to arrive at numerically converging results, particularly for the Schrödinger equation whose solution involves difference in probabilities. Both

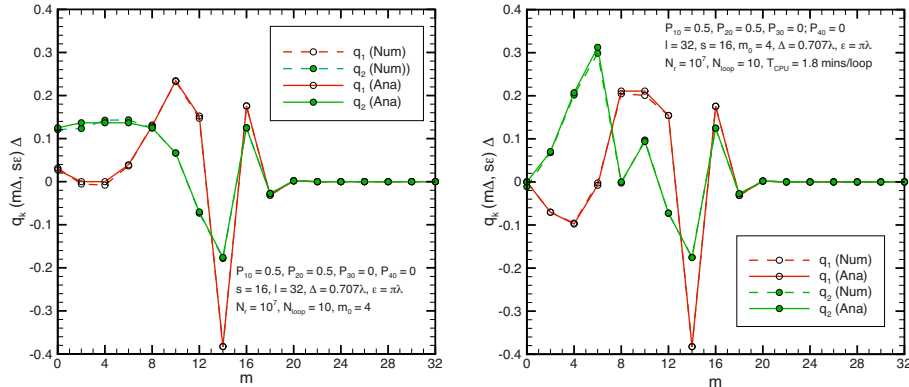


FIG. 2. (Color online) Comparison of the exact solution of Schrödinger equation with that obtained through counting paths in random walk simulations.

figures reveal that the numerical simulated results closely mimic the analytical formulas derived here. The numerical results also underscore the importance of a good numerical random number generator, particularly needed for large s , as the sample size grows exponentially with s . The use of entwined paths described in Ref. 17 is a possible means of getting around this difficulty, although details have only been demonstrated there for the relativistic case of bounded particle speed.

E. Appropriateness of the 4RW model to wave propagation problems

It might be worthwhile to comment a little on the relationship between the 4RW model and the continuous parabolic equation for which the former is being targeted in numerical computations. For the parabolic equation encountered in a number of wave propagation problems such as in underwater acoustics, radio wave propagation, and optical wave propagation in fibers, the governing equation for the field variable ψ in a homogeneous medium with time-harmonic excitation is of the form

$$\frac{\partial \psi}{\partial t} = \frac{i}{2k_0} \frac{\partial^2 \psi}{\partial x^2}, \quad (41)$$

where the independent variable t denotes the axial spatial coordinate and the variable x denotes the lateral spatial coordinate, $k_0 = 2\pi/\lambda$ is the wavenumber in the medium, and λ is the wavelength of the time-harmonic excitation. Equation (41) describes two-dimensional wave propagation in the t - x -plane subject to the approximation that all waves travel within an angle of $\theta = \pm 15^\circ$ about the axial direction.³ It can be shown that the maximum step size Δ in the lateral direction is restricted by $\Delta \leq \lambda/(2 \sin \theta_{\max})$, where θ_{\max} is the maximum angle of propagation with respect to the t -axis. As θ is restricted to a value less than 15° for the parabolic approximation to be valid, we may take $\sin \theta_{\max} \approx \tan \theta_{\max} \approx \Delta/\epsilon$. We then get the approximate relation

$$\pi\epsilon \gtrsim k_0\Delta^2. \quad (42)$$

It may be remarked parenthetically that the inequality (42) translates to the condition that the Schrödinger equation is valid for describing particle motion for nonrelativistic particle speeds with the normalized speed $v/c \lesssim \tan \theta_{\max} \approx 0.27$ for $\theta_{\max} = 15^\circ$, where c is the speed of light in free space. In the 4RW model, the relation between the step sizes of the form $\epsilon = k_0\Delta^2$ is implied and this is consistent with the inequality (42). If $\Delta = \lambda/\sqrt{2}$, then this relation implies that $\epsilon = \pi\lambda$. Both of these values are well within the maximum values permitted by the parabolic equation approximation and it is believed that the 4RW model constitutes a very appropriate discretization scheme for numerically handling the parabolic equation.

IV. CONCLUSIONS

Analytical expressions have been provided for the transitional probabilities of a 4RW model on a lattice constrained in space with dissimilar boundaries and subject to partially reflecting boundary conditions. Special cases of perfectly absorbing boundaries and perfectly reflecting boundaries have been treated. Solution for the transitional probabilities evaluated at time s to the diffusion process is shown to involve s th power of the averaging operator D_x , whereas those of the Schrödinger equation involve Chebyshev polynomials of the second kind of order s and $s-1$ with argument $D_x/\sqrt{2}$. These are the general characteristics of diffusion and Schrödinger processes in the 4RW model irrespective of the boundary conditions. Different boundary conditions will dictate different choices of the eigenfunctions in which the initial probabilities at $s=0$ are expanded. The eigenfunctions in the most general case will involve exponential function as well as harmonic functions. The exponential function will only exist when the parameters present in the boundary conditions satisfy certain relationship. While the results presented in this paper should have a significance of their own for random walk with dissimilar boundaries, it is hoped that they will also serve as benchmark cases for numerical stochastic methods designed to solve more complicated situations. Although it had not been the major focus of the current paper, numerical implementation of the random walk solution necessitates the availability of an effective random number generator to sufficiently populate all portions of the sample space. This is particularly critical for field evaluated at large times. Extension of these results to higher dimensions and to situations with a potential field is a topic worthy of further study and will be taken up in the future.

ACKNOWLEDGMENTS

This work was funded in part by the U.S. Army Research Office under ARO Grant No. W911NF-04-1-0228 and by the Center for Advanced Sensor and Communication Antennas, University of Massachusetts at Amherst, under the Air Force Research Laboratory Contract No. FA8718-04-C-0057.

- ¹G. N. Ord and A. S. Deakin, *J. Phys. A* **30**, 819 (1997).
- ²G. N. Ord and J. A. Gualtieri, *Phys. Rev. Lett.* **89**, 250403 (2002).
- ³F. B. Jensen, W. A. Kuperman, M. B. Porter, and H. Schmidt, *Computational Ocean Acoustics* (Springer, New York, 1994).
- ⁴J. R. Kuttler and R. Janaswamy, *Radio Sci.* **37**, 5-1 (2002).
- ⁵R. Janaswamy, IEEE Applied Electromagnetics Conference, Kolkata, India, 2007, Vol. 1, Paper No. AEMC.2007.4638046, pp. 1-4; available online at <http://ieeexplore.ieee.org/arnumber=4638046&isnumber=4637999&punumber=4629478>.
- ⁶B. V. Budaev and D. B. Bogy, *Q. J. Mech. Appl. Math.* **55**, 209 (2002).
- ⁷R. Janaswamy, *J. Phys. A: Math. Theor.* **41**, 155306 (2008).
- ⁸J. C. Strikwerda, *Finite Difference Schemes and Partial Differential Equations*, 2nd ed. (Society of Industrial and Applied Math, Philadelphia, PA, 2004).
- ⁹G. H. Weiss, *Aspects and Applications of the Random Walk* (North-Holland, New York, NY, 1994).
- ¹⁰F. B. Knight, *Essentials of Brownian Motion and Diffusion* (American Mathematical Society, New York, NY, 1981).
- ¹¹J. Masoliver, J. M. Porra, and G. H. Weiss, *Phys. Rev. E* **48**, 939 (1993).
- ¹²G. N. Ord, *Ann. Phys.* **250**, 51 (1996).
- ¹³G. Barton, *Elements of Green's Functions and Propagation* (Oxford University Press, New York, NY, 1989).
- ¹⁴W. Feller, *An Introduction to Probability Theory and Its Applications*, 2nd ed. (Wiley, New York, NY, 1970), Vol. 2.
- ¹⁵E. W. Montroll, *J. Math. Phys.* **6**, 167 (1965).
- ¹⁶S. A. Martucci, *IEEE Trans. Signal Process.* **42**, 1038 (1994).
- ¹⁷G. N. Ord, J. A. Gualtieri, and R. B. Mann, *Found. Phys. Lett.* **19**, 471 (2006).

Effective Local Absorbing Boundary Conditions for a Finite Difference Implementation of the Parabolic Equation

Selman Özbayat, *Student Member, IEEE*, and Ramakrishna Janaswamy, *Fellow, IEEE*

Abstract—Domain truncation by transparent boundary conditions for open problems where parabolic equation is utilized to govern wave propagation are in general computationally costly. We utilize two approximations to a convolution-in-space type discrete boundary condition to reduce the cost, while maintaining accuracy in far range solutions. Perfectly matched layer adapted to the Crank-Nicolson finite difference scheme is also verified for a 2-D model problem, where implemented results and stability analyses for different approaches are compared.

Index Terms—Crank-Nicolson finite-difference scheme, discrete transparent boundary condition, parabolic equation, perfectly matched layer.

I. INTRODUCTION

RADIOWAVE propagation governed by Helmholtz equation can be approximated by parabolic equation (PE) under certain circumstances if the spectral content of waves is narrow around the propagation axis and refractive index inhomogeneity of the atmosphere is smooth [1]. Conventional narrow-angle PE approximation of wave propagation assumes maximum ray angle to be within $\pm 15^\circ$ with respect to the axis of propagation (range). The main distinction between the Helmholtz equation and PE is the reduction of 2nd order derivative to a 1st order derivative along the range, which is based on ignoring back-scattering in the domain. This facilitates a marching-in range technique for numerical computation. Most practical PE applications are concerned with far-range wave behavior, e.g., in tropospheric calculations, where the grazing angles are already very small, which makes the error due to large propagating angles affordable. Another application of PE is propagation prediction in tunnels with lossy walls, where the wave content in long ranges is dominated by the small grazing angles as well [2]. Two schemes are available for the solution of PE, first of which is the split-step Fourier technique that is applicable when analytical eigenfunctions exist for the underlying geometry. Although this technique is numerically very efficient, it is inconvenient for boundary modeling [1].

Manuscript received June 16, 2010; revised October 01, 2010; accepted October 26, 2010. Date of publication March 03, 2011; date of current version May 04, 2011. This work was funded in part by Army Research Office under Grant W911NF-10-1-0305

The authors are with the Center for Advanced Sensor and Communication Antennas, University of Massachusetts Amherst, MA 01003 USA (e-mail: ozbayat@ecs.umass.edu; janaswamy@ecs.umass.edu).

Color versions of one or more of the figures in this paper are available online at <http://ieeexplore.ieee.org>.

Digital Object Identifier 10.1109/TAP.2011.2122300

A purely numerical scheme (such as the one based on finite differences (FD)) on the other hand is applicable for more general geometries with boundaries. The subject matter of the current paper is applicable to the latter and Crank-Nicolson FD scheme is assumed to be employed in particular.

Numerical solution of wave propagation in open geometries requires domain truncation at a designated reference. Thus an absorbing boundary needs to be placed for typical PE applications. Formulated first by Berenger [3] for Maxwell's Equations and used for several different electromagnetic problems, perfectly matched layer (PML) adapted to the Crank-Nicolson scheme is one way of domain truncation in open PE problems. Collino [4] implemented PML for a variational solution to PE, while Levy [5] proposed it as a straightforward truncation for FD and split-step Fourier techniques for PE. However, there are no numerical implementation results for PML adapted to FD schemes of PE so far. The first goal of this paper is to provide some numerical comparison results for PML, when adapted to a narrow-angle PE. A question that arises with the use of PML to PE is how effective it is, given that the PE is most accurate in the region of validity where the PML is most reflective, i.e. for zero grazing angle.

Domain truncation can also be achieved by placing transparent boundary conditions (TBC) and there are two approaches to implementing the TBCs. A TBC produces zero boundary reflections into the geometry it is defined for. Several authors [1], [6] introduced the discretized version of a continuous TBC. Reference [7] showed that this approach cannot assure unconditional stability when the FD discretization does not match the discretization of the continuous TBC. It can also be shown that this boundary condition (BC) is not reflection-free. Alternatively, one could start directly from the Crank-Nicolson FD discretization of PE, done by Ehrhardt and Arnold [7], and derive numerically exact discrete transparent boundary condition (DTBC), that involves all the boundary field values starting from the initial plane. For example, if the field is desired at the 1,000th range step, the exact discrete BC will involve convolution of field values on the boundary layer at all the previous 999 range steps. Although accurate, DTBC will increase the CPU time, particularly for long ranges and there is a need for considering approximate BCs that are local. The second goal of the paper is to propose some local boundary conditions and show numerical comparisons for their performance.

The first localization approach to DTBC will be to truncate the boundary layer convolution by relatively small number of terms, and utilize for convolution not only the boundary layer values but also some already computed interior field values,

thereby resulting in what we will call the localized DTBC (LDTBC). This is achieved by employing a rational approximation to the spectral transfer function. The second localization is also in the form of a rational approximation, namely an approximation by partial fractions using simple poles in the complex \mathcal{Z} -transform domain [8]. Both localizations will prove to be more accurate than simple truncation of the boundary layer convolution. The stability analysis for the first approximation will be carried out using a 3-layer reduced domain relying on pole locations in z -domain, which will turn out to be a sufficient check for the stability of the whole geometry. Simple pole locations in z -domain will determine whether the true discrete problem is stable for the second approximation.

The main task of numerical verification and simulation of different domain truncations for the discrete PE will be carried out on a simple model problem, i.e. 2-D free-space truncated by the absorbing layer of interest at some elevation and by Perfect Electric Conductor (PEC) as terrain ground plane. True terrain may be uneven which will tend to increase the grazing angles of waves upon reflection. We use flat PEC terrain for simplicity, but waves of larger grazing angles are included by modifying the parameters of the Gaussian source. Crank-Nicolson scheme adapted to the model problem is formulated in Section II-A, whereas in Section II-B the PML absorption will be verified for and applied to the problem. The exact DTBC, corresponding to an exact transfer function and its Taylor series in z -domain, is presented in Section II-C. The two approximate localizations to DTBC with stability analyses, implemented results for the model problem and efficiency comparisons will take place in Sections II-D, II-E and III.

II. THEORY

A. Standard PE

The standard PE in the reduced variable $\psi(x, t)$ is

$$\frac{\partial \psi}{\partial t} = \frac{i}{2k_o} \frac{\partial^2 \psi}{\partial x^2} + ik_o V \psi \quad (1)$$

which is obtained after narrow-angle approximation to the Helmholtz wave equation [9], $i = \sqrt{-1}$, k_o is the wave-number in free space at the radian frequency w and V is the modified refractive index of the medium. Here we use $V = 0$ for the simple free space domain, t represents the range coordinate variable and x the elevation coordinate variable of the computation domain depicted in Fig. 1. We denote x_h as the domain height and x_t as the elevation at which the excitation will be placed. This will be referred to as the mean height of the excited Gaussian source that will be discussed later in the paper. The more general case of non-zero but constant V for $x \geq x_h$, can be handled by making the transformation $\varphi = \psi e^{ik_o V t}$ in the end result as in [10].

Utilizing the discrete notation $\psi(j\Delta x, n\Delta t) = \psi_j^n$ and expanding central differences around discrete range $n + 1/2$ for the t derivatives in (1), the Crank-Nicolson discretization for (1) is

$$\begin{aligned} \psi_j^{n+1}(R + 2i) - i(\psi_{j-1}^{n+1} + \psi_{j+1}^{n+1}) \\ = \psi_j^n(R - 2i) + i(\psi_{j-1}^n + \psi_{j+1}^n) \end{aligned} \quad (2)$$

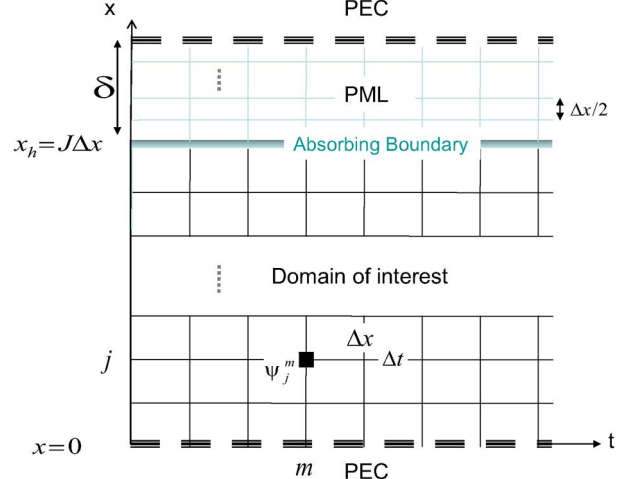


Fig. 1. Computation domain, top layer being absorbing boundary and bottom layer PEC.

where $R = (2k_o \Delta x)^2 / k_o \Delta t$ is a unit-less parameter. Note that field values at half-integer range $n + 1/2$ are avoided by averaging same fields at n and $n + 1$ and this scheme is of second order convergence [11]. As it will be discussed later, the solution to this system of equations will require updating by two tri-diagonal matrices after each march-in range.

B. PML Implementation

The two-dimensional PML is constructed by replacing the height x with complex stretched-coordinate \tilde{x} [4] given by

$$\tilde{x}(x) = x + i \int_0^x \sigma(s) ds. \quad (3)$$

We use a parabolic profile for the normalized conductivity σ (unit-less)

$$\sigma(x) = \begin{cases} \sigma_o \eta_o k_o (x - x_h)^2, & x \geq x_h \\ 0, & x < x_h \end{cases} \quad (4)$$

where η_o is the wave impedance in free space and σ_o is the true conductivity (S/m). Recall that the product $\sigma_o \eta_o$ has units m^{-1} thus $\sigma(x)$ remains unit-less. The coordinate transformation in (3) will be stable for the Sommerfeld radiation condition, since an $e^{-iw\tau}$ time convention in time τ is used. The standard PE in (1) in the stretched-coordinates becomes

$$\frac{\partial \psi}{\partial t} = \frac{i}{2k_o} \frac{1}{1 + i\sigma(x)} \frac{\partial}{\partial x} \left[\frac{1}{1 + i\sigma(x)} \frac{\partial}{\partial x} \psi \right]. \quad (5)$$

Equation (5) discretized utilizing Crank-Nicolson FD scheme with $\sigma(j\Delta x, t) = \sigma_j$ becomes [11]

$$\begin{aligned} \psi_j^{n+1} & \left[R + \frac{i}{1 + i\sigma_j} \left(\frac{1}{1 + i\sigma_{j+1/2}} + \frac{1}{1 + i\sigma_{j-1/2}} \right) \right] \\ & - \frac{i}{1 + i\sigma_{j+1/2}} \psi_{j+1}^{n+1} - \frac{i}{1 + i\sigma_{j-1/2}} \psi_{j-1}^{n+1} \\ & = \psi_j^n \left[R - \frac{i}{1 + i\sigma_j} \left(\frac{1}{1 + i\sigma_{j+1/2}} + \frac{1}{1 + i\sigma_{j-1/2}} \right) \right] \\ & + \frac{i}{1 + i\sigma_{j+1/2}} \psi_{j+1}^n + \frac{i}{1 + i\sigma_{j-1/2}} \psi_{j-1}^n. \end{aligned} \quad (6)$$

Note that $\sigma_o = 0$ basically reduces (6) to (2) (that governs the domain in Fig. 1 without PML above). The quadratic dependence of $\sigma(x)$ on height x given in (4) and the associated wave absorption provides the freedom to place a PEC on top of the PML, since the rays in the layer experience a controlled loss twice as they reflect back into the domain. The PML of thickness δ , a few wavelengths above x_h is backed with a PEC. We have control over σ_o and δ to meet a desired reflection coefficient Γ . The reflection coefficient from the PML for a ray with paraxial angle θ is [3], [4]

$$\Gamma(\theta) = -\exp[-i2k_o \sin \theta \tilde{x}(x_h + \delta)]. \quad (7)$$

For the parabolic profile this results in an equation for the true conductivity in terms of the desired reflection coefficient as

$$\sigma_o = \frac{-3 |\ln \Gamma(\theta_o)|}{2k_o^2 \sin \theta_o \eta_o \delta^3}. \quad (8)$$

One aspect to note about reflection is that, it is smaller for wider angle θ , which leads to the fact that PML simulates a better absorption for waves propagating at wider angles than those at shallower angles [1]. The reflection coefficient is one in magnitude for $\theta = 0$. That is why σ_o is chosen by setting the reflection Γ for a small grazing angle, i.e. a small θ_o , so that higher angle content will reflect even less back into the domain. One restriction on layer thickness δ is that it is not desirable to set it too high, since it will increase the matrix sizes for each marching-in range computation. Computation of (6) obviously involves two tri-diagonal matrices to update the field vector after each marching in range, and entries of both matrices are constants. Therefore, the matrix equation representation of (6) for the domain in Fig. 1 is of the form

$$\mathbf{S}\underline{\psi}^{n+1} = \mathbf{T}\underline{\psi}^n. \quad (9)$$

The length of the vector $\underline{\psi}$ is $J-1+\delta/\Delta x$ and since we need half-integer indices of $\sigma(x)$ in (6), we discretize the conductivity two times finer than we do the field $\underline{\psi}$.

C. DTBC Derivation

We will now derive and approximate the DTBC directly for the Crank-Nicolson scheme. The original derivation of DTBC is given in [7]. However, we derive a newer form that is amenable to approximations. Solving the discrete PE on and above the boundary layer while assuming a decaying nature of the fields above this layer results in [7]

$$\sum_{u=0}^n \kappa_u \psi_j^{n-u} + \sum_{v=0}^n \mu_v \psi_{j-1}^{n-v} = 0, \quad j \geq J. \quad (10)$$

κ_u and μ_v are weights of convolutions on a layer j and on the layer $j-1$, below it. Such a convolution-type relation of fields leads us to use \mathcal{Z} -transforms, which translates the relation of field values on successive layers on or above the boundary layer to a polynomial in the complex z -domain. We will define the \mathcal{Z} -transform as $\mathcal{Z}\{\psi_j^n\} = U_j(z) := \sum_{n=0}^{\infty} \psi_j^n z^n$ where $|z| < 1$ and the inverse \mathcal{Z} -transform as $\psi_j^n = (1/2\pi i) \oint_{C_z} U_j(z) z^{-n-1} dz$ [10].

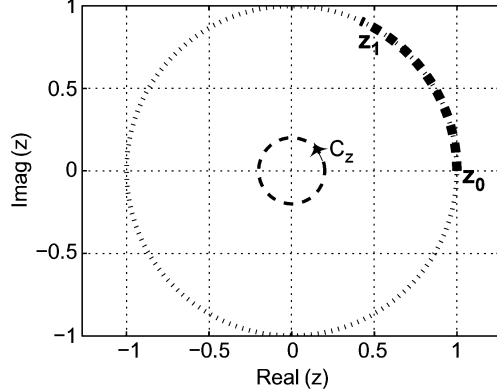


Fig. 2. Branch cut on z -plane for $|\nu(z)| = 1$, $R = 0.63$. C_z is the inversion circle around origin.

The inversion contour C_z is counter-clockwise as indicated in Fig. 2. Also, as in [7], $\psi_j^0 = 0$ is assumed for $j \geq J-2$. Taking the \mathcal{Z} -transform on both sides of (2) results in

$$(1+z)U_{j+1}(z) + [(1-z)iR - 2(1+z)]U_j(z) + (1+z)U_{j-1}(z) = 0 \quad (11)$$

where $j \geq J-1$. More specifically, the transfer function relating field on the boundary layer in z -domain to the field on the layer just below it is

$$\begin{aligned} \nu(z) &= \frac{U_{J-1}(z)}{U_J(z)} \\ &= 1 - i \frac{R}{2} \frac{1-z}{1+z} - \sqrt{-i \frac{R}{2} \frac{1-z}{1+z} \left(2 - i \frac{R}{2} \frac{1-z}{1+z} \right)}. \end{aligned} \quad (12)$$

The transfer function $\nu(z)$ in general is multi-valued, therefore the $\sqrt{\cdot}$ operator above is defined to ensure $|\nu(z)| > 1$, which reflects decaying nature of $U_j(z)$ for $j \geq J-1$. Let f denote a modified transfer function defined as

$$\begin{aligned} f(z) &= (1+z)\nu(z) \\ &= (1+z) - 2i(1-z) \tan \alpha_o \\ &\quad - 2 \tan \alpha_o \sqrt{-ie^{-i\alpha_o} \csc \alpha_o} \\ &\quad \times \sqrt{-z^2 e^{2i\alpha_o} + 2iz \sin \alpha_o e^{i\alpha_o} + 1} \end{aligned} \quad (13)$$

with $\tan \alpha_o = R/4$. We introduce a new variable $\zeta = -ize^{i\alpha_o}$ and take the first derivative of (13). This is so that the resulting function $1/\sqrt{\zeta^2 - 2 \sin \alpha_o \zeta + 1}$ can be expressed in terms of Legendre polynomials as $\sum_{m=0}^{\infty} \zeta^m P_m(\sin \alpha_o)$ where $P_m(\cdot)$ are the Legendre polynomials. The derivative of f with respect to ζ is

$$f'(\zeta) = A + B \frac{\zeta - \sin \alpha_o}{\sqrt{\zeta^2 - 2 \sin \alpha_o \zeta + 1}} \quad (14)$$

where

$$\begin{aligned} A &= -\sin \alpha_o + i \left(\frac{1 + \sin^2 \alpha_o}{\cos \alpha_o} \right) \\ B &= -2i \sqrt{\tan^2 \alpha_o + i \tan \alpha_o}. \end{aligned} \quad (15)$$

Using the Legendre function representation of the quantity under the radical sign gives

$$f'(\zeta) = A - B \sin \alpha_o \sum_{m=0}^{\infty} \zeta^m P_m(\sin \alpha_o) + B \sum_{m=0}^{\infty} \zeta^m P_{m-1}(\sin \alpha_o) \quad (16)$$

with $P_{-1}(.) = 0$. The Taylor-series expansion of $f'(\zeta)$ can be written as

$$f'(\zeta) = \sum_{m=0}^{\infty} c_m \zeta^m \quad (17)$$

with coefficients

$$\begin{aligned} c_0 &= A - B \sin \alpha_o P_o(\sin \alpha_o) \\ c_m &= B [P_{m-1}(\sin \alpha_o) - \sin \alpha_o P_m(\sin \alpha_o)] \\ m &= 1, 2, \dots \end{aligned} \quad (18)$$

As already indicated the multi-valued $\sqrt{\cdot}$ operator in (12) is defined such that $|f(0)| = |\nu(0)| > 1$. Using (17), the modified and exact transfer functions can finally be written as

$$\begin{aligned} f(\zeta) &= - \sum_{m=0}^{\infty} a_m \zeta^m \\ a_0 &= -f(0) \\ a_m &= -\frac{c_{m-1}}{m}, \quad m = 1, 2, \dots, \infty \end{aligned} \quad (19)$$

and

$$\nu(z) = \frac{f(z)}{1+z} = -\frac{\sum_{m=0}^{\infty} \gamma_m z^m}{1+z} \quad (20)$$

with $\gamma_m = (-i)^m e^{im\alpha_o} a_m$. The region of convergence of the series depends on the singularities of $\nu(z)$. This leads to the investigation of properties of the exact transfer function f in z -plane. The branch cut in z -plane for the function given in (12) is depicted in Fig. 2, as a bold dashed curve separating the two sheets with $|\nu(z)| = 1$ on it. It can be shown that the branch points are at $z_0 = 1$ and $z_1 = (R+4i)/(R-4i)$. The point z_1 in general could be in either of 1st or 2nd quadrants depending on R .

There is a practical reason why (12) or (20) is not suitable for direct use in the Crank-Nicolson scheme. Because we are interested in a bounded computation domain that starts at range $t = 0$, the infinite summation in (20) reduces to a convolution of size $N = t/\Delta t$ where t is the range of the present marching step. The upper limit in (20) will be referred as being N henceforth. This is usually a large number, especially for fine discretizations and far ranges. To have an idea of how this transfer function affects the boundary computation in the spatial domain and how ineffective the convolution is, the nodes used in convolution are depicted in Fig. 3. There, the boundary is at J^{th} discrete layer and all the nodes on that layer are involved in the first summation in (10). The two nodes on $J - 1^{st}$ layer contribute to the second summation in (10), i.e. only the first two

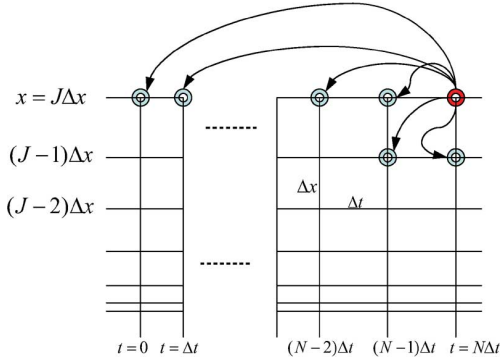


Fig. 3. Exact DTBC convolution stencil. The two layers of nodes correspond to the two convolutions in (10). This stencil is valid at all altitudes greater than $J\Delta x$.

terms are non-zero in the second summation. This is because of the second degree polynomial in the denominator of $\nu(z)$.

D. LDTBC Approximation

The first approximation we propose is replacing the length- $N + 1$ summation in (20) by a Padé approximant of order P/Q ,

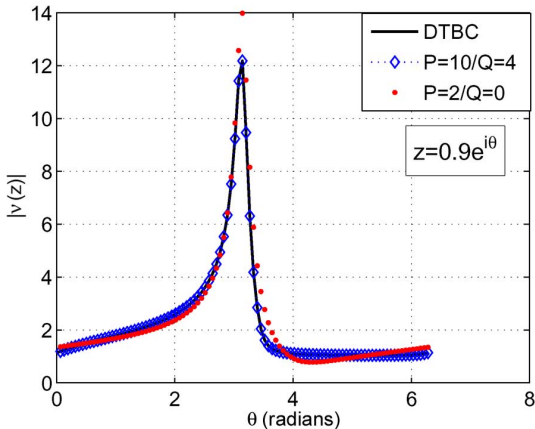
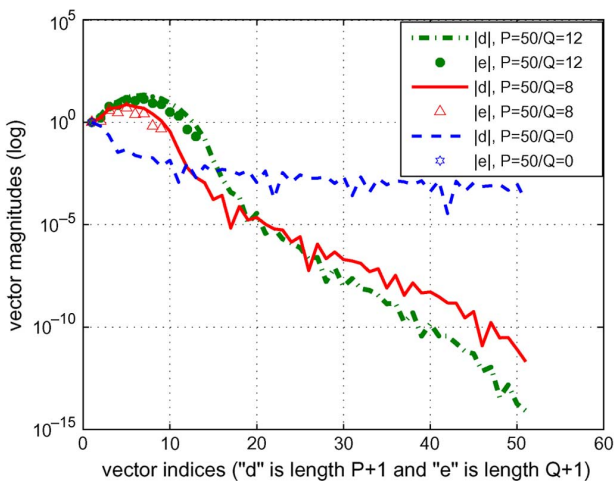
$$f(z) \approx -\frac{\sum_{u=0}^P d_u z^u}{\sum_{v=0}^Q e_v z^v} \quad (21)$$

where d_u 's and e_v 's are determined by conventional Padé approximant procedure [12]. The Taylor series expansion derived in (20) is very convenient in this regard. We will set the leading denominator coefficient $e_Q = 1$ for convenience. The relations (20) and (21) result in $\nu(z)$ also in a rational form

$$\nu(z) = \frac{f(z)}{1+z} \approx -\frac{\sum_{u=0}^P d_u z^u}{\sum_{v=-1}^Q g_v z^{v+1}} \quad (22)$$

where $g_v = e_v + e_{v+1}$ for $v = 0, 1, \dots, Q-1$, $g_Q = e_Q$ and $g_{-1} = e_0 = 1$.

The transfer function $\nu(z)$ in (22) is plotted in Fig. 4 for $z = 0.9e^{j\theta}$, $\theta = [0, 2\pi]$. It should be stressed at this point that the Padé approximation above is obtained by enforcing continuities at the origin in z -domain, thus an approximation of order P/Q is less valid at points closer to the unit circle than near the origin. Points on $|z| = 0.9$ circle are utilized above for the sake of demonstrating severity of the approximation (the approximation will be worst for $|z| = 1$). It is seen that an approximation of higher order is always favorable and that an approximation of order $P = 10/Q = 4$ is good enough to mimic the exact transfer function for this case. To appreciate the effect of using interior domain points, i.e. on one layer below the absorbing layer, the coefficient magnitudes for the two cases, $Q = 0$ case and $Q > 0$ case, are shown in Fig. 5 for the same P value. Clearly, the dominance of low order terms in vector \underline{d} against higher order terms in it is much more significant for approximations with

Fig. 4. $|\nu(z)|$ for the z values on the $|z| = 0.9$ circle, $R = 0.63$.Fig. 5. Pade coefficient magnitudes of different LDTBC approximations, $R = 0.63$. \underline{d} and \underline{e} are respective vectors of numerator and denominator coefficients of the corresponding approximation in each case.

higher Q . In other words to realize a given accuracy, a smaller P is needed with $Q = 12$ than with $Q = 8$, which will result in a smaller convolution in boundary terms. More simulation results for different P/Q pairs are shown in Section III.

Transforming from $\nu(z)$ in (22) back to the spatial domain through inverse \mathcal{Z} -transform, the boundary value at arbitrary range index n is determined in terms of already computed boundary values (convolution of length $P + 1$) and values on the uppermost computation layer (convolution of length $Q + 2$). Inverse \mathcal{Z} -transform of (22) gives the boundary value at arbitrary discrete range $n\Delta t$, $n = 1, 2, \dots, N = t/\Delta t$, as

$$\psi_J^n = -\frac{1}{d_0} \left[\sum_{u=1}^P d_u \psi_J^{n-u} + \sum_{v=0}^{Q+1} g_v \psi_{J-1}^{n-v} \right]. \quad (23)$$

The matrix representation of (6) with an absorbing boundary at the top and PEC boundary at the bottom will be of the form

$$\underline{\mathbf{S}}\underline{\psi}^{n+1} = \underline{\mathbf{T}}\underline{\psi}^n + i\underline{W}^n \quad (24)$$

where

$$\underline{\mathbf{S}} = \begin{bmatrix} R + 2i & -i & 0 & \cdot & \cdot \\ -i & R + 2i & -i & 0 & \cdot \\ 0 & -i & R + 2i & -i & 0 \\ \cdot & \cdot & \cdot & \cdot & \cdot \\ \cdot & \cdot & 0 & -i & s_c \end{bmatrix} \quad (25)$$

$$\underline{\mathbf{T}} = \begin{bmatrix} R - 2i & i & 0 & \cdot & \cdot \\ i & R - 2i & i & 0 & \cdot \\ 0 & i & R - 2i & i & 0 \\ \cdot & \cdot & \cdot & \cdot & \cdot \\ \cdot & \cdot & 0 & i & t_c \end{bmatrix} \quad (26)$$

$$s_c = R + 2i + i \frac{g_0}{d_0} \quad (27)$$

$$t_c = R - 2i - i \frac{g_1}{d_0} \quad (28)$$

and for $j = 1, 2, \dots, J - 1, Q > 0$,

$$W_j^n = \delta_j^{J-1} \left[\sum_{u=0}^{P-1} \left(\delta_0^u - \frac{d_{u+1}}{d_o} \right) \psi_J^{n-u} - \sum_{v=2}^{Q+1} \frac{g_v}{d_o} \psi_{J-1}^{n-v+1} \right]. \quad (29)$$

The unconditional stability of Crank-Nicolson scheme in free space is well known [11]. However, when the exact transfer function (20) is approximated as in (22), the scheme is not unconditionally stable anymore and it may not be trivial to derive a stability condition for a given geometry and discretization. Instead we study the reduced geometry depicted in Fig. 6, i.e. for a 3 layer problem—the top layer being absorbing boundary, the mid-layer being the computation domain and the bottom layer being the PEC. Although we do not prove that stability of this reduced geometry leads to stability of the larger domain in Fig. 1, it still provides a stability check since the instability comes only from associated approximate boundary conditions. The excitation we use in this case is a point source of magnitude A , located in the middle layer, i.e. at $j = J - 1 = 1$. Since an impulse in spatial domain will have components in all angular spectra, such an excitation is a worst-case test for the narrow-angle PE. For this small geometry, (2) reduces to

$$(R + 2i)\psi_1^{n+1} - i\psi_2^{n+1} = (R - 2i)\psi_1^n + i\psi_2^n \quad (30)$$

where $\psi_0^n = 0, n = 0, 1, \dots$ is enforced by the PEC bottom layer. Recalling $\psi_1^0 = A$, the z -domain version of (30) becomes

$$\begin{aligned} (R + 2i)z^{-1}U_1(z) - A(R + 2i)z^{-1} - iz^{-1}\frac{U_1(z)}{\nu(z)} \\ = (R - 2i)U_1(z) + i\frac{U_1(z)}{\nu(z)} \end{aligned} \quad (31)$$

where $U_j(z) = \mathcal{Z}\{\psi_j^n\}, j = 1, 2$ and $\nu(z) = U_1(z)/U_2(z)$. Furthermore, substitution of (22) for $\nu(z)$ gives

$$U_1(z) = A \sum_{l=0}^P \frac{r_l}{z - z_l} \quad (32)$$

r_l being residues and z_l poles of the function. Equation (32) is true if $P > Q$. This is always the case here, because P/Q pairs were obtained through truncating a very long convolution by P

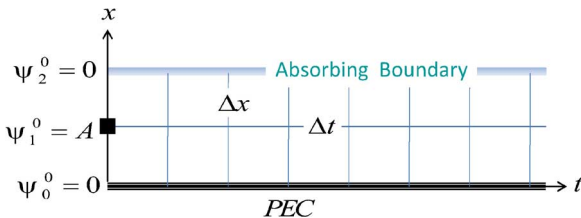


Fig. 6. Reduced geometry to study the approximation stability.

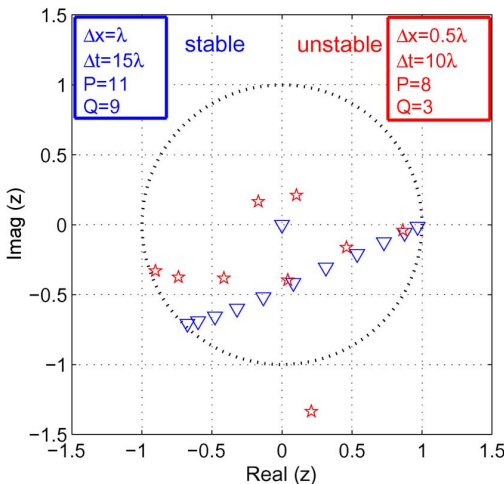


Fig. 7. Inverse pole locations $1/z_l$ for reduced-domain LDTBC solutions on complex \mathcal{Z} -domain, $l = 0, 1, \dots, P$. Stars are for the unstable case and inverted triangles are for the stable case.

terms and padding new terms to a length-2 convolution (revisit Fig. 3). Transforming (32) back to spatial domain gives

$$\psi_1^n = \mathcal{Z}^{-1} \{U_1(z)\} = A \sum_{l=0}^P r_l z_l^{-n-1}. \quad (33)$$

It is sufficient for the poles z_l of the system to all lie outside the unit circle for stability (or each $1/z_l$ should lie inside the unit circle). Fig. 7 depicts two cases, where the approximation is stable in one case and unstable in the other.

One point to emphasize about this stability analysis is that it may not always be trivial to find a stable P/Q pair for every discretization Δx and Δt , especially if P and Q are desired to be significantly large.

E. Approximation by Partial Fractions: LDTBC₂

LDTBC formulated above introduces tolerable inaccuracy while avoiding a convolution involving all boundary values. However, the numerical results for quite long ranges will show that a large order P/Q pair will have to be used in LDTBC approximation. The immediate question of how easy is it to find a stable P/Q pair for moderate orders comes up. Moreover, such a stable LDTBC approximation still requires two convolutions at each march-in range, i.e. one on boundary layer values of order $P+1$ and another of order $Q+2$ on one layer below the boundary. This may be undesirable.

A second approximation to the exact and modified transfer functions in (19) is still in the form of a Padé approximant, but of order $[L/(L+1)]$. This case has been proposed in [8] and corresponds to approximation by partial fractions with $L+1$

simple poles in the z -domain, assuming they all lie outside the unit circle (to assure stability). The polynomial corresponding to the spatial boundary layer convolution in (20) is approximated as

$$f(z) \approx - \sum_{m=0}^{M-1} \gamma_m z^m - z^M \sum_{l=0}^L \frac{b_l}{z - h_l}. \quad (34)$$

Namely, the approximation is

$$\begin{aligned} \sum_{m=0}^{n-M} \gamma_{m+M} z^m &\approx \sum_{m=0}^{n-M} \tilde{\gamma}_{m+M} z^m \\ &= \sum_{l=0}^L \frac{b_l}{z - h_l}. \end{aligned} \quad (35)$$

We retain the original coefficients for the first M terms so that

$$\tilde{\gamma}_m = \begin{cases} \gamma_m, & m = 0, 1, \dots, M-1 \\ + \sum_{l=0}^L \frac{b_l}{h_l^{M+m+1}}, & m \geq M \end{cases} \quad (36)$$

with $M \geq 1$ and $|h_l| > 1$, $l = 0, 1, \dots, L$. The standard Padé approximant that gives unique set of h_l 's involves a $(L+1) \times (L+1)$ linear system to solve [12] and b_l 's are determined by back-substitution; thus $\tilde{\gamma}_m = \gamma_m$ is satisfied for $m = 0, 1, \dots, 2L+M+1$. The higher order approximate coefficients given by (36) are desired to mimic exact γ_m at as many points as possible, and the quality of the approximation at orders higher than $2L+M+1$ will be the deciding factor for choosing L . A scheme with very large L is however prone to instabilities due to numerical roundoff. The stability condition of this approximation is directly given by the system pole locations, i.e. $|h_l| > 1$ is necessary for stability. However the original function will have branch point singularities at $|z| = 1$ as already demonstrated in Fig. 2, this implies that the approximation could be marginally stable at best. Any LDTBC₂ solution that turns out to be unstable is expected to possess almost all of its poles in the vicinity of the unit circle but some just inside. In other words, when approximate $f(z)$ is expanded by $L+1$ partial fractions, all or most of the poles of the solution are outside the unit circle, the rest are very close to and inside the unit circle if any.

Practical calculations reveal that the LDTBC₂ approximation with more than 30-to-40 simple poles (depending on R) turn out to be unstable. Approximation with fewer poles on the other hand cannot ensure the approximate coefficients in (36) to mimic high order exact coefficients. Such an approximation results in inaccuracy in long-range simulations. For instance, LDTBC₂ approximation of order $L > 100$ is necessary for $\tilde{\gamma}_m$ to accurately mimic γ_m in (36), $m = 0, 1, \dots, 2000$ for the given $R = 0.63$. The poles of the LDTBC₂ approximation that are inside the unit circle for this case are depicted in Fig. 8. Furthermore, given an unstable LDTBC₂ approximation with given number of poles and an R parameter, LDTBC₂ approximation with more poles for the same R is also another unstable approximation. Hence appropriate pole location modifications are necessary for the sake of stability. Because the poles making the approximation unstable are close to the unit circle, inverting their magnitudes, while their arguments kept unchanged, results in a new stable approximation with undetermined residues. The

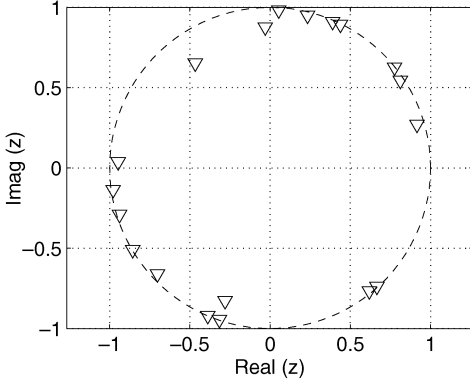


Fig. 8. The poles of $LDTBC_2$ approximate solution lying inside unit circle in the case of $L = 100$, $M = 0$ and $R = 0.63$.

way to set new residues for the “re-located” poles relies on enforcing continuity of the exact transfer function and its derivatives at $z = 0$, up to the order to give a linear system to uniquely determine these new residues. This way of stabilizing $LDTBC_2$ is summarized as follows.

- $LDTBC_2$ with $L+1$ partial fractions (Padé approximation of order $[L/L + 1]$) is applied to approximate the exact solution, B of the simple poles lying inside the unit circle.
- If $B \neq 0$, meaning the approximation is unstable, the poles inside are pushed out of the unit circle through $\tilde{h}_k \equiv h_k / |h_k|^2$, $k = 0, 1, \dots, B - 1$. Note here that h_k and \tilde{h}_k are reordered for convenience.
- $f^{(y)}(0) = (d^y/dz^y)[\sum_{l=0}^{L-B} (b_l/z - h_l) + \sum_{k=1}^B (\tilde{b}_k/z - \tilde{h}_k)]|_{z=0}$ is enforced for $y = 0, 1, \dots, B - 1$ giving unique solution of new residues \tilde{b}_k corresponding to re-located poles \tilde{h}_k . Here h_l are also reordered.

Although the two are in the same rational form, $LDTBC_2$, providing recursive computation, is superior to $LDTBC$. Namely there will not be a whole new boundary layer convolution at each march-in range. Instead, the history on the boundary layer will be cumulative, thus could be recursively computed by adding a new term after each march-in range. The approximation in (35) translates in the spatial domain as

$$\sum_{m=0}^n \gamma_m \psi_J^{n-m} \approx \sum_{m=0}^{M-1} \gamma_m \psi_J^{n-m} + \sum_{l=0}^L D_l(n-M) \quad (37)$$

where

$$D_l(s) = \begin{cases} \frac{b_l}{h_l} \psi_J^s + \frac{1}{h_l} D_l(s-1), & s > 0 \\ 0, & s \leq 0. \end{cases} \quad (38)$$

The convolution of order M in (37) is to be computed at each range step; on the other hand D_l are updated at each step recursively, that results in the boundary layer value at discrete range n

$$\psi_J^n = -\frac{1}{\gamma_0} \left[\sum_{m=1}^{M-1} \gamma_m \psi_J^{n-m} + \sum_{l=0}^L D_l(n-M) + \psi_{J-1}^n + \psi_{J-1}^{n-1} \right]. \quad (39)$$

The reason for keeping the first M -term convolution and not associating it in the approximation is revealed in the nature of

γ_m coefficients for small m . The low order terms of the Legendre polynomials with specific arguments make the first few coefficients very large compared with higher order coefficients [8]. This is why the first $M \tilde{\gamma}_m$ are set to be equal to γ_m . This makes the dynamic range of the coefficients that rational approximation is enforced on smaller, resulting in a more accurate approximation for orders higher than $2L + M + 1$. The fact that the first few coefficients are very large compared with higher order coefficients is depicted in Fig. 5, where \underline{d} reduces to $\underline{\gamma}$ in the case of simple convolution truncation ($Q = 0$ case). Choice of $M = 2$ will improve the coefficient approximation to an extent where it cannot be pushed further, due to the fact that γ_0 and γ_1 are those big coefficients making the dynamic range of coefficient magnitudes huge [8]. The dynamic range of $\underline{\gamma}$ in Fig. 5 ($|\underline{d}|$ in blue) will be more severe for smaller R , thus makes the need to shift the approximation termination by M terms inevitable.

III. NUMERICAL RESULTS

Numerical results for the Crank-Nicolson FD scheme outlined above for $LDTBC$ and $LDTBC_2$ as well as the PML are compared in this section. As mentioned previously, the initial domain truncation enforces $\psi_j^0 = 0$, $j \geq J - 2$ where the absorbing boundary is placed at J^{th} layer. We generate a Gaussian source with a standard deviation σ_x and centered at height x_t , by considering an infinite sum of eigenfunctions of an underlying geometry (parallel plate waveguide with PEC walls at $x = 0$ and $x = x_h$). The approximate Gaussian function is obtained by retaining only the first K number of eigenfunctions

$$\psi(x, t=0) = A \sum_{m=1}^K \sin \frac{m\pi x_t}{x_h} \sin \frac{m\pi x}{x_h} e^{-m^2 \pi^2 \sigma_x^2 / 2x_h^2}. \quad (40)$$

The standard deviation σ_x is chosen so that the effective beam-width remains well within the PE approximation. The solution of the standard PE in (1) at a range t for the excitation in (40) and a PEC boundary at $x = 0$ could be shown to be

$$\begin{aligned} \psi(x, t) = & -A \sqrt{\frac{i}{8}} \sum_{m=1}^K \sin \frac{m\pi x_t}{x_h} e^{-i \frac{m^2 \pi^2 t}{2k_o x_h^2}} e^{-\frac{m^2 \pi^2 \sigma_x^2}{2x_h^2}} \\ & \times \left\{ e^{i \frac{m\pi x}{x_h}} \left[\mathcal{F} \left(\sqrt{\frac{k_o x_h^2}{\pi t}} + \beta_- \right) \right. \right. \\ & \left. \left. + \mathcal{F} \left(\sqrt{\frac{k_o x_h^2}{\pi t}} - \beta_- \right) \right] \right. \\ & - e^{-i \frac{m\pi x}{x_h}} \left[\mathcal{F} \left(\sqrt{\frac{k_o x_h^2}{\pi t}} + \beta_+ \right) \right. \\ & \left. \left. + \mathcal{F} \left(\sqrt{\frac{k_o x_h^2}{\pi t}} - \beta_+ \right) \right] \right\} \quad (41) \end{aligned}$$

where $\mathcal{F}(x) = \int_0^x e^{i(\pi/2)t^2} dt$ is the Fresnel Integral and

$$\beta_{\pm} = \frac{1}{\sqrt{\pi}} \left(\sqrt{\frac{k_o x_h^2}{t}} \pm \sqrt{\frac{tm^2 \pi^2}{k_o x_h^2}} \right). \quad (42)$$

Note that there is no PEC boundary at $x = x_h$ for $t > 0$. The model geometry (2-D free space) is truncated at $x_h = 50\lambda$

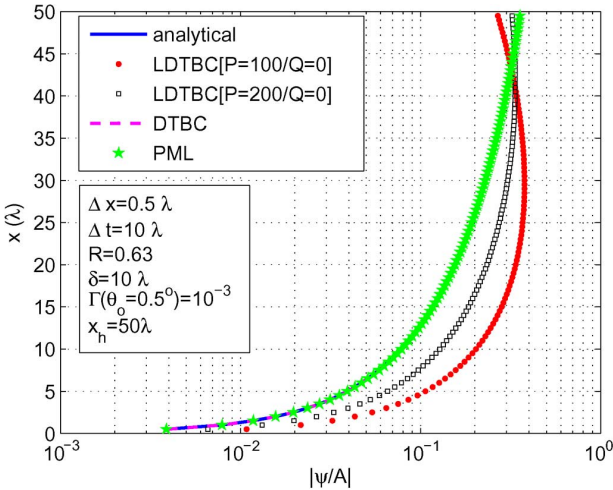


Fig. 9. Field magnitudes (V/m) at range $t = 10,000\lambda$, with $\sigma_x = 1\lambda$, $x_t = x_h/2$ and $K = 400$ for the excitation. The dashed DTBC solution curve is indistinguishable from the solid analytical solution curve.

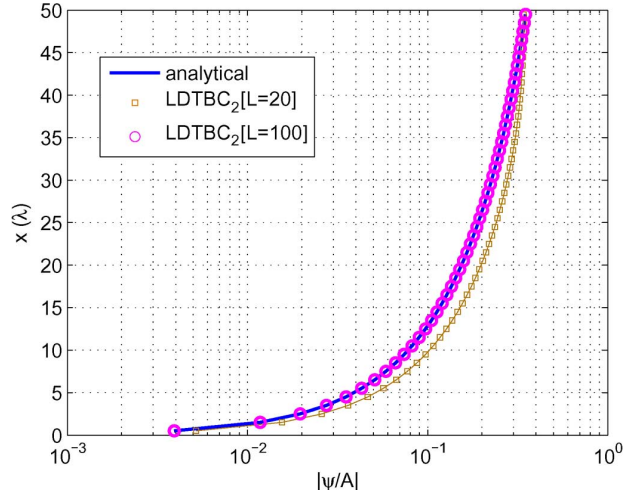


Fig. 11. Field magnitudes (V/m) at range $t = 10,000\lambda$. Simulation parameters are the same as in Fig. 9.

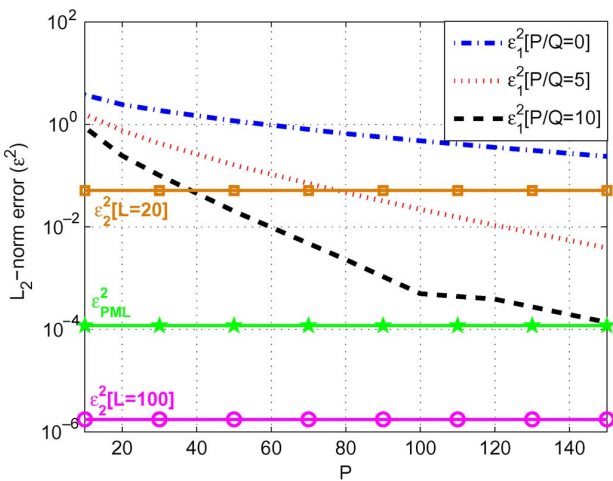


Fig. 10. L_2 -norm errors. The dashed curves show LDTBC errors for varying P . Straight solid lines with squares, pentagrams and circles denote error levels for other numerical solutions. Simulation parameters are the same as in Fig. 9.

above the ground plane. This deliberate choice of a short geometry helps simulate far-range solutions quickly, while each excited mode in (40) is assured to experience lot of reflections from both boundaries before arriving at the observation range. The standard deviation of the excitation in (40) is set as $\sigma_x = 1\lambda$, which results in half power points of approximately $\pm 7.5^\circ$ around the paraxial axis [13].

Fig. 9 depicts solutions at the given range. The exact DTBC solution (dashed) and the PML solution (pentagrams) are obviously very accurate, they match the analytical solution (solid curve) at every altitude of the model geometry. The two approximations, i.e. inaccurate LDTBC solutions are selected on purpose, just to demonstrate that LDTBC approximation is indeed severe and useless if $Q = 0$. In that case it is just truncation of the boundary layer convolution in Fig. 3 by P nodes. We choose an L_2 -norm to quantify magnitude of errors

$$\epsilon^2 = \frac{\sum_j |\psi_j^{soln} - \psi_j^{anal}|^2}{\sum_j |\psi_j^{anal}|^2} \quad (43)$$

where at discrete altitude j , ψ_j^{anal} is the analytical field solution and ψ_j^{soln} is the numerical field solution computed (could be one of PML, DTBC, LDTBC or LDTBC₂). This error is depicted in Fig. 10, where the three dashed curves show the L_2 -norm errors for LDTBC approximations with different Q . The horizontal axis is P varying from 10 to 150, and the three errors expectedly decay with increasing P . One thing to recall is that LDTBC is not necessarily stable for a given P/Q pair, therefore while generating the dashed curves, 10 stable P/Q pairs for each Q are first selected based on the 3-layer model discussed in Section II-D, then the curves are formed by linear interpolation of errors defined in (43). These errors are denoted as ϵ_1^2 .

Because it avoids the computational burden of convolutions, LDTBC₂ on the other hand offers for a fast and accurate approximate solution as depicted in Fig. 11. The LDTBC₂ approximation with 21 poles (brown squares) for given discretization and range is not as accurate; on the other hand the approximation with 101 poles (pink circles) was not stable originally. However, inverting the poles that are inside the unit circle, LDTBC₂ with 101 simple poles becomes stable and accurate as shown in Fig. 11. It avoids the stability problem through re-approximating the residues of re-located poles as outlined in Section II-E, and accurately mimics the analytical solution while being efficient in CPU time. These two LDTBC₂ solutions produce those L_2 -norm errors shown in Fig. 10 with respective color curves, denoted as ϵ_2^2 . These curves denote nothing but the error level for the respective approximations in Fig. 11, and they are independent of P .

The quantity ϵ_{PML}^2 in Fig. 10 denotes the error level for the PML solution (green pentagons) which was also depicted in Fig. 9. At this range, PML results are always accurate and robust. Having control over δ , Γ and hence over σ_o , excellent absorption could be achieved with PML even though a significant spectrum of the excitation contains low grazing angle waves. Another factor in favor of PML over DTBC and thus over LDTBC for long ranges is the computational effort, where the convolution in (23) is avoided altogether. To achieve the very low error level of ϵ_{PML}^2 in Fig. 10, a LDTBC approximation of order $P = 150/Q = 10$ would be needed, which is

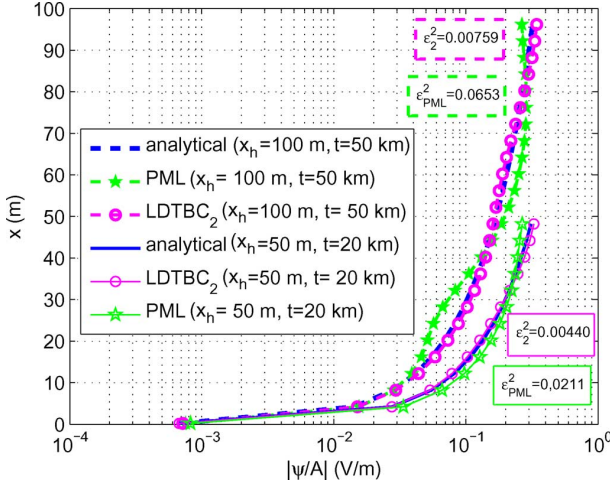


Fig. 12. Field magnitudes (V/m) for two different problems. The solid curves are solutions at $t = 20$ km range for a $x_h = 50$ m domain and dashed lines at $t = 50$ km range for $x_h = 100$ m. The simulation parameters are $\Delta x = 20$ cm, $\Delta t = 5$ m, $x_t = 10$ m, $\sigma_x = 30$ cm, $\delta = 3$ m, $L = 150$.

neither as accurate nor as fast at this range even if stable. Thus it is clear that PML and LDTBC₂ are the two efficient and accurate numerical solutions for domain truncation at moderate ranges.

Because the grazing angle content becomes very narrow for longer ranges, the large ratio between observation range and domain height can render the PML solution inaccurate, i.e. PML would fail to absorb dominant propagating ray [1]. The next set of simulation results will depict such a more realistic case, where the domain (in free space) sizes will be in metric units and larger along both altitude and range. The Gaussian source will reside at $x_t = 10$ m and the operating frequency will be $f = 1$ GHz. Two different cases are depicted in Fig. 12. The dashed curves are solutions at 50 km range for a 100 m domain truncation and the solid curves are solutions at 20 km range for 50 m domain truncation and both are cases of far-range and high-domain simulations for which the LDTBC approximation seemed to fail. For this reason only PML and LDTBC₂ are subject to comparison with respective L_2 -norm errors as marked in the figure. Although both are perfectly absorbing at moderate and small ranges, LDTBC₂ generally produces a smaller error than PML does at far ranges. This is mainly due to the fact that PML cannot be pushed further, i.e. using a thicker matching layer or setting an extremely small reference reflection Γ does not help beyond a certain limit. Indeed, the PML parameters used in Fig. 12 are the limits for this case which do not improve further. The parameter L on the other hand determines the order and the accuracy of LDTBC₂, thus could be set to reasonably large values to simulate accurate absorption. However, there is also a limit to L , thus there is a range-to-height ratio limit to accurate absorbing LDTBC₂ solutions. This limit will be discussed later.

Fig. 13 in this regard analyzes the effect of observation range and domain height with respect to the error. The range that PML or LDTBC₂ with fixed parameters start to fail at is closer when $x_h = 50$ m than when $x_h = 100$ m. This is obvious since each undesired boundary reflection adds inaccuracy to the solution, making smaller altitude boundary problems harder to

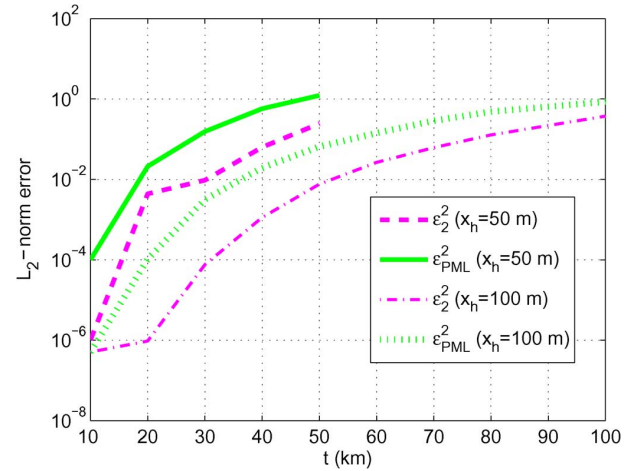


Fig. 13. L_2 -norm errors ϵ^2 . All parameters are the same as in Fig. 12.

simulate at far ranges. The error comparison is held up to a range where the L_2 -norm errors become comparable to 1 (which is huge in this case). The LDTBC₂ error, i.e. ϵ_2^2 in Fig. 13 is always smaller than its PML counterpart ϵ_{PML}^2 . Therefore LDTBC₂ with 151 simple poles for our case is clearly more accurate than any PML solution at far ranges. Is it possible then to improve it further by setting a bigger L ? As indicated before, there also is a certain limit to how big L would be chosen. Firstly, solving for the residues b_l and poles h_l in (38) involves inverting a $(L+1) \times (L+1)$ full-matrix. Moreover this matrix to be inverted contains the derivatives of the transfer function $f^{(y)}(z=0)$, $y = M, M+1, \dots, 2L+M$. Therefore depending on the nature of the transfer function $f(z)$ or of its exact Taylor coefficients $\underline{\gamma}$, this matrix could turn out to be ill-conditioned. Practical simulations for problems of our interest show that the condition number ρ of this matrix becomes extremely large if $L > 200$ and MATLAB cannot handle such ill-conditioned matrices. That is why our choices of L in above results represents approximation orders close to the practical limit.

Fig. 14 shows the CPU time for DTBC and LDTBC₂ convolutions with increasing range. Computing a whole new convolution of all the boundary layer values at each march-in range, exact DTBC solution has quadratic dependency on time for increasing order, whereas recursive computation in LDTBC₂ solution is linearly dependent on range. This comparison between DTBC and LDTBC₂ depicted in Fig. 14 is only for the boundary computation, i.e. the CPU time comparison does not consider time for matrix inversion and update operations, which is not as much as convolutions times at far ranges. Since PML is totally local, i.e. does not employ a boundary layer convolution, there really is no significant added cost to implement it even though the matching layer enlarges the computation domain height by δ . Therefore, we can surely say that PML is the fastest in CPU time among all techniques discussed here.

IV. CONCLUSIONS

The exact DTBC verified is unconditionally stable and presents reflection-free boundary layer for open PE problems. However, its computational deficiency depicted in Fig. 3 and in

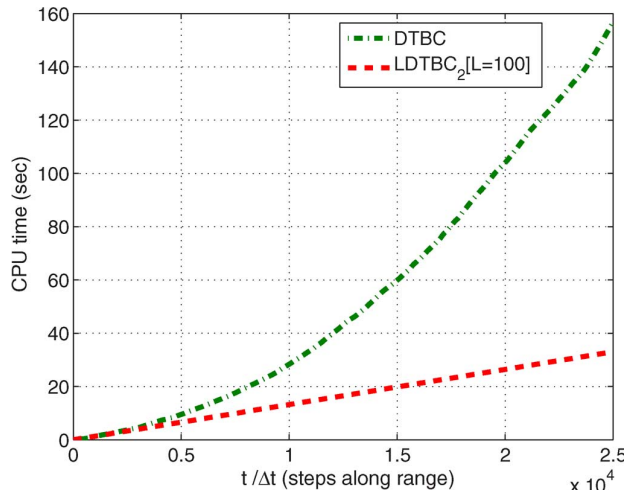


Fig. 14. CPU time taken by the boundary computation (convolution in DTBC case).

Fig. 14 motivates localization of the boundary layer convolution. Although they are conditionally stable and not always as accurate as DTBC, LDTBC and LDTBC₂ are computationally more efficient thus more practical. The FD and narrow-angle PE constraints apply for both exact and approximate transfer functions, therefore the approximations would be preferable at not so close ranges, because they reduce the convolution time significantly. LDTBC₂ especially reduces computation time dramatically and is assured to be stable due to the modifications to residue/pole locations suggested in the paper.

PML on the other hand is robust, fast and is alternative to LDTBC₂ at moderate ranges. We were able to verify that the degree of freedom to set the layer thickness and layer loss in according to the desired maximum reflection Γ_o makes it easily verifiable and applicable to truncate open geometries governed by PE using Crank-Nicolson scheme. Fig. 10 summarizes a comparison, that PML and LDTBC₂ are the appropriate truncation techniques for computations at moderate ranges. The study of these techniques at typical far ranges for high geometries in Fig. 12 and in Fig. 13, where PML fails, is interesting. There, LDTBC₂ remains as the best solution among all. The practical limit to L makes its operation range also limited. We do not delve to numerically improve this ill-condition, and avoiding this restriction would help simulate PE truncation at even farther ranges.

The procedure detailed here for the derivation of approximate boundary conditions is also applicable to the wide-angle PE as long as a suitable discretization scheme is available in the interior domain. This study will be taken up in the future.

REFERENCES

- [1] M. F. Levy, *Parabolic Equation Methods for Electromagnetic Wave Propagation*. London, U.K.: IEE Press, 2000.
- [2] R. Martelly and R. Janaswamy, "Modeling radio transmission loss in curved, branched and rough-walled tunnels with the ADI-PE method," *IEEE Trans. Antennas Propag.*, vol. 58, pp. 2037–2045, Jun. 2010.
- [3] J. P. Berenger, "A perfectly matched layer for the absorption of electromagnetic waves," *J. Comput. Phys.*, vol. 114, pp. 185–200, 1994.
- [4] F. Collino, "Perfectly matched absorbing layers for the paraxial equation," *J. Comput. Phys.*, vol. 131, pp. 164–180, 1997.
- [5] M. F. Levy, "Perfectly matched layer truncation for parabolic wave equation models," *Proc. R. Soc. Lond. A*, vol. 457, pp. 2609–2624, May 2001.
- [6] V. A. Baskakov and A. V. Popov, "Implementation of transparent boundaries for numerical solution of the Schrödinger equation," *Wave Motion*, vol. 14, pp. 123–128, Jan. 1991.
- [7] M. Ehrhardt and A. Arnold, "Discrete transparent boundary conditions for the Schrödinger equation," *Riv. Mat. Univ. Parma*, vol. 6, pp. 57–108, 2001.
- [8] A. Arnold, M. Ehrhardt, and I. Sofronov, "Discrete transparent boundary conditions for the Schrödinger equation: Fast calculation, approximation, and stability," *Commun. Math. Sci.*, vol. 1, no. 3, pp. 501–556, 2003.
- [9] M. F. Levy, "Transparent boundary conditions for parabolic equation solutions of radiowave propagation problems," *IEEE Trans. Antennas Propag.*, vol. 45, pp. 66–72, Jan. 1997.
- [10] R. Janaswamy, "Transparent boundary condition for the parabolic equation modeled by the 4RW," *IEEE. Antennas Wireless Propag. Lett.*, vol. 8, pp. 23–26, May 2009.
- [11] K. W. Morton and D. F. Mayers, *Numerical Solution of Partial Differential Equations*, 2nd ed. Cambridge, U.K.: Cambridge Univ. Press, 2008.
- [12] G. A. J. Baker and P. Graves-Morris, *Padé Approximants*, II ed. New York: Press Syndicate of Univ. Cambridge, 1996.
- [13] R. Janaswamy, "Radio wave propagation over a nonconstant imittance plane," *Radio Sci.*, vol. 36, pp. 387–405, May–Jun. 2001.



Selman Özbayat (S'08)

██████████. He received Bachelor's degree in electrical and electronics engineering from Bilkent University, Ankara, Turkey, in 2008.

In September 2008, he joined the Antennas and Propagation Laboratory, University of Massachusetts, Amherst, where he is currently working toward the Ph.D. degree. His research interests include parabolic equation methods for radio wave propagation, random walk methods for electrodynamics and computational electromagnetics.

Mr. Özbayat is a student member of the Applied Computational Electromagnetic Society (ACES).



Ramakrishna Janaswamy (F'03) received the Ph.D. degree in electrical engineering from the University of Massachusetts, Amherst, in 1986, the Master's degree in microwave and radar engineering from IIT-Kharagpur, India, in 1983, and the Bachelor's degree in electronics and communications engineering from REC-Warangal, India, in 1981.

From August 1986 to May 1987, he was an Assistant Professor of electrical engineering at Wilkes University, Wilkes Barre, PA. From August 1987 to August 2001, he was on the faculty of the Department of Electrical and Computer Engineering, Naval Postgraduate School, Monterey, CA. In September 2001, he joined the Department of Electrical and Computer Engineering, University of Massachusetts, where he is a currently a Professor. He is the author of the book *Radiowave Propagation and Smart Antennas for Wireless Communications* (Kluwer Academic, November 2000) and a contributing author in the *Handbook of Antennas in Wireless Communications* (CRC Press, August 2001) and *Encyclopedia of RF and Microwave Engineering* (Wiley, 2005). His research interests include deterministic and stochastic radio wave propagation modeling, analytical and computational electromagnetics, antenna theory and design, and wireless communications.

Prof. Janaswamy is a Fellow of IEEE and was the recipient of the R. W. P. King Prize Paper Award of the IEEE TRANSACTIONS ON ANTENNAS AND PROPAGATION in 1995. For his services to the IEEE Monterey Bay Subsection, he received the IEEE 3rd Millennium Medal from the Santa Clara Valley Section in 2000. He is an elected member of U.S. National Committee of International Union of Radio Science, Commissions B and F. He served as an Associate Editor of *Radio Science* from January 1999 to January 2004, and was an Associate Editor of the IEEE TRANSACTIONS ON VEHICULAR TECHNOLOGY from 2003 to 2006. He is currently an Associate Editor of IEEE TRANSACTIONS ON ANTENNAS AND PROPAGATION and of *IETE Technical Reviews*.